

Computer Simulations of Ultrafast Magnetisation Reversal

Thomas Andrew Ostler

A Thesis Submitted for the Degree of Doctor of Philosophy

Department of Physics

University of York

July 2012

Abstract

Magnetisation reversal is a process that is of paramount technological importance, as well as fascinating scientists in the field. Despite its importance, only recently have scientists begun to probe the limits of what can be achieved. Driven by consumer desire for compact devices using large scale storage, the size and time limit of magnetisation reversal have begun to be unravelled by exciting experiments using large scale national facilities and state of the art modelling. In the work presented here we develop a model of a ferrimagnetic material parameterised on experimental observations. The key magnetic features are shown to agree well with experimental measurements and provide a basis for more complex calculations. Using time and element resolved X-ray magnetic circular dichroism experiments, model calculations of laser induced magnetisation dynamics are compared to experimental measurements. We present results of switching on the sub-picosecond timescale and conclude that it is possible to reverse magnetisation using heat alone. The conclusion that magnetisation can be reversed without a directional stimulus is scientifically intriguing and never before predicted. Confirmation of such a reversal mechanism using heat alone is verified experimentally, comparing well with the model predictions.

Contents

List of Figures	7
List of Tables	11
Acknowledgements	12
Declaration	13
1 Introduction	14
1.1 Heat Assisted Magnetic Recording	15
1.2 The Limits of Magnetisation Reversal	17
1.3 Basic Quantities	18
1.3.1 Exchange Interaction	19
1.3.2 Anisotropy	20
1.3.2.1 Linear Reversal	21
1.4 Demagnetisation	23
1.4.1 Interpretation of Demagnetisation Due to Temperature	23
1.4.2 Models of Ultrafast Demagnetisation	23
1.4.3 Two Temperature Model	25
1.5 Models of Static Properties	25
1.5.1 Ising Model	26
1.5.2 Mean Field Model	27
1.6 Dynamic Models	29
1.6.1 The Landau-Lifshitz-Gilbert Equation	29
1.6.1.1 Landau-Lifshitz and Gilbert	30
1.6.2 The Landau-Lifshitz-Bloch Model	31
1.7 Ferrimagnets	33

1.7.1	Simple Ferrimagnet	33
1.8	Experimental Techniques	34
1.8.1	Femtosecond Lasers	35
1.8.2	Synchrotron Radiation	36
1.8.3	X-ray Magnetic Circular Dichroism	36
1.9	Concluding Remarks	38
2	Atomistic Spin Model	40
2.1	Introduction	40
2.2	Extended Heisenberg Hamiltonian	41
2.2.1	Landau-Lifshitz-Gilbert Langevin Equation	42
2.3	Noise Process	43
2.4	Solution of the Landau-Lifshitz-Gilbert Langevin Equation	45
2.4.0.1	The Heun Scheme	45
2.5	Atomistic Model of Amorphous Ferrimagnets	46
2.5.1	Computational Model of Amorphous Ferrimagnets	46
2.5.2	Angular Momentum Compensation	48
2.6	Concluding Remarks	49
3	Static Properties of Transition Metal-Rare Earth Ferrimagnets	50
3.1	Introduction	50
3.2	Summary of Experimental Results	51
3.3	Mean Field Approximation	54
3.4	Mean Field and LLG	57
3.5	Coercivity Calculations	60
3.6	Effect of Exchange	62
3.6.1	Atomistic Model Results	63
3.6.2	Dynamic Effect of TM-RE Exchange	64
3.7	Concluding Remarks	67
4	Relaxation and Damping in Transition Metal-Rare Earth Ferrimagnets	69
4.1	Ferrimagnetic Resonance	69
4.1.1	Effective Landau-Lifshitz-Gilbert Equation	70

<i>Contents</i>	5
4.1.2 Ferrimagnetic Resonance	72
4.1.2.1 Linearising the Effective Landau-Lifshitz-Gilbert Equations	72
4.1.2.2 Absorbed Power	73
4.2 Ferromagnetic Resonance Calculations	74
4.3 Transverse Relaxation and Precession Frequency of Ferrimagnets	76
4.4 Differential Longitudinal Relaxation Time Calculations	78
4.5 Domain Wall Velocity	80
4.6 Susceptibility Calculations	82
4.7 Concluding Remarks	85
5 Ultrafast and Distinct Spin Dynamics in Multi-Component Magnetic Al-	
loys	86
5.1 Introduction	86
5.2 Atomistic Spin Simulations of NiFe	86
5.2.1 Longitudinal Relaxation After a Step in Temperature	88
5.2.2 Calculations of Laser Demagnetisation in NiFe	88
5.3 Experimental Time-Resolved XMCD Dynamics	91
5.4 Compositional Variation of Longitudinal Relaxation in NiFe	94
5.5 Concluding Remarks	96
6 Ultrafast Heating as a Sufficient Stimulus for Magnetization Reversal	98
6.1 Introduction	98
6.2 Transient Ferromagnetic-like State Mediating Ultrafast Reversal	100
6.2.1 Experimental Results	100
6.2.2 Atomistic Model Results	102
6.3 Systematic Study of Physical Parameters on Switching Times	103
6.4 The Role of the Magnetic Field	105
6.5 Experimental Results: Thin Films	108
6.6 The Role of the Compensation Points	110
6.7 Verification in Microstructures	111
6.8 Preventing Reversal	112
6.9 Landau-Lifshitz-Bloch Analysis of Switching by Ultrafast Heating	116

6.9.1	Ferrimagnetic LLB Equation	117
6.9.2	The LLB Equation Close to the Curie Temperature of a Ferrimagnet	119
6.10	Concluding Remarks	124
7	Conclusions	126
7.1	Further Work	128
	Appendices	130
A	Experimental Details of Measuring Time-Resolved Magnetisation Dynamics in NiFe	130
B	Experimental details of Time-Resolved XMCD Measurements on GdFeCo	132
C	Details of Measurements on Microstructures of GdFeCo	135
D	Derivation of the Correlator	136
E	Table of Parameters Used for GdFeCo Simulations	140
	List of Symbols	142
	List of Abbreviations	146
	References	147
	List of Publications	159

List of Figures

1.1	Trilemma of Magnetic Recording	15
1.2	Example Hysteresis Curve of a Ferromagnet	16
1.3	Sketch of the Heat Assisted Magnetic Recording Principle	17
1.4	Magneto-Optical Images of GdFeCo Before and After Femtosecond Laser Excitation	18
1.5	Typical Magnetisation Curves of Nickel	21
1.6	Uniaxial Anisotropy Energy Landscapes	21
1.7	Uniaxial Anisotropy as a Function of Temperature for FePt	22
1.8	Schematic of Linear Reversal	22
1.9	Schematic Interpretations of Temperature Induced Demagnetisation	23
1.10	Typical Two Temperature Model Profile After Femtosecond Laser Heating	26
1.11	Reduced Magnetization for Different Spin Values Calculated Using the Brillouin Function	29
1.12	Multiscale Modelling in Spin Dynamics	33
1.13	Schematic of the B1 Structure	34
1.14	Magnetisation Curve of a Simple Ferrimagnet.	35
1.15	Time-Resolved Pump-Probe MOKE Set-Up	36
1.16	Synchrotron Photon Emission Schematic	37
1.17	Schematic Illustration of XMCD	37
1.18	XMCD Spectra for the Fe $L_{2,3}$ Edges of $CeFe_2$	38
2.1	Schematic of the Different Exchange Interactions in Amorphous Ferrimagnets	47
2.2	Magnetisation Curve of a Ferrimagnet with a Compensation Point.	48
3.1	Schematic Layout of the UE56/1 Beamline and the Experimental Setup at BESSY II	51

<i>List of Figures</i>	8
3.2 Schematic of GdFeCo Sample Thin Film Structure.	52
3.3 XMCD Spectra for $\text{Gd}_{25}\text{Fe}_{65.6}\text{Co}_{9.4}$	52
3.4 Element and Temperature Dependent Hysteresis Loops of GdFeCo using XMCD	53
3.5 Element Specific Temperature Dependence of the Coercive Field and Magnetisation with Temperature for GdFeCo	54
3.6 Experimental Data Showing Temperature Dependent Coercivity of a Range of GdFeCo Compositions.	54
3.7 Schematic of the Self Consistent Method in Mean Field	56
3.8 Magnetisation Curves for GdFeCo for a Range of Gd Concentrations with Comparison to Mean Field	58
3.9 Calculated Magnetisation Curves of GdFeCo for Different RE Concentrations . .	59
3.10 T_C and T_M as a Function of RE Concentration From Experimental Measurements: MFA and LLG	59
3.11 Magnetisation During Calculation of the Coercivity	60
3.12 Calculated Values of Coercivity for Various Concentrations of Gd	61
3.13 Variation of Curie Temperature with Composition and TM-TM Exchange	63
3.14 Variation of Curie Temperature with; Composition, RE-RE Exchange and TM-RE Exchange	64
3.15 Calculated Reduced Magnetisation of the Fe and Gd Sublattices as a Function of Inter Sublattice Exchange	65
3.16 Schematic of the Definition of the Effective Spin Temperature	66
3.17 Effective Spin Temperature as a Function of Time During Demagnetisation . . .	66
3.18 Effective Spin Temperature of the RE During Demagnetisation for a range of TM-RE Exchange	67
4.1 Schematic of the Magnetisation of a Two Sub-Lattice Ferrimagnet	71
4.2 Ferromagnetic Resonance Sketch	74
4.3 Ferromagnetic Resonance of Various Compositions of TM-RE at Zero K	75
4.4 Schematic of the Fitting of Transverse Magnetisation Relaxation Data	76
4.5 $\tau_{\perp}(x)$ Without Applied Field	77
4.6 $\tau_{\perp}(x)$ and ω with RE Content	77
4.7 Critically Damped Transverse Magnetisation	78

4.8	Calculated Integral Relaxation Times of the TM and RE sublattices as a Function of Composition	80
4.9	Schematic of Domain Wall Pinning	81
4.10	Calculated Domain Wall Velocity as a Function of Temperature for GdFeCo	81
4.11	Atomistic Model Calculations of $\tilde{\chi}_{\perp}$ and $\tilde{\chi}_{\parallel}$	84
5.1	Calculations of τ_{\parallel} for the Individual Species in NiFe	88
5.2	Calculation of Laser Demagnetisation in NiFe	89
5.3	Atomistic Model Results of Demagnetisation in NiFe and GdFeCo	90
5.4	Atomistic Model Results of Demagnetisation in Ni ₈₀ Fe ₂₀	91
5.5	Demagnetisation Times with Different Thermal Bath Coupling in NiFe	92
5.6	Experimental Demagnetisation Dynamics of FeNi and GdFeCo	93
5.7	Demagnetisation Time Constants as a Function of Magnetic Moment	94
5.8	Magnetic Moments and Curie Temperatures of Ni _x Fe _{1-x}	95
5.9	Variation of Longitudinal Relaxation Time with Ni _x Fe _{1-x}	96
6.1	Energy Barrier Schematic for Switching in a Magnetic Field	98
6.2	Energy Barrier Schematic of the Effect of Heat	99
6.3	Element-Resolved Dynamics of Gd and Fe Moments After Laser Excitation	100
6.4	XMCD Measurements on GdFeCo for Two Pump Fluences	101
6.5	Energy Transfer in the TTM and LLG	102
6.6	Calculated Time-Resolved Dynamics of Fe and Gd After Laser Excitation	103
6.7	Sublattice Reversal Times as a Function of $J_{\text{TM-RE}}$	104
6.8	Sublattice Reversal Times as a Function of $J_{\text{RE-RE}}$	105
6.9	Reversal Times as a Function of Peak Electron Temperature	106
6.10	Magnetisation Reversal Without a Field	107
6.11	Magnetisation of GdFeCo After a Sequence of Laser Pulses	108
6.12	Magneto-Optical Images of the State of GdFeCo After Laser Excitation, Comparing Above and Below All-Optical Threshold	109
6.13	Experimental Observations of Heat Induced Reversal for a Range of Compositions of GdFeCo, Precluding an Explanation via Crossing T_{M}	110
6.14	Atomistic Model Verification of Reversal Precluding Explanation via Crossing T_{M}	111

<i>List of Figures</i>	10
6.15 XMCD Images at Fe L ₃ Edge of 2 μm wide Gd ₂₅ Fe _{65.6} Co _{9.4} Structures	112
6.16 Calculated Reversal Probability as a Function of Anisotropy	113
6.17 Numerical Simulations Showing the Demagnetisation of a Ferrimagnet with Equal Magnetic Moments	114
6.18 Calculated Time-Resolved Dynamics of the Z-Component of the Fe and Gd Sub- lattice From Localized Atomistic Spin Dynamics	115
6.19 Numerical Calculations Showing the Magnetic Field Required to Prevent Reversal of the Fe Sublattice	115
6.20 Schematic of the Projection of the Magnetisation Vector of One Sublattice onto the Other	119
6.21 Longitudinal Relaxation Rates Close to T_C in the LLB Equation	120
6.22 Phase Portrait of Magnetisation Components During Heat Induced Switching . .	121
6.23 LLB Analysis of the Importance of the Presence of Perpendicular Components of Magnetisation	122
6.24 Precession Induced During Switching for Different System Sizes	123
6.25 Atomistic Model Calculations of a 50ps Transient Ferromagnetic-like State	124
A.1 Experimental XAS/XMCD Spectra of the NiFe alloys	131
B.1 Measured Element-Specific Hysteresis Curves	133
B.2 Schematic of Pump and Probe Mechanism	134

List of Tables

3.1	Relative Error in Coercivity Measurement	62
4.1	Fitting Constants for the Parallel and Perpendicular Susceptibilities	84
5.1	Input Parameters for $\text{Ni}_x\text{Fe}_{1-x}$ Calculations	87
5.2	Calculated Decay Time Constants After Laser Demagnetisation in $\text{Ni}_{50}\text{Fe}_{50}$ and $\text{Ni}_{80}\text{Fe}_{20}$	90
5.3	Experimental Decay Time Constants After Laser Demagnetisation in $\text{Ni}_{50}\text{Fe}_{50}$, $\text{Ni}_{80}\text{Fe}_{20}$ and $\text{Gd}_{25}\text{Fe}_{66}\text{Co}_9$	92
5.4	Input Parameters for $\text{Ni}_x\text{Fe}_{1-x}$	95
E.1	Input Parameters for GdFeCo Model Used to Calculate Equilibrium Magnetisation	140
E.2	Input Parameters for GdFeCo Model Used During Dynamic Calculations	141

Acknowledgements

I would firstly like to thank Professor Roy Chantrell, without whose guidance, support and experience, the work in this thesis would not exist. I also would like to thank all of the people involved in the collaborative works. In particular I would like to thank Professor Theo Rasing, Dr Alexey Kimel, Dr Andrei Kirilyuk, Dr Ilie Radu, Professor Frithjof Nolting and Dr Alexandra Kalashnikova.

I would also like to thank my family and friends for their continued friendship and support. In particular I thank Jamie Verwey for her infinite patience and my two children, Oliver and Benjamin for their endless kindness and love.

I thank also my colleagues at the University of York who have constantly helped me with discussion and feedback, Joe Barker, Richard Evans, Ondrej Hovorka and Cecilia Aas, to name but a few. I would also like to thank Jerome Jackson for his help and advice in putting together this thesis and for his guidance throughout my time in York.

I acknowledge funding from the European Unions framework seven programme, Ultramagneton and travel sponsorship by the European Collaboration Science and Technology “Multiscale Modelling of Materials” (COST P19) programme.

Declaration

In addition to the individual work of the author, this thesis contains the results of a number of collaborators. A range of experimental results are presented, performed by; Ilie Radu and coworkers at the Helmholtz-Zentrum Berlin für Materialien und Energie, Frithjof Nolting and coworkers at the Paul Scherrer Institute and Alexandra Kalashnikova and coworkers at Radboud University Nijmegen. These experimental results are included in chapters 3, 5 and 6. Theoretical contributions from Unai Atxitia and Oksana-Chubykalo-Fesenko of the Instituto de Ciencia de Materiales de Madrid. These contributions can be found in chapters 3 and 6.

All other work is the original work of the author except where explicitly indicated. This work has not been submitted to any other examining body or for any other degree. Much of the work has been published or publicly presented by the author.

Thomas Ostler
York, July 2012

Chapter 1

Introduction

Magnetisation reversal is an important process that has stimulated a great deal of research both experimentally and theoretically throughout the years. With ever increasing use of technological devices employing data storage, the need for larger storage capacity combined with faster access rates increases. Magnetic recording devices are still the most widely used large scale storage device giving the best price per unit of storage. The magnetic recording industry is constantly seeking to improve the areal densities and speed performance of their products. Traditional switching uses a magnetic field to overcome the intrinsic barrier to magnetisation reversal, though this process is fundamentally limited to GHz because the reversal of bits occurs via precession of the magnetisation of its constituents. The rate of this precession is limited by the magnitude of the applied field, typically around 1T in modern devices, meaning that the whole process of reversal takes around 1-2 nanoseconds. In recent years, other mechanisms of reversal have begun to be researched due to the limitation of the timescale of the traditional reversal mechanism.

The aim of the magnetic recording industry is to increase the areal density of the media, a goal that generally requires reduction in the sizes of the bits. Bits tend to be made up of a number of magnetic grains which are single domains. An important physical property of the constituent magnetic materials of these grains is the anisotropy energy. The anisotropy energy gives the magnetisation a preferred orientation with respect to a crystallographic axis. The stronger the anisotropy, the more strongly the magnetisation remains oriented in a particular direction, giving it a higher thermal stability. Decreasing the grain volume, however, means that they are more susceptible to thermal fluctuations, leading to data loss over time. To overcome the thermal stability problem the anisotropy must be increased, though the increase in the anisotropy means that larger fields are required to overcome the anisotropy barrier during writing. Larger fields require more power and on very high anisotropy materials the fields generated by the recording head is not sufficient to cause reversal. This is the so-called *trilemma* of magnetic recording, shown schematically in figure 1.1. The traditional switching mechanism, which involves applying a magnetic field in the opposite direction to the magnetisation, occurs by precession of the magnetisation. This reversal occurs over the intrinsic anisotropy energy barrier of the material. The applied field must be sufficient to overcome the energy barrier provided by the anisotropy for the magnetisation to be switched.

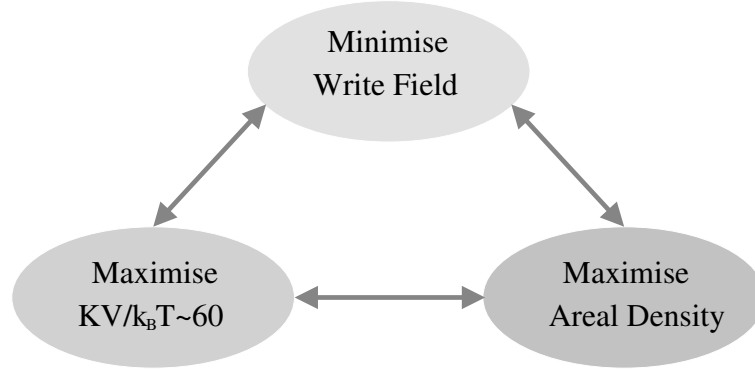


Fig. 1.1: A schematic showing the trilemma of magnetic recording. To increase areal density means the volume of the grains decreases, decreasing thermal stability. To increase thermal stability the anisotropy must be increased, which requires larger write head fields.

To optimise magnetisation switching it is necessary to consider a number of physical parameters. The energy barrier provided by the anisotropy is essential for thermal stability, especially when considering particles on the scale of 10nm, which is the typical grain size in current media. In such confined structures the magnetisation will fluctuate rapidly, depending on the magnitude of the anisotropy. The anisotropy energy barrier is proportional to the product of this anisotropy constant, K , and the volume, V , of the particle. For single domain particles subject to thermal fluctuations the probability for a particle to switch is governed by the Arrhenius-Néel law:

$$f = f_0 \exp\left(-\frac{\Delta E}{k_B T}\right), \quad (1.0.1)$$

where f_0 is the attempt frequency, usually quoted to be 10^9 to 10^{11} Hz for magnetic systems. ΔE is the energy barrier governed by the product, KV , and T is the temperature. For technological applications, a small volume for high areal density is desirable, thus a high anisotropy is needed to restore the KV product. There is a problem presented by increasing the anisotropy constant, which is the fact that higher field strengths are required to overcome the anisotropy barrier. A typical write head, which is a typical electromagnet will generate fields limited to 1-2T. Higher field write strengths are difficult to generate and the fringe effects generated by high fields also lead to difficulties.

1.1 Heat Assisted Magnetic Recording: Use of Lasers in Magnetisation Reversal

One possibility of overcoming the problems associated with improving the areal storage density of magnetic recording media is to temporarily reduce the anisotropy during writing without affecting the long term thermal stability. A relatively new technology which is under active development within the magnetic storage industry is Heat Assisted Magnetic Recording

(HAMR) [1]. Before discussing HAMR, the concept of coercivity should be discussed.

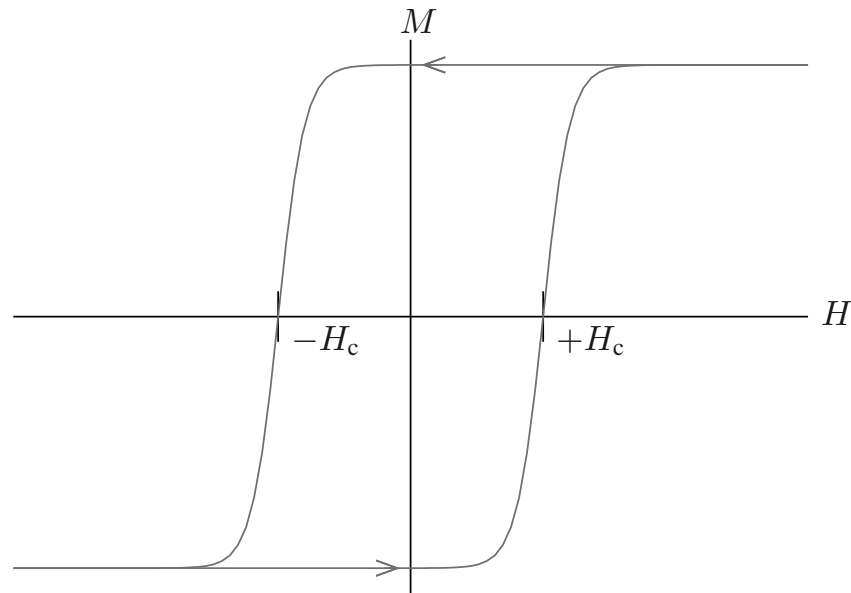


Fig. 1.2: Example of a simple M - H curve showing the coercivity of the ferromagnet. The coercivity is the field at which the magnetisation crosses zero. At high fields the magnetisation reaches saturation, M_s .

The coercivity [2] of a material is the field required to reverse its magnetisation. However, the coercivity depends on how fast the field that is applied to the sample is generated [3] i.e., the sweep rate or writing rate. Figure 1.2 shows how the magnetisation varies as a function of the applied magnetic field, H for a ferromagnet. The field at which the magnetisation crosses zero (for a given sweep rate) is known as the coercivity, H_c , (see figure 1.2). The coercivity of a material depends on many things, such as, the anisotropy, the presence of defects, morphology, chemical segregation, formation of magnetic grains, interface properties, as well as the field sweep rate.

Reversal mechanisms that use a magnetic field to switch a magnetic particle over its energy barrier occur on the nanosecond timescale, as this is the limiting speed of precessional switching. Precessional switching preserves the magnitude of the magnetisation, whereas HAMR employs a combination of heating, which causes a reduction in magnetisation, and precessional switching. The reduction of the magnetisation in turn reduces the anisotropy [4–6]. Such a reduction in the anisotropy then means smaller fields are required to reverse the magnetisation. The whole HAMR process can be achieved on the sub-nanosecond timescale [1], much faster than by precessional reversal alone [7, 8]. Figure 1.3 shows a schematic of the temperature dependence of the coercivity of ferromagnet with temperature. The grey region shows the achievable field head strengths (typically less than 2T), thus heating to the *write-temperature* must occur before magnetisation reversal.

The demonstration, in 2012, of HAMR writing by Seagate Technology (see Ref. [9]) has shown that the basic physics behind the principle is sound. There remain many engineering chal-

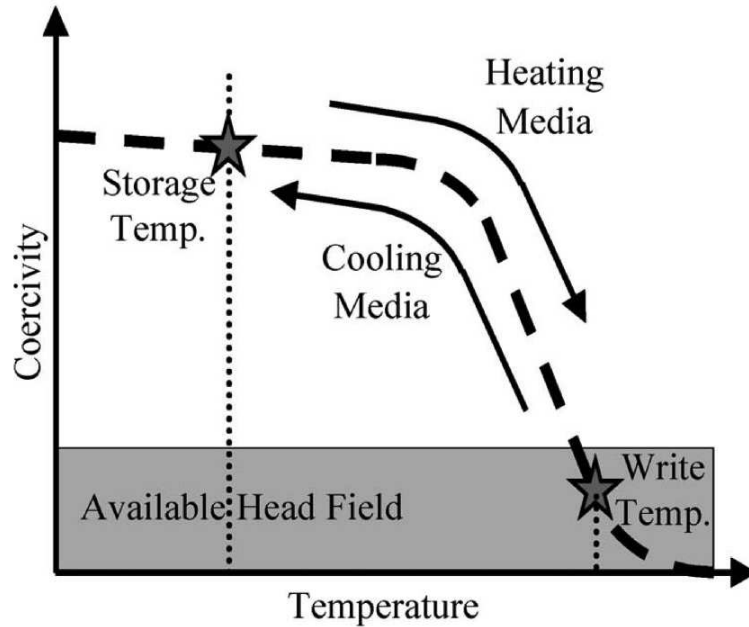


Fig. 1.3: A schematic showing the temperature dependence of H_C in a Heat Assisted Magnetic Recording Media and the principle of the writing process. Figure taken from Ref. [1].

lenges and questions to the technology. The $L1_0$ ordered phase of FePt has been extensively studied [8, 10–13] as a potential candidate for HAMR [14], this ordered phase gives rise to its high magneto-crystalline anisotropy, though little research has been done in terms of what happens to the crystalline structure if laser heating is repeatedly applied. The crystallographic ordering on repeated writes may be governed by the cooling time of the media. If repeated writes affect this ordering, the magnetic properties could also change. Despite the challenges to the technology, a great deal of research is under way into overcoming the problems and investing in future technologies beyond HAMR. It remains an open question as to the limits of HAMR and magnetic recording in general [15].

1.2 The Limits of Magnetisation Reversal

Despite the engineering challenges to overcome in HAMR technology, there is still a scientific interest in the fundamental limits of magnetisation reversal rates in HAMR. If the engineering challenges can be overcome the industry will look forward, beyond the HAMR method. The question of the fundamental limits of reversal has stimulated a great deal of research [15–20]. In Ref. [21], it was shown by Stanciu *et al.* that femtosecond laser pulses could trigger magnetisation reversal on the sub-picosecond timescale. The effect of femtosecond laser pulses of different light chiralities showed that helicity dependent control of the magnetisation was possible. In this experiment, the magnetisation in regions of a GdFeCo thin film were observed using the Faraday effect, which were sensitive to the magnetisation of the transition metal. The region was then excited by different polarisations of light and the magnetisation state was observed once more. Figure 1.4 shows the ground-breaking results of this experiment.

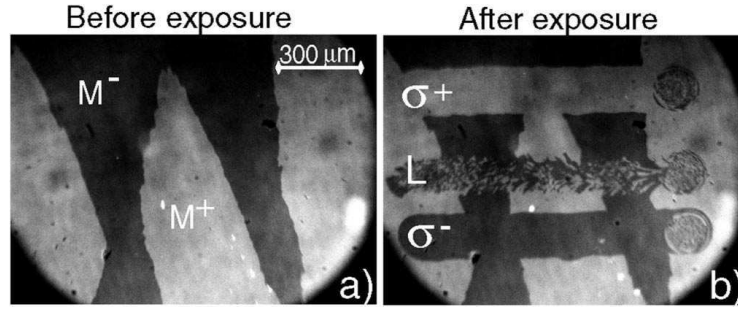


Fig. 1.4: The effect of femtosecond polarised laser pulses on magnetic domains of $Gd_{22}Fe_{74.6}Co_{3.4}$. (a) Magneto-optical images of the initial magnetic state of the sample before exposure to the laser. White and black areas correspond to up (M_+) and down (M_-) magnetic domains, respectively. (b) Domain pattern obtained by sweeping at low speed (around $30 \mu\text{m/s}$) with linear (L), right-handed (σ^+), and left-handed (σ^-) circularly polarised beams across the surface of the sample, with a laser fluence of around 11.4mJ/cm^2 . Image from Ref. [17].

In Ref. [17] Stanciu *et al.* a mechanism for reversal via the Inverse Faraday Effect [22, 23] (IFE) was proposed. This theory considers the effect of the electric field of light on magnetic materials. In Ref. [22], the author considers the magnetohydrodynamic equations of a free electron gas and shows that magnetisation can be induced when light of different helicities are applied to an optically active material:

$$\mathbf{M} \propto \mathbf{E} \times \mathbf{E}^*, \quad (1.2.1)$$

thus for light of opposite helicities, magnetisation is induced in opposite directions. Ref. [23] discusses the treatment of the induced magnetisation as an *effective* field. Time-resolved measurements were not available in Ref. [17] thus stimulating an effort to understand the dynamic behaviour and the role of the effective field generated from the IFE [24–26].

The work presented in this thesis was, in part, motivated by a desire to understand the observed experimental findings of Ref. [17]. In particular the role of the heat and the *effective* magnetic field arising from the IFE. The work presented here will show that any field generated via the IFE can be neglected on the femtosecond timescale in GdFeCo, confirmed by experiments by Khorsand *et al.* [27]. This surprising result represents one of the key findings of this thesis and will be discussed in depth in later chapters.

1.3 Basic Quantities

In this section we introduce the origin of the exchange interaction and a discussion of the anisotropy energy. The basic quantum mechanics of the exchange interaction provides proof of principle of the effect. The anisotropy energy will be discussed in combination with its technological importance, in particular in HAMR media.

1.3.1 Exchange Interaction

The exchange interaction was discovered independently by Heisenberg and Dirac in 1926 and gives rise to magnetic ordering of atomic moments in many magnetic materials. Here the simplest case of two electron wavefunction overlap shows the origin of the effect and provides proof of principle, however, it is not a viable method of calculating exchange values used in the atomistic model. Much of the work presented in this thesis involved atomistic spin dynamics with large numbers of atoms. To calculate such integrals for large systems would require first principles calculations, which are in general computationally quite expensive. Chapter 3 is dedicated to parameterising the exchange values between magnetic moments based on experimental observations. This form of direct exchange is responsible for long range magnetic order observed in all permanent magnets. The discussion in this section is standard, here we follow Blundell (Ref. [28]).

If one considers the simple case of two electrons, the wavefunction for the system can be described as a superposition of the wavefunctions associated with each particle, $\psi_i = \varphi_i(\mathbf{r}_i)\chi_i$; $\varphi_1(\mathbf{r}_1)$ and $\varphi_2(\mathbf{r}_2)$. The product does not obey exchange symmetry, which for electrons must be antisymmetric, therefore the spin part of the wavefunction must be anti-symmetric ($S = 0$) for symmetric spatial wavefunctions, or symmetric ($S = 1$) for anti-symmetric spatial part. Therefore we can write the wave function for the singlet case Φ_S and the triplet Φ_T as:

$$\begin{aligned}\Phi_S &= \frac{1}{\sqrt{2}}[\varphi_a(\mathbf{r}_1)\varphi_b(\mathbf{r}_2) + \varphi_a(\mathbf{r}_2)\varphi_b(\mathbf{r}_1)]\chi_S \\ \Phi_T &= \frac{1}{\sqrt{2}}[\varphi_a(\mathbf{r}_1)\varphi_b(\mathbf{r}_2) - \varphi_a(\mathbf{r}_2)\varphi_b(\mathbf{r}_1)]\chi_T.\end{aligned}\tag{1.3.1}$$

The energies of the two possible states are:

$$\begin{aligned}E_S &= \int \Phi_S^* \hat{\mathcal{H}} \Phi_S d\mathbf{r}_1 d\mathbf{r}_2 \\ E_T &= \int \Phi_T^* \hat{\mathcal{H}} \Phi_T d\mathbf{r}_1 d\mathbf{r}_2.\end{aligned}\tag{1.3.2}$$

The difference between the two integrals is:

$$E_S - E_T = 2 \int \varphi_a^*(\mathbf{r}_1)\varphi_b^*(\mathbf{r}_2)\hat{\mathcal{H}}\varphi_a(\mathbf{r}_2)\varphi_b(\mathbf{r}_2)d\mathbf{r}_1 d\mathbf{r}_2,\tag{1.3.3}$$

where $\hat{\mathcal{H}}$ is the Coulomb operator only. For the singlet state $\mathbf{S}_1 \cdot \mathbf{S}_2 = -\frac{3}{4}$ while for a triplet state $\mathbf{S}_1 \cdot \mathbf{S}_2 = \frac{1}{4}$. Hence the Hamiltonian can be written in the form of an effective Hamiltonian:

$$\hat{\mathcal{H}} = \frac{1}{4}(E_S + 3E_T) - (E_S - E_T)\mathbf{S}_1 \cdot \mathbf{S}_2.\tag{1.3.4}$$

Equation 1.3.4 is the sum of a constant term that can be absorbed into other energy terms, the second term represents the exchange part of interest. The exchange constant for this two

particle system can be written:

$$J = \frac{E_S - E_T}{2} = \int \varphi_a^*(\mathbf{r}_1)\varphi_b^*(\mathbf{r}_2)\hat{H}\varphi_a(\mathbf{r}_a)\varphi_b(\mathbf{r}_b)d\mathbf{r}_1d\mathbf{r}_2. \quad (1.3.5)$$

The sign of J is significant here, if it is greater than zero then, $E_S > E_T$. In this case the triplet state, $S = 1$ is favoured. Conversely if $E_S < E_T$, then $J < 0$ the singlet state ($S = 0$) is favoured. This has consequences for the atomistic model presented in this work, if the sign of the exchange integral between interacting spins is positive this favours parallel alignment of interacting spin moments, i.e. giving rise to ferromagnetic order. If the converse is true, $J < 0$, then the spins favour anti-parallel alignment leading to an anti-parallel ground state.

1.3.2 Anisotropy

The term anisotropy in magnetic media refers to the directional dependence of a materials' magnetic properties. There are a range of different types of anisotropy; shape, single or multi-ion magneto-crystalline anisotropies which have different origins. For example, shape anisotropy is due to the demagnetising energy of a sample and, as the name suggests, depends on the shape. The demagnetising energy in an *infinite* thin film will tend to align spins in the plane of the sample.

An important anisotropy term is the magneto-crystalline anisotropy. This kind of anisotropy leads to favoured magnetisation directions along particular crystallographic directions. In fcc Nickel, the easy axis is along the [111] direction, thus Ni is more easily magnetised in this direction as shown in Figure 1.5. The lowest order expansion of the *uniaxial* anisotropy can be written in spherical coordinates as:

$$E = K_1 \sin^2(\theta) + K_2 \sin^4(\theta) + \dots, \quad (1.3.6)$$

with θ , the angle from the easy axis [30]. If one considers the first uniaxial anisotropy constant, K_1 , depending on the sign, the energy landscape is shown in figure 1.6. Figure 1.6 a) is the case for a positive sign with easy axis and b) is for the negative case with easy plane orientation of the energy minimum.

Though equation 1.3.6 is sufficient for materials with uniaxial anisotropy only, there are other types, depending on the crystalline symmetry of the material such as *cubic*. For cubic systems, the expression for the energy density is:

$$E = K_1^c(m_x^2m_y^2 + m_y^2m_z^2 + m_z^2m_x^2) + K_2^cm_x^2m_y^2m_z^2\dots, \quad (1.3.7)$$

where $\mathbf{m} = (m_x, m_y, m_z)$ is the reduced magnetisation. The magneto-crystalline anisotropy arises from spin-orbit interaction [31].

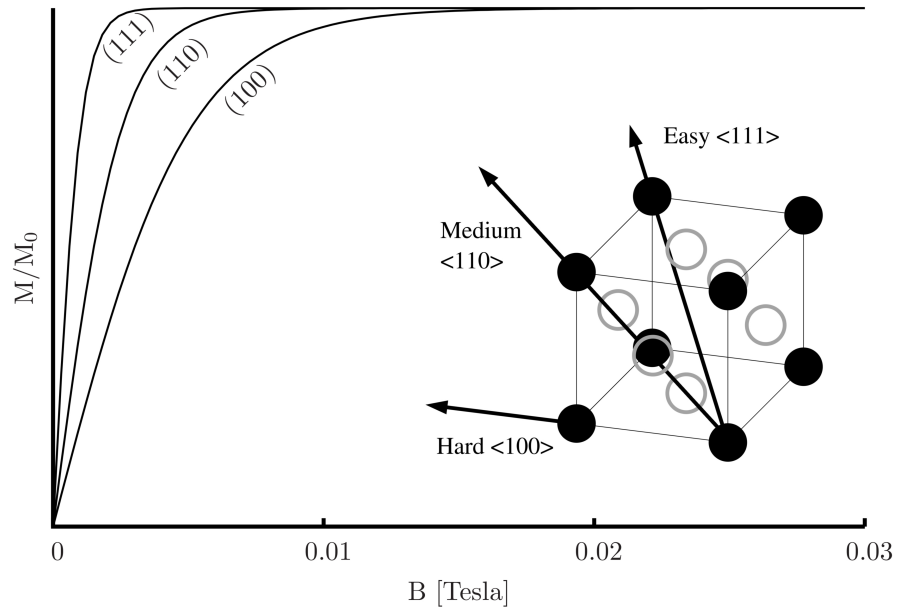


Fig. 1.5: Magnetisation curves for Ni along different crystallographic axes. The $[111]$ is the easy axis for this fcc material (scaled for clarity). The inset shows the different crystallographic axes with the solid circles representing the corners atoms and the circle atoms on the faces. Figure reproduced from Ref. [29].

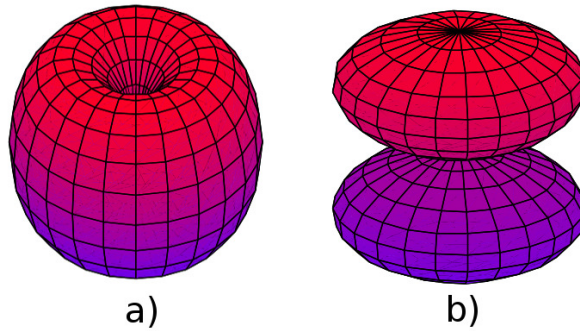


Fig. 1.6: Anisotropy energy landscapes for the uniaxial anisotropy constant, K_1 , for a positive K_1 , easy axis (a), and negative K_1 , easy plane (b).

1.3.2.1 Linear Reversal

A particularly important material, in terms of potential magnetic recording media, is L1₀ FePt [11, 12, 32]. Ab-initio calculations of this important alloy show a moderate *single ion* anisotropy, however the anisotropy of exchange origin is over an order of magnitude larger and is also uniaxial, having an easy axis in the $[001]$ direction. As has already been discussed, magnetisation reversal in an opposing magnetic field occurs via precession. During this type of reversal the magnitude of the magnetisation remains fixed and the vector spirals around on the surface of a sphere. It has recently been shown that in high anisotropy materials, such as FePt, the reversal in a field can occur via a different path. It has been shown that

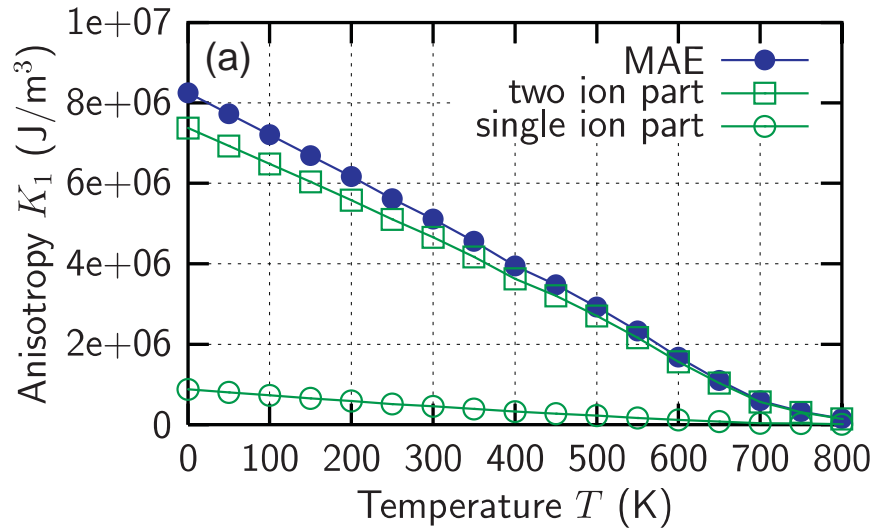


Fig. 1.7: Temperature dependence of the uniaxial anisotropy constant, K_1 . The figure shows the variation of the single ion (magneto-crystalline) and of exchange origin. Figure taken from Ref. [11].

the magnetisation vector, rather than spiralling on a sphere, takes an ellipsoidal trajectory at temperatures close to the Curie temperature and then becomes linear, with no transverse component of magnetisation throughout reversal, in the region very close to the transition temperature [8, 25, 33, 34]. This linear route to magnetisation reversal is faster than the usual precessional motion and is of potential importance in future HAMR devices. The reversal path is one which occurs via decreasing magnetization of the ensemble to zero and then re-magnetizing in the opposite direction as shown schematically in figure 1.8. The linear reversal

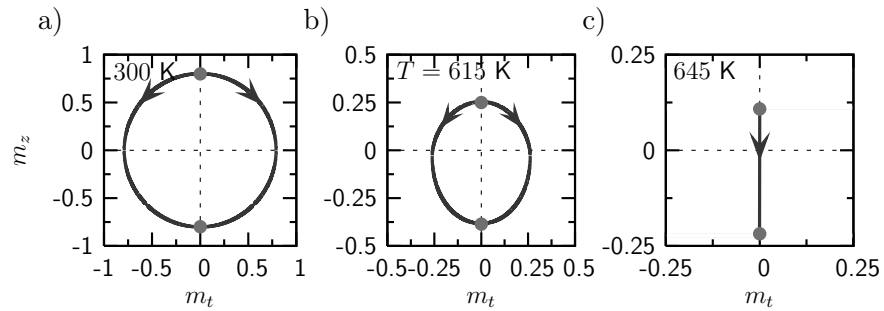


Fig. 1.8: Schematic of linear reversal showing the traditional route to magnetization reversal via precession (a). As the temperature increases the route becomes more elliptical (b) and via the linear reversal mechanism in FePt near the Curie temperature (c). Figure taken from Ref. [33].

mechanism shown in figure 1.8 is important when one considers the heating of magnetic materials to high temperatures. The reversal, without any growth (over the macrospin) of a transverse component of magnetisation is an important concept for discussing the heat induced switching mechanism that we present in chapter 6.

1.4 Demagnetisation

1.4.1 Interpretation of Demagnetisation Due to Temperature

At zero Kelvin, the structure of magnetic moments in a single domain ferromagnetic material can be pictured quite simply as an ordered array of magnetic moments without deviation (figure 1.9a). The length of the arrow, in figure 1.9, depicts the magnitude of the atomic moment. For highly localised moment contributing electrons, such as in some rare-earth metals, magnetic order decreases with temperature because thermal disorder brings about deviations from the ground state with very little reduction in the magnitude of the moment. This is shown in figure 1.9 c). This picture breaks down, however, when we consider itinerant magnetic materials [31] with de-localized magnetic moments. In the *Stoner* model of excitations the Curie temperature can be explained by excitation between spin up (\uparrow) and spin down (\downarrow) states and lead to a reduction in the size of the moment as depicted in figure 1.9 b). For Fe, Co and Ni, the Stoner theory greatly overestimates the Curie temperature by up to five times [31]. In Fe and Co, the excitations responsible for the decrease in magnetisation are localised, as in figure 1.9 c).

In reality for itinerant magnetic materials the degree of localisation near the Curie temperature is often somewhere between the Stoner and Heisenberg pictures (figure 1.9 b) and c)). This suggests that there is the possibility of short range magnetic order which helps to explain the non-vanishing magnetic moment above the Curie or Néel temperature [35]. This picture of short range magnetic order means that order exists on a very localised level. For our model of GdFeCo we are reasonably well justified to consider the case c), though we always bear in mind that other more itinerant effects may be playing a role [36].

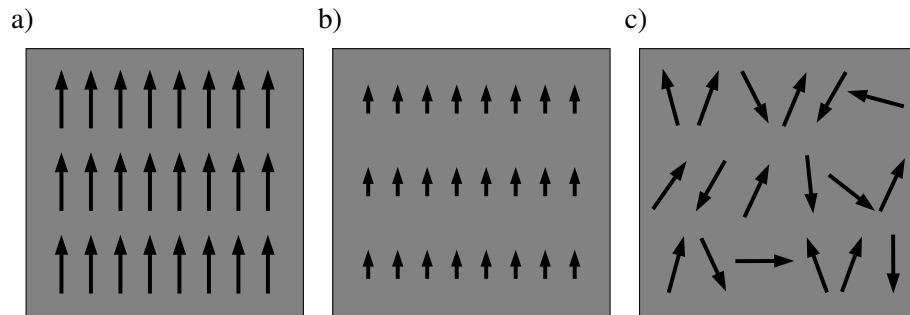


Fig. 1.9: Spin structures in a ferromagnetic material showing a) complete alignment of the magnetic moments, b) the reduction of moments due to stoner excitations and c) overall moment reduction due to thermal disorder.

1.4.2 Models of Ultrafast Demagnetisation

The rising use of femtosecond and picosecond lasers to manipulate spin order has been well documented in the literature in recent years. Beaurepaire *et al.* showed that, using such measurements it is possible to induce demagnetisation on the sub-ps time-scale [37].

There are a number of models of demagnetisation in response to laser excitation. As discussed by Koopmans *et al.* in Ref. [38], the underlying mechanism of demagnetisation remained elusive. The mechanism by which energy is transferred into the spin system has been the theme of a number of papers [38,39]. One successful mechanism for explaining the mechanism of energy transfer is the Elliot-Yafet type of elastic scattering. This mechanism defines a probability that a spin flip will occur in a scattering process with a phonon or defect [40].

In the theory of Koopmans [38], the authors address the problem of the timescales of demagnetisation seen in different elements. For example the timescale for the overall demagnetisation in elemental Gd is shown to be much longer than that of the transition metal elements. In this paper Koopmans writes a Hamiltonian for the conduction electron, spin and phonon energies and their respective interactions. The paper shows that depending on the Elliot-Yafet spin-mixing parameter, good agreement could be obtained between theory and experiment in terms of the timescale of demagnetisation. There have been a number of papers [39,41–43] supporting this observation, making such a microscopic process a good candidate for the underlying mechanism of demagnetisation.

Another possible demagnetisation mechanism involving electron-electron Coulomb scattering, similar to the Elliot-Yafet theory, was discussed by Krauß *et al.* [44]. The treatment showed good agreement with experimental observations when the choice of the scattering parameter (similar to the Elliot-Yafet spin-mixing parameter) was chosen appropriately.

Ref. [45] Battiato *et al.* showed that the demagnetisation in Ni could be demonstrated by considering a ballistic model of spin-polarised excited electrons. The model assumed absorption of photons excited electrons from d to sp -like bands above the fermi level, where they are more mobile. This meant that d electrons were considered as localised, and the ballistic equations were applied to the sp -like electrons. The photon-electron process was considered to be spin conserving generating spin-polarised transport. This diffusive transport model predicted that demagnetisation could occur because the excited spin majority and minority electrons have different lifetimes. This model showed that demagnetisation within around 200 fs is possible without the need for considering angular momentum conservation. They conclude that on longer timescales other effects would need to be included into their model, such as anisotropy or exchange interaction.

The different models show that it is possible to produce, numerically, similar demagnetisation times for different microscopic processes, however a complete description remains elusive. This still leaves the mechanism behind femtosecond demagnetisation processes under debate. The aim of this work was not to investigate the microscopic details of the energy transfer into the spin system, but to look at the magnetisation dynamics on this sub-picosecond timescale. The interpretation of demagnetisation in the model that we present, based on the stochastic LLG equation, is caused by random thermal fluctuations. This model is described in chapter 2. The stochastic process requires a well defined temperature, thus if we are to study laser induced magnetisation dynamics we need a model that can describe the temperature of the system. We do this by employing the two temperature model, which defines a conduction electron

temperature and a temperature of the phonon system, outlined below.

1.4.3 The Two Temperature Model

In this section the so-called two temperature model [46] (TTM) is introduced as a tool for describing spin temperature effects during laser excitation of a media. The two temperature model in the form presented in this section is a semi-classical heating model that we use to investigate thermal transport in metals caused by laser heating. The solution of the dynamic equations of motion provides a well defined electronic temperature associated with conduction electrons and a temperature associated with a phonon bath. A laser heating source is coupled to the electronic temperature (not the phonon temperature). The essential equations are:

$$\begin{aligned}
 C_e \frac{\partial T_e(\mathbf{r}, t)}{\partial t} &= -\nabla \cdot \mathbf{Q}_e - G(T_e(\mathbf{r}, t) - T_l(\mathbf{r}, t)) + S(\mathbf{r}, t) \\
 \tau_e \frac{\partial \mathbf{Q}_e}{\partial t} + \mathbf{Q}_e &= -K_e \nabla T_e(\mathbf{r}, t) \\
 C_l \frac{\partial T_l(\mathbf{r}, t)}{\partial t} &= -\nabla \cdot \mathbf{Q}_l + G(T_e(\mathbf{r}, t) - T_l(\mathbf{r}, t)) \\
 \tau_l \frac{\partial \mathbf{Q}_l}{\partial t} + \mathbf{Q}_l &= -K_l \nabla T_l(\mathbf{r}, t)
 \end{aligned} \tag{1.4.1}$$

where C_e and C_l are the electron and phonon heat capacities; T_e and T_l the electron and phonon temperatures; \mathbf{Q}_e and \mathbf{Q}_l are the electron and phonon heat flows; τ_e and τ_l are the electron and phonon energy relaxation time; K_e and K_l are the thermal conductivities of the electron and phonon system; $S(\mathbf{r}, t)$ is the volumetric laser heat source.

Equations 1.4.1 can be simplified for relatively small systems that are simulated throughout this thesis by ignoring any heat flow between electrons and phonons and assuming uniform heating from the laser source. This means that $\mathbf{Q}_{e,l}$ are both zero and $S(\mathbf{r}, t)$ becomes $S(t)$. Furthermore the temporal distribution of the laser profile is assumed to be Gaussian. Figure 1.10 shows an example of a typical solution of equations 1.4.1 with starting temperature, T_{start} , equal to 82 K and maximum (peak) electron temperature, T_{max} , of 1492 K. The lower (dashed) curve is the phonon temperature and the upper (solid) curve is the electronic temperature. The electronic temperature shows a rapid increase initially, being reduced on the picosecond timescale to be in equilibrium with the phonon temperature.

1.5 Models of Static Properties

All of the materials we are concerned with in this thesis are disordered magnetic materials with two or more species. The two key materials we are interested in are the ferrimagnet, GdFeCo and the ferromagnet NiFe.

There are a wide range of models that are capable of describing the properties of multi component magnetic materials, such as GdFeCo, for example mean field models [47] [48] [49], mixed spin Ising models [50] and Green's function studies [51]. There are a number of factors that

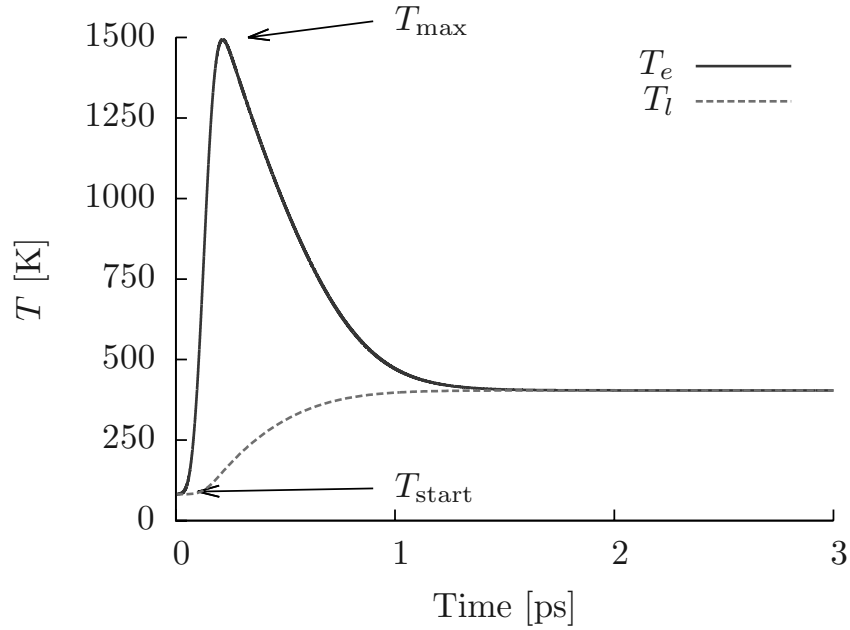


Fig. 1.10: A typical profile of the lattice and electron temperature as a function of time after excitation with a 50fs FWHM laser pulse. The starting temperature, T_{start} , was 82K and the maximum (peak) temperature, T_{max} was 1492 K. The upper (solid) curve represents the electronic temperature and the lower (dashed) curve represents the phonon temperature.

have to be considered when choosing a model, for example length-scale, timescale, energetics or material type. In this section some of the more relevant models appropriate for the work in this thesis will briefly be discussed together with a mention of their relative merits and limitations. Particular attention will be paid to the atomistic form of the Landau-Lifshitz-Gilbert (LLG) equation and its origin, as this forms the foundation of most of the work presented here.

A number of models exist that are capable of describing the equilibrium properties of a magnetic system. Two different models that we will discuss are the Ising model and the mean field model. In the following chapters of this thesis we will look at static (equilibrium) properties of ferrimagnetic materials so it is worth pointing out the basic theory of some different models. We will also use a mean field model as a means of verifying our atomistic treatment of a ferrimagnet, showing that the model agrees with the static properties, and use this as a starting point for more complex dynamic calculations.

1.5.1 Ising Model

The Ising model describes the energetics of a lattice, Λ , of spin-1/2 spins. The Hamiltonian in its simplest form can be written [52]:

$$\mathcal{H}_{\text{Ising}}(\sigma) = - \sum_{i \neq j} J_{ij} \sigma_i \sigma_j - \sum_i h_i \sigma_i, \quad (1.5.1)$$

where $i, j \in \Lambda$, J_{ij} is the exchange interaction between spins σ_i and σ_j , and h_j is the applied field. Though a simple model of magnetic materials, it is still widely used in the magnetism community for the study of ferromagnetic materials [53], exchange biased systems [54], spin glasses [55] and exotic Ising like systems, usually containing highly anisotropic rare-earth metals [56]. The Ising model is usually solved using Monte Carlo methods, particularly with, but not limited to, the well known Metropolis algorithm [57]. The model is widely used to study phase transition theory, for example for finite scaling analysis [58], though it is also a realistic model for a limited number of exotic *Ising-like* systems such as $\text{Dy}(\text{C}_2\text{H}_5\text{SO}_4)_3 \cdot 9\text{H}_2\text{O}$ [56] where the intrinsic anisotropy allows only up and down spin configurations. The formalism used to describe the Ising model cannot be applied however to most magnetic materials that are presented in this thesis. This is because the materials studied in this thesis undergo precession of the magnetic moment and show large angle fluctuations away from their easy axes, because their anisotropy is not as high as the more exotic rare-earth materials. Unlike the Ising model the materials studied here have an energy barrier arising from finite anisotropy, unlike Ising spins where the anisotropy is effectively infinite.

1.5.2 Mean Field Model

The main idea behind mean field theory for magnetic systems is that spins *feel* an identical average exchange field produced by their neighbours. In the mean Field, this field is proportional to the magnetisation of the body. In the original theory presented by Weiss, the mean (or “molecular”) field was written:

$$\mathbf{H}_e = \kappa \mathbf{M}, \quad (1.5.2)$$

with κ representing the molecular field constant. The mean field model is considered a good approximation of the order within a single ferromagnetic domain of a material [29]. However, the mean field model is easily generalized to two or more sublattices such as ferrimagnets, antiferromagnets and non-collinear magnets [31]. For comparisons to the static properties calculated using the atomistic model the mean field model provides an adequate description of finite temperature magnetisation. Mean field theory breaks down at low temperatures where the deviations from the ground state take the form of spin waves, and at high temperature where critical fluctuations interfere. Mean field does not take these two aspects into account, leading to drastic overestimations of the Curie temperature [31, 59].

The relation given by equation 1.5.2 arises by considering the Heisenberg Hamiltonian 2.2.1 and replacing the sum over the neighbours as a field arising from its neighbours. This does not yet give us a way of predicting the magnetisation as a function of temperature. The formal treatment of mean field theories is a general one that considers the Helmholtz free energy of a system (ignoring volume effects) written in terms of the temperature and magnetic field. This, combined with an approach similar to the *variational method* is used as a proof of the mean field principle [60, 61].

If one considers the magnetic energy of an atom

$$E = -\boldsymbol{\mu} \cdot \mathbf{H}, \quad (1.5.3)$$

where the magnetic moment (μ) is proportional to the total angular momentum, $\hbar J$, of the atom. In the quantum mechanical description J_z can only take values between $-J$ and $+J$ in integer steps. Thus the possible magnetic energies, E_m are also quantised. The probability that an atom is in a state m is given by:

$$P_m \propto \exp(-\beta E_m) = \exp(\beta \mu H m). \quad (1.5.4)$$

We can find the average z-component of its magnetic moment, $\mu_z = \mu m$, by considering the average thermodynamic equation for an observable, A :

$$\langle A \rangle = \frac{\sum_{\{s\}} A \exp(-\beta \mathcal{H})}{\sum_{\{s\}} \exp(-\beta \mathcal{H})} \quad (1.5.5)$$

where $\{s\}$ is all of the possible states, which for our single atom is just a sum over the orbital angular momentum quantum numbers:

$$\langle \mu_z \rangle = \frac{\sum_{m=-J}^J \mu_z m \exp(\beta \mu H m)}{\sum_{m=-J}^J \exp(\beta \mu H m)} = \frac{1}{\beta} \frac{\partial Z}{\partial \mathcal{H}}, \quad (1.5.6)$$

where Z is the partition function. Using the relations:

$$\langle \mu_z \rangle = \frac{1}{\beta} \frac{\partial \ln Z}{\partial H} = \frac{1}{\beta} \frac{\partial \ln Z}{\partial(\beta \mu H)} \frac{\partial(\beta \mu H)}{\partial H} = \mu \frac{\partial \ln Z}{\partial(\beta \mu H)}, \quad (1.5.7)$$

and by expanding the partition function as a series that can be written as a hyperbolic trigonometric function, the average magnetic moment can be written:

$$\langle \mu_z \rangle = \mu J B_J(\beta \mu H), \quad (1.5.8)$$

where

$$B_J(\beta \mu H) = \frac{1}{J} \left[\left(J + \frac{1}{2} \right) \coth \left(J + \frac{1}{2} \right) \beta \mu H - \frac{1}{2} \coth \frac{1}{2} \beta \mu H \right]. \quad (1.5.9)$$

Equation 1.5.9 is known as the Brillouin function [61,62] and can be solved in a self-consistent manner to find the magnetisation for a particular temperature and field. Figure 1.11 shows the reduced magnetisation as a function of temperature for different values of the spin contributing to the total angular momentum, the figure is taken from Ref. [60]. Different forms

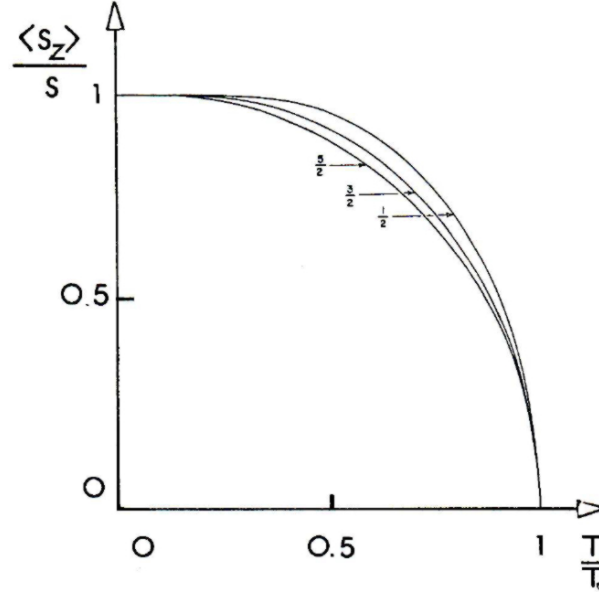


Fig. 1.11: Magnetization curves as a function of reduced temperature. The lines are solutions to the Brillouin function for different spin quantisations contributing to the total angular momentum. Figure taken from Ref. [60].

of the Hamiltonian can be derived to describe the mean field, which can give rise to different temperature dependent behaviour of the magnetisation. In chapter 3 a mean field Hamiltonian for a disordered ferrimagnetic material will be derived and comparisons made to the atomistic model of a ferrimagnet.

1.6 Dynamic Models

The majority of the work presented in this thesis uses an atomistic model with dynamic behaviour described by the Landau-Lifshitz-Gilbert (LLG) [63] Langevin equation, which describes the dynamics of magnetic moments in an effective field. Solving the dynamical equations of motion for a set of coupled spins allows us to study not only the macroscopic dynamics but the behaviour on the atomic scale. Thermal effects are introduced via a fluctuating magnetic field whose properties will be discussed in chapter 2. This time and spatial resolution provides insight into magnetization processes occurring that macroscopic equations of motion do not. A number of dynamic models will be presented in this section with a discussion of their merits and limitations.

1.6.1 The Landau-Lifshitz-Gilbert Equation

This section is devoted to the discussion of the equation of motion of magnetic bodies. In particular the Landau-Lifshitz (LL) and Landau-Lifshitz-Gilbert (LLG) equations for the time evolution of the magnetisation will be introduced together with some of the background and

theoretical details. Finally the LLG equation for atomistic spins will be shown.

We show firstly that we can express the equation of motion of a spin in a magnetic field, beginning with the time derivative of the angular momentum of any body:

$$\frac{d\mathbf{L}}{dt} = \mathbf{T}, \quad (1.6.1)$$

where \mathbf{L} is the angular momentum of the body and \mathbf{T} is the torque acting on it. Equation 1.6.1 holds for quantum mechanical systems, and in particular also for spin as well [63]:

$$\frac{d\mathbf{S}}{dt} = \mathbf{T}. \quad (1.6.2)$$

However we wish to obtain an equation that is a representation of spin in the classical limit, thus equation 1.6.2 must be replaced by expectation values [63]. By converting equation 1.6.2 to an equation in which the only dynamical variable is the magnetic moment, which is related to spin by [64]:

$$\boldsymbol{\mu} = -g \frac{e}{2m_e} \mathbf{s}, \quad (1.6.3)$$

where e is the electron charge and m_e is the electron rest mass and g is the *g-factor* which is approximately 2. Also note that $e/2m_e$ is equal to the gyromagnetic ratio for free electrons, γ . Equation 1.6.3 remains valid in both classical and quantum mechanics. The torque exerted by a magnetic field on a moment $\boldsymbol{\mu}$ is:

$$\mathbf{T} = \boldsymbol{\mu} \times \mathbf{H}. \quad (1.6.4)$$

Equations 1.6.2, 1.6.3 and 1.6.4 may then be combined to give the equation of motion for a magnetic moment in an effective field:

$$\frac{d\boldsymbol{\mu}}{dt} = -|\gamma| \boldsymbol{\mu} \times \mathbf{H}. \quad (1.6.5)$$

Using equation 1.6.3 we retrieve the first term in the all important LLG equation 1.6.8 which, we will present in the following section.

1.6.1.1 Landau-Lifshitz and Gilbert

Observations of magnetic materials show that in reality, magnetisation does not precess infinitely as equation 1.6.5 suggests, rather, its motion is damped. One may write an equation of motion for a spin that undergoes damped precession in a number of ways. Landau and Lifshitz first proposed an equation of the form [65,66]:

$$\frac{d\mathbf{M}}{dt} = -|\gamma|(\mathbf{M} \times \mathbf{H}) - \frac{|\gamma|\lambda}{M} \mathbf{M} \times \mathbf{M} \times \mathbf{H}. \quad (1.6.6)$$

Gilbert derived his expression from Lagrangian analysis and considered his equation a more fundamental equation stating that eddy-current damping is a direct result of such analysis [66]. Gilbert's equation was written in the form:

$$\frac{d\mathbf{M}}{dt} = -|\gamma|(\mathbf{M} \times \mathbf{H}) - \alpha \frac{\mathbf{M}}{M} \times \frac{d\mathbf{M}}{dt}. \quad (1.6.7)$$

Both equations 1.6.6 and 1.6.7 introduce a damping term to the precessional term (equation 1.6.5). The LL equation is essentially different only in that the damping term does not effect the precession rate whereas in the LLG form it does. The LL and LLG formulations agree in the low damping limit but in general neither are exact as the damping torque is neither local in time or space [67], for a more thorough description see Ref. [63].

For complete relaxation to equilibrium there must be some coupling to some "sufficiently large" thermal reservoir. The damping as written in equation 1.6.7 can be considered as an "intrinsic" coupling to this thermal reservoir. This is typically not the damping seen experimentally as experiments tend to take spatial averages which are affected by, for example, spin wave relaxation and is often called in the literature Gilbert damping or distributed damping [67].

The origin of the damping term, α , is not a trivial matter. In the LLG equation, the damping term is so-called because it results in the dissipation of energy and angular momentum from the spin system and leads to relaxation of the moment to the direction of the net effective field. The damping arises from several phenomena acting over different timescales. Throughout this thesis however the damping term will be called the *coupling to the thermal bath*.

As we are interested in processes that are occurring on the atomic length-scale we need to go further than the LLG equation for macroscopic magnetization towards a description of the behaviour of individual atomic moments. To this end we write an LLG equation for the individual coupled atomic moments as:

$$\frac{\partial \mathbf{S}_i}{\partial t} = -\frac{|\gamma_i|}{(1 + \lambda_i^2)\mu_i} \left(\mathbf{S}_i \times \mathbf{H}_i + \lambda_i \mathbf{S}_i \times \mathbf{S}_i \times \mathbf{H}_i \right). \quad (1.6.8)$$

The LLG equation (1.6.8) is written in such a way that properties such as the coupling constant, λ_i , the magnetic moment, μ_i and the gyromagnetic ratio γ_i can be varied on a site-wise basis. This will be discussed in more detail when considering ferrimagnetic materials. This equation will be discussed in further detail in chapter 2, but will form the core of the calculations performed throughout chapters 3, 4, 5 and 6.

1.6.2 The Landau-Lifshitz-Bloch Model

The Landau-Lifshitz-Bloch (LLB) model is a relatively new model of magnetisation dynamics, proposed by Garanin [68]. It offers an alternative (or a bridge from atomistic modelling) to traditional micromagnetics in terms of length scale. The LLB model describes the dynamic behaviour of a single macrospin (or set of macrospins), in much the same way as a micromagnetic approach. The LLB equation, however, is somewhat unique in its form as it allows

fluctuations in the magnitude of the magnetization. There are numerous examples of the use of the LLB equation in the literature in a wide range of systems and situations, including multi-scale modelling [12], investigating domain wall motion [69], laser induced magnetisation dynamics [7, 26], investigating linear reversal mechanisms [33] as well as being checked against atomistic simulations showing excellent agreement [70]. The equation for the (ferromagnetic) LLB model contains the usual precessional and damping terms that are present in the LLG equation of motion, however the LLB model also contains another term that deals with changes in the longitudinal relaxation of the magnetisation. The usual equation of motion for the LLB model can be written as [7]:

$$\dot{\mathbf{m}}_i = -|\gamma|(\mathbf{m}_i \times \mathbf{H}_{\text{eff}}) + \frac{|\gamma|\alpha_{\parallel}}{m_i^2} (\mathbf{m}_i \cdot \mathbf{H}_{\text{eff}}) \mathbf{m}_i - \frac{|\gamma|\alpha_{\perp}}{m_i^2} (\mathbf{m}_i \times [\mathbf{m}_i \times \mathbf{H}_{\text{eff}}]), \quad (1.6.9)$$

where α_{\parallel} and α_{\perp} are the dimensionless longitudinal and transverse damping parameters given by:

$$\begin{aligned} \alpha_{\parallel} &= \lambda \frac{2T}{3T_C}, \\ \alpha_{\perp} &= \lambda \left(1 - \frac{T}{3T_C}\right). \end{aligned} \quad (1.6.10)$$

T_C is the Curie temperature of the material and λ is the coupling constant to the thermal bath, thus it is responsible for the transfer of energy and angular momentum into and out of the system. The effective field is given by

$$\begin{aligned} \mathbf{H}_{\text{eff}}^i &= \mathbf{H} + \mathbf{H}_A + \mathbf{H}_{\text{ex}} \\ &+ \begin{cases} \frac{1}{2\tilde{\chi}_{\parallel}} \left(1 - \frac{m_e^2}{m_e^2}\right) \mathbf{m}_i, & T \leq T_C \\ \frac{J_0}{\mu} \left(1 - \frac{T}{T_C} - \frac{3}{5} \frac{m_e^2}{m_i^2}\right) \mathbf{m}_i, & T \geq T_C. \end{cases} \end{aligned} \quad (1.6.11)$$

In equation 1.6.11 m_e is the zero field equilibrium magnetisation for a given temperature, $J_0 = zJ$ for an atomistic nearest neighbour exchange of Heisenberg type with exchange parameter J and z nearest neighbours, and μ is the atomistic magnetic moment. \mathbf{H} , \mathbf{H}_A and \mathbf{H}_{ex} are the applied, anisotropy and exchange effective fields:

$$\mathbf{H}_A^i = -(m_x^i \mathbf{e}_x + m_y^i \mathbf{e}_y) / \tilde{\chi}_{\parallel}, \quad (1.6.12)$$

and

$$\mathbf{H}_{\text{ex}}^i = -\frac{A(T)}{m_e^2} \frac{2}{M_s^0 \Delta^2} \sum_{j \in \text{neigh}i} (\mathbf{m}_j - \mathbf{m}_i). \quad (1.6.13)$$

Interestingly there are a number of temperature dependent input parameters in this model that characterise the material being studied, namely, the susceptibilities, the exchange stiffness and the equilibrium magnetisation. These parameters can be taken (or rather calculated) from a mean field treatment [7]. An alternative to a mean field treatment is by calculation from an atomistic model [12] bringing in the possibility of so-called multi-scale modelling.

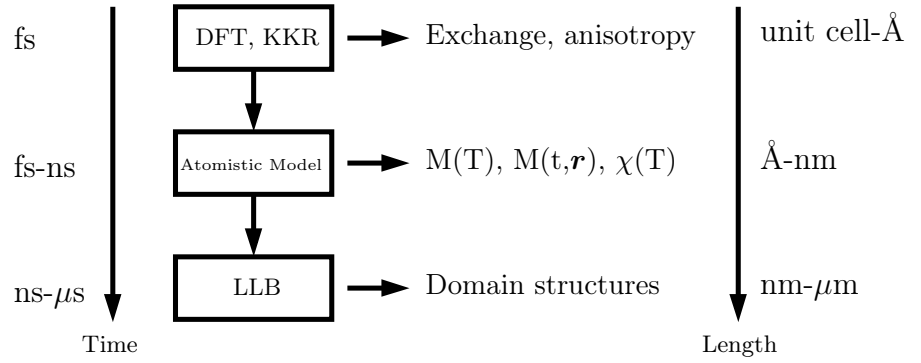


Fig. 1.12: A schematic showing the time/length scales involved in the principle methods of describing spin dynamics. These scales can be linked by calculations of various properties at different levels of calculation.

The idea behind the multiscale modelling technique is to join the various length/time scales involved in spin dynamics without losing any physical information. Using *ab-initio* techniques such as the Korringa-Kohn-Rostoker approximation (KKR) or DFT methods exchange and anisotropy values can be calculated. These can then be input into models for atomistic spin dynamics. Finally the atomistic model can be used to calculate susceptibilities, magnetisations and the exchange stiffness for input into the LLB model. This is shown schematically on figure 1.12.

1.7 Ferrimagnets

The term ferrimagnet refers to a type of magnetically ordered material that has two or more species with different atomic moments. The moments are anti-ferromagnetically coupled between the two different species. This definition encompasses a wide range of materials too numerous to mention here. The work presented here concentrates on a class of *amorphous* transition metal-rare earth (TM-RE) metallic alloys. During the 1980's there was a great deal of interest in these materials, specifically for magneto-optical devices [48, 71]. However, since then the interest has decreased, though, in recent years this trend has reversed [19, 21, 24, 26, 72–75]. This recent interest, particularly the studies using femtosecond lasers has stimulated this work into magnetisation dynamics on the (sub)picosecond timescale.

1.7.1 Simple Ferrimagnet

Consider a material with a B1 structure (F_{M3M} space group) as shown in Figure 1.13, with the two species being represented by the grey and white atoms. Considering nearest neighbour interactions only, species of the same type do not interact. If the two species are magnetic and coupled antiferromagnetically then, as in the case of the simplest anti-ferromagnet, the exchange interactions give rise to two ordered sublattices. The term sublattice throughout this work refers to a set of spins that share a common direction in their ground state. This exchange

coupling and the resulting two sublattice system is shown schematically in figure 1.13. In this

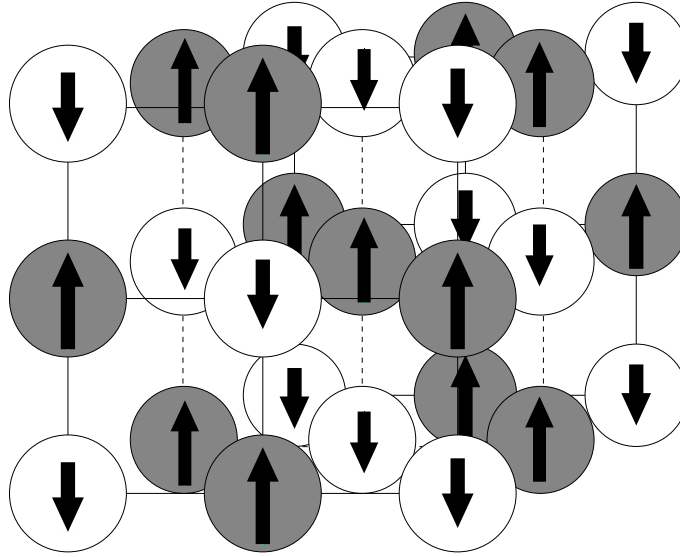


Fig. 1.13: Schematic representing the simplest three dimensional ferrimagnet, the B1 structure.

simple case, because there is only one exchange interaction, $J_{AB} = J_{BA}$, the temperature dependence is the same, though their ground state is with sublattices A and B pointing anti-parallel. As is shown schematically in figure 1.13, in a ferrimagnet, one sublattice has a larger moment than the other, this means that for our simple ferrimagnet, the sublattice with the larger moment always dominates.

As is shown on figure 1.14, the individual sublattices of the simple ferrimagnet shown in figure 1.13 show the same temperature dependence, but note that, one sublattice has a smaller magnetisation than the other.

The samples that are of main interest throughout this work are various compositions of GdFeCo. This metallic alloy (and other RE-TM alloys) in thin film form exhibits a strong perpendicular anisotropy [48] with an out-of-plane magnetisation, making them particularly useful for Faraday effect readout.

1.8 Experimental Techniques

The main body of work carried out here is based on theoretical considerations and computational models, where appropriate and possible the results from calculations have been compared to experimental observations. In some cases the model calculations were driven by experimental observations, in others, as seen in later chapters, the modelling has stimulated effort for experimental confirmation.

In this section the key experimental techniques will be briefly discussed. Though the author did not perform any experiments, it is worth giving the reader a brief introduction to the

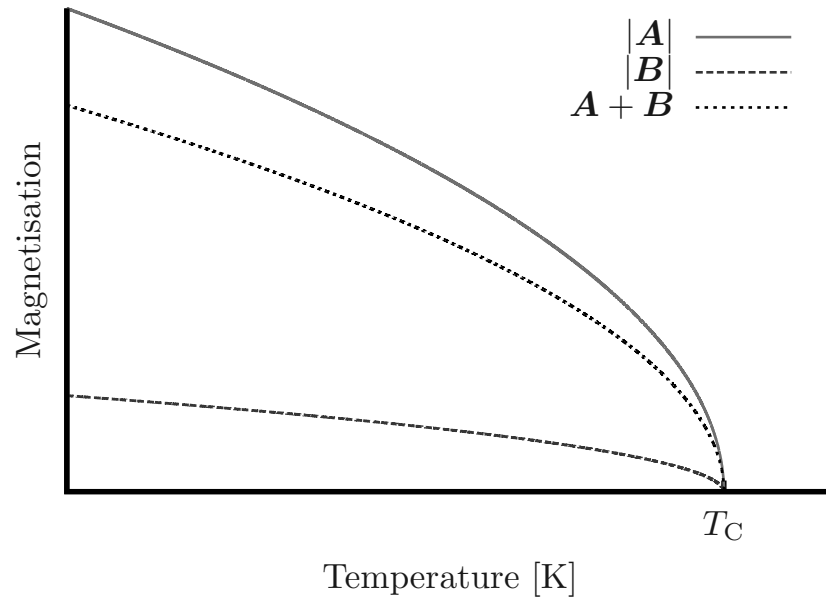


Fig. 1.14: *Temperature dependence of the magnetisation of a simple ferrimagnet, such as the one in figure 1.13. The sublattice A has a larger magnetic moment and thus has a greater magnetisation than that of sublattice B. The orientation of sublattice B is opposite to that of A. The temperature dependence of sublattices A and B is the same because of the fact that the exchange constants are the same. The net magnetisation also has the same temperature dependence and a smaller moment than that of sublattice A, but larger than B.*

ideas and background as the experimental observations will be later discussed in the context of the model results.

1.8.1 Femtosecond lasers

Using femtosecond laser systems it is possible to stimulate magnetic materials on the timescale of the exchange interaction. The lasers are characterised by high peak intensities thus a large amount of energy can be transferred to the excited medium. As discussed in section 1.4.3, this large amount of energy transfer into metallic systems can give rise to extremely hot electrons. Typically the experiments presented in this thesis uses laser pulses with 50-100 fs width (FWHM) at a particular repetition rate, usually KHz.

Combining the use of femtosecond laser excitation with arrays of optics it is possible to investigate time-resolved magnetisation dynamics after laser excitation. In a pump-probe set-up, a beam splitter is used to split the beam into two parts; a pump which excites the material (about 90% of the power), and a probe beam, which, is usually frequency doubled, detects the magnetisation state. Introducing a delay in between the pump and probe pulses allows a stroboscopic way of measuring magnetisation changes. This technique requires a *resetting* of the magnetisation after each measurement [76]. A typical experimental set-up is shown in figure 1.15.

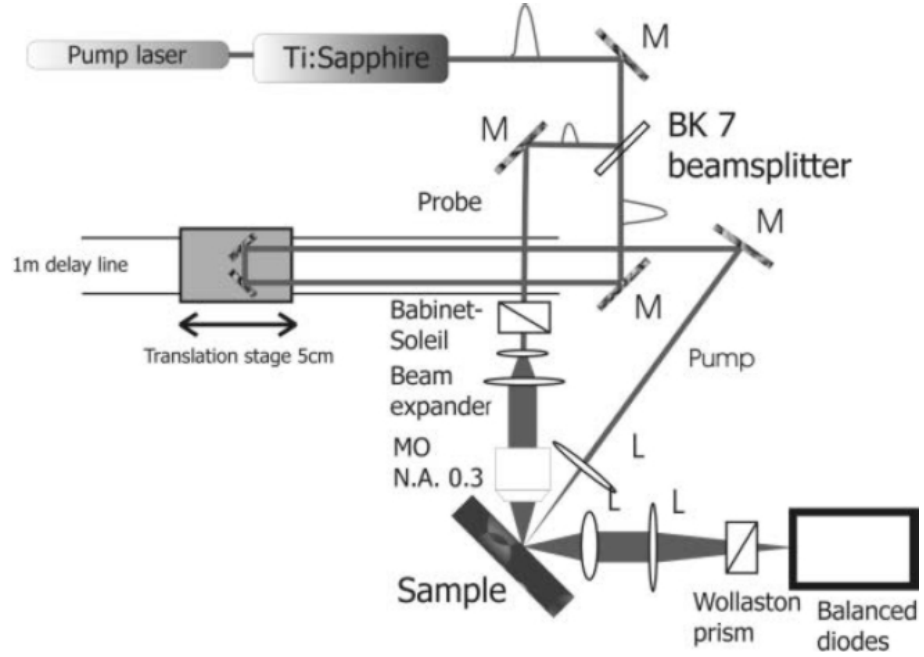


Fig. 1.15: *Experimental set-up for a time-resolved magneto-optical Kerr effect (MOKE) measurement of magnetisation dynamics. The beam splitter changes the delay between the pump and the probing beams allowing a stroboscopic measurement of transient magnetisation dynamics. Image taken from Ref. [76]*

1.8.2 Synchrotron Radiation

Synchrotron X-ray sources provide highly intense and collimated X-rays of variable and well-defined polarisation. The basic principle of how the radiation is generated is by *Bremsstrahlung*, or braking radiation. Large synchrotrons use oscillating magnetic fields and electric fields with the electron path being maintained by magnetic devices such as bending magnets. The electrons are highly relativistic with energies in the gigaelectron volt range, i.e. $E/mc^2 > 1000$, radially accelerated onto a circular motion [77]. The spectrum of emitted radiation is a broad continuum of collimated X-rays. The radiation has a well defined polarization as shown in figure 1.16. The profile shown in figure 1.16 shows the intensity and polarisation profile from *bending magnets*. Other devices can be used to modify the electron's path to generate stronger circularly polarised photons such as *helical wigglers* and *undulators*. The details of the different devices are not within the scope of this work, though for a very good overview of synchrotron radiation see reference [77].

1.8.3 X-Ray Magnetic Circular Dichroism

The interaction of X-rays with different materials gives distinct energy dependent cross sections. The absorption cross section exhibits element specific absorption edges if the X-ray energy is equal to the element specific binding energy of inner atomic electron levels. Because of the high energy of the photons generated by the synchrotron the transitions can occur from

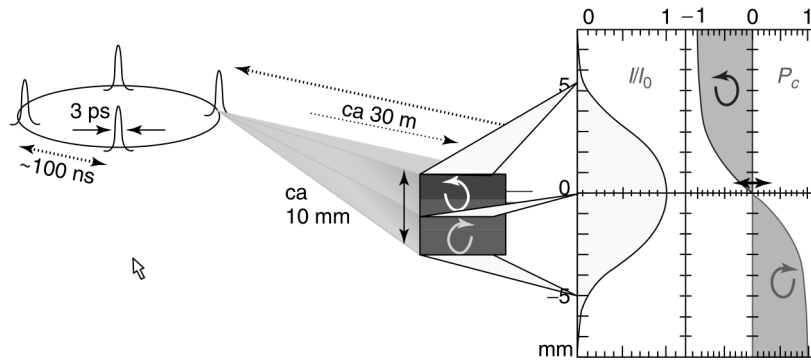


Fig. 1.16: A schematic representing the degree of polarisation and intensity from a simple bending magnet. Figure taken from [77].

1s (K), 2s and 2p (L), and 3s, 3p and 3d (M) states. Furthermore, the spin-orbit quantum number is labelled, $2p_{1/2}$ for the L_2 edge, $2p_{3/2}$ for the L_3 edge, $3d_{3/2}$ for the M_4 edge, and $3d_{5/2}$ for the M_5 edge. It is worth pointing out here that the magnetic cross section scales with the dot product of the polarisation vector from the light source and the magnetisation of the sample [77]. The principle of the XMCD effect is that a circularly polarised X-ray photon carries a quantum of angular momentum to, for example, a core 2p electron. According to the optical selection rules, left-handed circularly polarised photons ($+\hbar$) excite spin-up photoelectrons. Right handed circularly polarised photons ($-\hbar$) excite spin-down electrons. Figure 1.17 shows a schematic illustration of the XMCD effect. At the photon energy associated with the

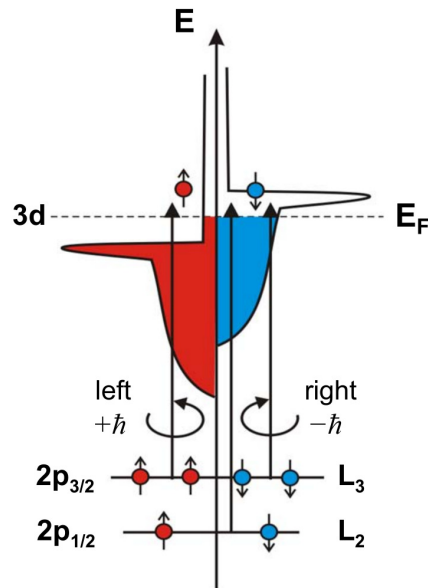


Fig. 1.17: A schematic showing the basic idea behind the X-ray Magnetic Circular Dichroism (XMCD) technique. The electrons in the spin-orbit split orbitals ($2p_{1/2}$ and $2p_{3/2}$) undergo optical transition according to the selection rules upon excitation with circularly polarised light. Figure taken from Ref. [78].

edge transition, there is a difference in absorption intensity because of the spin split valence band. The difference between the absorption intensities for the left (μ^+) and right (μ_-) gives the XMCD spectrum, shown schematically for Fe in figure 1.18. In later chapters, more details

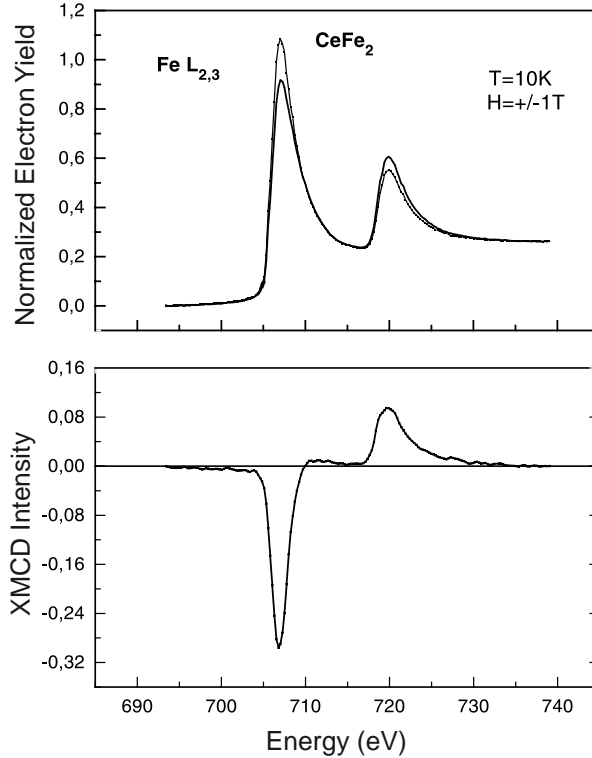


Fig. 1.18: The X-ray Magnetic Circular Dichroism spectra of the L_2 and L_3 edges of Fe in $CeFe_2$. The difference between the signals of the upper panel is shown in the lower panel. Figure taken from Ref. [79].

will be given about the particular XMCD measurements and the time-resolved measurements.

1.9 Concluding Remarks

In this chapter we have introduced the importance of magnetisation dynamics and switching, emphasising its technological importance. The basic ideas behind the current technology and the next generation (HAMR) and its limits were also presented. The work in this thesis shows that it is possible to go beyond HAMR, though many engineering challenges remain. We present a mechanism for magnetisation switching that does not require a magnetic field, or indeed, any directional stimulus and can be achieved using only heat.

The origin of the physical quantities that we incorporate into our model were also discussed. These quantities are included in the model as inputs but require calculations or measurements to determine their value. This will be addressed in chapter 3.

A potential candidate for HAMR, FePt, was discussed because of its high uniaxial anisotropy. The mechanism for magnetisation reversal in FePt via a linear route was also introduced and

will be shown to be an important consequence when considering laser induced magnetisation dynamics and switching in later chapters.

The interpretation of demagnetisation in the atomistic model, presented in chapter 2, was also discussed. A number of models of ultrafast demagnetisation were discussed, leading us to a discussion of the two-temperature model of laser heating.

A number of models capable of describing static and dynamic behaviour of magnetic materials were discussed and we also introduced ferrimagnetic materials. Some of the important experimental methods for measuring static and dynamic properties of ferrimagnetic materials (and magnetic materials in general) were introduced, together with the essential physics for understanding the measurements.

Chapter 2

Atomistic Spin Model

As was discussed in the previous chapter there are a number of models capable of describing the dynamic behaviour of magnetic materials. There are, however, limits to the regime in which some of these models can be used. For example, a micromagnetic formalism cannot be used to describe individual atomic magnetic moments as it breaks down in this limit. To this end in this chapter we outline an approach based on the Landau-Lifshitz-Gilbert equation for atomistic magnetic moments. The energy dissipation is included phenomenologically into this model. Furthermore we augment the equation with a stochastic term to include thermal effects. The model assumes that the magnetic moments can be localised to an atomic site. With the atomistic model in mind, we outline how we construct the model of an amorphous TM-RE ferrimagnet.

2.1 Introduction

The Landau-Lifshitz-Gilbert equation of motion for individual spins was introduced in chapter 1. The form of the equation used is rewritten below:

$$\frac{\partial \mathbf{S}_i}{\partial t} = -\frac{\gamma_i}{(1 + \lambda_i^2)\mu_i} \left(\mathbf{S}_i \times \mathbf{H}_i + \lambda_i \mathbf{S}_i \times \mathbf{S}_i \times \mathbf{H}_i \right). \quad (2.1.1)$$

Here, and from now on we assume that the gyromagnetic ratio is the absolute value. The effective field, \mathbf{H}_i , is made up of a number of contributions such as exchange, anisotropy and Zeeman terms. Such terms were introduced in the previous chapter. In this section the field terms will be further discussed beginning with a discussion of the extended Heisenberg Hamiltonian. The inclusion of stochastic thermal terms will also be introduced and the methods of integrating such a set of coupled equations will be included.

2.2 Extended Heisenberg Hamiltonian

The Hamiltonian employed in the majority of calculations is an extended Heisenberg Hamiltonian. We use the term *extended* Heisenberg Hamiltonian as the basic form originally derived by Heisenberg [80] considered the exact solution of two electrons (discussed in section 1.3.1). The extended form is an approximation that allows interactions between all spins in a system and the addition of other terms such as anisotropy, Zeeman and demagnetising terms. The extended form of the Hamiltonian allows us to write the energy terms important in the magnetic system in a straightforward way and will be used throughout this thesis. Without the demagnetising field the Hamiltonian can be written as:

$$\mathcal{H} = -\frac{1}{2} \sum_{i=1}^N \sum_{j=1}^N J_{ij} \mathbf{S}_i \cdot \mathbf{S}_j - \sum_{i=1}^N K_i (\mathbf{S}_i \cdot \mathbf{n}_i)^2 - \sum_{i=1}^N \mu_i \mathbf{B} \cdot \mathbf{S}_i. \quad (2.2.1)$$

The first term is the isotropic exchange interaction between spins i and j in the system and in theory is a double sum over the entire system, though truncations to an interaction range tend to be made. The spin, \mathbf{S} , is a vector that can take any orientation on the unit sphere. The second term in the Hamiltonian 2.2.1 is the uniaxial anisotropy term, the third is the Zeeman term. The terms in the Hamiltonian can be represented as effective fields for the spin i , which are defined through:

$$\mathbf{H}_i = -\frac{\partial \mathcal{H}}{\partial \mathbf{S}_i}. \quad (2.2.2)$$

Giving the effective field for spin i in the form:

$$\mathbf{H}_i = \sum_j J_{ij} \mathbf{S}_j + 2K_i \mathbf{n}_i (\mathbf{S}_i \cdot \mathbf{n}_i) + \mu_i \mathbf{B}. \quad (2.2.3)$$

The Hamiltonian given by equation 2.2.1 is a truncation of the complete form of the Heisenberg type exchange to the bilinear term. Further terms can also be included into the Hamiltonian, such as the next term in the expansion, the bi-quadratic term [81, 82]. Equation 2.2.3 can also be expanded to include the off-diagonal components of the exchange tensor. Such terms are important in, for example, canted antiferromagnets where the Dzyaloshinskii-Moriya (DM) interaction gives rise to a weak net magnetisation [83].

In developing our model of disordered magnetic materials, such as GdFeCo or NiFe that we present later, we require a means of determining the constants in equation 2.2.1. There are a number of ways of determining these constants, for example via DFT parameterisation.

For the model of GdFeCo, chapter 3 shows how we determine the exchange parameters by comparing to experimental observations, the temperature dependent magnetisation of the individual sublattices of GdFeCo. This allows us to determine the strength of the exchange between the two sublattices. The Fe-Fe and Fe-Gd exchange interactions mostly determine the temperature dependent behaviour because for the composition range we are interested

in, the proportion of Gd-Gd interactions is relatively small. For the Gd-Gd interaction we choose a value that gives us the correct Curie temperature for pure Gd. For the anisotropy we choose a value that is large enough to give an out-of-plane magnetisation in thin film form. The magnetic moments were taken from literature values of bulk materials. Tables of the parameters used for the GdFeCo simulations can be found in appendix E.

The model of NiFe presented in chapter 5, it was assumed that the Ni-Fe, Fe-Fe and Ni-Ni interactions are all ferromagnetic and equal. The value of the exchange constant is chosen to give the correct Curie temperature. All other parameters were taken from the literature except where otherwise stated. The parameters for the NiFe simulations are given in tables 5.4 and 5.1.

2.2.1 Landau-Lifshitz-Gilbert Langevin Equation

Until now the equation of motion as shown in equation 2.1.1 has been valid only at zero Kelvin only as the equation of motion does not include any temperature dependence. The atomistic LLG equation can, however, be augmented with a stochastic term to mimic thermal fluctuations.

Thermal effects are extremely important to the work undertaken in this thesis, particularly as some of the work will involve calculations of femtosecond demagnetisation. Though temperature can be incorporated into an atomistic model using Monte Carlo methods, this approach, does not in general quantify a timescale for any processes observed and does not allow precession. It is well known that thermal effects lead to reductions in magnetisation, in the LLG model with thermal effects the interpretation of this decrease is as follows:

- Increased temperature leads to on-site thermal fluctuations of the individual moments
- The size of the spin moment remains constant for each site
- Disorder of the moments leads to overall reductions over the ensemble of the magnetisation (thermal magnons)

Clearly this interpretation of magnetisation dynamics is not necessarily the whole picture. This form of the LLG model assumes that magnetic moments are localised to atomic sites and are not reduced by temperature, which we know is not always true, for example in metallic magnetic materials. However, this simple model works well in comparison to experimental measurements.

In order to introduce thermal effects the local effective fields in the LLG equation 2.1.1 can be augmented with an additional term at each site:

$$\frac{d\mathbf{S}_i}{dt} = -\frac{\gamma_i}{(1 + \lambda_i)\mu_i} \{ \mathbf{S}_i \times [(\mathbf{H}_i^{\text{eff}} + \mathbf{H}_i^{\text{th}}) + \lambda_i \mathbf{S}_i \times (\mathbf{H}_i^{\text{eff}} + \mathbf{H}_i^{\text{th}})] \}. \quad (2.2.4)$$

Equation 2.2.4 can be written as a Langevin type stochastic differential equation with multiplicative noise. The term, *multiplicative noise*, refers to the fact that the pre-factor for the

stochastic process, $H_i^{\text{th}}(t)$, is a function of \mathbf{S} . This can be shown by writing, in compact form, the LLG equation using Einstein summation convention for each Cartesian component, Γ for the spin i :

$$\frac{dS_{i,\Gamma}}{dt} = -\frac{\gamma_i}{(1+\lambda_i)\mu_i}[\mathbf{S}_i \times \mathbf{H}_i]_{\Gamma} - \frac{\lambda_i\gamma_i}{(1+\lambda_i)\mu_i}[\mathbf{S}_i \times \mathbf{S}_i \times \mathbf{H}_i]_{\Gamma}, \quad (2.2.5)$$

using the definition of the cross product, $\mathbf{A} \times \mathbf{B} = \mathbf{C}$ where $C_{\Gamma} = \epsilon_{\Gamma\Delta\Theta}A_{\Delta}B_{\Theta}$ and the triple cross product, $\mathbf{D} = \mathbf{A} \times \mathbf{B} \times \mathbf{C}$ where $[D]_{\Gamma} = \epsilon_{\Gamma\Delta\Theta}A_{\Delta}\epsilon_{\Theta\Lambda\Xi}B_{\Lambda}C_{\Xi}$. Here ϵ is the Levi-Civita symbol, defined in the usual way as:

$$\epsilon_{\Gamma\Delta\Theta} = \begin{cases} +1 & \text{if } (\Gamma,\Delta,\Theta) \text{ is } (x,y,z), (z,x,y) \text{ or } (y,z,x), \\ -1 & \text{if } (\Gamma,\Delta,\Theta) \text{ is } (x,z,y), (z,y,x) \text{ or } (y,x,z), \\ 0 & \text{if } i = j \text{ or } j = k \text{ or } k = i. \end{cases} \quad (2.2.6)$$

Using the definition of the cross and triple cross products shown above, we can write equation 2.2.4 as:

$$\begin{aligned} \frac{dS_{i,\Gamma}}{dt} = & -\gamma'_i\epsilon_{\Gamma\Delta\Theta}S_{i,\Delta}H_{i,\Theta}^{\text{eff}} - \gamma'_i\lambda_i\epsilon_{\Gamma\Delta\Theta}S_{i,\Delta}\epsilon_{\Theta\Lambda\Xi}S_{i,\Lambda}H_{i,\Xi}^{\text{eff}} \\ & - \gamma'_i\epsilon_{\Gamma\Delta\Theta}S_{i,\Delta}H_{i,\Theta}^{\text{th}} - \gamma'_i\lambda_i\epsilon_{\Gamma\Delta\Theta}S_{i,\Delta}\epsilon_{\Theta\Lambda\Xi}S_{i,\Lambda}H_{i,\Xi}^{\text{th}}. \end{aligned} \quad (2.2.7)$$

Here, $\gamma'_i = \gamma_i/(1+\lambda_i^2)\mu_i$. Replacing the first two terms with:

$$A_{i,\Gamma}(\mathbf{S}_i, t) = -\gamma'_i\epsilon_{\Gamma\Delta\Theta}S_{i,\Delta}H_{i,\Theta}^{\text{eff}} - \gamma'_i\lambda_i\epsilon_{\Gamma\Delta\Theta}S_{i,\Delta}\epsilon_{\Theta\Lambda\Xi}S_{i,\Lambda}H_{i,\Xi}^{\text{eff}}, \quad (2.2.8)$$

the final two terms can be written:

$$-\gamma'_i\epsilon_{\Gamma\Delta\Theta}S_{i,\Delta}H_{i,\Theta}^{\text{th}} - \gamma'_i\lambda_i(S_{i,\Xi}S_{i,\Gamma}H_{i,\Xi} - S_{i,\Lambda}S_{i,\Lambda}H_{i,\Gamma}). \quad (2.2.9)$$

Using the identity $S_{i,\Xi}S_{i,\Gamma}H_{i,\Xi} - S_{i,\Lambda}S_{i,\Lambda}H_{i,\Gamma} = (S_{i,\Gamma}S_{i,\Theta} - \delta_{\Gamma\Theta}S_{i,\Delta}S_{i,\Delta})H_{i,\Theta}$, we can define:

$$B_{i,\Gamma\Theta}(\mathbf{S}_i, t) = -\gamma'_i\epsilon_{\Gamma\Delta\Theta}S_{i,\Delta} - \gamma'_i\lambda_i(S_{i,\Gamma}S_{i,\Theta} - \delta_{i,\Gamma\Theta}S_{i,\Delta}S_{i,\Delta}). \quad (2.2.10)$$

The LLG equation with the augmented field can then be written as a general Langevin equation [84]:

$$\frac{dS_{i,\Gamma}}{dt} = A_{i,\Gamma}(\mathbf{S}_i, t) + B_{i,\Gamma\Theta}(\mathbf{S}_i, t)H_{i,\Theta}^{\text{th}} \quad (2.2.11)$$

2.3 Noise Process

In terms of the Landau-Lifshitz-Gilbert Langevin equation, the temperature effects or thermal activation is caused by perturbations of very high frequency. Specifically, one usually assumes that the thermal fields apply perturbations to the system at a higher frequency than the precession period of the spin. The fluctuation field can then be treated as a stochastic

process. In this work the stochastic process is assumed to be Gaussian white noise, because the fluctuations are assumed to be due to the microscopic degrees of freedom with equivalent stochastic properties. It is very important to point out here that of the assumption of white noise becomes less reliable as the timescale of the magnetization dynamics we are considering occurs on, or faster than the timescale of one (or more) of the microscopic degrees of freedom. These microscopic degrees of freedom are assumed to be the origin of the fluctuations and if we are considering ultrafast laser induced processes the assumption of white noise is brought into doubt [85]. The form of the stochastic noise was discussed by Atxitia *et al.* in Ref. [85], where, an extension of the approach used by Miyazaki and Seki [86], based on a single spin model, was used. This approach introduced a coloured noise formalism where the phenomenological damping parameter in the LLG equation was replaced by two phenomenological parameters: the correlation time and a coupling constant to the bath. The problem with this approach, however, is that we do not have any information on the correlation times in GdFeCo.

A stochastic process $\zeta(t)$ is Gaussian white noise given the following relations:

$$\langle \zeta(t) \rangle = 0, \quad (2.3.1)$$

states that the time average of any component (in Cartesian coordinates in our case) is zero. Furthermore the second moment of the correlator must be able to be written:

$$\langle \zeta(t)\zeta(t + \tau) \rangle = \sigma^2\delta(t). \quad (2.3.2)$$

It can be shown that the process described by equations 2.3.1 and 2.3.2 is white noise having a continuous frequency distribution. Consider the Fourier transform of the second moment of the process [87].

$$\begin{aligned} F(\omega) &= \int d\tau \langle \zeta(t)\zeta(t + \tau) \rangle \exp(i\omega\tau) \\ &= \sigma^2 \int d\tau \delta(\tau) \exp(i\omega\tau) \\ &= \sigma^2, \end{aligned} \quad (2.3.3)$$

thus the process does not depend on ω .

The strength of the noise process in the Landau-Lifshitz-Gilbert Langevin equation is given by:

$$\langle \zeta_{i,a}(t)\zeta_{j,\beta}(t') \rangle = \frac{2\lambda_i k_B T \mu_i}{\gamma_i} \delta_{ij} \delta_{\alpha\beta} (t - t'). \quad (2.3.4)$$

The correlator defining the strength of the noise in our stochastic LLG-Langevin equation is an important one, and has consequences for laser induced demagnetisation. Our interest in ferrimagnetic materials with, potentially on-site γ_i , λ_i and μ_i means that for different species we have different correlators which mean that the size of the noise is different, though the correct equilibrium properties are reproduced. For a full derivation of the correlator see

appendix D.

The use of the atomistic model means that, as well as giving the correct behaviour for low and high temperatures, unlike a mean field model, allows the model to reproduce realistic energy barriers to magnetization reversal. The atomistic model has also been shown to go beyond the micromagnetic approach, for example, demonstrating a linear reversal mode close to the Curie temperature [88] (see section 1.3.2.1). Calculations of static properties are, in general, more computationally expensive than a mean field model as it requires reasonably large systems for a good ensemble average and to reduce finite size effects. Such calculations also require good time averaging (after thermal relaxation) which can be a problem particularly close to the Curie temperature.

2.4 Solution of the Landau-Lifshitz-Gilbert Langevin Equation

A key feature of the model is its ability to investigate dynamic processes at elevated temperatures. Here we introduce the physical formalism, which is based on the stochastic form of the LLG equation referred here as the LLG-Langevin equation. The equation of motion of each of the spins is given by equation 2.2.4, with effective fields including; anisotropy, exchange and Zeeman terms. There are many integration schemes that can be used for equations such as 2.2.4 with stochastic fields. Such integration schemes include, for example, the Heun predictor-corrector algorithm; some implicit and semi-implicit schemes have been widely used [89–91]. Implicit and semi-implicit schemes have the advantage that they conserve the spin length, important for equation 2.2.4 as the spin length should always be equal to one. Throughout this work the integration scheme that will be used will be the Heun scheme, this is because of the fact that it is a simpler scheme to understand and implement. The Heun integration scheme also converges to the Stratonovich solution of stochastic calculus. Furthermore it is a widely used integration scheme for such problems even though it can potentially require smaller time-steps and normalisation of the spin length at each numerical integration step.

2.4.0.1 The Heun Numerical Scheme

For the site i , the Heun scheme can be written:

$$S_{i,\Gamma}^{(n+1)} = S_{i,\Gamma}^{(n+1)} + \frac{1}{2} \left(A_{i,\Gamma}(S_{i,\Gamma}^{(n)}, t^{(n)}) + A_{i,\Gamma}(\bar{S}_{i,\Gamma}^{(n+1)}, t^{(n+1)}) \right) \Delta t + \frac{1}{2} \left(B_{i,\Gamma\Theta}(S_{i,\Gamma}^{(n)}, t^{(n)}) + B_{i,\Gamma\Theta}(\bar{S}_{i,\Gamma}^{(n+1)}, t^{(n+1)}) \right) H_{i,\Theta}^{\text{th}} \quad (2.4.1)$$

$$\bar{S}_{i,\Gamma}^{(n+1)} = A_{i,\Gamma}(S_{i,\Gamma}^{(n)}, t^{(n)}) \Delta t + B_{i,\Gamma\Theta}(S_{i,\Gamma}^{(n)}, t^{(n)}) H_{i,\Theta}^{\text{th}} \quad (2.4.2)$$

Equation 2.4.2 is a simple Euler step and is the predictor part of the integration scheme. It is important to point out that because of the site dependent properties of the ferrimagnetic

material studied during this work, care must be taken to ensure that the scheme is working correctly. The site dependent properties mean that the pre-factor in equation 2.2.4 is different for each species and in theory can be different for each site.

2.5 Atomistic Model of Amorphous Ferrimagnetic Materials

2.5.1 Computational model of amorphous ferrimagnets

Unlike the simple picture of ferrimagnetism discussed in chapter 1, the ferrimagnetic materials that we are interested in show a number of interesting features. For example they exhibit a magnetisation compensation point. This is a temperature dependent effect that results in zero net magnetisation at temperatures below the Curie temperature. This effect arises because of the fact that the two (or more) sublattices have a different temperature dependence, unlike the simple ferrimagnet. This difference in the temperature dependence is a result of a more complex structure of the magnetic exchange interactions.

The majority of the samples that are considered in this work are in the composition range 18% to 30% rare earth. Within this composition range, GdFeCo is an amorphous alloy, which means that we do not have a repeating magnetic unit cell. To approximate the amorphous nature of the alloys, the work here assumes a fixed lattice with spins placed randomly. The procedure for creating the random lattice of spins is as follows:

1. A perfect lattice is constructed to the specified dimensions
2. Randomly chosen sites are replaced with new species
3. The loop is repeated until the desired percentage is populated
4. Steps 2 and 3 are repeated for all of the different species

A schematic of a simple 2D lattice with a simple cubic base for the structure and 33% up spins is shown in figure 2.1. This method of approximating an amorphous system does not accurately represent the physical structure because the Gd (or other RE atoms) are much larger than that of the TM series. As will be shown, however, in later chapters, our approximation to the amorphous alloy using randomly placed spins actually provides good agreement with experiment. Other methods of characterising the structural properties are possible, for example through the use of molecular dynamics simulations. However, the problem with this kind of structural characterisation is that because of the (relatively) small sizes of the systems possible to simulate with the atomistic model, averaging over many configurations is required. This means that multiple molecular dynamics simulations would be required with different starting configurations. The second problem is how the spatial dependence of the exchange is characterised. There exist simple approximations to the spatial dependence of the exchange such as Ruderman-Kittel-Kasuya-Yoshida (RKKY) [92], however none are satisfactory. If one were to use ab-initio techniques, for example using density functional theory methods to

parameterise the exchange, again one would require a large super cell with many different configurations. This method quickly becomes very computationally expensive. Alloy methods, such as the coherent potential approximation (CPA) do exist for random materials but have not been studied in the work presented in this thesis. Other methods such as Green's function methods [93] can be used to study disordered alloys, though most studies are of atoms with a similar atomic size. Characterising the exchange from first principles would be a good way to extend the scope of this work, though this simple model as is shown in later chapters provides a good description of the important magnetic processes.

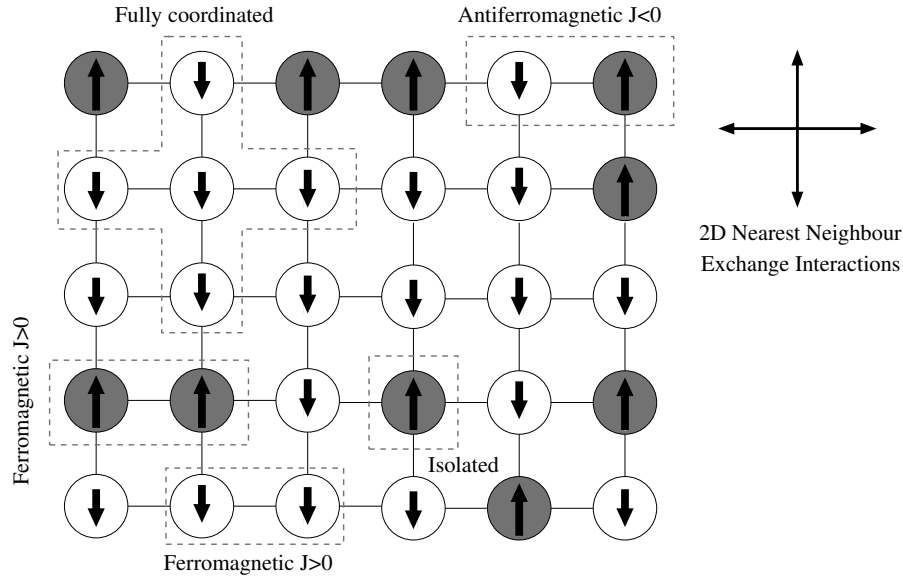


Fig. 2.1: A schematic showing the principle of the disordered model of a ferrimagnet to approximate the amorphous nature of TM-RE alloys. The principle interactions are shown; atoms interacting with the same species interact ferromagnetically. Interactions between different species are antiferromagnetic (AFM). These interactions lead to the two sublattices in the anti-parallel ground state observed experimentally. Because the spins are allocated at random there will be areas with different types of coordination, some spins will be surrounded by the opposite species and some will be fully coordinated with their own species.

The nature of the exchange interactions in this type of ferrimagnetic material leads to different temperature dependences of the magnetisation of each sublattice. In chapter 3, measurements (performed by I. Radu) of the magnetisation as a function of temperature for each sublattice, using the X-ray magnetic circular dichroism (XMCD) technique, are compared to the atomistic model of a ferrimagnet. This leads to a number of important findings including a magnetising effect of one sublattice to the other, which, effects the rate at which the system relaxes after a change in temperature.

Figure 2.2 shows an example of the temperature dependence of each sublattice in a TM-RE alloy (in the TM rich region of the phase diagram). Figure 2.2 has two distinct regions; below the magnetisation compensation point, T_M , the RE species dominates, above this temperature the TM dominates. The Fe species has more intra-sublattice interactions and in general interact more strongly, thus the magnetisation decreases more slowly with temperature. The

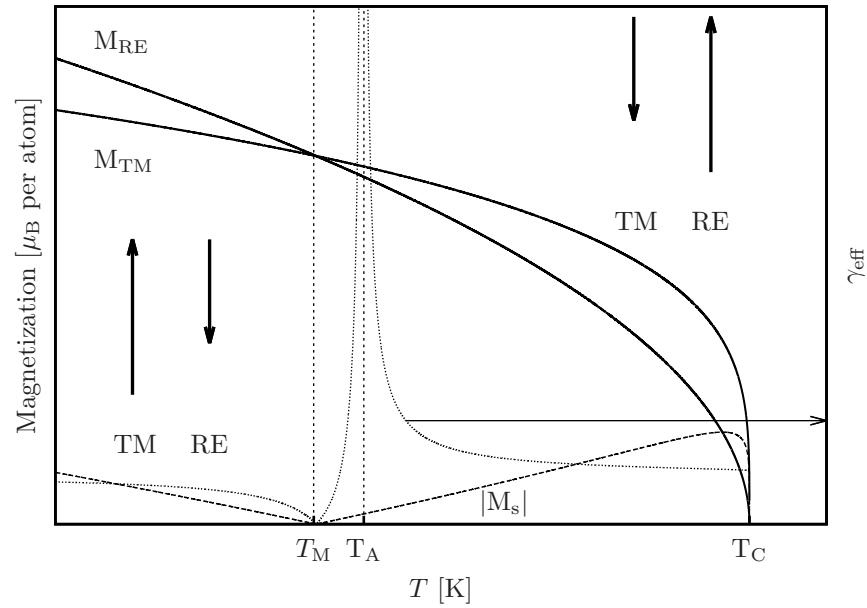


Fig. 2.2: Magnetisation curve of a ferrimagnet with a compensation point, T_M at which the magnetisation of the two sublattices cancel. The TM sublattice has a lower magnetisation at low temperature than that of the RE sublattice. At temperatures above T_M the TM has a higher magnetisation. The point T_A is the angular momentum compensation point. The arrow pointing right shows that this curve is the effective gyromagnetic ratio as discussed in section 2.5.2.

RE sublattice magnetisation on the other hand decreases more strongly with temperature because there are fewer RE-RE interactions, that are also weaker than TM-TM interactions. The main exchange contribution to the temperature dependence of the RE in this composition range is due to TM-RE interactions. This interaction is anti-ferromagnetic giving rise to the anti-parallel ground state and a magnetising effect of one sublattice on the other. Because the two sublattices are exchange coupled, they also share a common Curie temperature. At low temperatures, the RE species dominates due to its higher moment. As the temperature is increased the RE magnetisation decreases more rapidly with temperature, at some point the TM magnetisation cancels with that of the RE giving rise to the magnetisation compensation point, T_M , at which the magnetisation vanishes. Above this point the TM sublattice dominates as shown schematically on figure 2.2.

2.5.2 Angular Momentum Compensation Point in Ferrimagnets

The angular momentum compensation temperature, shown on figure 2.2 as T_A , arises when the two sublattices have different gyromagnetic ratios. The temperature is defined as the point at which the denominator in equation 2.5.1 goes to zero.

$$\gamma_{\text{eff}} = \frac{M_1 - M_2}{\left(\frac{M_1}{\gamma_1} - \frac{M_2}{\gamma_2}\right)}. \quad (2.5.1)$$

The origin of the different gyromagnetic ratios of the individual species arises because of a difference in the contributions to the angular momentum from spin-orbit coupling and crystal field potential [94]. In the 3d TM metals the orbital angular momentum is (almost) quenched because the crystal field interaction is much larger than the spin-orbit interaction [28]. The orbital angular momentum of the TM species is small and can thus be treated as a perturbation and can mix with states with non-zero angular momentum. This results in a g-factor that is not quite equal to 2. Ferrimagnets at T_A exhibit interesting behaviour, for example, there is a large increase in the resonance frequency and a large drop in the transverse relaxation time. This means that, for example, the domain wall velocity should be very large at this point. The converse is true at the magnetisation compensation point, there is a large increase in the transverse relaxation time and a drop in the resonance frequency. More details of this will be given in chapter 4.

2.6 Concluding Remarks

The beginning of this chapter introduced a model of atomistic spin dynamics (ASD) based on the LLG equation for individual magnetic moments. It was shown that when the LLG equation is augmented by a stochastic term that mimics thermal fluctuations, the equation can be written as a standard Langevin equation. Interpreting the stochastic integrals in the Stratonovich form, and writing the non-equilibrium probability distribution, the properties of the stochastic process have been shown. The Heun numerical scheme for solving the LLG Langevin equation was also shown. An important part of any computational model is to test the numerical calculations against known analytic solutions, this will be shown in chapters 3 and 4.

A specific model for amorphous ferrimagnetic materials, with a discussion of the exchange interactions has also been presented. The form of the exchange interactions combined with the LLG model should be a good way to reproduce many of the essential properties of ferrimagnets, such as the magnetisation compensation point. Some of the assumption regarding the exchange interactions and structure of the ferrimagnetic material will be tested against experimental observations in chapter 3.

Chapter 3

Static Properties of Transition Metal-Rare Earth Ferrimagnets

Following the introduction of the atomistic model in Chapter 2, in the proceeding chapter the physical input parameters will be determined based on experimental observations. This section includes a comparison of magnetisation and coercivity calculations to experimental measurements on samples of GdFeCo, performed by I. Radu. A comparison of the experimental and atomistic model results to those of an adapted mean field model is also presented. Comparison with the mean field results is used as a test of the validity of the atomistic model, providing a basis for more complex calculations.

3.1 Introduction

As discussed in Chapter 2, it is well known that transition metal (TM) rare-earth (RE) ferrimagnets used in magneto-optical recording may contain a magnetisation compensation point (T_M). This can be well explained in terms of a two-sublattice mean field model [47, 49]. Other approaches to describing the static properties of ferrimagnetic materials include mixed spin Ising models [50] and Greens' function studies [51]. During the 1980s a great deal of work was carried out on amorphous TM-RE alloys for use with magneto-optical recording media [95], however since then the interest has dwindled somewhat. In recent years this trend has begun to reverse, mainly because of the increased interest in studying their behaviour on the picosecond and femtosecond timescale [17]. Because of this, there is a need for a model that can capture the physics of these materials with high time and spatial resolution.

In order to construct and validate the atomistic model of ferrimagnetic GdFeCo, results for T_M , and the temperature dependent behaviour of the sublattices, obtained using X-ray Magnetic Circular Dichroism (XMCD) measurements, are compared. The experimental measurements were performed by I. Radu of the Helmholtz-Zentrum, Berlin, as part of a collaborative effort to parameterise the atomistic model.

3.2 Summary of Experimental Results

The element-specific XMCD technique, as discussed in section 1.8.3, was employed in order to measure the magnetisation of the Fe and Gd sublattices. The XMCD measurements were performed by I. Radu [59] at the PM3 and UE56/1 beamlines at the synchrotron light source BESSY II, Berlin. Both beamlines provide soft X-rays with variable light polarisation. XMCD was measured in transmission geometry with the X-ray at normal incidence and collinear with the external magnetic field. The X-ray intensity was recorded at fixed light helicity for opposite magnetic-field orientations (up to $\pm 0.7\text{T}$). As discussed in section 1.8.3, the difference of the resulting spectra (for the two field orientations) defines the XMCD value.

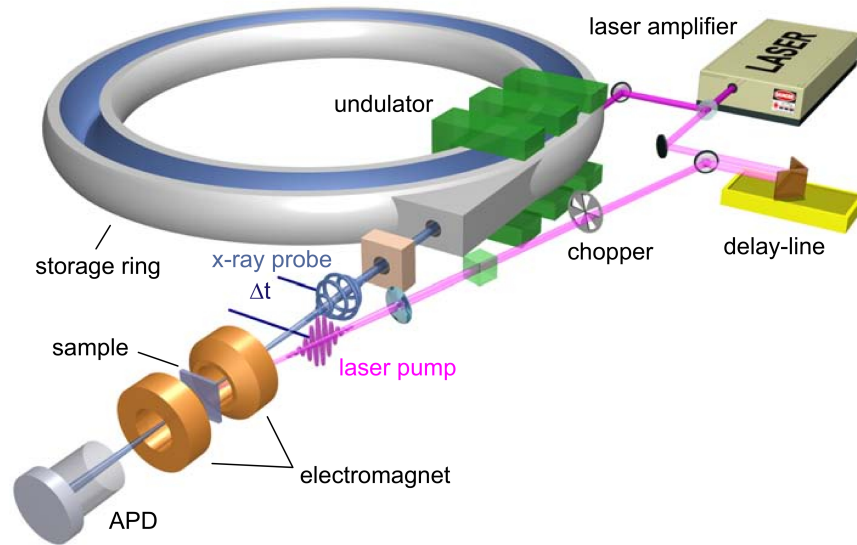


Fig. 3.1: Schematic layout of the UE56/1 beamline and the experimental setup at BESSY II used to measure the static properties in the current chapter and laser induced dynamics in chapters 3, 5 and 6. Experiments were performed by I. Radu and the figure is taken from Ref. [78].

A schematic of the UE56/1 beamline is shown in figure 3.1. This figure was obtained from Ref. [78] and is the setup used for experimental observations carried out by I. Radu in chapters 3, 5 and 6. In this chapter the setup was used without the laser pump as it is concerned with static measurements.

The samples studied are amorphous GdFeCo thin films of various compositions grown by magnetron sputtering on a SiN substrate that prevents against corrosion. The SiN substrate was chosen because of its transparency in the soft X-ray region. The samples were typically 30 nm GdFeCo thin films sandwiched between two SiN layers. Figure 3.2 shows a schematic representation of a typical sample. Element specific hysteresis loops were measured, by I. Radu, and were taken at the Fe and Gd absorption edges as a function of temperature to identify the magnetisation compensation point, where the coercive field, H_c , diverges. The photon energy was set at the maximum absorption edges; L_3 for Fe and M_5 for Gd. Figure 3.3 shows

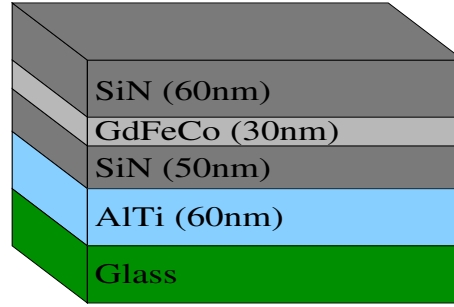


Fig. 3.2: A schematic of a typical sample of a GdFeCo Thin Film Structure. The GdFeCo is grown on a SiN substrate and sandwiched between two layers of SiN to avoid oxidation. The AlTi layer acts as a heat sink. The whole structure is deposited on a SiN substrate 150 nm thick supported by a Si Wafer.

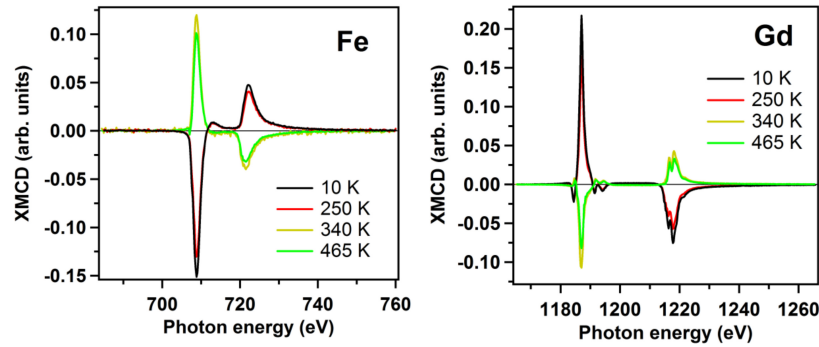


Fig. 3.3: XMCD spectra for $Gd_{25}Fe_{65.6}Co_{9.4}$ for a range of temperatures, Fe left and Gd right. The change in sign is due to the crossing of the magnetisation compensation point. Measurements performed by I. Radu and taken from Ref. [24].

sample XMCD spectra for $Gd_{25}Fe_{65.6}Co_{9.4}$, measured by I. Radu and published in Ref. [24]. This particular sample was used to make comparisons of dynamic behaviour to our model in chapter 6 and serves to show a typical XMCD spectra for GdFeCo. Figure 3.3 shows very clearly how the peaks in the XMCD spectra do not shift their energy with temperature as one would expect. The strong peak at around 708eV (left panel) is typical of the Fe L_3 (as in figure 1.18), the peak around 723eV is typical of the L_2 edge for Fe. Similarly the M_5 edge of Gd (right panel) located at around 1186eV and the M_4 edge at 1218eV are shown not to vary with temperature. Because the magnetic field was kept orientated in the same direction, when the compensation temperature was crossed, there was a change in the sign of the spectra.

The transmitted X-ray intensity was recorded as a function of magnetic field for a number of different compositions of GdFeCo. Figure 3.4 shows the temperature dependent hysteresis loops as measured at both the Fe and Gd edges for one particular composition, $Gd_{23.4}Fe_{73.3}Co_{3.3}$.

Accounting for the experimental geometry, an out-of-plane magnetisation orientation of the sample is deduced from the square shape of the hysteresis loop. The out-of-plane magnetisa-

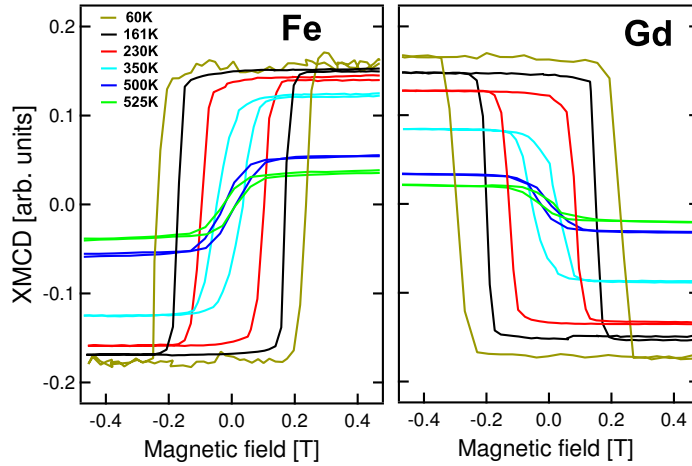


Fig. 3.4: Element and temperature dependent hysteresis loops measured for the Gd and Fe elements in $Gd_{23.4}Fe_{73.3}Co_{3.3}$ using XMCD. The two species have the same coercive field, however their magnetisations are opposite showing that they are anti-ferromagnetically coupled. Measurements carried out by I. Radu at BESSY II and published in Ref. [59].

tion in the thin film samples suggests a reasonably strong magneto-crystalline anisotropy to overcome the demagnetising field.

For the same sample shown in figure 3.4, the magnetisation, M and the coercive field, H_c , were measured, by I. Radu, at various temperatures. The result of this temperature dependent measurement is shown on figure 3.5. The coercivity measured for Gd and Fe sublattices are the same within the experimental error. This is to be expected as the two sublattices, as shown by figure 3.4, are strongly coupled by exchange. The variation of H_c with temperature shows diverging behaviour at the lowest temperature measured, indicating the presence of the magnetisation compensation point. However, for this particular sample, the compensation point is not crossed within the investigated temperature range, from 60K to 525K, with just temperatures above T_M being measured. It is worth pointing out here that the coercive field never truly diverges at the compensation temperature, except for a system in which the two sublattices are infinitely exchange coupled. The effect of such strong exchange coupling would keep the two sub-lattices exactly anti-parallel (rigid) and thus no torque would act from the applied field. Because in real systems the magnetisation is never fully compensated, due to the statistical nature of thermal fluctuations, at any instant there is some net torque from the field. This net torque then leads to magnetisation reversal.

By fitting the measured $M_s(T)$ data with a power law function, $M(T) = M(0)(1 - T/T_C)^\rho$ (solid lines in figure 3.5), the Curie temperature can be deduced for both the Fe and Gd sublattices of 540 ± 10 K. Varying the Gd content from 23.4% to 29%, the magnetisation compensation temperature can be tuned from below 60 K to 350 K. The results of the experimental measurements of the coercive field for four different Gd concentrations is shown on figure 3.6.

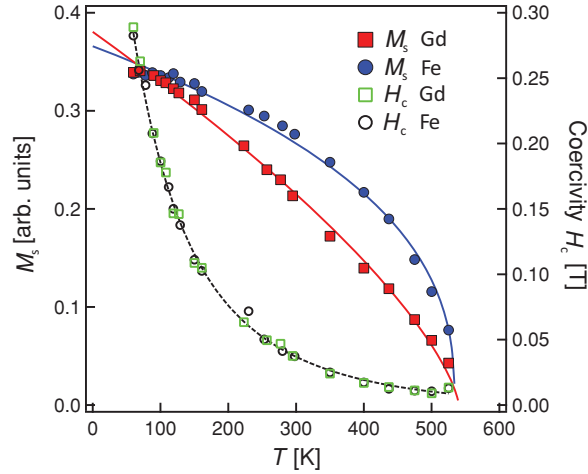


Fig. 3.5: Element specific variation of the coercive field, H_c , and saturation magnetisation, M_s , as a function of temperature for $Gd_{23.4}Fe_{73.3}Co_{3.3}$. The coercive fields were deduced from hysteresis measurements such as those shown in figure 3.4. The diverging coercivity just below 100K suggests the magnetisation compensation point. The solid lines are fits according to a power law, dashed lines are guides to the eye. Measurements carried out by I. Radu at BESSY II and published in Ref. [59].

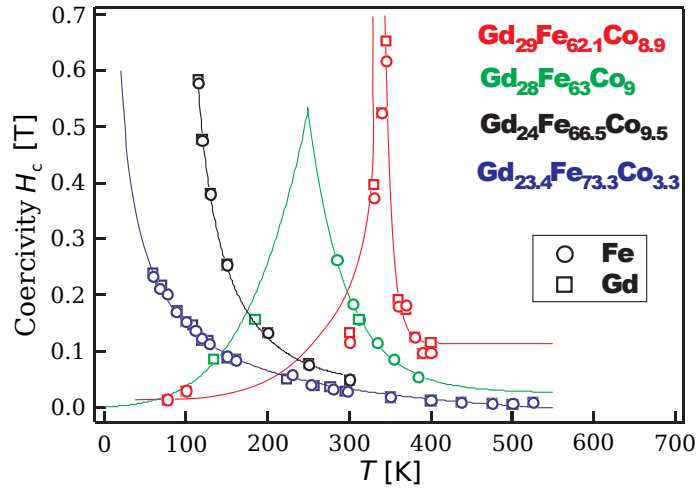


Fig. 3.6: Experimental data showing the temperature dependent coercivity for a range of GdFeCo compositions. The divergence in the coercivity indicates the magnetisation compensation temperature. The solid lines are guides to the eye. Measurements carried out by I. Radu at BESSY II and published in Ref. [59].

3.3 Mean Field Approximation for Two Sublattice Disordered Systems

A successful atomistic model should demonstrate that it can reproduce analytic results and be consistent with other models. To this end, an adapted mean field approximation (MFA) has been developed based on the free energy of the two sublattice ferrimagnetic system [30, 47, 48, 96]. This model allows a comparison of the magnetisation compensation temperature,

Curie temperature and the temperature dependence of the magnetisation calculated from the atomistic model.

The free energy $\mathcal{F} = -k_B T \ln \mathcal{Z}$ of a spin system, where \mathcal{Z} is the partition function, described by the Hamiltonian in equation 2.2.1, can be calculated in the MFA by considering each spin on a site i , as an isolated spin, with the effective field containing contributions determined by the mean values of the neighbours [97]. For our ferrimagnetic system, we can divide the system into two asymmetric sublattices; the impurity sublattice with RE spins and the bulk one with TM spins, written

$$\begin{aligned} \mathcal{H} \Rightarrow \mathcal{H}^{\text{MFA}} = & \mathcal{H}_{00} - \mu_{\text{TM}} \sum_{\text{TM}} \mathbf{H}_{\text{TM}}^{\text{MFA}} \cdot \mathbf{s}_{\text{TM}} \\ & - \mu_{\text{RE}} \sum_{\text{RE}} \mathbf{H}_{\text{RE}}^{\text{MFA}} \cdot \mathbf{s}_{\text{RE}}, \end{aligned} \quad (3.3.1)$$

with \mathcal{H}_{00} being given by:

$$\mathcal{H}_{00} = \sum_{ij} J_{ij} \boldsymbol{\sigma}_i \cdot \boldsymbol{\sigma}_j + \sum_i K_i \sigma_{z,i}^2. \quad (3.3.2)$$

The spin polarisation, $\boldsymbol{\sigma}_i = \langle \mathbf{s}_i \rangle$, and the molecular field, $\mathbf{H}_i^{\text{MFA}}$ associated with the site i are given by:

$$\mu_i \mathbf{H}_i^{\text{MFA}} = \mu_i \mathbf{H} + 2K_i \sigma_{z,i} \mathbf{e}_z + \sum_j J_{ij} \boldsymbol{\sigma}_j. \quad (3.3.3)$$

The exchange part is then divided by dividing the sum over the neighbours in two, i.e., $\sum_j \rightarrow \sum_{\text{TM}} + \sum_{\text{RE}}$. The anisotropy is then written as, $\mathbf{H}_{A,i} = (2K_i/\mu_i) \sigma_{i,z} \mathbf{e}_z$, and, passing to the continuous limit, $\boldsymbol{\sigma}_i \Rightarrow \boldsymbol{\sigma}(\mathbf{r})$, and assuming $\Delta \boldsymbol{\sigma}(\mathbf{r}) = 0$, the molecular field then reads:

$$\mu_i \mathbf{H}_i^{\text{MFA}} = \mu_i (\mathbf{H} + \mathbf{H}_{A,i}) + \sum_{\text{TM}} J_i^{\text{TM}} \boldsymbol{\sigma}_{\text{TM}} + \sum_{\text{RE}} J_i^{\text{RE}} \boldsymbol{\sigma}_{\text{RE}}. \quad (3.3.4)$$

If z is the number of nearest neighbours and x is the RE concentration, then a TM moment will have on average zx neighbouring RE moments and $z(1-x) = zq$ neighbouring TM moments and the converse for the RE moments. Averaging over the system configurations and defining $\mathbf{H}'_{\text{eff},i} = \mathbf{H} + \mathbf{H}_{A,i}$, we can write the average molecular field acting at each sublattice spin as:

$$\mu_{\text{RE}}^{\text{MFA}} \mathbf{H}_{\text{RE}}^{\text{MFA}} = \mu_{\text{RE}} \mathbf{H}'_{\text{eff,RE}} + x J_{0,\text{RE-RE}} \boldsymbol{\sigma}_{\text{RE}} + q J_{0,\text{TM-RE}} \boldsymbol{\sigma}_{\text{TM}}, \quad (3.3.5)$$

$$\mu_{\text{TM}} \mathbf{H}_{\text{TM}}^{\text{MFA}} = \mu_{\text{TM}} \mathbf{H}'_{\text{eff,TM}} + q J_{0,\text{TM-TM}} \boldsymbol{\sigma}_{\text{TM}} + x J_{0,\text{TM-RE}} \boldsymbol{\sigma}_{\text{RE}}. \quad (3.3.6)$$

In equations 3.3.5 and 3.3.6, $J_{0,ij} = z J_{ij}$, is the mean field exchange. Note that to recover the Hamiltonian for the pure ferromagnetic in equations 3.3.5 and 3.3.6, x must be set to zero and $J_{0,\text{TM-TM}} = 0$. The free energy then takes the form

$$\mathcal{F} = \mathcal{H}_{00} - \mathcal{N} k_B T \ln(4\pi) - k_B T \sigma_i \Pi(\xi_i), \quad (3.3.7)$$

where $\Pi(\xi) \equiv \ln(\sinh(\xi)/\xi)$, $\xi_i \equiv |\xi_i|$, and $\xi \equiv \mu_i \mathbf{H}_i^{\text{MFA}}/k_B T$. The mean field free energy determined by equations 3.3.5, 3.3.6 and 3.3.7 can be minimized with respect to the spin averages, σ_{RE} and σ_{TM} , to find the equilibrium solution. Finding stationary points, $\partial\mathcal{F}/\partial\sigma_{\text{RE}} = \mathbf{0}$ and $\partial\mathcal{F}/\partial\sigma_{\text{TM}} = \mathbf{0}$ leads to the coupled Curie-Weiss equations:

$$\sigma_{\text{RE}} = L(\xi_{\text{RE}}) \frac{\xi_{\text{RE}}}{\xi_{\text{RE}}}, \quad \sigma_{\text{TM}} = L(\xi_{\text{TM}}) \frac{\xi_{\text{TM}}}{\xi_{\text{TM}}}, \quad (3.3.8)$$

where $L(\xi) = \coth(\xi) - 1/\xi$ is the Langevin function. The magnetisation can be calculated using a standard self-consistent solution method. The self consistent method works as follows:

- The Hamiltonian for the particular temperature is calculated.
- The spin polarisation is looped over, at each value of the spin polarisation, the Langevin function is calculated using the field calculated in the first step and the temperature.
- When the Langevin function and the spin polarisation are the same (within some tolerance) the value of the magnetisation has been found.

The self-consistent method is shown schematically in figure 3.7, where the two lines meet this is the value of the spin polarisation used. The total equilibrium magnetisation per atom is

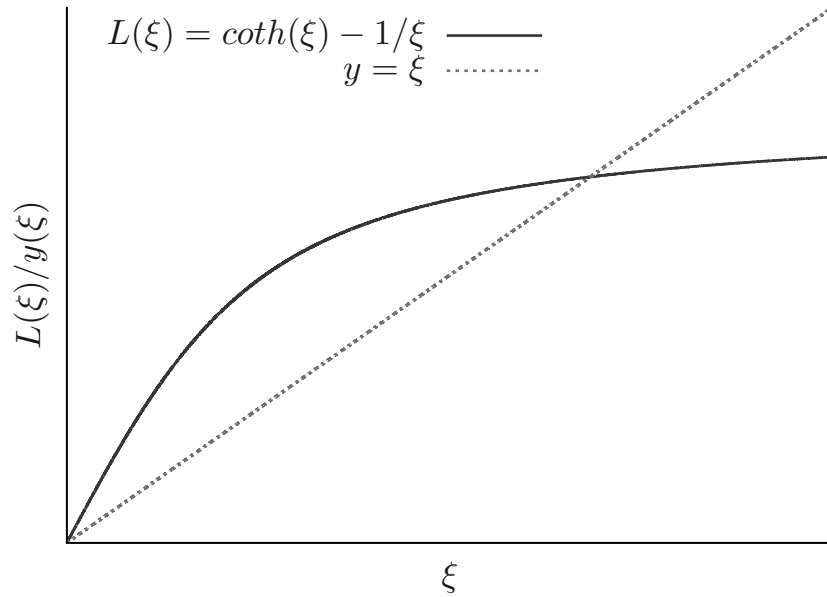


Fig. 3.7: A schematic showing a self-consistent method of finding the magnetisation in the mean field. The solid curve represents the Langevin function, the dashed is the spin polarisation that is looped over. Where the two lines cross, this value of the spin polarisation is the magnetisation. At the Curie temperature gradients of the lines through zero are equal.

evaluated as

$$M = \mu_{\text{TM}} q \sigma_{e,\text{TM}} - \mu_{\text{RE}} x \sigma_{e,\text{RE}}. \quad (3.3.9)$$

Close to T_C , the Langevin function can be expanded as $L(\xi) \approx \xi/3$, and the MFA Curie temperature of the ferrimagnet can be shown to be

$$T_C^{\text{MFA}} = \frac{2a}{3k_B b} \frac{1}{\sqrt{1 + 4a/b^2} - 1}, \quad (3.3.10)$$

where

$$\begin{aligned} a &= qx(J_{0,\text{TM-RE}}^2 - J_{0,\text{RE-RE}}J_{0,\text{TM-TM}}), \\ b &= qJ_{0,\text{TM-TM}} + xJ_{0,\text{RE-RE}}. \end{aligned} \quad (3.3.11)$$

In the low concentration limit we obtain a linear decrease of the Curie point, $T_C^{\text{MFA}} = qJ_{0,\text{TM-TM}}/3k_B T$.

3.4 Comparison Between Atomistic and Mean Field Models

Using the mean field approximation (MFA) described in section 3.3, we can compare results for the temperature dependence of the magnetisation, the Curie temperature and compensation temperature with the atomistic model. In this section all of the results of the atomistic model calculations are calculated for a face-centred cubic (fcc) structure with TM and RE spins allocated randomly as discussed in chapter 2.

It is well known that the MFA overestimates the Curie temperature because of the fact that at high temperatures there exist areas where there is order, i.e. correlated regions, however over the ensemble the average is zero, an effect that is not taken into account in MFA [31] because spin fluctuations are neglected.

To calculate the magnetisation in the atomistic model, 62,500 spins were simulated with periodic boundary conditions, equilibrating at each temperature until there was no change in the time-averaged magnetisation. The thermodynamic average of the magnetisation was calculated over a further period of 60ps. The average magnetisation was calculated for each sub-lattice by finding the reduced magnetisation, m_i , of the sublattice i at each step and averaging over the number of timesteps, t_{max} :

$$\langle m \rangle = \frac{1}{t_{\text{max}}} \sum_{t=0}^{t_{\text{max}}} m_i(t), \quad (3.4.1)$$

Figure 3.8 shows temperature dependent magnetisation curves for GdFe for a range of Gd concentrations in zero applied field. The temperature axis is reduced to the Curie temperature of each composition to overcome the MFA overestimation. As discussed in section 3.3, the Curie temperature for a ferrimagnet is known analytically and can be compared by direct calculation from the atomistic model. It is also possible to solve (using the self consistent method described above) the magnetisation with temperature and find the magnetisation compensation point as a function of the composition. To perform such a comparison for real temperatures (rather than reduced temperatures), the J_{ij} values in the MFA were rescaled to

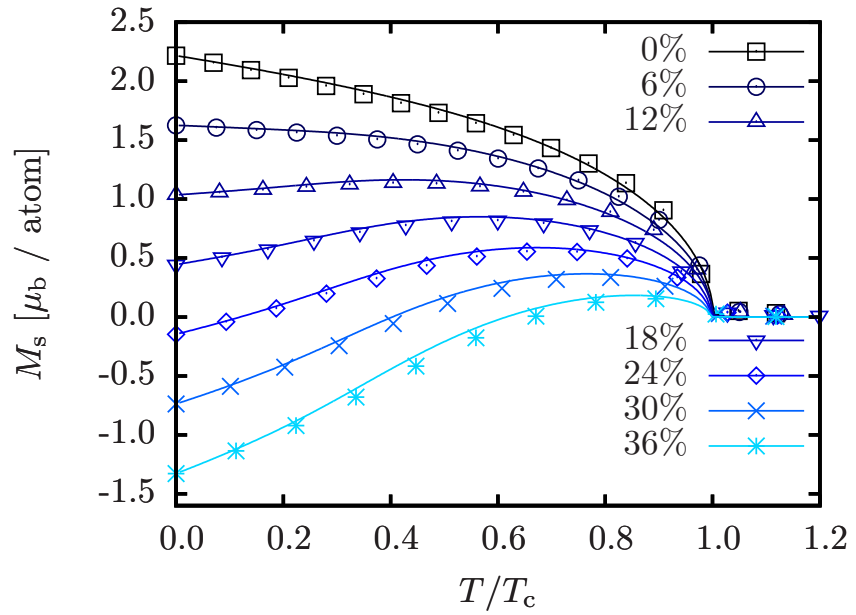


Fig. 3.8: Magnetisation curves as a function of temperature (normalised to T_C for each composition) for a range of RE concentrations. The points are the calculations via the atomistic model, the solid lines are calculated via the MFA.

be comparable with the atomistic model. The procedure for doing so was as follows:

- Take J_{ij} for each interaction in atomistic model, i.e. $J_{\text{TM-TM}}$, $J_{\text{RE-RE}}$ and $J_{\text{TM-RE}}$.
- Find the Curie temperature that is associated with a system if it had purely that interaction given by $3.18J = k_B T_C$ for an fcc lattice [98].
- For each T_C associated with each exchange value, find J_{ij} for the MFA using $zJ_0 = 3k_B T_C$ [31].

Figure 3.9 shows magnetisation curves for a range of Gd concentrations, at high RE concentrations in panel a), there is a compensation point, T_M , arising at around the 24% Gd line. Below T_M the magnetisation is dominated by the RE sublattice, above this point it is dominated by the TM. This point occurs at a temperature which decreases with decreasing x , consistent with experiment [71]. With decreasing x , the compensation temperature decreases, vanishing at a critical concentration, x_c . For values of $x < x_c$ the magnetisation shows a peak value at some temperature greater than zero. The addition of the RE also reduces the Curie temperature because the weaker TM-RE and RE-RE interactions reduce the average exchange. Using the data from the atomistic model presented in figure 3.9 a comparison between the MFA, atomistic model and experiment can be made.

Figure 3.10 shows the experimental compensation temperature, T_M , as a function of RE concentration, x , showing also the MFA results and that of the atomistic model results. The Curie temperature was calculated from magnetisation curves and by fitting to the numerical

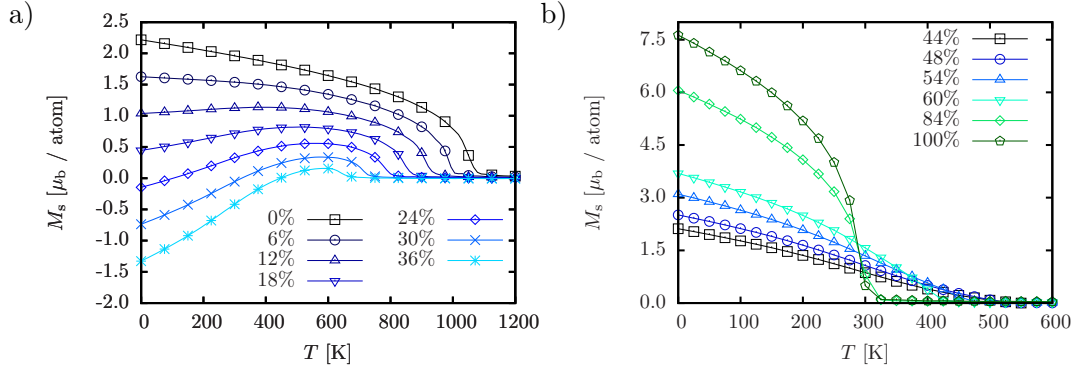


Fig. 3.9: Magnetisation as a function of temperature for different concentrations of RE (Gd) calculated using the atomistic model. a) TM dominated concentration region showing that around 24% there exists a magnetisation compensation temperature. b) For the RE dominated magnetisation curves, the Curie temperature is lower as it tends towards the value for pure Gd.

data as described in Ref. [12]. To find T_C the magnetisation curves were interpolated to $M = 0$, representing the phase transition. These Curie temperatures are then compared to the analytic results from the MFA. As can be seen in figure 3.10, the atomistic model agrees

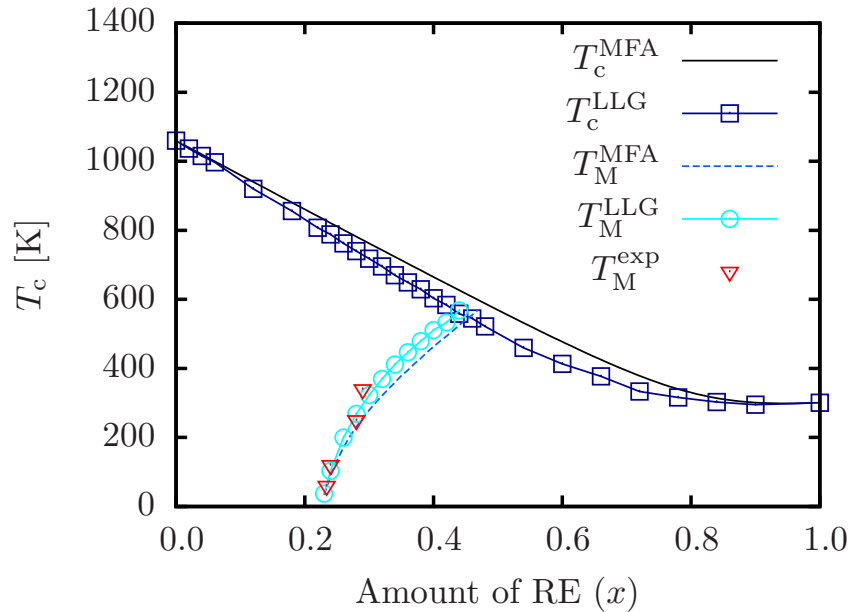


Fig. 3.10: Compositional dependence of the Curie temperature (T_C) and magnetisation compensation temperature (T_M). The mean field approximation (lines) with renormalised exchange parameters is shown to agree very well with the atomistic model (square and circular line points). The experimentally measured compensation temperatures deduced from temperature-dependent hysteresis curves show excellent agreement with the mean field and atomistic model.

very well with the MFA predictions. The magnetisation compensation temperature appears at the same composition, x_c , in both models and disappears again at around the same point,

showing the strength of the MFA for predicting static properties of this kind of ferrimagnetic system. The composition range for which the magnetisation compensation point exists is also in good agreement with the experimental data in Ref [71].

3.5 Coercivity Calculations Using Atomistic Model

As a next step towards checking the validity of the atomistic model, calculations of the coercivity of the system for a range of RE concentrations were performed. These calculations

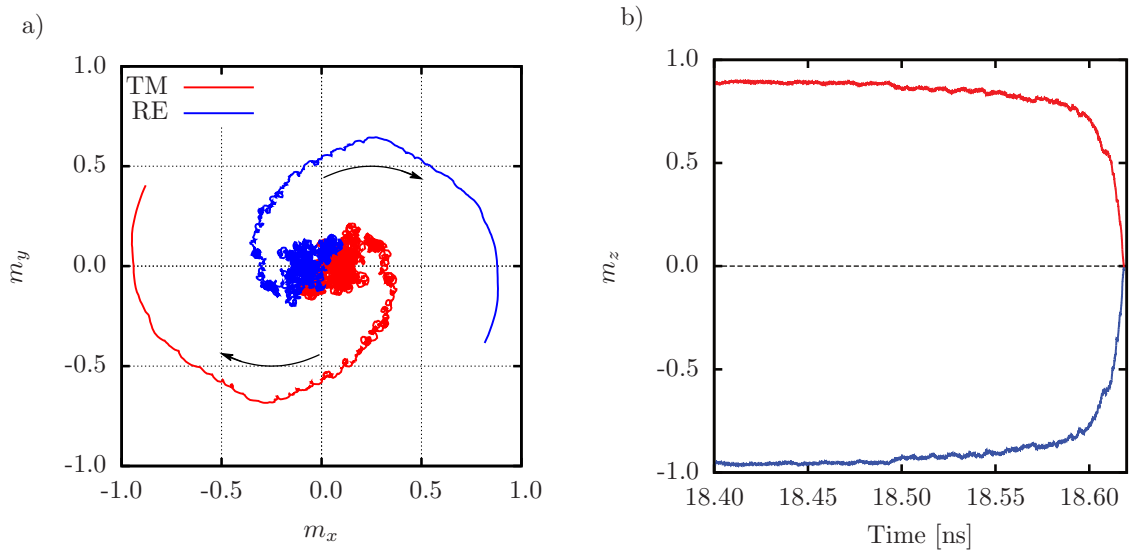


Fig. 3.11: a) Phase space plot of the x and y components of the magnetisation of the TM and RE sublattices are shown, showing large amplitude precession of the sublattice magnetisation in a field. The arrows represent the time evolution of the system. b) From the same data set as a), with the z -component of the magnetisation shown as a function of time. The temperature at which the coercivity was calculated here was $T = 50$ K and the Gd concentration was 32%. The sweep rate used was 0.1T/ns , meaning that switching occurred at just above 1.86T .

were performed on the same systems sizes and boundary conditions as in section 3.4. The sweep rate for the magnetic field used was 0.1T/ns , which means that the results cannot be compared quantitatively to those in figure 3.6, as the sweep rates used in the lab, typically KHz, give timescales that are not accessible in the simulations. The results should, however, be comparable qualitatively as the same feature, a large increase in coercivity, should be observed at the magnetisation compensation point.

The small system sizes simulated using the atomistic model show a single domain state, where switching is observed via precessional switching only. To calculate the coercivity the system was equilibrated to the temperature specified. The field was subsequently ramped in the direction opposite to the net magnetisation. An example of the system reversing via precession can be seen in panel a) of figure 3.11. The arrows in this figure represent the time evolution of the system. The z -component of the magnetisation is shown as a function of time for the same data set in panel b).

The value of the coercivity was found by averaging over 10 different seeds of the random number generator, a statistically small amount due to the computational expense for such a calculation. The value of the coercivity for each sample was reduced to the calculated value for pure Fe (at zero K for the same sweep rate). The results of the numerical calculations of the coercivity are shown in figure 3.12 for a range of Gd concentrations and if we compare to the experimental results in figure 3.6 we can see that there is good qualitative agreement between the two. It should also be pointed out that the mean is calculated over only 10 runs

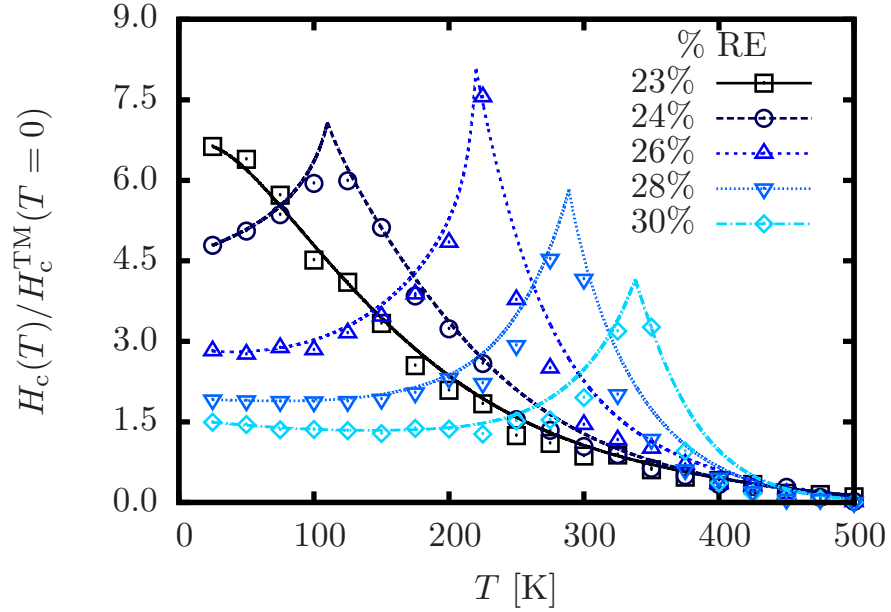


Fig. 3.12: Numerical values of the coercive field (points), for a range of RE compositions. The values were calculated using the atomistic model at a sweep rate of $0.1T/ns$, and by averaging over 10 realisations of the random number generator. The data is normalised to the zero temperature, pure TM coercivity with the same sweep rate. Results show good qualitative agreement with experiment (figure 3.6), with the divergence representing the magnetisation compensation point. Lines are guides to the eye.

so some statistical error is inevitable. The relative error (equation 3.5.1) for the 23% curve in figure 3.12 is shown in table 3.1.

$$\Delta_c = \frac{\sigma_c}{\sqrt{N}\bar{H}_c}, \quad (3.5.1)$$

The relative error in table 3.1 shows a general increase with increasing temperature rising to over 20% around 500K. For the low temperatures the spread in the data is quite small, only a few percent.

Temperature	Δ_c [%]
50	0.327843
100	0.987253
150	0.767684
200	2.31382
250	2.82149
300	6.06139
350	4.47959
400	4.57261
450	9.89974
500	21.9129

Table 3.1: Relative error in coercivity measurement (equation 3.5.1) for the 23% RE content in figure 3.12. As one might expect there is a general increase in the error with increasing temperature. For low temperatures there is only a few percent spread about the mean increasing to over 20% at 500K.

3.6 Effect of Varying Exchange Parameters: Mean Field Results

The exchange interactions in GdFeCo, as in all systems, define the Curie temperature as they give rise to the order between the magnetic spins within the system. Without exchange between the two sublattices each one will act independently as a ferromagnetic material with missing exchange links. As the strength of the TM-RE exchange interaction is increased, the two sublattices will be more strongly coupled and the Curie temperature will increase. The mean field approximation described in section 3.3 allows us to quickly see the effect of varying the exchange parameters on the Curie temperature. Figure 3.13 shows the variation of the Curie temperature as given by equation 3.3.10 as a function of composition for a range of TM-TM interaction strengths. The lowest curve shows the Curie temperature as a function of the TM-RE exchange when there is no coupling between the TM species. This means that the interaction energy comes from the RE species alone.

Whilst varying the TM-TM exchange up to the maximum value, $J_{\text{TM-TM,max}}$, which gives the correct Curie temperature for Fe, the values of $J_{\text{TM-RE}}$ and $J_{\text{RE-RE}}$ are kept constant at $J_{\text{TR,max}}$ and $J_{\text{RR,max}}$. The value of $J_{\text{RR,max}}$ was chosen to give the correct Curie temperature for Gd and $J_{\text{TR,max}}$ gives a Curie temperature of 251K in the mean field. It will be shown in the following section that the Curie temperature of 251K corresponds to a particular exchange constant in the atomistic model that gives good agreement with the temperature dependence of GdFeCo shown experimentally.

The TM-TM interaction gives the strongest variation of the Curie temperature for different strengths of the exchange, $J_{\text{TM-TM}}$, particularly in the low RE concentration region where the TM-TM interactions dominate. In the same way it is possible to look at the strength of the RE-RE exchange and the TM-RE exchange. Figure 3.14 shows the variation of the Curie temperature given by equation 3.3.10 as a function of composition for a range of RE-RE and

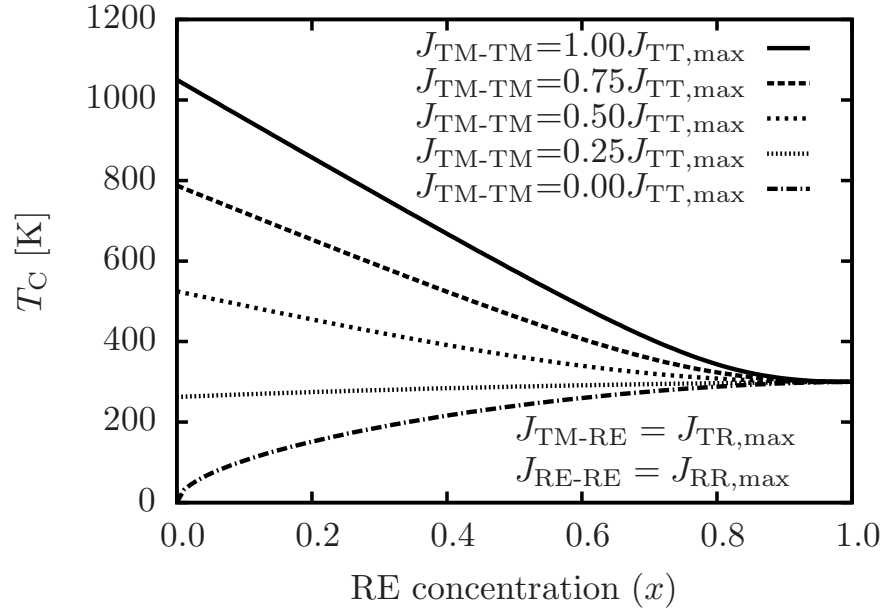


Fig. 3.13: Variation of the Curie temperature as a function of composition for a range of TM-TM exchange given by equation 3.3.10. For the pure TM with zero TM-TM interactions, the Curie temperature is zero. For pure RE ($x=1$) the Curie temperatures converge as there are no TM-TM interactions. The value of $J_{TT,max}$ gives the correct Curie temperature for Pure Fe in the mean field. Similarly the TM-RE exchange is set to $J_{TR,max}$ and the RE-RE exchange is set to $J_{RR,max}$.

TM-RE interaction strengths.

Figure 3.14 shows that the RE-RE and TM-RE exchange have a similar effect on the Curie temperature for low RE concentrations. This is because the TM-TM interaction is dominant for low RE concentration (low x). As x increases, more RE spins are replaced by TM spins and thus there are fewer TM-TM interactions. This leads to changes in the Curie temperature in different ways for the variation of the TM-RE and RE-RE exchange. For $J_{TM-RE} = 0$, there are two valid solutions for the Curie temperature for all compositions except where the relation $b^2 = 4a$, from equation 3.3.11. Physically the reason is because if $J_{TM-RE} = 0$ then the TM and RE act as individual ferromagnets thus there is a separate Curie temperature for the TM and the RE species.

3.6.1 Atomistic Model Results for the Temperature Dependence of the Magnetisation

As was shown in figure 3.14 b), for a given concentration, x , there is an increase in T_C with increasing J_{TM-RE} . This figure, however, does not show how the temperature dependence of the magnetisation changes. Figure 3.15 shows the results of atomistic model calculations, of the temperature dependence of the magnetisation for a range of J_{TM-RE} . J_{max} in this figure is -2.18×10^{-21} J. The RE concentration is 30% and the TM-RE exchange interaction is varied

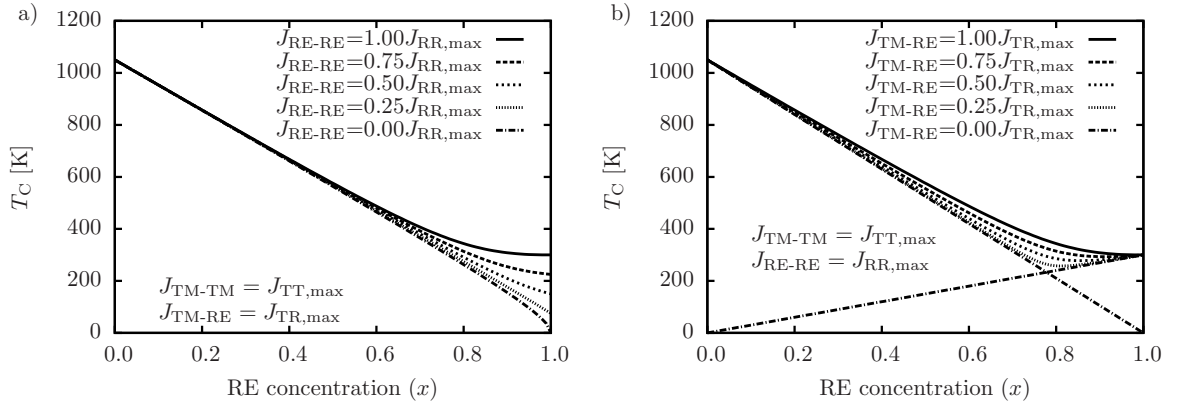


Fig. 3.14: a) Variation of the Curie temperature as a function of composition for a range of RE-RE and b) TM-RE exchange given by equation 3.3.10. The other exchange interaction values are set to the maximum value as described above. In panel a), for the TM dominated region, there is almost a linear decrease in the Curie temperature with increasing RE content. In panel b) the TM-RE exchange has a similar effect on the Curie temperature for low concentrations.

giving rise to an increase in the Curie temperature and a polarising effect of one sub-lattice on the other. The polarisation effect of one sublattice on the other gives rise to the two sublattices sharing a common Curie temperature. In the limit of zero TM-RE exchange the two sublattices show separate Curie temperatures in agreement with the MFA.

Comparing the temperature dependence of each sublattice to XMCD measurements, shown in figure 3.5, it is possible to gauge the strength of the inter-sublattice exchange interaction. Figure 3.5 shows that the RE magnetisation varies almost linearly with temperature, thus from the atomistic model calculations one can deduce that the strength of the exchange is in the range $-1.09 \times 10^{-21} \text{ J} > J_{\text{TM-RE}} > 1.635 \times 10^{-21} \text{ J}$.

3.6.2 Atomistic Model Results for the Dynamic Effect of TM-RE Exchange

Atomistic models have been previously used for studying short timescale magnetisation dynamics [99] after excitation by femtosecond laser pulses, giving good agreement with experimental timescales for the demagnetisation process [99]. The atomistic model requires a well defined temperature and is generally based on a two-temperature model approach [46], discussed in section 1.4.3. The laser power is assumed to be absorbed by the conduction electrons, which are coupled to the phonon system by a phenomenological coupling constant. Kazantseva *et al.* [99] developed a model of ultrafast heating of a ferromagnet, assuming that the energy transfer mechanism is via conduction electrons into the spin system. Here, the energy transfer between the incident laser pulse and the spin system is less clear-cut. It seems reasonable to assume that there exists a channel via the conduction electrons into the TM spin system as in the pure ferromagnet. However, the dominant mechanism of transfer of energy into the RE sublattice is more complex.

As shown in figure 3.14 (right), the TM-RE exchange results in small changes in the Curie

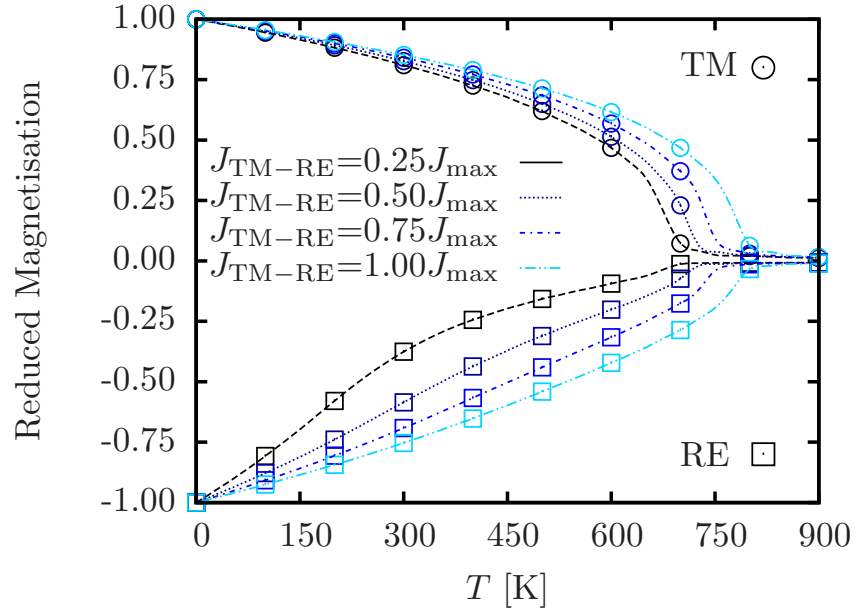


Fig. 3.15: Reduced magnetisation of the Fe and Gd sublattices for various inter-sublattice exchange constants ($J_{\text{TM-RE}}$) calculated using the atomistic model. Magnetisation is normalised to the sublattice magnetisation. Here $J_{\text{max}} = -2.18 \times 10^{-21}$ J.

temperature (for concentrations up to $x \approx 0.5$). Figure 3.15 shows that the TM-RE exchange changes the temperature dependence of the magnetisation. However it is not clear what effect this parameter has on the dynamics of the system. To this end, the atomistic model was used to observe the effect of the inter-sublattice exchange constant on the demagnetisation of this TM-RE system. To look at the effect of TM-RE exchange coupling an effective spin temperature T_{eff} was defined. The effective spin temperature is defined in the following way. For any set of exchange parameters ($J_{\text{TM-RE}}$, $J_{\text{TM-TM}}$ and $J_{\text{RE-RE}}$), a magnetisation curve for each sublattice (as in figure 3.15) was calculated. Below the Curie temperature (in equilibrium) the magnetisation of a sublattice has a well-defined effective temperature, shown schematically in figure 3.16. The black dashed line shows that the two sublattices have a particular magnetisation value in equilibrium at 250 K. The grey dotted line shows, for example, that the TM sublattice has a particular value of the magnetisation that gives an effective spin temperature of 425 K and that of the RE as 450 K.

Using the magnetisation curves from figure 3.15 to define the effective spin temperature, the atomistic model was used to investigate the rate of energy transfer and the rate of relaxation of the TM and RE sublattices. To calculate the effective spin temperature, the TM-RE system was initially set in its ground state at zero K (anti-parallel sublattices) before instantaneously increasing the temperature to 300K. The instantaneous magnetisation of each sublattice is then used to define the effective spin temperature as a function of time. Figure 3.17 shows the variation of the effective spin temperature for different values of the TM-RE exchange constant. The relaxation process as shown in figure 3.17 is governed by the longitudinal relaxation of the magnetisation as described in section 1.4.1. The TM sublattice (square

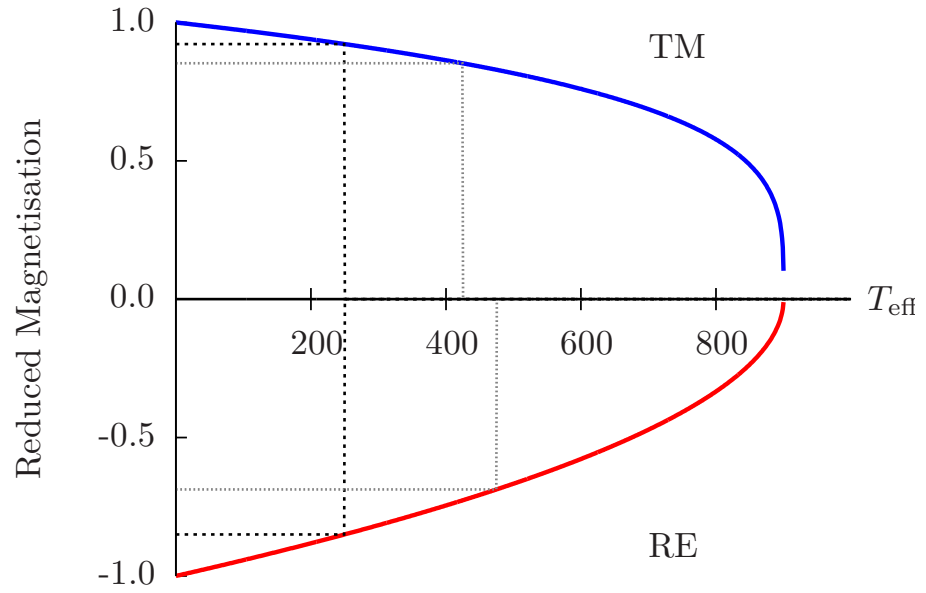


Fig. 3.16: Schematic showing the definition of the effective spin temperature. For any set of exchange parameters, a magnetisation curve is calculated giving any value of the magnetisation a unique temperature. Using this magnetisation each sublattice can be shown to have an effective spin temperature. The black dashed lines show the system in equilibrium at 250 K. The dotted grey lines show the system out of equilibrium with the TM and RE having different effective spin temperatures.

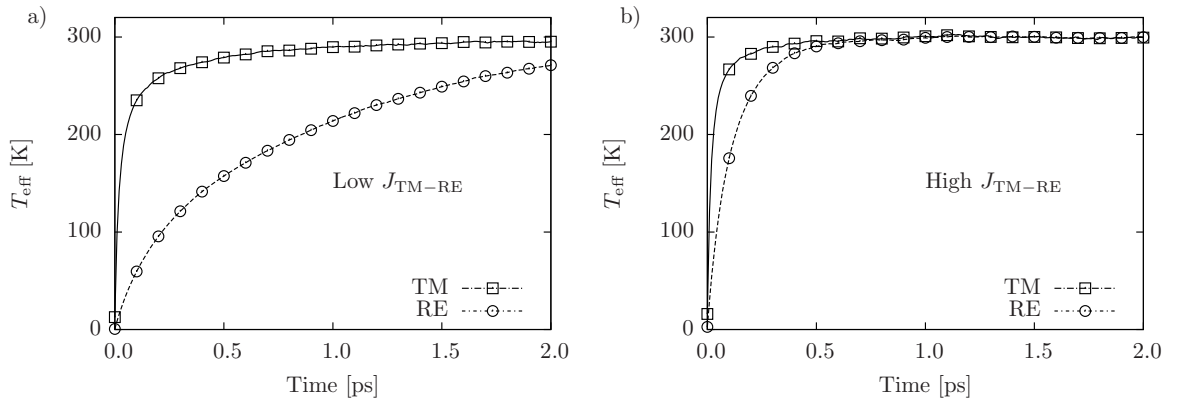


Fig. 3.17: Effective spin temperature as a function of time for low TM-RE exchange (a) and high TM-RE exchange (b). The effective spin temperature for both sublattices is shown showing that the TM and RE sublattices relax at different rates. The low TM-RE exchange case (a) shows a very slowly relaxing RE, in contrast to the much faster RE relaxation for the high coupling case (b).

points) shows a smaller variation of relaxation time than the RE, but, is still faster for higher exchange. The difference between the TM and RE demagnetisation times is driven by the difference in the magnetic moment. The higher exchange between the TM and RE species has a much larger effect on the demagnetisation rate in the RE spin system (circled points), showing an almost order of magnitude change between panels a) and b).

There are a number of key parameters in the model that determine the rate of longitudinal relaxation of the magnetisation; the effective exchange acting on each magnetic moment, the size of the magnetic moment and the thermal bath coupling constant. For the low $J_{\text{TM-RE}}$ case, the effective exchange acting on the RE moments is lower than that of the high $J_{\text{TM-RE}}$ case, resulting in slower relaxation. The difference in the relaxation times between the TM and RE sublattices is an interesting observation, which is shown in the following chapters to be a common feature of two sublattice magnets whether ferromagnetic or ferrimagnetic. As will be seen in later chapters the difference in the relaxation times of the two sublattices in this type of ferrimagnetic material is also important for switching dynamics.

As is shown in figure 3.17 the RE is most strongly affected, in terms of relaxation time, by the $J_{\text{TM-RE}}$ exchange interaction. Figure 3.18 shows the effective spin temperature of the RE sublattice as a function of time for a range of TM-RE exchange constants.

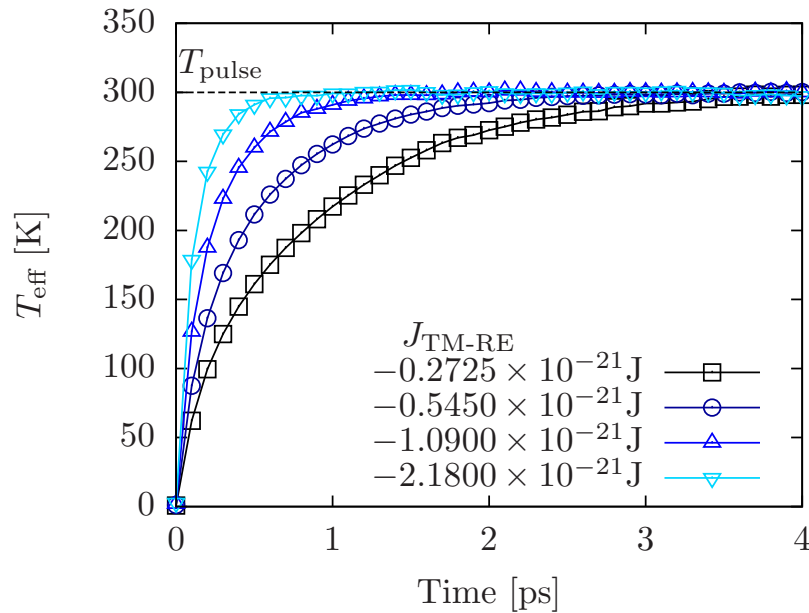


Fig. 3.18: Atomistic model results of the effective RE spin temperature (T_{eff}) as a function of time. A range of different TM-RE exchange constants are shown, the higher this value the faster the relaxation rate.

3.7 Concluding Remarks

The results of the static magnetic properties from the atomistic model, and the comparison with the experiment (performed by I. Radu) and the MFA (derived by U. Atxitia) act as both a validation of the computational model and MFA approach and a method for parameterising the physical inputs to the model. The atomistic model is capable of reproducing Curie temperatures and magnetisation compensation temperatures comparing well with experimental measurements and results from the MFA. The calculated temperature dependence of the

magnetisation of each sublattice has been compared with that of the element specific XMCD measurements. This comparison presents a means by which the model can be parameterised. For GdFeCo, this kind of parameterisation, based on experimental observations, is more efficient than *ab-initio* techniques [11]. To parameterise this kind of material using electronic structure methods would require averaging over many configurations of supercells with a large number of atoms. Although methods for random alloys do exist, the random configurations of the atoms would mean that the calculations would become very computationally expensive using standard density functional theory (DFT) techniques, because no symmetry could be exploited.

The effect of the compensation point on the coercivity was found to be qualitatively similar when comparing the simulations and experiments. The importance of the TM-RE exchange interaction on the time-resolved magnetisation dynamics was shown. The difference in the timescale of the two sublattices is important, and, as will be discussed in later chapters, is a general feature of exchange coupled alloys with two or more magnetic sublattices.

The atomistic model based on Langevin dynamics provides the capability to study time-resolved and element specific magnetisation dynamics. The capabilities of the model are important for later chapters of this thesis where we make comparisons between the atomistic model calculations and measurements of sub-picosecond magnetisation dynamics.

Chapter 4

Relaxation and Damping in Transition Metal-Rare Earth Ferrimagnets

This chapter concerns the damping, transverse relaxation time and longitudinal relaxation time in TM-RE ferrimagnetic materials. Transverse relaxation processes and damping are often probed using ferromagnetic resonance (FMR) techniques. The measurements can be used to determine properties such as resonance frequency, damping and gyromagnetic ratio. Such properties have implications for dynamic magnetic behaviour such as domain wall velocity or energy dissipation.

The transverse and longitudinal dynamic properties of TM-RE ferrimagnets are studied as a function of both temperature and concentration of RE, and are compared with known results [100]. An analytic treatment is used to obtain expressions for the absorbed power during FMR, revealing interesting compositional dependence of the damping and transverse relaxation rates. The atomistic model is used to predict an interesting difference in the longitudinal timescales for each sub-lattice, supporting the observations in chapter 3. The susceptibility of the ferrimagnetic system is calculated using the atomistic model showing interesting behaviour at the compensation point. The domain wall velocity is also calculated and discussed in terms of the angular momentum compensation point and the susceptibilities. Finally, the different longitudinal relaxation times of the two sublattices of the TM-RE ferrimagnet are calculated using the atomistic model.

4.1 Ferrimagnetic Resonance

Ferromagnetic resonance is an important experimental technique for probing the magnetic properties of a system. Properties such as damping [101], gyromagnetic ratio [102], anisotropy constants [103], magnetisation [104] and resonance frequency can be measured using FMR. Transverse relaxation and damping are of particular interest, showing large increases in measured damping at the magnetisation compensation point [105]. In Ref. [105], Wangsness showed that the effective damping of a two sublattice ferrimagnetic system could be written as a function of; the intrinsic coupling parameter of each species, the gyromagnetic ratios and

the magnetisation of each sublattice. Even at zero Kelvin, the effective measured damping is not equal to the intrinsic coupling parameter (input damping) but, is equal to some effective damping parameter [105,106]. Moreover, as well as an effective damping, this type of system also precesses at frequencies, that are a combination of the effective gyromagnetic ratio and an effective field. According to these expressions, the frequency diverges at the magnetisation compensation point and goes to zero at the angular momentum compensation point. These interesting properties affect the dynamics of, for example, the domain wall mobility [107], important in the domain erasure in recording situations.

4.1.1 Effective Landau-Lifshitz-Gilbert Equation

The aim of this section is to derive an expression for the absorbed power as a function of frequency for a two sub-lattice ferrimagnet, for which we follow Mansuripur [47]. Beginning with two coupled Landau-Lifshitz-Gilbert equations for the two sub-lattices in a ferrimagnet, a single equation is obtained similar to that for a single sub-lattice. A strong inter-sublattice exchange value, that would keep the two sublattices in the anti-parallel ground state, is assumed. From this single equation, an analytic solution can be found for the power absorbed during a magnetic resonance experiment. Beginning with two coupled LLG equations for each sub-lattice:

$$\begin{aligned}\dot{\mathbf{M}}_1 &= -\gamma_1 \mathbf{M}_1 \times \mathbf{H}_1 + \frac{\lambda_1}{M_1} [\mathbf{M}_1 \times \dot{\mathbf{M}}_1] \\ \dot{\mathbf{M}}_2 &= -\gamma_2 \mathbf{M}_2 \times \mathbf{H}_2 + \frac{\lambda_2}{M_2} [\mathbf{M}_2 \times \dot{\mathbf{M}}_2],\end{aligned}\tag{4.1.1}$$

where \mathbf{M}_i , λ_i , γ_i , \mathbf{H}_i are the magnetisation, intrinsic damping parameter, gyromagnetic ratio and effective field of the sub-lattice, i , respectively. The time derivatives of the magnetisation are represented with dot notation, $\dot{\mathbf{M}}_i$. The effective field here includes Zeeman, anisotropy and inter-sublattice exchange terms written as:

$$\begin{aligned}\mathbf{H}_1 &= \mathbf{H}'_1 - J_{12} \mathbf{M}_2 \\ \mathbf{H}_2 &= \mathbf{H}'_2 - J_{21} \mathbf{M}_1,\end{aligned}\tag{4.1.2}$$

with J_{ij} is now an inter sub-lattice exchange energy and \mathbf{H}'_i contains the anisotropy and Zeeman energies. Defining a unit vector in the direction of the magnetisation, \mathbf{u} . Therefore $\mathbf{M} = \mathbf{M}_1 + \mathbf{M}_2 = \mathbf{u}(M_1 - M_2)$, assuming sub-lattice 1 is dominant and that the exchange between the two is strong enough to ensure the sub-lattices remain anti-parallel, shown schematically in figure 4.1. Equations 4.1.1 can be written:

$$\begin{aligned}M_1 \dot{\mathbf{u}} &= -\gamma_1 M_1 \mathbf{u} \times \mathbf{H}_1 + \lambda_1 M_1 \mathbf{u} \times \dot{\mathbf{u}} \\ M_2 \dot{\mathbf{u}} &= -\gamma_2 M_2 \mathbf{u} \times \mathbf{H}_2 + \lambda_2 M_2 \mathbf{u} \times \dot{\mathbf{u}},\end{aligned}\tag{4.1.3}$$

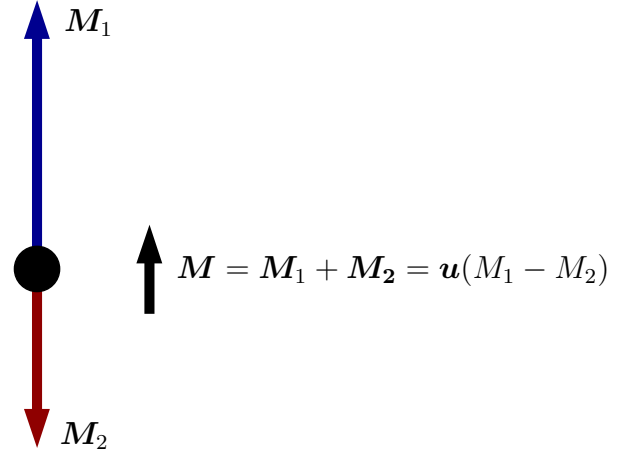


Fig. 4.1: Schematic of the magnetisation of a two-sub-lattice ferrimagnet.

dividing each side by γ_i and adding equations 4.1.3 also noting that $\mathbf{u} \times \mathbf{u} = \mathbf{0}$:

$$\begin{aligned} \left(\frac{M_1}{\gamma_1} - \frac{M_2}{\gamma_2}\right) \dot{\mathbf{u}} = & -\mathbf{u} \times (M_1(\mathbf{H}'_1 - J_{12}\mathbf{M}_2) - M_2(\mathbf{H}'_2 - J_{21}\mathbf{M}_1)) \\ & + \left(\frac{\lambda_1 M_1}{\gamma_1} - \frac{\lambda_2 M_2}{\gamma_2}\right) \mathbf{u} \times \dot{\mathbf{u}}, \end{aligned} \quad (4.1.4)$$

where J_{ij} is the exchange integral between sub-lattices i and j , and $J_{12} = J_{21}$. Dividing through by $\left(\frac{M_1}{\gamma_1} - \frac{M_2}{\gamma_2}\right)$:

$$\dot{\mathbf{u}} = -\frac{\mathbf{u} \times (M_1\mathbf{H}_1 - M_2\mathbf{H}_2)}{\left(\frac{M_1}{\gamma_1} - \frac{M_2}{\gamma_2}\right)} \left(\frac{M_1 - M_2}{M_1 - M_2}\right) + \frac{\left(\frac{\lambda_1 M_1}{\gamma_1} + \frac{\lambda_2 M_2}{\gamma_2}\right)}{\left(\frac{M_1}{\gamma_1} - \frac{M_2}{\gamma_2}\right)} \mathbf{u} \times \dot{\mathbf{u}}. \quad (4.1.5)$$

Defining the effective gyromagnetic ratio and the effective field as:

$$\gamma_{\text{eff}} = \frac{M_1 - M_2}{\left(\frac{M_1}{\gamma_1} - \frac{M_2}{\gamma_2}\right)}, \quad (4.1.6)$$

$$\mathbf{H}_{\text{eff}} = \frac{M_1\mathbf{H}_1 - M_2\mathbf{H}_2}{M_1 - M_2}, \quad (4.1.7)$$

also defining an effective damping parameter, λ_L :

$$\lambda_L = \frac{\frac{\lambda_1 M_1}{\gamma_1} + \frac{\lambda_2 M_2}{\gamma_2}}{\left(\frac{M_1}{\gamma_1} - \frac{M_2}{\gamma_2}\right)}, \quad (4.1.8)$$

equation 4.1.5 can then be written:

$$\dot{\mathbf{u}} = -\gamma_{\text{eff}} \mathbf{u} \times \mathbf{H}_{\text{eff}} + \lambda_L \mathbf{u} \times \dot{\mathbf{u}}. \quad (4.1.9)$$

Taking the cross product of $\dot{\mathbf{u}}$ from the left with \mathbf{u} and using the identity $\mathbf{a} \times \mathbf{b} \times \mathbf{c} = \mathbf{b}(\mathbf{a} \cdot \mathbf{c}) - \mathbf{c}(\mathbf{a} \cdot \mathbf{b})$ equation 4.1.9 can be written:

$$\mathbf{u} \times \dot{\mathbf{u}} = -\gamma_{\text{eff}} \mathbf{u} \times \mathbf{u} \times \mathbf{H}_{\text{eff}} + \lambda_L \mathbf{u} \times \mathbf{u} \times \dot{\mathbf{u}}, \quad (4.1.10)$$

$$\mathbf{u} \times \dot{\mathbf{u}} = -\gamma_{\text{eff}} \mathbf{u} \times \mathbf{u} \times \mathbf{H}_{\text{eff}} + \lambda_L (\mathbf{u}(\mathbf{u} \cdot \dot{\mathbf{u}}) - \dot{\mathbf{u}}(\mathbf{u} \cdot \mathbf{u})). \quad (4.1.11)$$

Noting here that due to conservation of the magnetisation, $\mathbf{u} \cdot \dot{\mathbf{u}} = 0$, thus the third term on the right goes to zero. This can then be reinserted into equation 4.1.9 to give:

$$\dot{\mathbf{u}} = -\frac{\gamma_{\text{eff}}}{1 + \lambda_L^2} \mathbf{u} \times \mathbf{H}_{\text{eff}} - \frac{\lambda_L \gamma_{\text{eff}}}{1 + \lambda_L^2} \mathbf{u} \times \mathbf{u} \times \mathbf{H}_{\text{eff}}. \quad (4.1.12)$$

4.1.2 Ferrimagnetic Resonance

4.1.2.1 Linearising the Effective Landau-Lifshitz-Gilbert Equations

By linearising the effective LLG equation and solving the equations of motion during a typical resonance experiment, the analytic solution to the resonance spectrum may be obtained. If we define $\gamma' = \gamma_{\text{eff}}/(1 + \lambda_L^2)$ and linearise the components of the equation 4.1.12 around small amplitudes in x and y, defining the anisotropy field along the z-axis, we obtain:

$$\begin{aligned} \dot{u}_x &= -\gamma' u_y H_{\text{eff}}^z - \gamma' \lambda_L (-H_{\text{eff}}^x + u_x H_{\text{eff}}^z), \\ \dot{u}_y &= -\gamma' (H_{\text{eff}}^x - u_x H_{\text{eff}}^z) - \gamma' \lambda_L u_y H_{\text{eff}}^z. \end{aligned} \quad (4.1.13)$$

Considering oscillations about the z-axis in the rotating frame and defining, $u^+ = u_x + iu_y$, the dynamic equations in this frame can be constructed from equations 4.1.13:

$$\dot{u}^+ = -\gamma' H_{\text{eff}}^z u^+ (\lambda_L - i) + \gamma' H_{\text{eff}}^x (\lambda_L - i) \quad (4.1.14)$$

Similarly rotations in the opposite sense, $u^- = u_x - iu_y$ gives:

$$\dot{u}^- = -\gamma' u^- H_{\text{eff}}^z (\lambda_L + i) + \gamma' H_{\text{eff}}^x (\lambda_L + i) \quad (4.1.15)$$

The equations 4.1.14 and 4.1.15 are inhomogeneous first order differential equations, which we can solve using the integrating factor method or solving for the homogeneous part and then the inhomogeneous part. Solving the homogeneous equation of motion basically gives the solution for a magnetic moment in a static applied field, with damped oscillations. Then solving the inhomogeneous part of the equation gives us the full solution with the driven perpendicular magnetic field. The homogeneous part of the solution can be ignored as the static applied field $H_{\text{eff}}^z \gg H_{\text{eff}}^x$ and also we are assuming a linearised set of equations. The homogeneous part of the solution will, however, be shown as it allows us to define the resonance frequency and the relaxation constant due to damping. Ignoring the last term in equation 4.1.14 we obtain a homogeneous equation. The solution of this equation can be written in the form of

a decaying oscillator with relaxation constant, τ and resonance frequency, ω_0 :

$$\begin{aligned} u_{\text{hom}}^+ &= \exp(\gamma' H_{\text{eff}}^z (i - \lambda_L) t) \\ &= \exp(-t/\tau) \exp(i\omega_0 t), \end{aligned} \quad (4.1.16)$$

with the relaxation constant and resonance frequency given by:

$$\tau = \frac{1}{\gamma' H_{\text{eff}}^z \lambda_L}, \quad (4.1.17)$$

$$\omega_0 = \gamma' H_{\text{eff}}^z. \quad (4.1.18)$$

Assuming the applied magnetic field has the form, $\mathbf{B} = (B_x \exp(i\omega t), 0, B_z)$, with B_x sufficiently small and small oscillations of the magnetisation, we solve for the inhomogeneous part by using the trial solution, $u_{\text{inhom}}^+ = C \exp(i\omega t)$, we get for the constant, C :

$$C = \frac{\gamma' B_{\text{eff}}^x (\lambda_L - i)}{\frac{1}{\tau} + i(\omega - \omega_0)} \quad (4.1.19)$$

If we then multiply top and bottom by the complex conjugate of the denominator we obtain:

$$u_{\text{inhom}}^+ = \frac{\gamma' B_{\text{eff}}^x (\lambda_L - i) (\frac{1}{\tau} - i(\omega - \omega_0))}{\frac{1}{\tau^2} + (\omega - \omega_0)^2} \exp(i\omega t) \quad (4.1.20)$$

Applying a similar treatment to u^- we obtain:

$$u_{\text{inhom}}^- = \frac{\gamma' B_{\text{eff}}^x (\lambda_L + i) (\frac{1}{\tau} + i(\omega + \omega_0))}{\frac{1}{\tau^2} + (\omega + \omega_0)^2} \exp(i\omega t) \quad (4.1.21)$$

4.1.2.2 Absorbed Power

The absorbed power during ferromagnetic resonance is given by:

$$P_{\text{FMR}}(\omega) = - \int_0^T \mathbf{M}(t) \cdot \frac{\partial \mathbf{B}(t)}{\partial t} dt. \quad (4.1.22)$$

The specific case considered here, there is zero rate of change of applied field with time in y and z , the oscillating driving field is applied in x , as shown in figure 4.2, thus the equation reduces to:

$$P_{\text{FMR}}(\omega) = - \frac{\omega}{2\pi} \int_0^{\frac{2\pi}{\omega}} M_x(t) \dot{B}_x dt. \quad (4.1.23)$$

In an FMR experiment we need to consider the measurable part of the absorbed power given by the real part of the solution:

$$P_{\text{FMR}}(\omega) = - \frac{\omega M_s}{2\pi} \int_0^{\frac{2\pi}{\omega}} \Re \left\{ \left(\frac{u_x^+ + u_x^-}{2} \right) \dot{\mathbf{B}} \right\} dt, \quad (4.1.24)$$

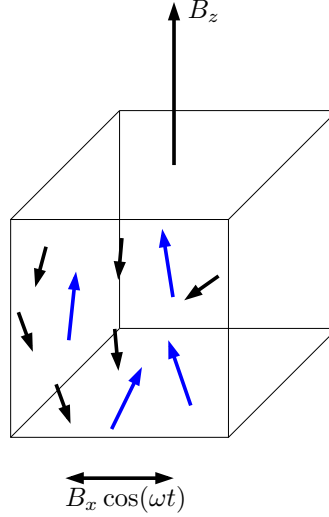


Fig. 4.2: A sketch showing the fields during ferromagnetic resonance. The frequency of the transverse applied field is varied with constant amplitude in the x direction. A large field is applied in z .

where the negative solution and positive solution are added to give the positive and negative parts of the frequency spectrum. Thus solving the integral we obtain:

$$P_{\text{FMR}}(\omega) = \frac{M_s \gamma' B_x^2 \lambda_L}{4} \left(\frac{\omega^2}{(\omega - \omega_0)^2 + \lambda_L^2 \omega_0^2} - \frac{\omega^2}{(\omega + \omega_0)^2 + \lambda_L^2 \omega_0^2} \right). \quad (4.1.25)$$

Equation 4.1.25 allows us to test the dynamic of the atomistic model of a ferrimagnet. The width of the resonance curve (at zero Kelvin) is governed by the parameter, λ_L , which by equation 4.1.8, is an effective damping parameter that takes into account the individual magnetic properties of each sublattice.

4.2 Ferromagnetic Resonance Calculations

Equation 4.1.25 has been compared to zero Kelvin atomistic calculations for a range of compositions. To calculate the FMR curve for each composition, a small system was simulated in a small oscillating field, B_x , of amplitude 0.001T. A static applied field was applied along the z -direction (B_z) of 0.1T. The system was initially in the anti-parallel ground state at zero K. The system was allowed to equilibrate for 10 cycles of the oscillating applied field, then averaging occurred over a further 10 periods to calculate the power loss. At zero Kelvin it was found that 10 cycles was sufficient to obtain a good value of the absorbed power. For elevated temperatures a large number of cycles is generally required to find good statistical averages [32]. The results of the FMR calculations are shown in figure 4.3. The integral given by equation 4.1.22 was calculated using a simple first order trapezium integration scheme. The parameters used were as follows:

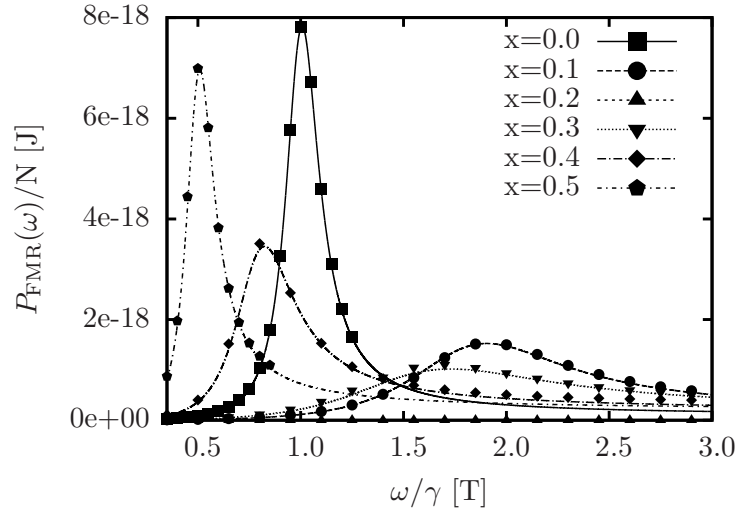


Fig. 4.3: Ferromagnetic resonance curves measuring power loss as a function of frequency at zero K . A range of compositions are displayed with x giving the RE concentration, $TM_{1-x}RE_x$. Lines are given by equation 4.1.25 and the points are calculated by integration of equation 4.1.22.

- The exchange constants used were, $J_{TM-TM} = 2.835 \times 10^{-21} J$, $J_{RE-RE} = 1.26 \times 10^{-21} J$ and $J_{TM-RE} = -1.09 \times 10^{-21} J$. These exchange constants for 24% Gd give a compensation temperature at $T = 250K$ and a Curie temperature of around $T_C = 550K$, similar to the experimental sample used in Chapter 6. The lattice was fcc with periodic boundary conditions.
- The input coupling constants (intrinsic damping) were equal, $\lambda_{TM} = \lambda_{RE} = 0.1$. The gyromagnetic ratios were also equal at $1.76 \times 10^{11} T^{-1}S^{-1}$.
- Uniaxial anisotropy constant for both the TM and RE sites was, $K = 0.807243 \times 10^{-23} J$. The magnetic moments were $\mu_{TM} = 1.92\mu_B$ and $\mu_{RE} = 7.63\mu_B$.

Figure 4.3 shows the power absorbed during FMR as a function of frequency for a range of compositions. The points on the curve correspond to numerical calculations by integration of equation 4.1.22 and the lines are given by the analytical expression 4.1.25. The figure shows that as the doping concentration changes, the resonance curve changes significantly, even though the input damping for both species is the same. For the parameters described above, when $x=0.201$, the system is fully compensated giving an infinitely broad power spectrum density (PSD) as seen by the triangles in figure 4.3. The resonance frequency changes by a factor of five between $x=0.0$ and $x=0.1$ in the same applied field.

4.3 Transverse Relaxation and Precession Frequency of Ferrimagnets

Using the equations for the effective parameters γ_{eff} , \mathbf{H}_{eff} and λ_{L} (4.1.6, 4.1.7 and 4.1.8) the compositional dependence of the transverse relaxation time and frequency can be compared analytically with the atomistic model. The transverse relaxation time at zero K is related to the effective damping parameter by:

$$\tau_{\perp} = \frac{1}{\lambda_{\text{eff}}\gamma_{\text{eff}}H_{\text{eff}}}. \quad (4.3.1)$$

To calculate the damping and resonance frequencies using the atomistic model, two methods are often used. The first method involves calculating the damping from the line width and resonance frequency in FMR. The second method is to deviate the spins from their ground state and use a fitting function to the resulting magnetisation dynamics. The latter method is used here. The value of τ_{\perp} was calculated by fitting the x component of the magnetisation to $m_x(t) = A \cos(\omega t) \exp(-t/\tau)$, where C is a constant determined by the amplitude of the deviation of the spins from the axis, ω is the frequency and τ is the relaxation time. An example is shown on figure 4.4. The values of the parameters found by the fitting procedure correspond to the resonance frequency, ω_0 , and the transverse relaxation time, τ_{\perp} .

Figure 4.5 shows the compositional dependence of the transverse relaxation time with the same parameters to those listed above, except now the gyromagnetic ratio of the TM is 1.25γ where γ is the free electron value. The coupling parameter, λ , for the TM and RE is now set to 0.02. The difference in the gyromagnetic ratio gives rise to an angular momentum compensation, at a composition indicated by the dashed line, x_A . As is shown in figure 4.5 the transverse relaxation time goes to zero at the angular momentum compensation point. This is potentially important for studying the domain wall velocity, because, at this point the domain wall velocity will diverge. Because of the absence of any static applied field used to calculate the result of figure 4.5, there is no divergence of the transverse relaxation time at

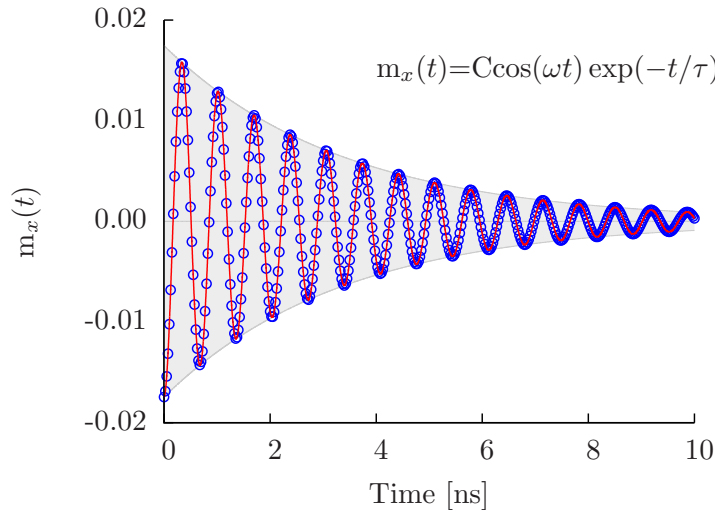


Fig. 4.4: Schematic showing the fit (solid lines) to data (points) for transverse magnetisation data (reduced) as a function of time. The fitting function is written on the figure.

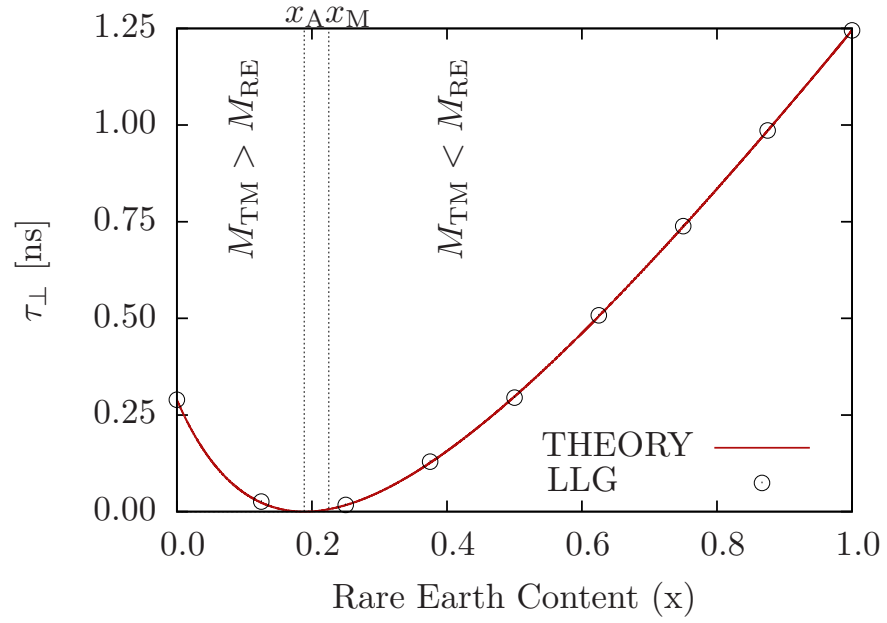


Fig. 4.5: Transverse relaxation time as a function of RE content, x , without static applied field. The anisotropy then gives rise to the quantisation axis. At the angular momentum composition, x_A , the relaxation time goes to zero. The line represents equation 4.3.1 and the points are the numerical results from the atomistic model.

the point where the magnetisation is compensated, x_M .

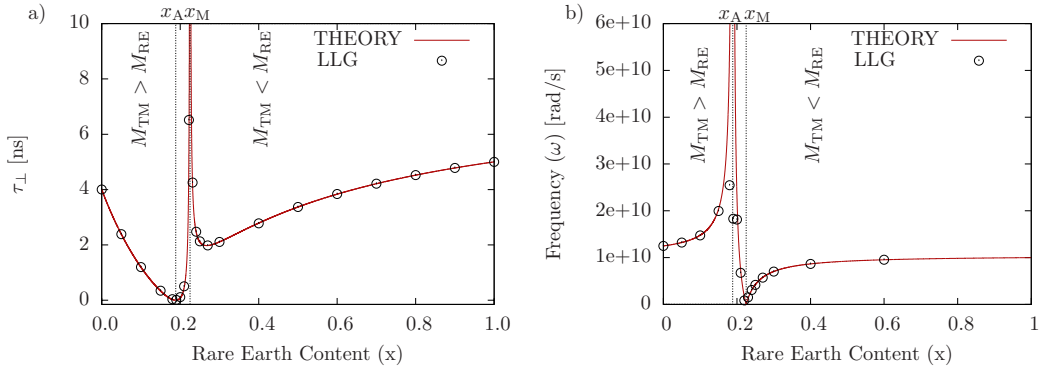


Fig. 4.6: Transverse relaxation time (a) and FMR resonance frequency (b) as a function of RE content.

Figure 4.6(a) shows the transverse relaxation time as a function of composition in a small applied static magnetic field. At the angular momentum compensation point, the relaxation rate tends to zero as in figure 4.5. At the magnetisation compensation point, the relaxation time diverges, meaning the damping goes to zero. The fit to the analytic solution is excellent, though it should be pointed out that around the angular momentum compensation temperature, the timestep used in the LLG integration had to be reduced by an order of magnitude, because of the increase in the frequency of the system (see (b)). Figure 4.6(b) shows the variation of the frequency with composition compared to the analytic solution. Above and below

the angular momentum compensation point the analytic solution agrees very strongly with the atomistic simulations. However around the angular momentum compensation temperature the analytic solution does not match the atomistic model. The disagreement with the analytic solution could be because of the fact that the relaxation time is going to zero, which means that by equation 4.3.1 the damping diverges. The consequence of diverging damping is that the system is critically damped, thus there are not enough precession cycles to achieve a sufficient fit. In the atomistic model, the damping will never truly diverge as we consider a finite system. It is possible that this error could be due to a finite size effect. The fit to the highly damped case is shown by the x component of the magnetisation in figure 4.7.

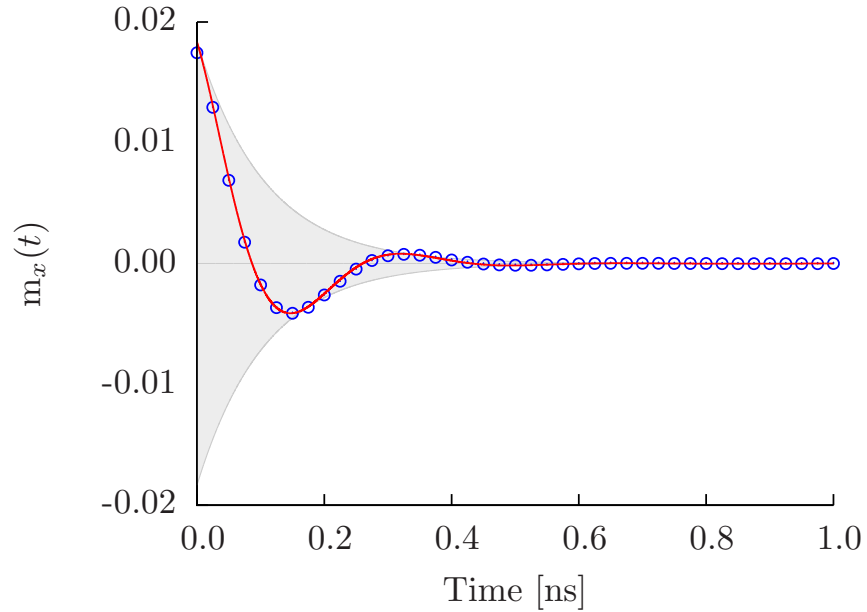


Fig. 4.7: *Transverse (x) magnetisation as a function of time for $x = 0.2$, in the critically damped regime close to the angular momentum compensation temperature. Note here the timescale compared to figure 4.4 is much shorter and only has 2 precession cycles to fit the frequency.*

4.4 Differential Longitudinal Relaxation Time Calculations

Here we investigate the longitudinal relaxation time of the two sublattices in a TM-RE ferrimagnetic system. If one considers a ferromagnet in a perfectly ordered (zero K) state, then the system is in the ground state. Upon instantaneous application of a change in temperature, the order is very quickly destroyed as thermal fluctuations overcome the exchange interactions leading to a reduced spontaneous magnetisation. The rate at which the system arrives at its new equilibrium depends on the change in temperature of the system. Below the Curie temperature the relaxation is relatively fast. Approaching the Curie temperature, this relaxation becomes (in theory) infinitely slow, corresponding to a diverging correlation length in a second order magnetic phase transition.

Since the pioneering work of Beaurepaire *et al.* [37] there has been a great deal of debate about the mechanism of rapid demagnetisation. Recent work by Koopmans *et al.* [108] used a model based on Elliot-Yafet scattering of electrons by phonons, arguing that this mechanism contributes significantly to the very fast demagnetisation of ordered magnetic materials. That work resulted in an expression for the demagnetisation time:

$$\tau_d \approx c_0 \frac{\hbar}{k_B T_C \alpha}, \quad (4.4.1)$$

where, c_0 , is a material parameter and, α , is the Gilbert damping factor, i.e. an inverse relationship between the demagnetisation time and the Gilbert damping factor. This relationship was studied by Radu *et al.* [109], by doping permalloy with different RE materials, who showed however that the relationship does not hold in this case.

Another estimate of the demagnetisation time in terms the atomistic model was shown by Kazantseva *et al.* [99] to be related to the correlator of the thermal field:

$$\tau_d \sim \mu_s / (2\lambda\gamma k_B T), \quad (4.4.2)$$

where μ_s is the magnetic moment, λ and γ are the coupling constant and the gyromagnetic ratio respectively.

In this section the prediction given in equation 4.4.2 will be shown to hold, although incompletely; the demagnetisation rate also depends on the exchange acting on the species. By varying the composition and applying a change in temperature from 0 K to 300 K and calculating the Integral Relaxation Time (IRT) [110]:

$$\tau_{\text{int}} = \int_0^\infty \frac{\langle M_z(\infty) \rangle - \langle M_z(t) \rangle}{\langle M_z(\infty) \rangle - \langle M_z(0) \rangle} dt, \quad (4.4.3)$$

where the angle brackets represent ensemble averages, the effect can be studied.

Figure 4.8 shows the calculation of the integral relaxation time as a function of RE content, x . The angular momentum and magnetisation compensation point do not affect the longitudinal relaxation processes. The difference between the two curves for any particular composition is due to the fact that the correlators are different (equation 4.4.2). The change in the trend of the curve as x increases is because the effective exchange changes. This can be seen quite clearly in our mean field expressions 3.3.5 and 3.3.6. These expressions show that the average field is determined by not only the exchange constants but also the average coordination with the neighbours, determined by the concentration, x . As is shown in figure 4.8 the TM relaxation is intrinsically faster than the RE because of the smaller moment. In the following chapters the difference in the rate of precession will be shown to be very important in switching using femtosecond laser pulses.

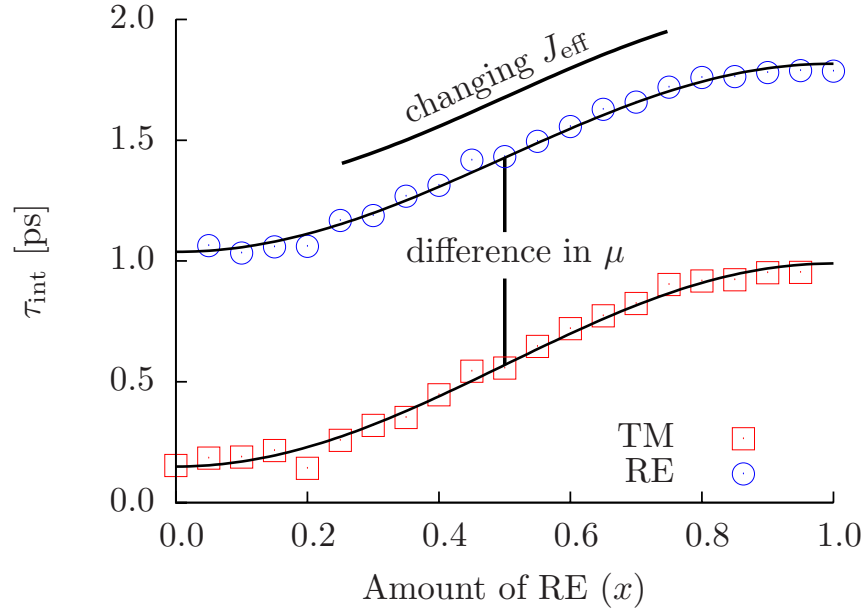


Fig. 4.8: Integral relaxation time as a function of x for the TM and RE sublattice. The final temperature is 200 K with the system beginning in the anti-parallel, 0K, ground state. The trend is governed by the effective exchange acting on each spin. The difference in height of the two curves is due to the different correlator (equation 2.3.4), determined by the difference in the moment.

4.5 Domain Wall Velocity

As discussed in section 4.2, at the angular momentum compensation point the transverse relaxation time goes to zero, giving rise to a critically damped system. The obvious consequence of this is on the domain wall velocity. The domain wall velocity of a system is dependent on the transverse relaxation time as most domain wall processes occur on the nano-second timescale. The domain wall velocity has been calculated as a function of temperature below the Curie temperature. The method by which this is done for the ferrimagnetic system is to simulate a thin *rod* of material (in this case $110 \times 15 \times 15$ unit cells) as shown schematically in figure 4.9, a). At either end of the rod the TM spins are pinned in opposite directions, the opposite is done for the RE. Once the spins have been pinned, the system is equilibrated (the pinned spins are not integrated) forcing in a pseudo domain, the z-component of the magnetisation along the x direction is shown on figure 4.9, b). The domain that is forced in is not stable as demagnetising fields are not considered in the calculation. Once the domain wall has equilibrated the spins at either end are unpinned and a field applied in the anisotropy direction which forces the domain wall to propagate, resulting in a single domain particle with all spins aligned. Considering the magnetisation of each sublattice along the x-direction a $\tanh(x)$ function can be fitted through the magnetisation profile. Then by solving for the centre of the wall, the displacement as a function of time can be found. The initial gradient of the domain wall position with time then gives the domain wall velocity. Figure 4.10 shows the calculated domain wall velocity as a function of temperature. The temperature ranges from

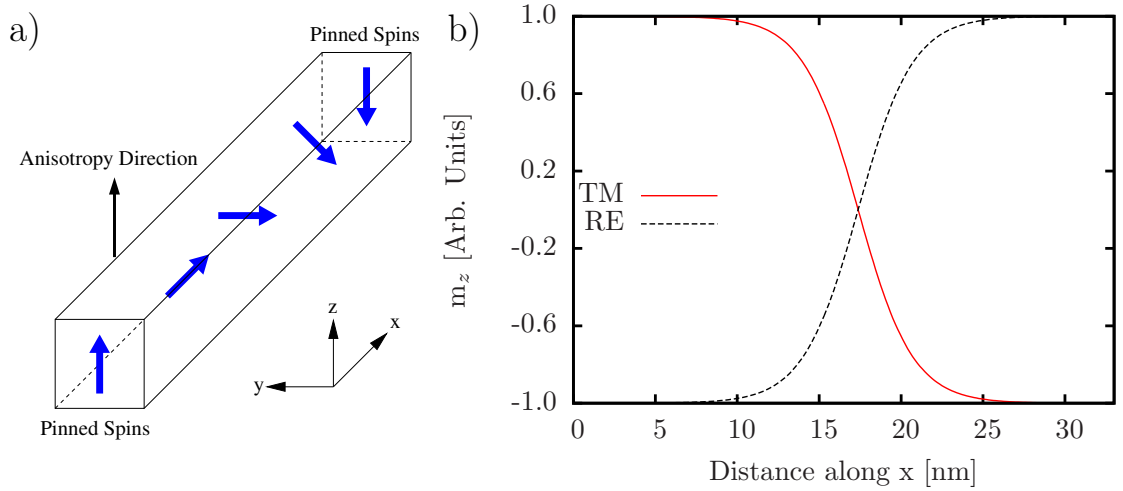


Fig. 4.9: Schematic diagram showing how the domain wall is forced into the atomistic model in the rod like structure, a). The TM spins are pinned in opposite directions at either end, the RE spins are pinned in the opposite sense. z -component of the magnetisation as a function of x position along the rod for both the TM and RE sublattices after the domain wall has been pinned and the system equilibrated, b).

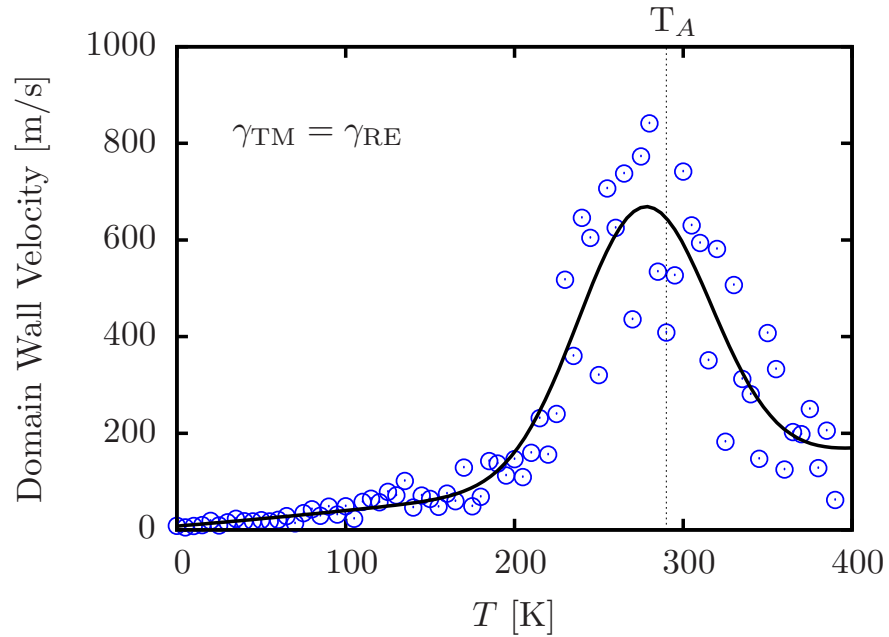


Fig. 4.10: Domain wall velocity as a function of temperature for GdFe showing a large increase near the angular momentum compensation temperature, $T_A=290$ K.

0K to 400K, the magnetisation compensation temperature is equal to the angular momentum compensation temperature in this case, as the gyromagnetic ratios for each species are equal. At T_A , the domain wall velocity is an order of magnitude faster than below around 200K. Each temperature is averaged over only 6 runs with different random number generator seeds, thus, there is still a reasonably large amount of scatter in the data, although the trend is

quite clear. This could have interesting consequences for applications that utilise the motion of domain walls, such as the Spin-Seebeck effect [111].

4.6 Susceptibility Calculations

The interesting behaviour of this TM-RE system, in terms of resonance frequencies and transverse relaxation times, leads one to consider the susceptibility of the ferrimagnet. As seen in the previous section, the domain wall velocity increases substantially at the angular momentum compensation point, suggesting that the system is highly susceptible to a magnetic field. The atomistic model is capable of calculating the susceptibility [12] from the fluctuations of the spin. We begin with the Hamiltonian for a spin system with exchange and applied field terms in the mean field, the same derivation applies if we include other energy terms:

$$\mathcal{H} = - \sum_{i=1}^N (\mu_i B S_i + H_i S_i), \quad (4.6.1)$$

where μ_i is the localised magnetic moment of the i^{th} spin, B the magnetic field in Tesla and H_i is an exchange field acting on that spin. The partition function is then:

$$Z = \sum_{\underline{\sigma}} \exp \left(\beta \left[\sum_{i=1}^N (B \mu_i S_i + H_i S_i) \right] \right), \quad (4.6.2)$$

where $\underline{\sigma}$ is the spin configuration (or state). Taking the derivative with respect to the field, with $\beta = 1/k_B T$:

$$\begin{aligned} \frac{1}{Z} \frac{\partial Z}{\partial B} &= \frac{\partial \ln(Z)}{\partial B} = \frac{\beta \sum_{\underline{\sigma}} \left[\sum_{i=1}^N \mu_i S_i \right] \exp \left(\beta \left[\sum_{i=1}^N (B \mu_i S_i + H_i S_i) \right] \right)}{\sum_{\underline{\sigma}} \exp \left(\beta \left[\sum_{i=1}^N (B \mu_i S_i + H_i S_i) \right] \right)} \\ &= \frac{\beta \sum_{\underline{\sigma}} M(\underline{\sigma}) \exp \left(\beta \left[\sum_{i=1}^N (B \mu_i S_i + H_i S_i) \right] \right)}{\sum_{\underline{\sigma}} \exp \left(\beta \left[\sum_{i=1}^N (B \mu_i S_i + H_i S_i) \right] \right)} \\ &= \beta \sum_{\underline{\sigma}} M(\underline{\sigma}) p(\underline{\sigma}) \\ &= \beta \langle M \rangle. \end{aligned} \quad (4.6.3)$$

Using $\mathcal{F} = -k_B T \ln(Z)$, the magnetisation is then:

$$\langle M \rangle = k_B T \frac{\partial \ln(Z)}{\partial B} = - \frac{\partial \mathcal{F}}{\partial B}. \quad (4.6.4)$$

Similarly to the treatment above it can be shown that:

$$\frac{1}{Z} \frac{\partial^2 Z}{\partial B^2} = \beta^2 \langle M^2 \rangle. \quad (4.6.5)$$

Now, $\frac{\partial}{\partial B} \ln Z = \frac{1}{Z} \frac{\partial Z}{\partial B}$ and

$$\begin{aligned} \frac{\partial^2}{\partial B^2} \ln Z &= \frac{1}{Z} \frac{\partial^2 Z}{\partial B^2} - \frac{\partial Z}{\partial B} \left(\frac{\partial Z}{\partial B} Z^{-2} \right) \\ &= \beta^2 [\langle M^2 \rangle - \langle M \rangle^2]. \end{aligned} \quad (4.6.6)$$

Now considering that the susceptibility is expressed as, $\chi = \frac{\partial \langle M \rangle}{\partial B}$, from the expression for the magnetisation (equation 4.6.4) the susceptibility is:

$$\begin{aligned} \chi &= \frac{1}{\beta} \frac{\partial}{\partial B} \left(\frac{\partial \ln(Z)}{\partial B} \right) \\ &= \frac{1}{\beta} \frac{\partial^2 \ln(Z)}{\partial B^2} \\ &= \beta [\langle M^2 \rangle - \langle M \rangle^2]. \end{aligned} \quad (4.6.7)$$

Writing the magnetisation of the TM-RE system as

$$\begin{aligned} \langle M \rangle &= \sum_{i=1}^N \mu_i S_i = \mu_{\text{RE}} \sum_{i=1}^{N_{\text{RE}}} S_{\text{TM}}^i + \mu_{\text{TM}} \sum_{j=1}^{N_{\text{TM}}} S_{\text{RE}}^j \\ &= N_{\text{RE}} \mu_{\text{RE}} \langle S_{\text{RE}} \rangle + N_{\text{TM}} \mu_{\text{TM}} \langle S_{\text{TM}} \rangle \\ &= N (x \mu_{\text{RE}} \langle S_{\text{RE}} \rangle + q \mu_{\text{TM}} \langle S_{\text{TM}} \rangle), \end{aligned} \quad (4.6.8)$$

where $\langle S \rangle$ is the reduced magnetisation of the sublattice (TM or RE), N_{TM} and N_{RE} are the number of TM and RE spins respectively. The last line is written in terms of the concentration of the TM-RE system. Using this, the reduced susceptibility is then:

$$\tilde{\chi} = \frac{N_{\text{TM}} \mu_{\text{TM}} + N_{\text{RE}} \mu_{\text{RE}}}{k_B T} [\langle S^2 \rangle - \langle S \rangle^2], \quad (4.6.9)$$

where $\langle S \rangle = \frac{N_{\text{TM}} \mu_{\text{TM}} \langle S_{\text{TM}} \rangle + N_{\text{RE}} \mu_{\text{RE}} \langle S_{\text{RE}} \rangle}{N_{\text{TM}} \mu_{\text{TM}} + N_{\text{RE}} \mu_{\text{RE}}}$. Using the atomistic model the transverse (χ_{\perp}) and longitudinal (χ_{\parallel}) susceptibility have been calculated as shown in figure 4.11. The solid lines through the data points in figure 4.11 is a fit to a polynomial expression with the perpendicular susceptibility separated into three regions and written:

$$\tilde{\chi}_{\perp} = \begin{cases} \frac{a_1 T_C}{4\pi(T-T_C)} + \frac{a_2 T_C}{4\pi(T-T_C)^2} + a_3 \exp\left(-\frac{T-T_C}{a_4}\right) & T > T_C + 7 \\ a_5 + a_6 T^2 + a_7 T^3 & 450 < T \leq T_C + 7 \\ a_8 + a_9 T^2 + a_{10} T^3 + a_{11} T^4 & 0 < T \leq 450, \end{cases} \quad (4.6.10)$$

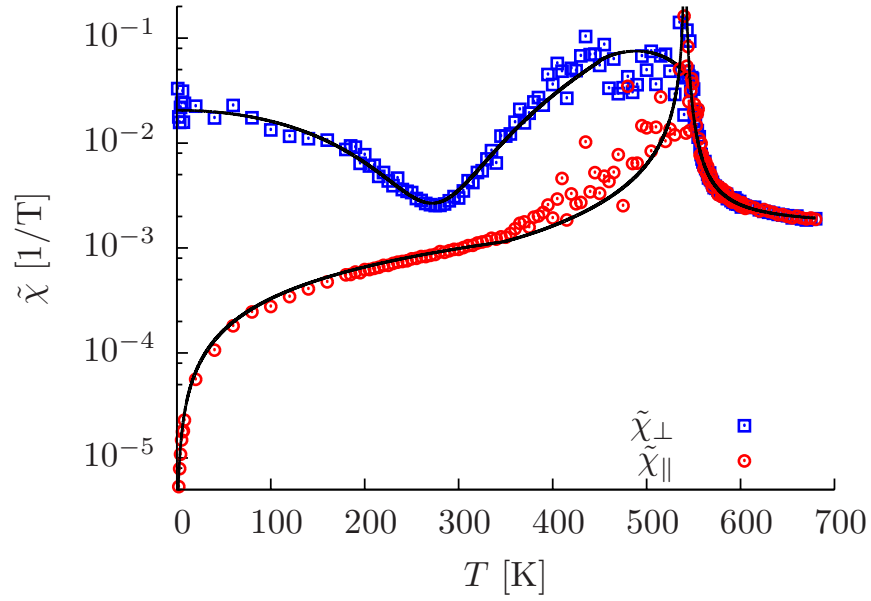


Fig. 4.11: Atomistic model calculations of the reduced parallel and perpendicular susceptibilities via equation 4.6.9. The longitudinal susceptibility is as one might expect, beginning at zero and slowly increasing to a divergent behaviour at the Curie temperature. The transverse susceptibility however shows a clear decrease (over an order of magnitude) at the angular momentum compensation temperature, 290K.

with the constants given below in table 4.1. The expression for the parallel susceptibility is also separated into three regions:

$$\tilde{\chi}_{\parallel} = \begin{cases} \frac{b_1 T_C}{4\pi(T-T_C)} + \frac{b_2 T_C}{4\pi(T-T_C)^2} + b_3 \exp\left(-\frac{T-T_C}{b_4}\right) & T > T_C \\ b_5 \frac{b_6 T_C}{4\pi(T-T_C)} + b_7(T_C - T) + b_8(T_C - T)^5 + b_9(T_C - T)^7 & 350 < T \leq T_C \\ b_{10} \tanh(T/b_{11}) & 0 < T \leq 350, \end{cases} \quad (4.6.11)$$

As was shown in Ref. [70] the longitudinal and transverse relaxation rates (the inverse of

a_1	0.000885167	b_1	0.000885167
a_2	0.030060705	b_2	0.030060705
a_3	0.00158989956800121	b_3	0.00158989956800121
a_4	3.95735470274007e+15	b_4	3.95735470274007e+15
a_5	-0.716850451143909	b_5	-0.0002
a_6	9.94783338367863e-06	b_6	0.006029657
a_7	-1.35697893261432e-08	b_7	0.006029657
a_8	0.020519775569942	b_8	2.18357900624424e-16
a_9	-4.49484462044283e-07	b_9	-9.47520470065338e-22
a_{10}	-2.52393669491439e-10	b_{10}	1.97077804535035
a_{11}	3.7423456415879e-12	b_{11}	597545.137537171

Table 4.1: Table showing the fitting constants of the parallel and perpendicular susceptibility as shown in equations 4.6.11 and 4.6.10.

the relaxation time) are inversely proportional to the susceptibility. As figure 4.11 shows the longitudinal susceptibility is not affected by the presence of the compensation points of the system, supported by the calculation of the longitudinal relaxation time in figure 4.8. The transverse susceptibility shows a large decrease around the angular momentum compensation temperature, in agreement with figures 4.6 and 4.5.

4.7 Concluding Remarks

Analytic expressions for a coupled two sublattice ferrimagnetic system have been derived and compared to the results of the atomistic model. The model agrees very well with the analytic expressions for the power absorbed as a function of frequency, transverse relaxation time as a function of composition and resonance frequency as a function of composition. These analytic expressions provide interesting insights into the behaviour of this type of TM-RE ferrimagnet near the magnetisation and angular momentum compensation points.

The longitudinal relaxation time for an instantaneous temperature step from 0K to 200K has been calculated for each sublattice. There is a constant difference in the demagnetisation rate of the two sublattices with composition, arising because of the different correlators (equation 2.3.4) associated with each species. Notably, the moment and thermal bath coupling parameters in equation 2.3.4 lead to different demagnetisation rates. The compositional dependence shows the effect of the composition on the relaxation rate. The changing concentration changes the effective exchange interaction on each species, demonstrated clearly in equations 3.3.5 and 3.3.6. It is worth pointing out that the relaxation time also depends on the temperature change, diverging when going from an ordered state to the Curie temperature. A step change to 200K was chosen to show the trend in changing composition because for the pure RE case the exchange constant will give the Curie temperature of pure Gd, 293K. This would mean that the calculations would have been more computationally expensive without providing any more information.

Domain wall velocities have been calculated as a function of temperature showing a large increase across the angular momentum compensation point. The calculation of the susceptibilities and their relationship to the transverse relaxation time [70] provides a partial explanation for the large increase in the domain wall velocity.

Chapter 5

Ultrafast and Distinct Spin Dynamics in Multi-Component Magnetic Alloys

5.1 Introduction

In the previous chapter we predicted that the demagnetisation times in GdFeCo depended on the effective exchange and the size of the magnetic moment. This differential demagnetisation occurs despite the strong exchange coupling between the two sublattices. Following this interesting insight, this chapter looks at the generality of this observation by extending the calculations to a two sublattice ferromagnet, $\text{Ni}_x\text{Fe}_{1-x}$ of various compositions. The calculations are supported by experimental observations using femtosecond laser pulses that act as a heating source. The response is observed using element specific XMCD in a stroboscopic pump-probe mode.

The atomistic model approach to modeling magnetisation dynamics, as we saw in chapter 4, is capable of describing the behaviour of individual components of an alloy. Models that utilise a macrospin [26] approach, representing individual sublattices as a single magnetisation vector, are incapable of describing this longitudinal behaviour. In this chapter we will show that this view holds for the individual species in ferromagnetic $\text{Ni}_x\text{Fe}_{1-x}$. This result has consequences for models of, for example, permalloy, which is widely used in current hard disk drives. This result could also have implications for potential new applications, such as, race-track memory that uses domains within permalloy nanowires to store information [112].

5.2 Atomistic Spin Simulations of NiFe

Various compositions of $\text{Ni}_x\text{Fe}_{1-x}$ are studied computationally in this section, beginning with a description of the model and the physical parameters used. Most of the ideas behind the atomistic model have already been introduced (see chapter 2), therefore here, only the specific details of the model will be discussed. As in the model of the TM-RE system, the NiFe model is based on a fixed lattice. In this fixed lattice model the spins (Ni or Fe) are placed randomly

on a bcc or fcc structure, depending on the concentration. Like in the model of the TM-RE system, interactions within each sublattice (i.e. the Fe-Fe and Ni-Ni interactions) are ferromagnetic. The Ni-Fe interactions are also ferromagnetic, giving rise to two sublattices coupled ferromagnetically. The exchange constants used are limited to nearest neighbours and the exchange constants were scaled to give the correct Curie temperature taken from the literature [113]. The simulations are compared directly to time resolved XMCD measurements, performed by I. Radu. The two samples studied were $\text{Ni}_{50}\text{Fe}_{50}$ and $\text{Ni}_{80}\text{Fe}_{20}$, the literature values of the Curie temperature were, 800K and 830K respectively [113]. The samples studied here were prepared by magnetron sputtering and were shown to have in-plane anisotropy deduced from element specific hysteresis. The physical parameters in the model are shown in table 5.1. The magnetic moments were directly obtained from XMCD measurements. This

Parameter	$\text{Ni}_{50}\text{Fe}_{50}$	$\text{Ni}_{80}\text{Fe}_{20}$
μ_{Ni} [μ_{B}]	1.18	0.98
μ_{Fe} [μ_{B}]	2.09	2.31
γ_{Fe} [$\text{T}^{-1}\text{S}^{-1}$]	1.76×10^{11}	1.76×10^{11}
γ_{Ni} [$\text{T}^{-1}\text{S}^{-1}$]	1.76×10^{11}	1.76×10^{11}
$J_{\text{Fe-Fe}}$ [J]	3.47×10^{-21}	3.60×10^{-21}
$J_{\text{Ni-Ni}}$ [J]	3.47×10^{-21}	3.60×10^{-21}
$J_{\text{Fe-Ni}}$ [J]	3.47×10^{-21}	3.60×10^{-21}
T_{C} [K]	830	880
K [J]	-3.55×10^{-26}	-3.55×10^{-26}
λ_{Fe}	0.01	0.01
λ_{Ni}	0.01	0.01
Crystal Structure	fcc	fcc
System Size	$30 \times 30 \times 7$ nm	$30 \times 30 \times 7$ nm

Table 5.1: Physical parameters for $\text{Ni}_x\text{Fe}_{1-x}$ in the atomistic model. The magnetic moments were deduced from XMCD measurements, performed by I. Radu. The Curie temperatures are taken from the literature [113]. The coupling constants (λ) are within reasonable limits for this type of material. The gyromagnetic ratios were assumed to be independent of species in the first instance.

remainder of this section looks at demagnetisation in $\text{Ni}_{80}\text{Fe}_{20}$ and $\text{Ni}_{50}\text{Fe}_{50}$ using the atomistic model. The section begins by looking at the variation of the demagnetisation time for a step pulse in temperature. These relatively simple calculations show us that even for simple step increases in temperature, the individual elements demagnetise on different timescales. We then apply femtosecond laser pulses to the NiFe systems and compare our atomistic simulations to experimental observations. The analysis in chapter 4, describing the demagnetisation time in terms of the magnetic moment is shown to hold for the $\text{Ni}_x\text{Fe}_{1-x}$ alloys.

5.2.1 Longitudinal Relaxation After a Step in Temperature

In chapter 4, calculations showing the variation of the longitudinal relaxation time for different compositions of GdFe were shown. These calculations showed that there was a difference in the demagnetisation rates of Gd and Fe due to their magnetic moments. In this section, demagnetisation times are calculated as a function of temperature. These calculations provide a prediction that the different relaxation rates of the constituent elements of an alloy is not unique to a TM-RE ferrimagnetic system. The calculations of the longitudinal relaxation time are for the two NiFe compositions described above in section 5.2. The demagnetisation times were calculated by simulating a Heaviside step function in temperature of varying magnitude (shown on the x-axis of figure 5.1). Each point corresponds to a different simulation starting at 0 K (i.e. the ferromagnetic ordered system).

The calculation of τ_{\parallel} in figure 5.1 was achieved by fitting a single exponential to the demagnetisation data. The figure shows that there is a difference between the two sublattices in both the compositions of NiFe. The dashed vertical lines show the Curie temperatures of each of the compositions; T_C of $\text{Ni}_{50}\text{Fe}_{50}$ is 800 K and that of $\text{Ni}_{80}\text{Fe}_{20}$ is 830 K.

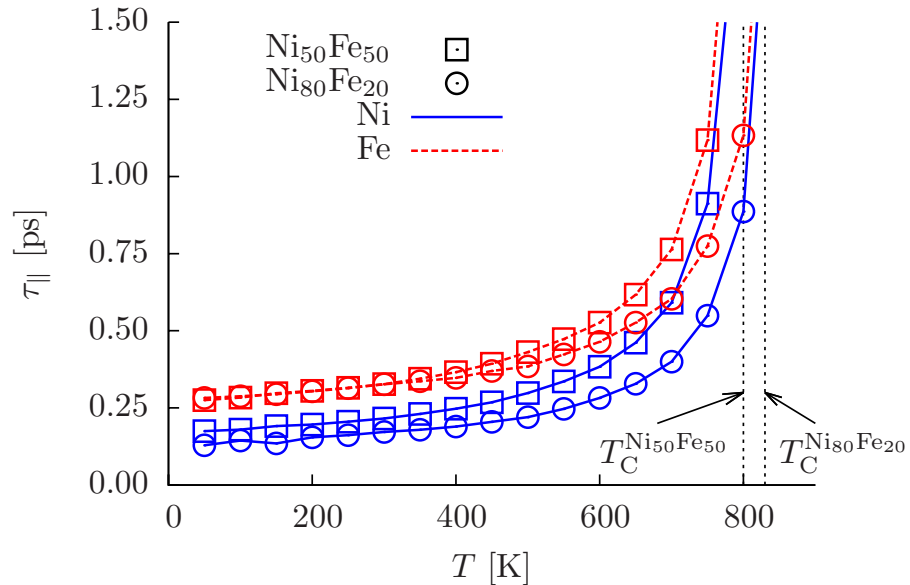


Fig. 5.1: Calculation of longitudinal relaxation time as a function of temperature for $\text{Ni}_{50}\text{Fe}_{50}$, square points, and $\text{Ni}_{80}\text{Fe}_{20}$, circles. The longitudinal relaxation time is shown for each species, Ni (solid lines) and Fe (red lines). The values of τ_{\parallel} are obtained by fitting transient magnetisation data to $m_z(t) = (1 - A) + A \exp(-t/\tau_{\parallel})$.

5.2.2 Calculations of Laser Demagnetisation in NiFe

To emphasise the effect of the effective exchange and correlator (equation 2.3.4) on the demagnetisation time, the longitudinal response of the magnetisation under the influence of 50fs (FWHM) Gaussian laser pulses have been calculated using the atomistic model. Beginning

at room temperature, the action of the laser pulse causes a very rapid increase of the electron temperature (to which both Ni and Fe are coupled), as described by the two temperature model in section 1.4.3. After the rapid heating of the electronic system on the sub-picosecond timescale, the temperature drops below the Curie temperature of the system. The system initially demagnetises, the rate of which depends mainly on the combination of the magnetic moment, the gyromagnetic ratio and the effective exchange (equation 2.3.4). The magnetisation subsequently recovers as the temperature drops below that of the Curie temperature [99]. The magnetisation of the system is then fitted to a double exponential in the form:

$$m_z(t) = A + B \exp(-t/\tau_1) + C \exp(-t/\tau_2), \quad (5.2.1)$$

where A , B and C are fitting constants and the τ 's are the time constants which we wish to calculate. The first exponential describes the demagnetisation and the second the recovery. Figure 5.2 shows an example of the fit to the calculated reduced magnetisation for each sublattice. The starting temperature was 300K and each sublattice magnetisation was fit to

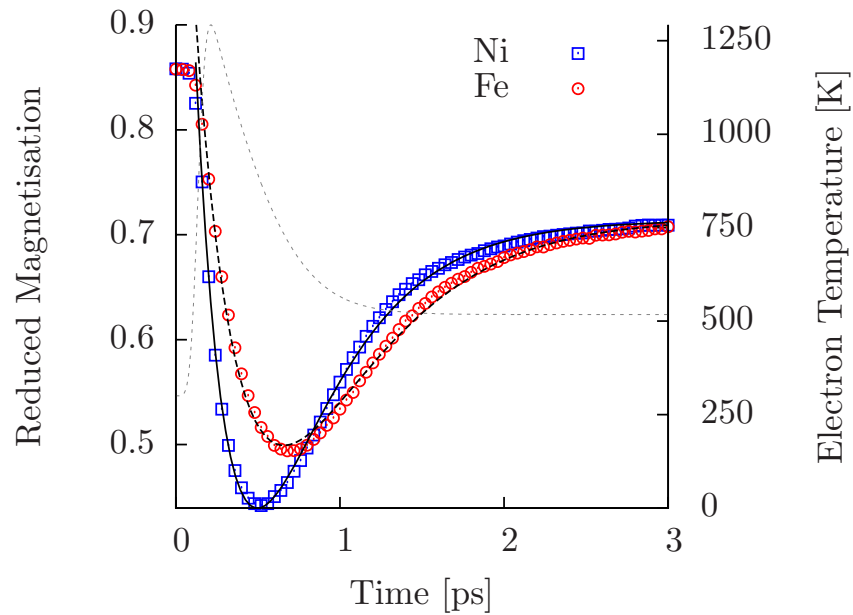


Fig. 5.2: Calculation of the demagnetisation in $Ni_{80}Fe_{20}$ for each sublattice. The two sublattices (Ni squares and Fe circles) are assumed to have equal exchange, thus the difference in the demagnetisation is due to differences in the magnetic moment. The fits (Ni solid Fe dashed lines) use equation 5.2.1 and show good agreement to the data. The grey dashed curve represents the electron temperature variation to which the Ni and Fe species are coupled.

equation 5.2.1, shown by the solid and dashed black curves. The grey dashed curve shows how the electron temperature is changing with time. The two species are assumed to have the same exchange constants, thus the different demagnetisation times arise from the difference in the correlator (the difference arising from the different magnetic moments) according to equation 2.3.4.

Beginning at room temperature, calculations of GdFeCo and $Ni_{50}Fe_{50}$, under the influence

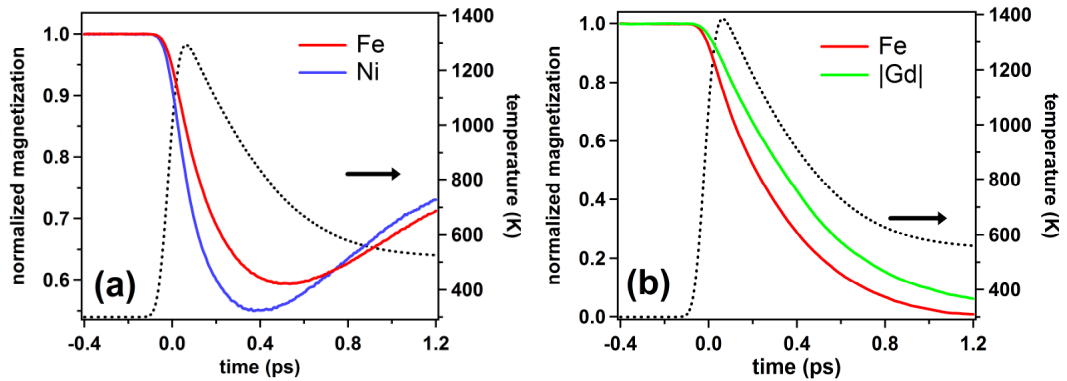


Fig. 5.3: The response of the longitudinal component of the magnetisation of Ni and Fe in $Ni_{50}Fe_{50}$ (a) and of Fe and Gd in $Gd_{25}Fe_{75}$ (b) to a 50fs laser pulse, calculated using the atomistic model. The dashed lines in both panels display the time-dependant electronic temperature used in the simulation. The starting temperature for the simulation is 300 K.

of a 50fs laser pulse, have been performed. The pump fluence is the same in each case, resulting in a complete demagnetisation of GdFeCo (which has the lower Curie temperature of the two materials) and a partial demagnetisation of the NiFe alloy. The results of the simulations are shown in figure 5.3, showing that the ferromagnetically coupled Ni and Fe sublattices demagnetise at different rates even though their exchange constants are the same. The difference in the demagnetisation arises because of the difference in the moments of Ni and Fe as discussed in section 4.4.

The important consequence of figure 5.3 is the prediction that the individual sublattices of multicomponent magnetic materials can have distinct demagnetisation times independently of whether the exchange between them is ferromagnetic or antiferromagnetic.

Figure 5.4 shows the same calculation for $Ni_{80}Fe_{20}$, the two species again clearly demagnetise at different rates. Figures 5.3 and 5.4 were performed with a thermal bath coupling constant of 0.01, which we chose arbitrarily and which may not necessarily reflect the exact value of the phenomenological constant. To this end, we have carried out a parametric study of the variation of the longitudinal relaxation times of each sub-lattice in $Ni_{50}Fe_{50}$ and $Ni_{80}Fe_{20}$ for a range of different values of this coupling constant, the results of which are shown in table 5.2 and plotted in figure 5.5. For the high coupling case in figure 5.5 (coupling parameter of 0.1),

Parameter	$\lambda=0.001$	$\lambda=0.01$	$\lambda=0.1$
τ_{Ni} [fs] in $Ni_{50}Fe_{50}$	316 ± 7.2	234 ± 2.6	93 ± 1.2
τ_{Fe} [fs] in $Ni_{50}Fe_{50}$	625 ± 14.0	371 ± 14.0	99 ± 1.0
τ_{Ni} [fs] in $Ni_{80}Fe_{20}$	404 ± 3.7	240 ± 5.3	83.3 ± 4.1
τ_{Fe} [fs] in $Ni_{80}Fe_{20}$	761 ± 11.3	404 ± 2.3	92 ± 3.6

Table 5.2: Calculated decay time constants after laser demagnetisation in $Ni_{50}Fe_{50}$ and $Ni_{80}Fe_{20}$.

the two species demagnetise almost on the same timescale as the rate of energy transfer into the

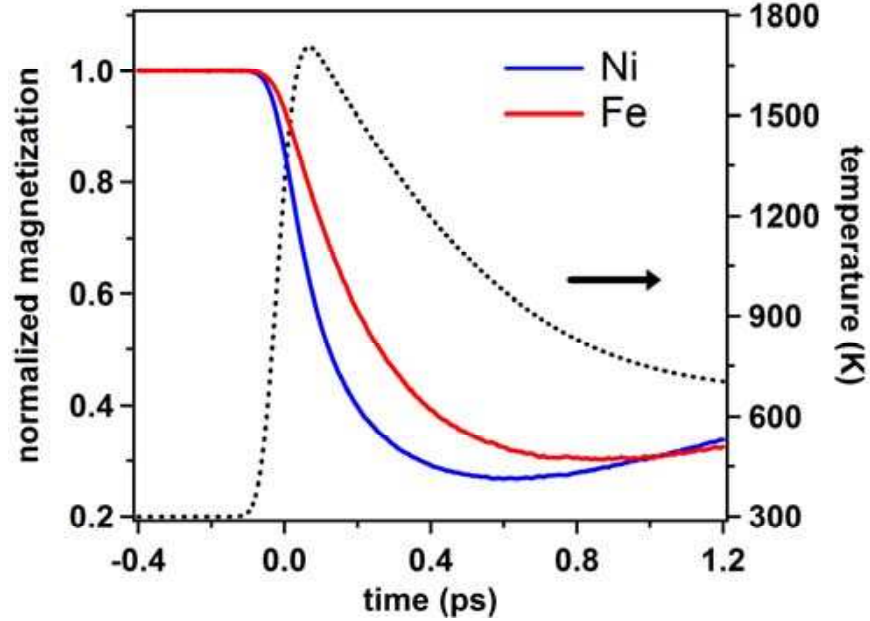


Fig. 5.4: Atomistic model results for the transient dynamics of the Fe and Ni species of $Ni_{80}Fe_{20}$.

spin system is very high, although the Ni species is still slower because of its lower moment. As the coupling constant decreases there is an increasing difference between the relaxation times of the individual species in the NiFe systems. This difference arises because at low coupling constants, the strength of the noise is dominated by differences in the magnetic moment, given by equation 2.3.4. At the same time, energy is leaving the system via the damping term in the LLG equation 1.6.8 again at a lower rate. There is also a difference between the same species in $Ni_{80}Fe_{20}$ and $Ni_{50}Fe_{50}$ alloys. This figure shows how the timescale of the demagnetisation in the atomistic model can be drastically changed by varying this coupling parameter.

5.3 Experimental Time-Resolved XMCD Dynamics of the Elemental Magnetic Moments

To compare the simulations in section 5.2 and confirm the observations experimentally, the transient demagnetisation dynamics of the magnetic sublattices of NiFe and GdFe alloys were measured as part of a collaboration with experiments performed by I. Radu at the Femtoslicing facility [114, 115] of the Helmholtz-Zentrum, Berlin. The element specific XMCD technique was used to probe the magnetisation dynamics after excitation with 60fs laser pulses. More information regarding the experiments is included in appendix A.

The element-specific demagnetisation of ferromagnetic $Ni_{50}Fe_{50}$ is shown in figure 5.6. Upon femtosecond laser excitation, the alloy is demagnetised to about 50%, shown in both the Fe and Ni edges. Although the same degree of demagnetisation is shown by both elements, their transient demagnetisation behaviour is considerably different: while Fe reaches the equilib-

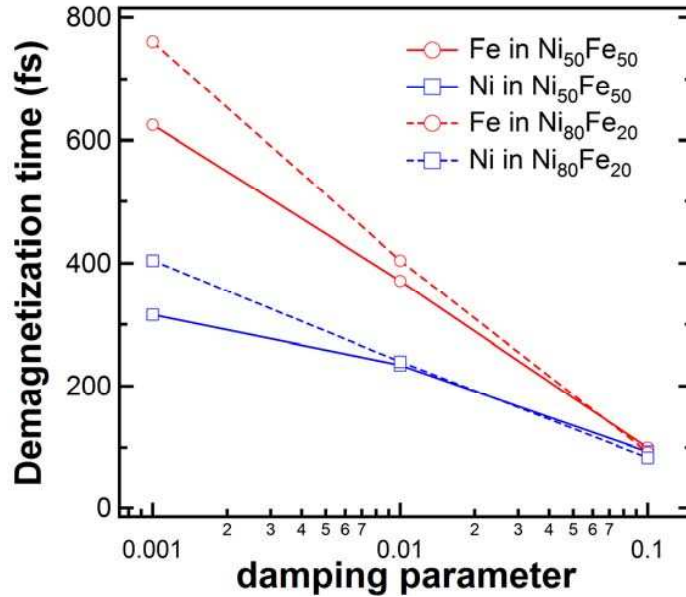


Fig. 5.5: Simulated value of demagnetisation times of the Ni and Fe species in $Ni_{80}Fe_{20}$ and $Ni_{50}Fe_{50}$ for a range of coupling parameters measured after laser excitation. For each value of the coupling to the thermal bath, the same laser fluence is applied and the response of the magnetisation fitted via equation 5.2.1. For the individual species NiFe (two solid or two dashed lines) there is a separation of timescale because of the fact that there is a difference in the strength of the thermal noise, driven by the difference in moment (equation 2.3.4). There is also a difference between the same species in the different $Ni_{80}Fe_{20}$ and $Ni_{50}Fe_{50}$ alloys (comparing curves with the same point shapes). This is mainly due to differences in the exchange.

rium magnetisation within around 800fs, it takes only around 300fs for Ni to demagnetise to reach equilibrium, in qualitative agreement with the predictions of the atomistic model (figure 5.3(a)). The distinct demagnetisation behaviour leads to an apparent decoupling of the Fe and Ni magnetic moments on the timescale of ~ 200 fs.

Essentially, a similar decoupled demagnetisation behaviour of the constituent, but antiferromagnetically coupled, magnetic moments is encountered for ferrimagnetic $Gd(FeCo)$, as shown in figure 5.6(b). In this case the demagnetisation of Fe takes around 400fs while Gd demagnetises within around 1.2ps. Because of the lower Curie temperature of $GdFeCo$ (around 550K) compared to $NiFe$, the sample is completely demagnetised at this laser fluence. Using the bi-exponential fit function as described in Ref. [24], the time constants for demagnetisa-

Parameter	$Ni_{50}Fe_{50}$	$Ni_{80}Fe_{20}$	$Gd_{25}Fe_{66}Co_9$
$\tau_{Ni}[fs]$	80 ± 30	180 ± 40	-
$\tau_{Fe}[fs]$	280 ± 50	300 ± 50	150 ± 55
$\tau_{Gd}[fs]$	-	-	450 ± 100

Table 5.3: Experimental Decay Time Constants After Laser Demagnetisation in $Ni_{50}Fe_{50}$, $Ni_{80}Fe_{20}$ and $Gd_{25}Fe_{66}Co_9$.

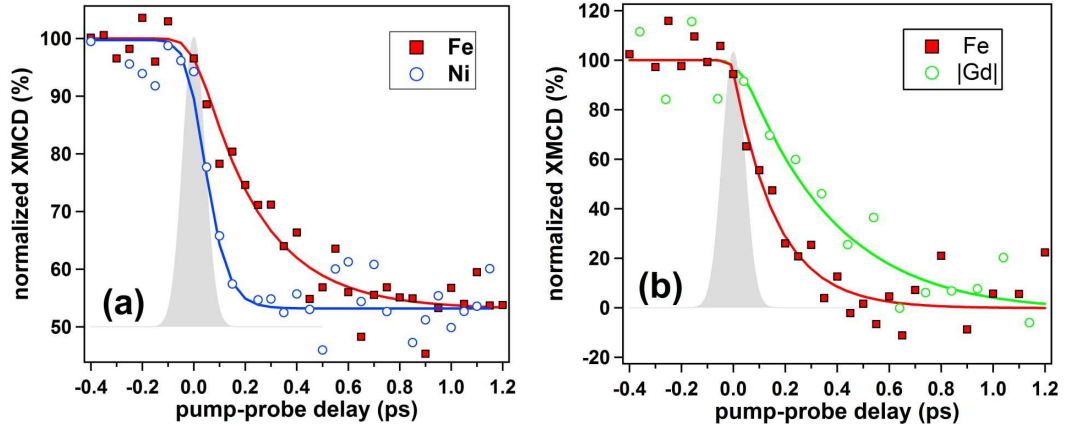


Fig. 5.6: *Experimental demagnetisation dynamics of Fe and Ni magnetic moments in $Ni_{50}Fe_{50}$ (a), and of Fe and Gd magnetic moments in $GdFeCo$ (b), measured by time-resolved XMCD with fs time-resolution. Element specific measurements in (a) $Ni_{50}Fe_{50}$ are taken at the $Fe(L_3)$ and $Ni(L_3)$ edges and (b) in $Gd_{25}Fe_{66}Co_9$ alloy at the $Fe(L_3)$ and $Gd(M_5)$ edges. The solid lines are fits according to a bi-exponential fit function [24]. The Gaussian profiles depict the time resolution of the XMCD measurements of 100fs. All measurements are performed at 300K. Measurements were performed by I. Radu and are published in Ref. [116].*

tion of the constituent magnetic moments of the alloys were obtained and are summarised in table 5.3.

The data in table 5.3 is plotted in figure 5.7, though presented in a slightly different way. The demagnetisation times are plotted as a function of the magnetic moment. The atomistic model predicts that there will be a linear increase in the demagnetisation time with the magnetic moment. This assumes that the coupling to the thermal baths is the same and that the demagnetisation is primarily driven by the initial phase of demagnetisation, where the temperature of the system is above that of the Curie temperature, so the exchange plays less of a role. The experimental data presented in figure 5.7 shows that although there is a general increasing trend in the demagnetisation time with magnetic moment, the data are not inconsistent with the theoretical prediction but there are insufficient data points to fully support the theory.

The XMCD data in this section and that of the simulations in section 5.2 show that, despite the strong ferromagnetic exchange coupling between the Ni and Fe sublattices in NiFe, they demagnetise at different rates. This shows that this kind of differential demagnetisation is not a only feature unique to amorphous TM-RE ferrimagnetic materials, but is also present in ferromagnetically coupled alloys.

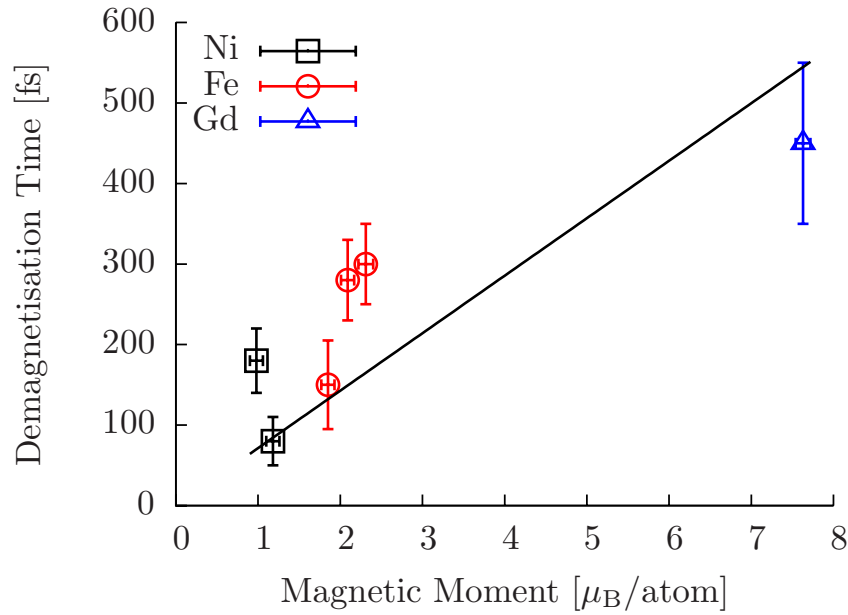


Fig. 5.7: Measured demagnetisation time constants as a function of magnetic moment. The magnetic moment values are measured from the constituent elements of $Ni_{80}Fe_{20}$, $Ni_{50}Fe_{50}$ and $Gd_{25}Fe_{66}Co_9$. The line is a linear line of best fit through the data, constrained through zero. Measurements were performed by I. Radu and the data is a reproduction from Ref. [116]

5.4 Calculated Longitudinal Relaxation Times for Various Compositions of NiFe After Laser Excitation

In this section we extend the calculations on $Ni_{80}Fe_{20}$ and $Ni_{50}Fe_{50}$, presented in section 5.2. Using input parameters obtained from the literature, a compositional variation in Ni_xFe_{1-x} can be studied. This compositional variation allows us to look at the effects of variations in the moment and exchange. The moments were obtained from Ref. [117], the Curie temperatures from Refs. [118] and [119] and the gyromagnetic ratios from Ref. [120]. The compositions and their corresponding parameters are summarised in table 5.4. To calculate the demagnetisation times as a function of composition, the same procedure as in section 5.2.2 was used; with the same fluence and starting temperature. Figure 5.8 shows the Curie temperature and individual magnetic moments of the Fe and Ni species as a function of Nickel content, x . The exchange is proportional to the Curie temperature by the two relations:

$$k_B T_C = \begin{cases} 3.18 J_{ij} & \text{fcc} \\ 2.05 J_{ij} & \text{bcc,} \end{cases} \quad (5.4.1)$$

where J_{ij} is the exchange energy between neighbouring spins. The first relation is for fcc lattices and the second for bcc lattices with nearest neighbour exchange.

The variation in the Curie temperature sets the trend for the demagnetisation times, and the difference in the moments should separate the two sublattice relaxation times, as predicted

x [%]	μ_{Ni} [μ_{B}]	μ_{Fe} [μ_{B}]	Structure	$J_{\text{Fe-Fe/Ni-Ni/Ni-Fe}}$ [J]	T_{C} [K]	γ_i/γ
0.0	-	2.35	bcc	7.021×10^{-21}	1043	0.958
8.5	1.15	2.41	bcc	6.200×10^{-21}	921	0.957
20.5	1.10	2.37	bcc	5.130×10^{-21}	762	0.956
27.0	1.05	2.43	bcc	4.645×10^{-21}	690	0.955
37.0	0.79	2.60	bcc	3.958×10^{-21}	588	0.954
40.0	0.80	2.45	bcc	3.790×10^{-21}	563	0.953
49.0	0.76	2.36	fcc	3.490×10^{-21}	804	0.952
56.5	0.62	2.26	fcc	3.745×10^{-21}	863	0.951
68.5	0.72	2.90	fcc	4.090×10^{-21}	942	0.949
76.0	0.63	2.52	fcc	4.018×10^{-21}	926	0.947
82.5	0.66	2.57	fcc	3.936×10^{-21}	907	0.944

Table 5.4: Input parameters for $\text{Ni}_x\text{Fe}_{1-x}$. The magnetic moments are taken from Ref. [117], the Curie temperatures from Refs. [118] and [119], and the gyromagnetic ratios from [120].

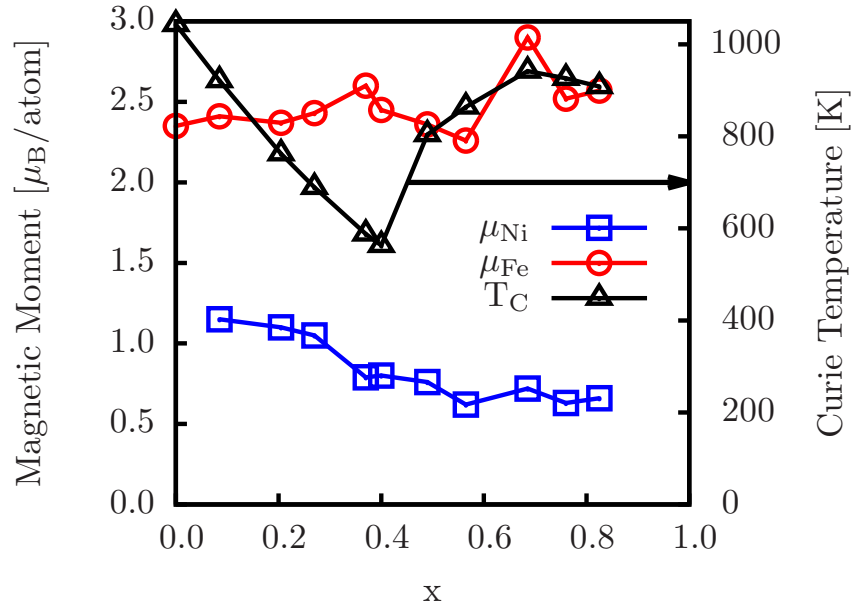


Fig. 5.8: Magnetic moments of individual species in $\text{Ni}_x\text{Fe}_{1-x}$ and their corresponding Curie temperatures. This figure shows the moment and Curie temperature data of table 5.4. Equation 4.4.2 predicts that there will be an almost constant difference in the demagnetisation time for any particular value of x (Ni content). The dashed line separates the region between the bcc and fcc phases.

by equation 4.4.2. Figure 5.9 shows the demagnetisation time, fitted (using the double exponential equation 5.2.1) to the demagnetisation data. The data is plotted for the thermal bath coupling parameter equal to 0.01 over the whole composition range. Comparing the Curie temperature as a function of composition in figure 5.8 with the longitudinal relaxation time in figure 5.9, we see a similar trend. In both figures there is an initial decrease to around 40% Ni, then an increase followed by a levelling off. This shows a direct relation between the Curie temperature of a particular sample and its demagnetisation time. The relaxation

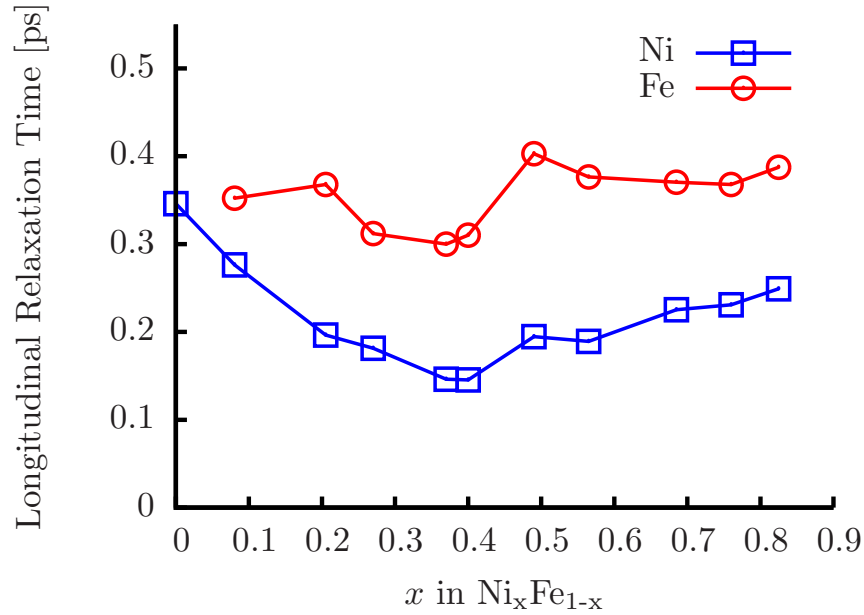


Fig. 5.9: Longitudinal relaxation time as a function of composition in Ni_xFe_{1-x} after laser excitation from room temperature. The variations in the relaxation times with compositions are directly proportional to the magnitude of the exchange interaction. The difference between the relaxation times between the species is approximately constant throughout as predicted by equation 4.4.2, which is governed by the strength of the stochastic process, $\lambda_i\gamma_i k_B T / \mu_i$ (equation 2.3.4). The time constants are obtained by fitting the sublattice magnetisation trace to the double exponential function given by equation 5.2.1.

time is largely governed by the exchange field experienced by the magnetic moments. The difference in timescales of the two individual species observed by the Ni and Fe moments is governed by the magnitude of the second moment of the stochastic process as predicted by equation 4.4.2.

5.5 Concluding remarks

The atomistic model in this chapter has shown conclusively that individual elements in an alloy demagnetise on different timescales. The atomistic modelling has been supported by element-specific time-resolved XMCD experiments, performed by I. Radu. The interpretation of demagnetisation in the atomistic model shows that the different rates is driven by the strength of the thermal noise. The different magnetic moments mean that the response of the sublattices is different, as smaller moments can respond more quickly to the change in temperature. Furthermore, it has been shown that differential demagnetisation exists, not only in materials with two different species coupled antiferromagnetically, but also in those coupled ferromagnetically. This further supports the simple analytic model and demonstrates that the strong exchange force coupling the two species is not sufficient to couple to such an extent that they demagnetise at the same rate.

Although the different rates of demagnetisation of the different atomic moments is governed by the difference (mainly) in the exchange and the magnetic moments, the strength of the coupling to the thermal bath can completely change the timescale of the process. While the atomistic model has proven successful in reproducing the essential physics of the experiments, to reproduce the experimental observations in a more quantitative manner one would require a more detailed and accurate description of the underlying microscopic processes.

Chapter 6

Ultrafast Heating as a Sufficient Stimulus for Magnetization Reversal

6.1 Introduction

There are a number of ways of reversing magnetization deterministically, such as using a magnetic field, electric field [121], circularly polarised light [17] or even by spin injection [122]. These methods of magnetization reversal have one important aspect in common, namely, that they require a *directional* stimulus. The requirement of a directional stimulus seems an obvious one, to give the magnetization vector something to align with. Figure 6.1 shows a schematic of the energy barrier of a magnetic material. The anisotropy provides a barrier to reversal

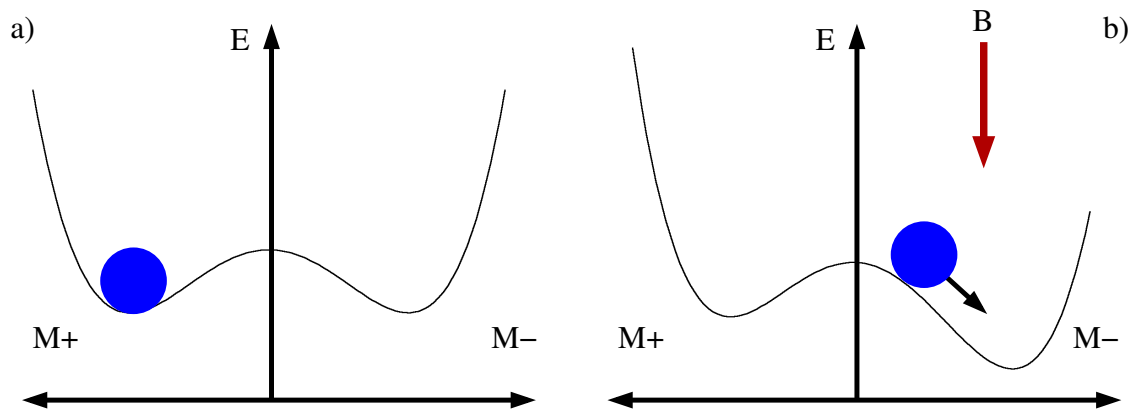


Fig. 6.1: Schematic of the energy barrier for an ordered magnetic material with uniaxial anisotropy. In the absence of any applied field (a) there is no energy difference between the system magnetized up ($M+$) or down ($M-$). If a field is applied then the symmetry is broken (b) leading to a lowering of the energy associated with the $M-$ state (with the applied field).

between magnetization *up*, $M+$, and *down*, $M-$, states. In the absence of an applied field (figure 6.1a), the energy associated with the up or down state is equal. The application of an applied field breaks this symmetry and lowers the energy in the direction of the applied field (figure 6.1b). If the field is sufficiently large, it can drive the system into this reversed state.

It is generally accepted that the effect of heat on a magnetic system is to lower the energy barrier associated with the anisotropy. This makes reversal with smaller magnetic fields possible, this is the basis of HAMR [1]. This principle is shown schematically on figure 6.2 showing that the height of the energy barrier between magnetisation states $M+$ and $M-$ is lowered. As well as lowering the energy barrier, heat also has the effect of thermal activation. Due to the random nature of thermal fluctuations, it is possible for the magnetisation to reverse over the energy barrier, though this process is not, in general deterministic. In this chapter,

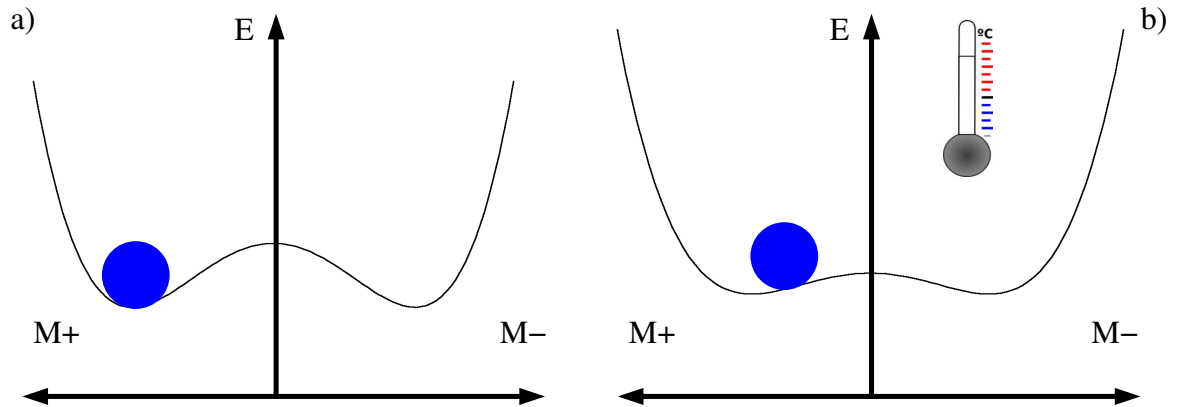


Fig. 6.2: Energy barrier schematic showing the effect of temperature on a magnetic material.

using a combination of atomistic modelling and comparison with experimental measurements made by collaborators, a new way of reversing magnetization without a directional stimulus is demonstrated. This new method uses femtosecond heating as the stimulus to induce switching. This switching is shown to occur via a *ferromagnetic-like* state that results in the two sublattices, aligning against the exchange field coupling them, for a short amount of time.

The results presented in this chapter are for the two sublattice ferrimagnet GdFeCo. The results of the atomistic model are compared qualitatively to time-resolved XMCD measurements as in chapter 5. There have been a number of studies of magnetisation reversal in this kind of ferrimagnetic material [21, 73, 74]. In one study by Stanciu *et al.* [73], heating across the compensation temperature using picosecond laser pulses in applied magnetic fields lead to reversal of the magnetisation in 100's of picoseconds. In this paper it was shown that the pump fluence is an important factor for magnetisation reversal in a magnetic field requiring heating to a point where the coercivity was sufficiently reduced. In this chapter we go beyond this view and show that femtosecond pulses, without a field, can reverse magnetisation within a few picoseconds.

Using a combination of heat and magnetic field it is shown in this chapter that GdFeCo can be driven into a highly susceptible ferromagnetic state far from equilibrium. Supported by time and element resolved XMCD measurements, the transient magnetisation dynamics can be observed after excitation with femtosecond laser pulses. The aim was to provide some insight into the range of different and often contradictory interpretations of experimental results on GdFeCo. Interestingly, it turns out that despite their strong antiferromagnetic coupling,

reversal in a magnetic field, under the influence of femtosecond laser pulses, is possible and occurs via a ferromagnetic-like state. This highly non-equilibrium, transient state exists for over a picosecond, much longer than the applied laser pulse. The different moments give rise to different demagnetisation times as seen in the previous chapter, which, as we will show in this chapter, is essential for reversal to occur. Furthermore, the role of the field is also studied showing that on this timescale the magnetic field plays no role in the switching mechanism.

6.2 Transient Ferromagnetic-Like State Mediating Ultrafast Reversal of Antiferromagnetically Coupled Spins

6.2.1 Experimental Results

In this section dynamic measurements of GdFeCo thin films are presented. The measurements were performed by I. Radu [24] at the Femtosecond slicing facility [114,115] of the Helmholtz-Zentrum, Berlin. Details of the characterisation of the samples and the experimental details of the time-resolved measurements are shown in appendix B.

Figure 6.3 shows the results of time-resolved measurements of the dynamics of the Fe and Gd sublattice magnetisations after excitation with 50fs linearly polarised laser pulses in a constant magnetic field, used to reset the magnetisation to the initial state. Each time the magnetisation is reset, the probe delay is adjusted to allow the whole time series to be created in a stroboscopic way.

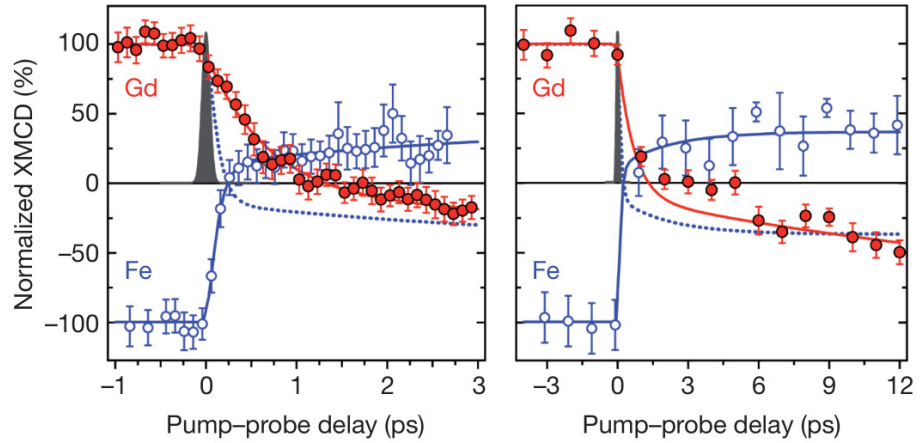


Fig. 6.3: Element-resolved dynamics of the Fe and Gd magnetic moments measured by time-resolved XMCD with femtosecond time-resolution. a) Transient dynamics of the Fe (open circles) and Gd (filled circles) magnetic moments measured within the first 3 ps. b) The same as a) but on a 12 ps timescale. Error bars of the experimental data represent the statistical standard error. The measurements were performed at a temperature of 83 K for an incident laser fluence of 4.4 mJ/cm^2 . Experimental time resolution of 100 fs is depicted by the solid Gaussian profile. The solid lines are fits according to a double exponential fit. The dashed line in both panels depicts the magnetisation of the Fe sublattice with opposite sign. Measurements performed by I. Radu, figure taken from Ref. [24].

Figure 6.3 firstly that the net magnetisation of both sublattices rapidly decreases. The net magnetisation of the Fe sublattice collapses within 300 fs and that of the Gd takes 1.5 ps. From the observations, despite the strong antiferromagnetic exchange coupling between the sublattices, they apparently lose their net magnetisation independently, in a similar manner to the results shown in chapter 5. During the time between the Fe reversing and that of the Gd reversing, the two sublattices align parallel in a *ferromagnetic-like* state with the applied field. The lines are fits to a bi-exponential fit function:

$$f(t) = G(t) \otimes [A - B(1 - \exp(-t/\tau_1)) - C(1 - \exp(-t/\tau_2))], \quad (6.2.1)$$

where A is the value of the transient signal at negative delays, τ_1 and τ_2 are the time constants characterising the two processes; the initial (fast) drop in magnetisation and the (slower) remagnetisation. B and C are exponential amplitudes and $G(t)$ is a Gaussian function denoting the time resolution of the measurements of 100fs (FWHM).

The existence of spin states whereby the sublattices are canted (spin-flop), in ferrimagnets, has previously been observed [123, 124], though generally such states are induced by strong magnetic fields. The experimental results shown in figure 5.3 show that this non-equilibrium state occurs within a few hundred femtoseconds and, as we will show, arises because of the action laser heating alone. A further interesting observation is that when the pump fluence is reduced, the transient ferromagnetic state exists for longer as is shown on figure 6.4. Figure 6.4

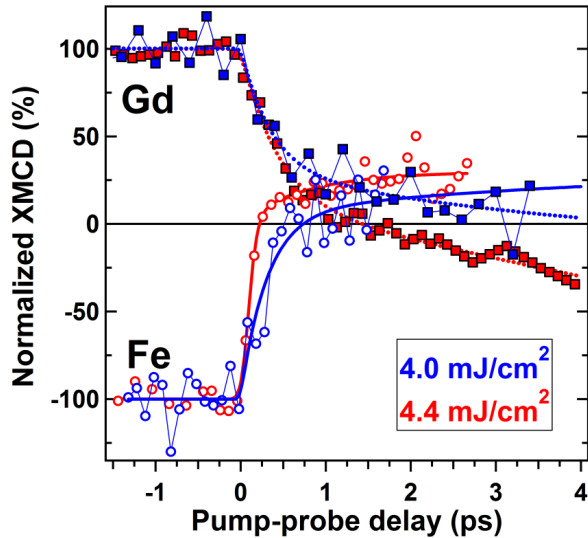


Fig. 6.4: Fluence dependence of Fe and Gd switching dynamics. The change of the magnetisation switching times for Fe and Gd moments upon varying the incident laser fluence as labelled in the figure. The lines are fits to the data according to a bi-exponential fit function (equation 6.2.1).

shows XMCD measurements of each sublattice when subjected to two different pump fluences (4.0 mJ/cm^2 and 4.4 mJ/cm^2). The lower pump fluence shows that it takes longer to arrive at the transient state, presumably because the lower fluence case results in less heating, so the system demagnetises more slowly. It is also clear from figure 6.4 that the transient state

exists much longer for the lower fluence case, this will be further discussed in section 6.3.

6.2.2 Atomistic Model Results

Using the afore-mentioned atomistic model, combined with the two temperature model, the experiments described in the previous section 6.2.1 can be compared qualitatively. Using the model, systematic variations of the physical parameters can be easily achieved, giving insight into the experimental observations. In these simulations, we assume the laser has a Gaussian profile temporally and uniform heating throughout. The laser is coupled directly to the electronic heat bath in the two-temperature model, which is in turn coupled to the phonon heat bath.

In the model proposed here there is no direct coupling between the spin system and the temperature of the phonon bath, though it is possible to couple the spin system to multiple heat baths [125]. In the TTM, the phonons play the role of removing heat from the conduction electron system, reducing the temperature of the conduction electron system after the initial increase. The coupling parameter in the LLG equation, λ , then describes the rate of energy

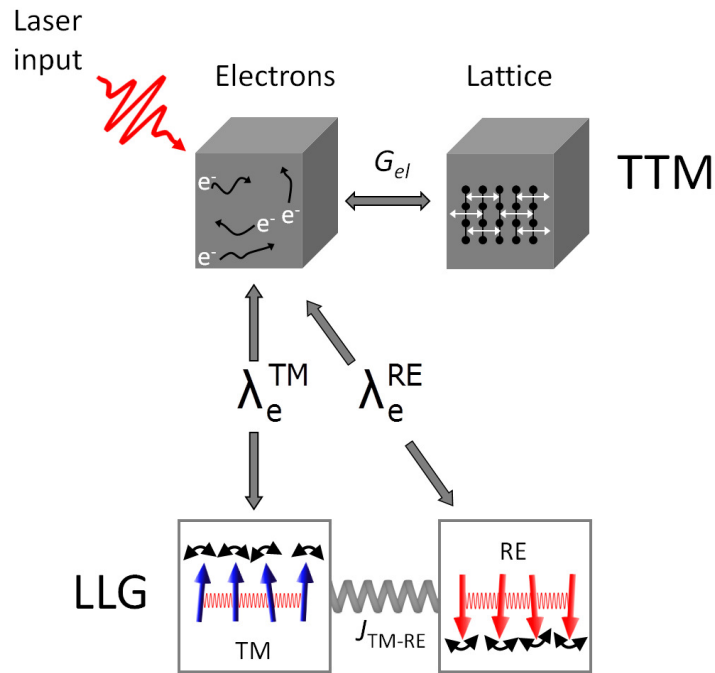


Fig. 6.5: Schematic of the energy transfer channels in both the two temperature model and the Landau-Lifshitz-Gilbert equation.

and angular momentum transfer into and out of the spin system. The damping parameter allows the system to come into equilibrium with the temperature of whatever bath to which it is coupled. Figure 6.5 shows the various energy transfer channels within both the two temperature model and the LLG model of a ferrimagnet. The TM and RE species are coupled to the conduction electron temperature, and in turn coupled to each other via inter and intra sublattice exchange constants.

At any instant in time the system will move toward equilibrium with the bath at the instantaneous temperature, thus if the temperature is rapidly varying then (for sensible values of the coupling constant) the system will not be able to be in equilibrium. For the laser induced processes that we are considering, the solutions to the two temperature model show a very rapid increase in temperature to greater than the Curie temperature for this system. The experimental results show that the two sublattices take different times to reach their equilibrium values, thus the system is in a strongly non-equilibrium state. Using the atomistic model it is also possible to investigate the effect of the magnetic field used in the experimental measurements in section 6.2.1. Figure 6.6 shows the results of the atomistic model for a maximum electron temperature of 1492K. It is clear from the inset that the calculations reproduce the transient ferromagnetic-like state. The agreement with figure 6.3 is qualitatively very good, in terms of the timescale for demagnetisation and duration of the transient state.

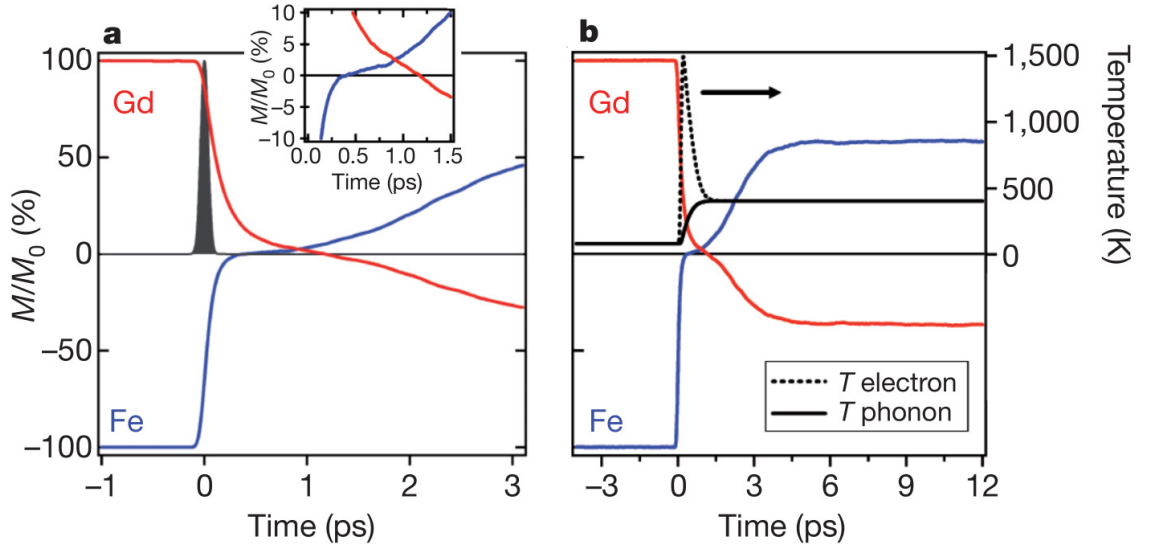


Fig. 6.6: Computed time-resolved dynamics of the Fe and Gd magnetic moments from the atomistic spin model. a) shows the dynamics for the first 3ps with the inset showing clearly the transient ferromagnetic-like state observed experimentally. b) shows the first 12 ps after laser excitation. The solutions to the two temperature model equations are the solid (phonon temperature) and dashed (electronic) black lines in panel b). The magnetisation is normalised to the magnetisation values at negative delay (*i.e.* reduced to the equilibrium value at 82 K). The agreement with figure 6.3 shows excellent qualitative agreement.

6.3 Systematic Study of Physical Parameters on Switching Times

One of the major advantages of a computational model is its ability to make predictions beyond experiment by variation of the physical parameters. In this section the effect of the variation of particular physical parameters of the model will be shown. In particular it is shown that the exchange integrals between spins can be varied to manipulate the reversal time and length of the transient ferromagnetic-like state. The effect of other parameters such as

the laser pump width, fluence and the effect of magnetic field will also be investigated. Using the atomistic model, calculations of the reversal time as a function of the inter-sublattice exchange constant have been performed. Figure 6.7 shows the result of variation of the TM-RE sublattice exchange on the reversal times of the TM and RE sublattices.

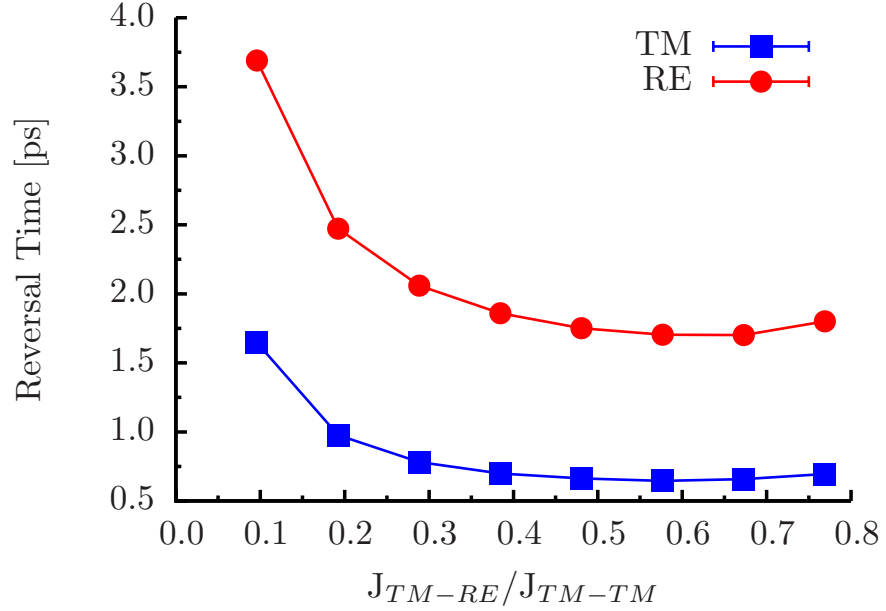


Fig. 6.7: Atomistic model calculations of reversal times of the TM and RE sub-lattices as a function of the inter-sublattice exchange parameter. As the exchange is reduced the system tends towards two uncoupled ferromagnets with no reversal.

The inter-sublattice exchange in figure 6.7 is reduced to the TM-TM exchange interaction, J_{TM-TM} , which in this case has a value of 2.835×10^{-21} J. The system simulated contained 500,000 spins in a field of 0.5 T as was the case in figure 6.6. The coupling constant, λ , used was 0.02 for both species, the anisotropy constant was 0.807243×10^{-23} J. The amount of RE was 24% with a magnetic moment of $7.63 \mu_B$ and a TM moment of $1.92 \mu_B$. The starting temperature was 82 K, to which all spins were equilibrated. The width of the laser pulse was 50 fs and the peak electronic temperature was 1492 K. This figure shows that when the two sublattices are decoupled, as the curve tends towards zero, the reversal time increases. In the limit of zero inter-sublattice exchange, the TM and RE species will act as individual ferromagnets with missing exchange (less than full coordination). In this case the two systems act as ferromagnetic materials and no reversal occurs. This observation is evidence of the fact that the antiferromagnetic exchange interaction in this system is important for reversal.

Because the materials of interest are TM rich ferrimagnetic materials, there are very few RE-RE interactions. This suggests that the RE-RE interaction plays very little role in the reversal of the system. Figure 6.8 shows the reversal time of each sublattice, this time, as a function of the RE-RE exchange parameter.

In section 6.2.1 it was shown that for a higher pump fluence, both sublattices reach zero

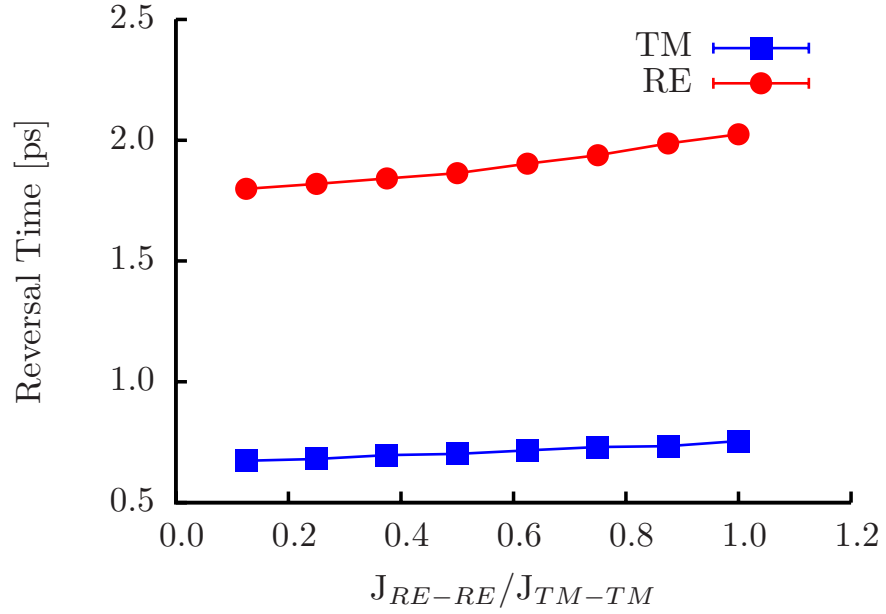


Fig. 6.8: Atomistic model calculations of reversal times of the TM and RE sub-lattices as a function of the inter-sublattice exchange parameter. Due to the (relatively) low numbers of RE-RE interactions the variation of the exchange between them does not vary the reversal time significantly. Figure reproduced from Ref. [24].

magnetisation in a shorter time (figure 6.4), although the two pump fluences shown represent a small data set. The transient state was also shown to be shorter for the higher fluence case. Figure 6.9 shows calculations of the reversal time as a function of the peak electronic temperature from the two temperature model, which corresponds to a higher pump fluence. The data shows that, as the laser fluence increases, the time for the TM to cross the zero axis (reversal time) gets smaller. For the case of the RE species the converse is true showing a large increase in reversal time with increasing laser fluence. The overall effect of this is that the transient ferromagnetic-like state exists for a longer time. It is worth pointing out that this result disagrees with the experimental observations in figure 6.4. The decrease in the reversal time of the Fe sub-lattice with increasing pump fluence seems to agree with the atomistic calculations (figure 6.9). The reduction in the reversal time of the Gd, experimentally is in disagreement with the result of figure 6.9. This interesting observation would require a more systematic investigation to determine the origin of the disagreement and a larger set of experimental data.

6.4 The Role of the Magnetic Field

So far in this chapter all of the experimental and theoretical results of switching have used a combination of heat (from a laser source) and magnetic field. The non-equilibrium ferromagnetic-like state predicted experimentally in section 6.2, occurred on the sub-picosecond timescale in a 0.5 T magnetic field. The question is what is the role of the field in the reversal? The

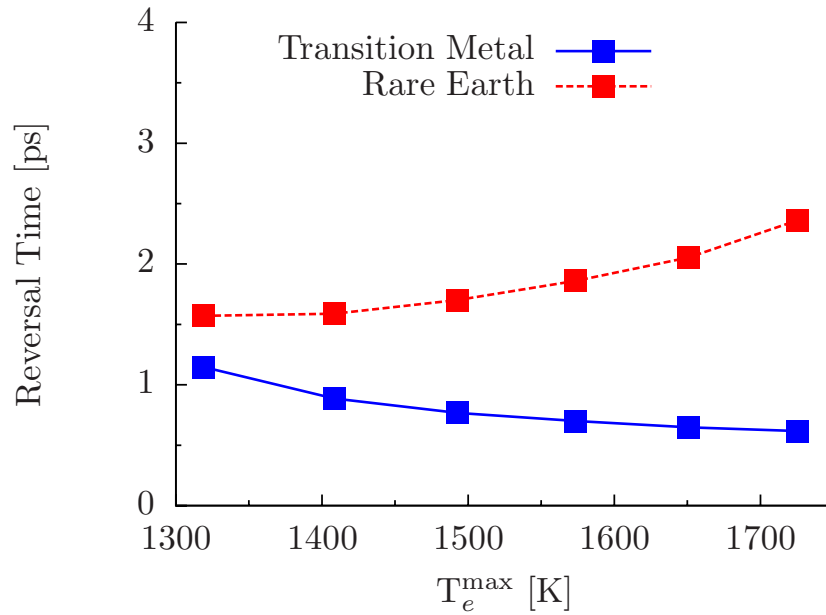


Fig. 6.9: Atomistic model calculations of the reversal times of the individual sublattices in *GdFeCo* as a function of peak electronic temperature. The dashed line represents the RE and the solid line the TM.

switching shown in the previous section occurs on the timescale of 100's of femtoseconds. It is questionable that a magnetic field of 0.5T can play a large role on this timescale, compared with the size of the thermal effects and the exchange fields. As discussed in the introduction of this chapter, the author will show results of switching without the application of any applied magnetic field. Another set of experiments have also been performed to confirm this surprising result. The later part of this chapter will be dedicated to attempting to explain the observed phenomenon.

Using the model as described in section 6.2, another set of simulations have been performed, but this time without the application of a magnetic field. A sequence of laser pulses is then applied to the ferrimagnetic system. The two-temperature model is augmented with a cooling term that couples the system to a constant temperature heat bath at constant temperature, in this case 300K. This extra bath removes heat from the phonon system. The removal of this heat could be important for any potential applications as applying a sequence of heat pulses with a very fast (picosecond) repetition rate would invariably heat the system above the Curie temperature. The heat in our simulations was withdrawn over 100's of picoseconds which was necessary for the computational resources available. It is worth pointing out that heat is usually drawn out (depending on the heat sink) on the nanosecond timescale. Figure 6.10 shows the results of the sublattice and overall magnetisation as a function of time (panels b and c), after a sequence of pulses (panel a). Note here that there is no applied field, although the system can be clearly seen to reverse everytime a heat pulse is applied. This surprising result is completely counter intuitive, with heat providing no directional stimulus at all, which until now was assumed to be essential [127] [128]. Figure 6.10 also shows that this kind of

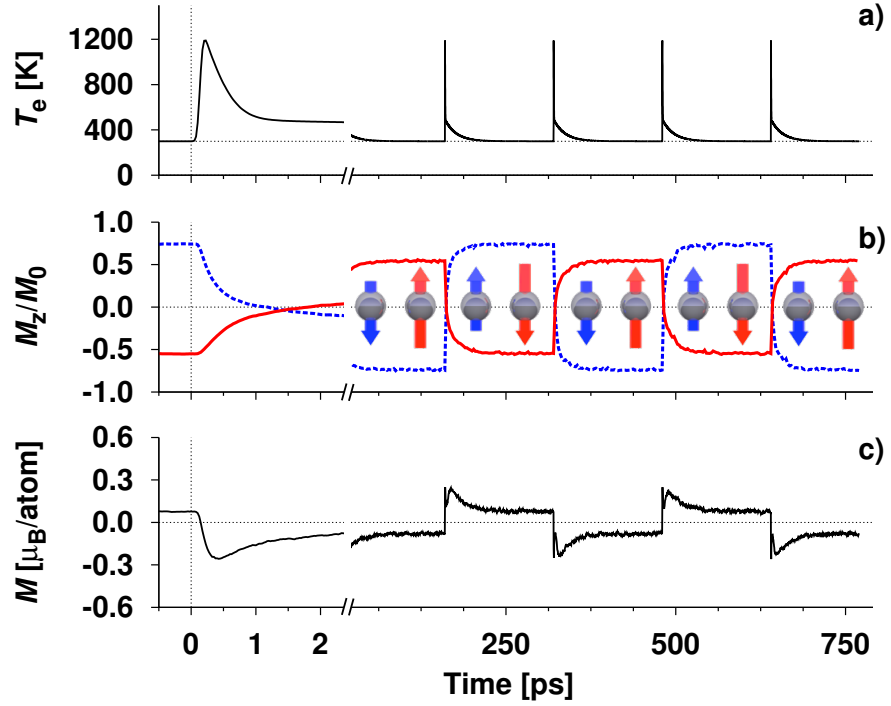


Fig. 6.10: Atomistic model calculations of magnetisation reversal after a sequence of pulses, panel a). The response of the sublattices is shown in panel b) with the orientation of the sublattices shown schematically. The solid red lines are the Gd sublattice and the dashed blue are the TM (FeCo). Panel c) is the net magnetisation showing clearly that magnetisation is reversed after each pulse. Figure published in Ref. [126].

reversal is deterministic, occurring each time a heat pulse is applied. Later in this section it will be shown that the method of switching presented in figure 6.10, is not affected by the anisotropy field (within reasonable limits). This observation could have implications for future magnetic storage devices.

Initially, this result seems to contradict the earlier work of Ref. [17], which, predicted that the orientation of magnetisation could be controlled by femtosecond lasers with a given light chirality. The laser light in Ref. [17] should still provide a heating of the system, which, according to the atomistic results, should result in magnetisation reversal independently of the helicity of the light. These two seemingly contradictory results raise the issue, of what is the role of the heat and the chirality of the light? The observations in Ref. [17] were explained by an effective field generated by the IFE [22] in this material, predicting that fields of up to 20T could be induced in the material. In Ref. [26], micromagnetic simulations were performed that used an LLB model of a ferromagnetic material. This paper used a phenomenological approach to the field arising from the IFE, assuming a Gaussian field. In this paper the field was essential for reversal of the magnetisation. In the remainder of this chapter the author will present results showing that this field plays almost no role in the reversal of the magnetisation. Furthermore, atomistic model and experimental results will

eliminate an explanation whereby reversal has to occur over the magnetisation or angular momentum compensation points. Finally, we conclude the chapter by setting out some of the key physical properties a system must have for this kind of switching to occur.

6.5 Experimental Results of Switching on GdFeCo Thin Films

In this section we present measurements of laser induced magnetisation reversal using right handed circularly polarised light ($\sigma+$), and demonstrate that reversal occurs independently of the polarisation. This initial result seemed to contradict that of Ref. [17], further measurements indicate that the all-optical control reported in Ref. [17] can be obtained by controlling the laser fluence, results of which will also be shown in this section.

The sample studied in this section was $\text{Gd}_{24}\text{Fe}_{66.5}\text{Co}_{9.5}$ under the action of 100 fs laser pulses. These experiments were performed by Alexandra Kalashnikova of the Ioffe Technical Institute, St. Petersburg, Russia. The final state, after the action of single pulses, were obtained using

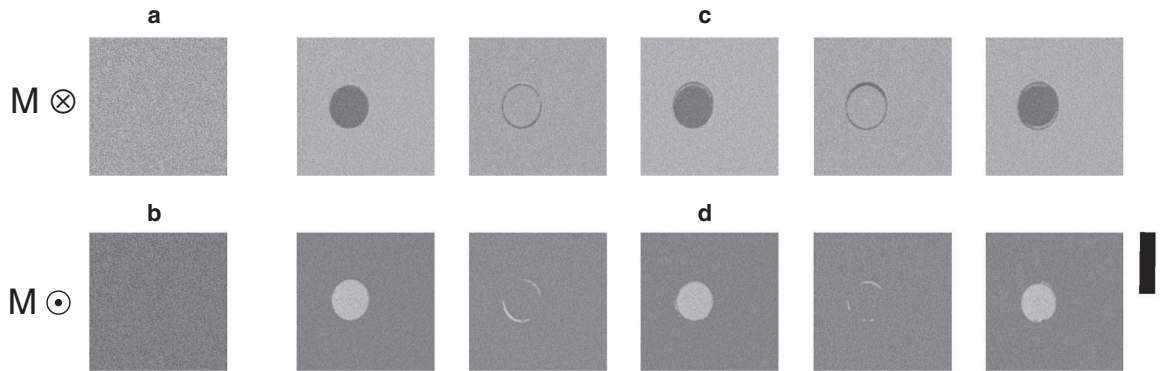


Fig. 6.11: The magneto-optical images of a $\text{Gd}_{24}\text{Fe}_{66.5}\text{Co}_{9.5}$ continuous film obtained after the action of a sequence of N , 100 fs laser pulses. (a) and (b) Initial homogeneously magnetised state of the film with magnetisation “up” and “down” as represented by the circled dot and cross respectively. The light grey region represents magnetisation pointing “down” and the darker grey “up”. (c) and (d) The film after excitatin with N ($N=1,2\dots5$) pulses with a fluence of 2.30 mJ cm^{-2} . Each laser pulse excites the same circular region of the film and reverses the magnetisation within it. The scale bar on the right corresponds to $20 \mu\text{m}$. Figure published in Ref. [126].

a magneto-optical microscope sensitive to the out-of-plane orientation of the FeCo sublattice magnetisation via the magneto-optical Faraday effect. The results of this experiment are shown in Figure 6.11 and seem to contradict the results of Ref. [17], showing that the reversal occurs independently of the initial state. In the previous study (Ref. [17]) it was shown that if the light of a particular chirality was exposed to the sample, the reversal only occurred if the magnetisation was in a particular orientation, however the measurements shown in figure 6.11 were for higher pump fluences than that used in Ref. [21]. Figure 6.12 shows the results comparing the reversal for two different fluences. The system was initialised in the same state for both experiments (panels a and b). In the first experiment (panel c), a fluence of 2.30

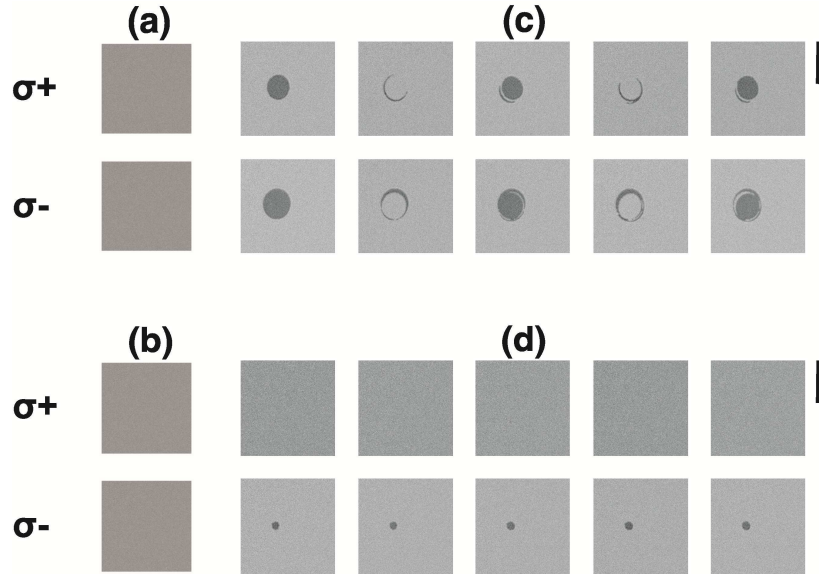


Fig. 6.12: The magneto-optical images of $Gd_{24}Fe_{66.5}Co_{9.5}$ continuous thin film obtained after the action of a sequence of the N right-handed ($\sigma+$) and left-handed ($\sigma-$) circularly-polarised 100 fs laser pulses. Initial homogenously magnetised state with magnetisation up (a,b). Panel c) shows the film after an excitation with N ($N=1,2\dots5$) circularly polarised pulses with a fluence of 2.30 mJ/cm^2 . Panel d) shows the film after excitation with N ($N=1,2\dots5$) circularly polarised pulses with a fluence of 2.25 mJ/cm^2 . The scale bar represents a length of $20 \mu\text{m}$. Figure published in Ref. [126].

mJ/cm^2 was applied. In the second experiment (panel d) a fluence of 2.25 mJ/cm^2 was used. The result shows that above a minimum threshold there is no control of the orientation of the magnetisation, reversal occurs independently of the light polarisation, in the same way as figure 6.11, the reversal occurs each time the sample area is excited. In the second instance (2.25 mJ/cm^2), the pump fluence is within the narrow range for the controlled magnetisation reversal reported in Ref. [17]. The mechanism of deterministic reversal using heat seems to be realized over a wider range of fluences than the rather narrow range in which the chirality of the light controls the magnetisation.

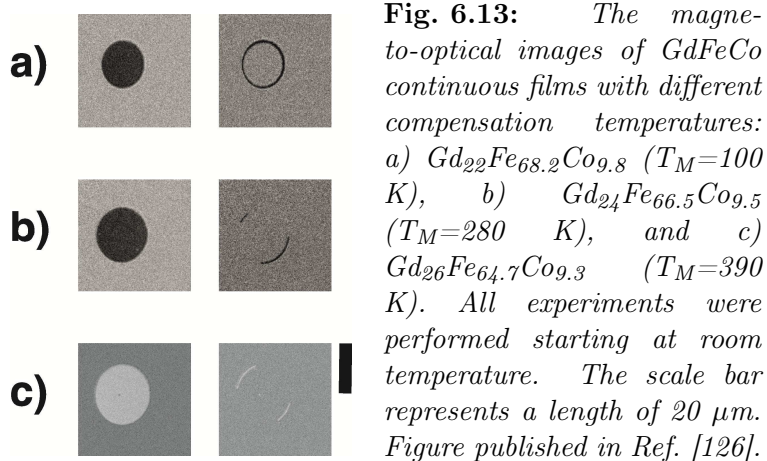
Figure 6.12 demonstrates that there is still an effect of the IFE for the observed reversal in thin films. Though it remains an open question as to the importance of the IFE and the heat input into the system. After the results of Ref. [126] a further explanation of the result in figure 6.12 was shown by Khorshand *et al.* [27]. This paper provided further evidence in support of the heat driven reversal mechanism, presented in this thesis, showing that reversal is subjected to a threshold fluence and occurs independently of the absorbed light. Furthermore, a *circular dichroism* was cited as a possible explanation for the chirality dependence of switching reported in Ref. [17], whereby more or less power is absorbed depending on the chirality of the light and the orientation of the magnetisation.

6.6 The Role of the Compensation Points

Several explanations of the mechanism of reversal after laser excitation in ferrimagnetic materials, have included a discussion of a magnetisation and angular momentum compensation temperatures [74] [116]. These explanations involve a discussion of the change in magnetisation dynamics at or around compensation. However, experimental observations presented in figure 6.13 show that the magnetisation and compensation temperatures play no role on this reversal mechanism by precluding increasing the temperature across these points. In order to confirm experimentally that the observed reversal does not rely on crossing the compensation point, we studied the reversal in several GdFeCo alloys, which, have different compensation points. Figure 6.13 shows the results of the action of a single pulse on the films with the compensation temperature, T_M , below (a,b) and above (c) room temperature.

The results in figure 6.13 clearly demonstrate that reversal happens. This suggests that crossing the compensation point is not required in all three samples. This result is also important from a technological point of view, as all experiments were performed at room temperature, an important aspect in the design of any devices. The atomistic model has also been employed to confirm the experimental observations in figure 6.13. In contrast to the experimental method used in figure 6.13, whereby the sample composition was varied to adjust the compensation temperature, in figure 6.14 the starting temperature and pump fluence were varied.

In panel a), the starting temperature was below the compensation temperature and heated through to a temperature above T_M (dashed grey line). The upper part of panel a) shows the response of the individual sublattices (dashed for TM and solid for RE). In panel b) the starting temperature was above the compensation temperature, thus no heating through the compensation point occurred. A lower pump fluence was required to stop the final temperature of the conduction electron bath being higher than the Curie point. Switching is clearly visible for both cases, supporting the experimental measurements in figure 6.13.



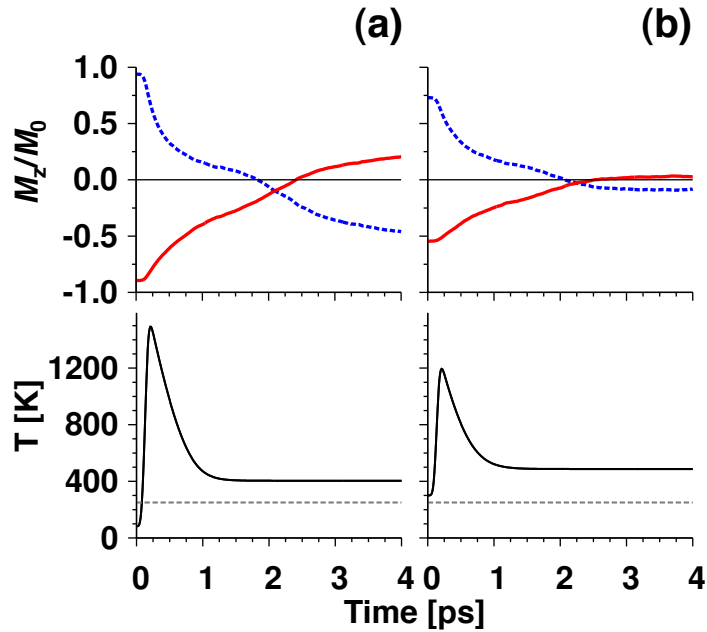


Fig. 6.14: Time resolved magnetisation dynamics of the z-component of the two sublattices (upper panels). Dashed blue lines are the Fe sublattices and the solid red lines are the Gd. Lower panels show the temperature profile during the simulation with a) having $T_{start}=82$ K (lower than the compensation temperature) and b) $T_{start}=300$ K (above the compensation temperature). The dashed grey line shows the compensation temperature for the simulated system. The result clearly shows switching for both of the sublattices, independent on whether the temperature of the electronic system goes through the compensation point. Figure published in Ref. [126].

6.7 Experimental Verification of Heat Induced Switching in Microstructures of GdFeCo

The results of the atomistic model in the previous section were performed for structures around $(30\text{nm})^3$, without demagnetising fields included into the Hamiltonian. This should be a reasonably good approximation, as the timescales that we are considering are too short for such long wavelength considerations. Furthermore, the net magnetisation in the samples is quite small. However in extended thin films, when we consider the quite rapid demagnetisation process, one may argue that small domains may form, allowing an explanation via interplay of these domains. In this section we try to eliminate an explanation by this interplay of domains by presenting experimental results of lithographically grown microstructures. The microstructures presented have a diameter of around $2\mu\text{m}$, though more importantly, are separated by a distance larger than this. This reduces any interplay between the stray fields of these microstructures.

The measurements were performed by the group of F.Nolting at the Paul Scherrer institute. The details of the growth techniques and measurements of the magnetisation states of the samples are shown in appendix C. First, structures with an out-of-plane anisotropy, similar to

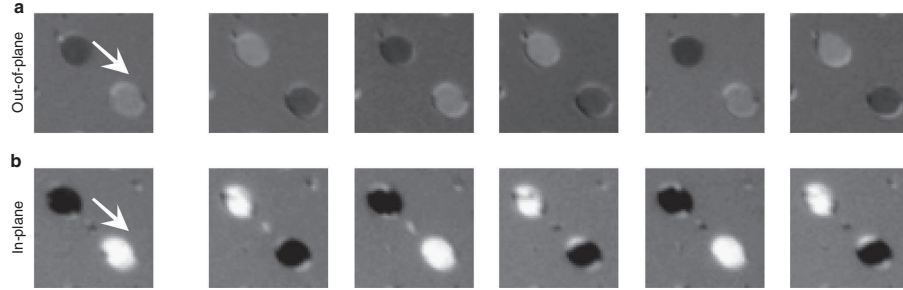


Fig. 6.15: *a) Images of microstructures with out-of-plane anisotropy, magnetised perpendicular to the sample plane. The first image in a) shows the initial state of the microstructures where the magnetisation of the darker structure points down while the magnetisation of the brighter one points up. The next image is taken after excitation with a single linearly polarised laser pulse and shows that the magnetisations of both elements are reversed. This reversal occurs after every laser pulse, as can be seen in the subsequent images in a). b) Images of microstructures with in-plane anisotropy. The bright and dark areas correspond to magnetisation directions in the plane of the sample pointing parallel or anti-parallel to the X-ray direction indicated by the white arrows. The subsequent images are taken after each excitation with a single linearly polarised laser pulse demonstrating the reversal of the magnetisation. The X-ray is indicated by an arrow and the structures have a size of $2 \mu\text{m}$. Figure published in Ref. [126].*

the thin films in figure 6.11 were studied and XMCD images recorded at the L_3 edge (708eV). The results of such observations after excitation of the samples is shown in figure 6.15a). This figure shows two microstructures, one with grey and one with a light grey contrast, which correspond to magnetisations pointing in opposite directions, up and down respectively, out of the sample plane. Starting from the initial state (figure 6.15 a)), a series of linearly polarised femtosecond laser pulses were applied.

Figure 6.15 shows that after the first pulse, and every subsequent pulse, the contrast is reversed, meaning that the magnetisation has switched relative to the previous panel. Figure 6.15 also shows that GdFeCo microstructures with in-plane anisotropy also reverse upon laser excitation (panel b)).

6.8 Preventing Reversal

Using the atomistic model, the effect of variation of the anisotropy constant on the probability of reversal has been calculated. For a single laser fluence with a high bath coupling factor, $\lambda = 0.1$, the anisotropy constant was varied from 1×10^{-27} to 1×10^{-20} J. Typical values are in the range 1×10^{-27} to 1×10^{-22} J, the higher value typical for 11_0 ordered FePt [12]. By beginning at zero K with the system in the ground state and applying a heat pulse, taking the temperature to a peak of 1071K, the probability of reversal is found by looking at the final state and taking averages over 80 realisations of the random number generator seed. The result is shown on figure 6.16, showing that reversal occurs deterministically over a wide range of anisotropy constant. As the magnitude of the anisotropy constant reaches values that are

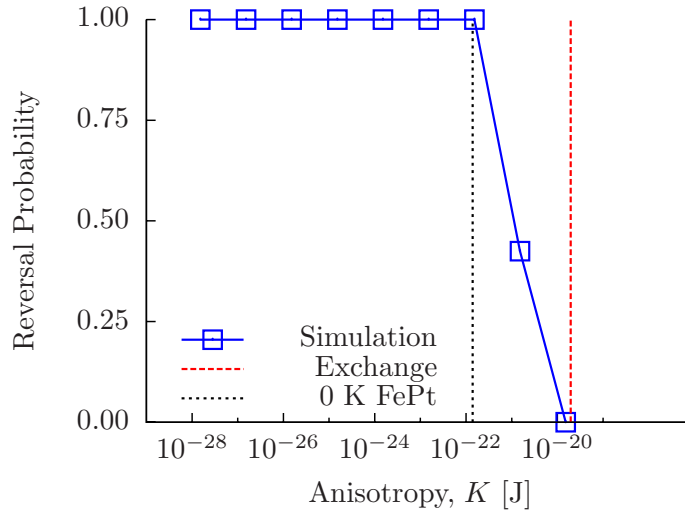


Fig. 6.16: Reversal probability of $TM_{76}RE_{24}$ as a function of uniaxial anisotropy constant, K . Blue (square) points show the calculated reversal probabilities. The initial temperature was 250K and the pulse width 50fs. The damping constant used (or coupling to the thermal bath) was 0.1. The peak electron temperature was 1071 K. The dotted black curve shows the anisotropy value for 0K FePt [12] and the dashed red line the inter-sublattice exchange constant from the nearest neighbours.

generally typical of the exchange interaction the reversal probability goes to zero.

The importance of the different demagnetisation times of the two sublattices for the switching mechanism can be tested in a simple way using the atomistic model. This can be achieved by repeating the simulation that produced figure 6.10, keeping all physical parameters the same, except for the magnetic moment on the RE sites. Figure 6.17 shows the case where the system begins at 82 K and we apply a 50fs laser pulse, with the moments equal. Panel a) shows the case in which the moments are equal to that of the transition metal and b) shows the case where both are equal to the RE moment. In both cases no reversal occurs, showing that having unequal moments (or at least different timescales for demagnetisation) is essential for this process.

Figure 6.17 shows that in spite of the fact that the two sublattices have different intra-sublattice exchange, they are practically equivalent in their longitudinal response, at least for the short time. It can be clearly seen from figure 6.17 that no reversal occurs, thus the non-equivalence of the sublattices in terms of their longitudinal response plays a key role in this mechanism of heat induced switching.

To gauge the strength of the reversal mechanism, atomistic model calculations were performed on a system that would normally undergo switching. For each of the simulations, the system begins in the ordered ground state at zero K and a laser pulse is applied. Throughout the simulation, a field was applied to prevent the reversal of the TM sublattice magnetisation against that of the RE. The critical strength of the field required to prevent reversal (the field at which no reversal of the TM occurs) was shown to be dependent on the time at which the

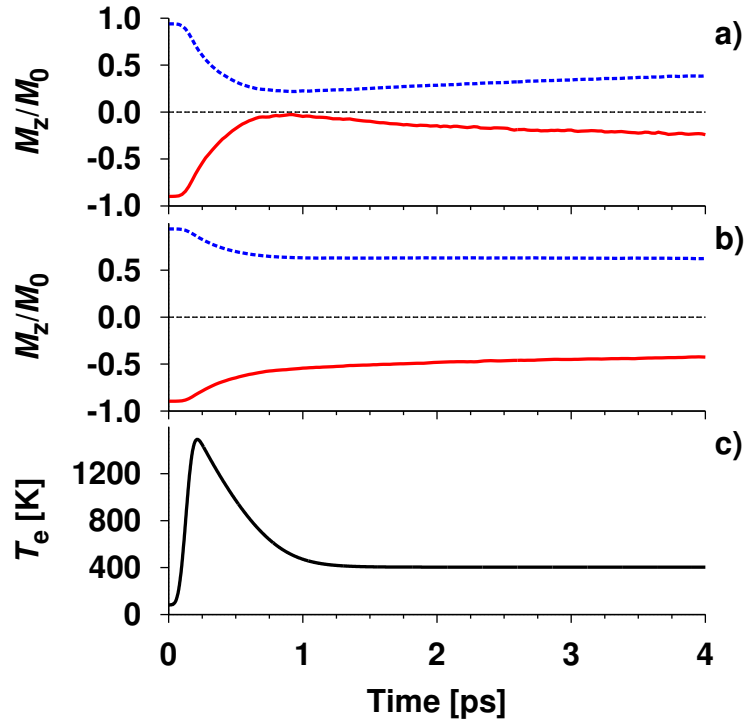


Fig. 6.17: Panel a) shows the response of the sublattice A (blue dashed lines) and sublattice B (solid red lines) moments to a laser pulse when the local moments of each species are equal to the Fe moment. Panel b) shows the same as a) but with the moments equal to that of Gd. Panel c) shows the evolution of the electronic temperature. Figure published in Ref. [126].

measurement was taken. This is as expected, because, as the timescale for the simulation increases, the applied magnetic field induces precession which occurs on a longer timescale than the thermal relaxation.

Figure 6.18 shows the magnetisation dynamics of the individual sublattices in an opposing 10, 40 and 50T applied field, respectively. As figure 6.18 b) shows, a 40T field is insufficient to prevent the TM sublattice reversing against the RE, though it quickly reverses back.

If the TM sublattice crosses zero we consider that reversal has occurred against the RE. Then, by averaging over different seeds of the random number generator for the thermal term and the allocation of the TM and RE spins, the reversal probability as a function of field can be calculated.

Figure 6.19 shows the results of the field required to prevent reversal as a function of applied field. Note that the point at which the reversal probability drops to zero depends on the measurement time, as noted above. If the measurement time was sufficiently long, the field at which the probability would drop to zero would be the equal to the anisotropy of the system.

The results of figure 6.19 were averaged over 100 realisations of the random number generator seed, thus a single run would have the typical magnetisation dynamic profile as presented in figure 6.18. Figure 6.19 clearly shows that if we consider the short timescale, the field required for preventing the formation of the transient ferromagnetic-like state is of the order of 10's of

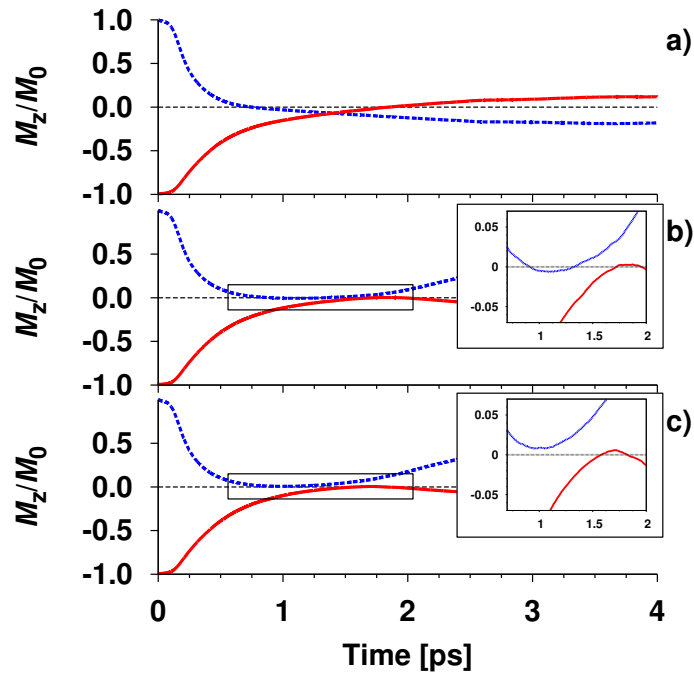


Fig. 6.18: (a-c) Dynamics of the Fe (blue dashed) and Gd (red solid lines) sublattice with applied fields of 10, 40 and 50 T, respectively, to prevent reversal of the Fe sublattice. The system is initially in the anti-parallel ground state at 0 K and a Gaussian laser pulse is applied driving the system into a non-equilibrium state whereby the sublattices attempt to align against the exchange interaction and the applied field. Figure published in Ref. [126].

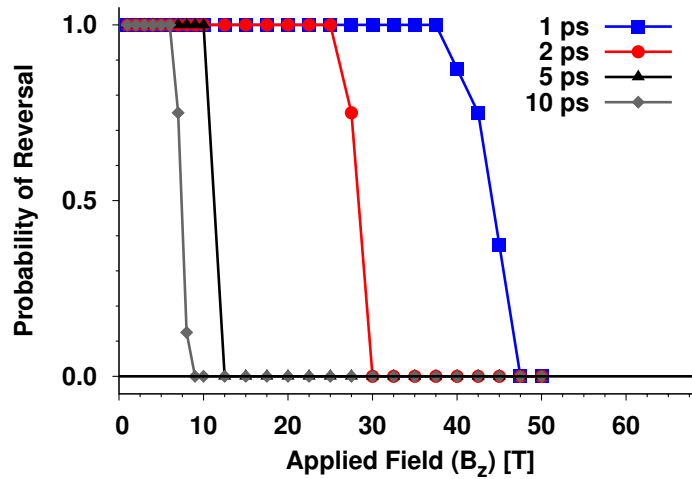


Fig. 6.19: Numerical calculations showing the magnetic field required to prevent reversal of the Fe sublattice. The required field depends on the time at which the magnetisation is measured, as precessional reversal starts to push the magnetisation back into alignment with the applied field. Each point is averaged over 100 runs, each with a different seed for the random number generator. Each run begins at 0K, with the electronic temperature increasing rapidly before dropping below the Curie temperature. Figure published in Ref. [126].

Tesla. These high fields required to prevent reversal are getting into fields of the order of the exchange field, providing further evidence of the exchange origin of this mechanism.

6.9 Landau-Lifshitz-Bloch Analysis of Switching by Ultrafast Heating

So far we have presented results that conclude that it is possible for magnetisation, in a ferrimagnetic material, to be reversed using femtosecond heat pulses. We have shown that the different demagnetisation rates of the two sublattices is an important property of the materials for switching to occur. Furthermore, we have shown key results suggesting that this is an exchange driven effect. Although we have presented results of some of the key physical properties required for this heat driven switching, no actual mechanism for reversal has so far been presented. This section will be devoted to discussing the mechanism. We provide analysis from a two macro-spin approach based on the LLB formalism of a ferrimagnet. The LLB model of a ferrimagnet was developed by U. Atxitia of the Instituto de Ciencia de Materiales de Madrid. The full derivation can be found in Ref. [129]

The femtosecond heating of the ferrimagnetic material as we have shown results in different demagnetisation rates of the two sublattices. The effect of this is to drive the system out of equilibrium. Reference [130] has attempted to explain the observed process using an approach based on the Onsager relations [131]. This approach allows one to define a parameter known as the *affinity*, A , defined as [131]:

$$A = -\left(\frac{\partial G}{\partial \iota}\right)_{P,T}, \quad (6.9.1)$$

where G is the Gibbs free energy, ι is a set of variables that describe the state of a system and P is the pressure. Using this relation it is possible to define the phenomenological coefficients of the Onsager relations. The affinity is zero when the system is in equilibrium. However, this approach is only valid when a system is close to equilibrium [131]. The phenomenological coefficients relate the thermodynamic forces of a system to the various entropy production/flux terms.

In Ref. [130], Mentink *et al.* have applied the phenomenological equations [131] to the system after the laser pulse and the temperature of the electron system is assumed to be constant. This gives the system a well defined ground state to which the system can move towards, such a scenario is a requirement of the Onsager relations. The results of this analysis do indeed show that if the system is placed in a non-equilibrium state, just after the laser pulse (see figure 6.6), the system will tend towards a reversed state. The mechanism driving this behaviour is said to arise from *exchange relaxation* [132]. Ref. [130] assumes that on this short timescale any dissipation to an external bath does not occur, thus, is a consequence of spin-spin interactions only. Also they assume that any transverse components of the magnetisation can be ignored. In the remainder of this section we present a different kind of analysis to that presented in

Ref. [130]. Our analysis requires a transverse component of the magnetisation and shows that the switching in this kind of material is driven by a transfer of angular momentum from the longitudinal component to the transverse. We ascribe this transfer to the excitation of an exchange mode associated with the antiferromagnetic exchange interaction between the two sublattices. The analysis of Ref. [130] precludes such a description as any transverse motion is ignored.

6.9.1 Ferrimagnetic Landau-Lifshitz-Bloch Equation

The LLB equation, as described in section 1.6.2, is a macrospin model of magnetisation in ferromagnetic materials. The formalism is intrinsically temperature dependent via input parameters, such as; the parallel and perpendicular susceptibilities, the temperature dependent magnetisation and the temperature dependent exchange stiffness. This formalism goes beyond the usual micromagnetic approach [133], allowing contractions of the length of the magnetisation towards its equilibrium. Although this form been used to describe the behaviour of ferromagnetic materials [26], as we have shown in this chapter, a single sublattice formalism is insufficient. The LLB equation for a ferromagnetic material, for example, is unable to describe the different demagnetisation times of the two sublattices. The formalism also cannot take into account the behaviour around the compensation points as shown in section 4.3 of chapter 4.

An LLB equation for a two sublattice ferrimagnet has been derived by U. Atxitia, the full details of which can be found in his Ph.D thesis [129]. The equation of motion that arises is similar in form to the LLB equation for a ferromagnet (equation 1.6.9), but now we have two equations; one for each sublattice:

$$\begin{aligned} \frac{1}{|\gamma_{\text{TM}}|} \frac{d\mathbf{m}_{\text{TM}}}{dt} = & -\mathbf{m}_{\text{TM}} \times \left[\mathbf{H}_{\text{TM}} + \frac{\alpha_{\text{TM}}^{\perp}}{m_{\text{TM}}^2} \times \mathbf{H}_{\text{TM}} \right] \\ & - \alpha_{\text{TM}}^{\parallel} \left[\frac{1}{2\Lambda_{\text{TM-TM}}} \left(\frac{m_{\text{TM}}^2}{m_{e,\text{TM}}^2} - 1 \right) - \frac{1}{2\Lambda_{\text{TM-RE}}} \left(\frac{\tau_{\text{RE}}}{\tau_{e,\text{RE}}^2} - 1 \right) \right] \mathbf{m}_{\text{TM}}, \end{aligned} \quad (6.9.2)$$

for the TM and:

$$\begin{aligned} \frac{1}{|\gamma_{\text{RE}}|} \frac{d\mathbf{m}_{\text{RE}}}{dt} = & -\mathbf{m}_{\text{RE}} \times \left[\mathbf{H}_{\text{RE}} + \frac{\alpha_{\text{RE}}^{\perp}}{m_{\text{RE}}^2} \times \mathbf{H}_{\text{RE}} \right] \\ & - \alpha_{\text{RE}}^{\parallel} \left[\frac{1}{2\Lambda_{\text{RE-RE}}} \left(\frac{m_{\text{RE}}^2}{m_{e,\text{RE}}^2} - 1 \right) - \frac{1}{2\Lambda_{\text{TM-RE}}} \left(\frac{\tau_{\text{TM}}}{\tau_{e,\text{TM}}^2} - 1 \right) \right] \mathbf{m}_{\text{RE}}, \end{aligned} \quad (6.9.3)$$

for the RE. In equations 6.9.2 and 6.9.3, \mathbf{m}_v is the reduced magnetisation of the sublattice v and $m_{e,v}$ is its equilibrium value, \mathbf{H}_{TM} is the effective field, which we assume for simplicity here only contains exchange terms. τ_v is the projection of sublattice v onto the other, which we discuss below, and the Λ_{ij} parameters are the relaxation rates. The temperature dependent

damping constants are given by:

$$\begin{aligned}\alpha_v^{\parallel} &= \frac{2\lambda_v}{\beta\tilde{J}_{0,v}} \\ \alpha_v^{\perp} &= \lambda_v \left(1 - \frac{1}{\beta\tilde{J}_{0,v}} \right),\end{aligned}\tag{6.9.4}$$

where the λ_v parameters are the coupling constants, similar to the LLG equation and $\tilde{J}_{0,v}$ is the effective exchange. Equations 6.9.4 are similar in form to that of the ferromagnetic case (equation 1.6.10) as the effective exchange depends on the inter and intra sublattice exchange constants, which define the Curie temperature. The exchange parameters are given by:

$$\begin{aligned}\tilde{J}_{0,\text{TM}} &= \frac{J_{0,\text{TM}}m_{e,\text{TM}} - J_{0,\text{TM-RE}}m_{e,\text{RE}}}{m_{e,\text{TM}}} \\ \tilde{J}_{0,\text{RE}} &= \frac{J_{0,\text{RE}}m_{e,\text{RE}} - J_{0,\text{RE-TM}}m_{e,\text{TM}}}{m_{e,\text{RE}}},\end{aligned}\tag{6.9.5}$$

where the exchange parameters, $\tilde{J}_{0,\text{TM}}$, $\tilde{J}_{0,\text{RE}}$, $\tilde{J}_{0,\text{TM-RE}}$ and $\tilde{J}_{0,\text{RE-TM}}$ are the compositional dependent exchange constants:

$$\begin{aligned}J_{0,\text{TM}} &= qJ_{0,\text{TM-TM}} \\ J_{0,\text{RE}} &= xJ_{0,\text{RE-RE}} \\ J_{0,\text{TM-RE}} &= xJ_{0,\text{TM-RE}} \\ J_{0,\text{RE-TM}} &= qJ_{0,\text{RE-TM}}\end{aligned}\tag{6.9.6}$$

Finally the rate parameters, $\Lambda_{\text{TM-TM}}$, $\Lambda_{\text{RE-RE}}$ and $\Lambda_{\text{TM-RE}}$ depend on the susceptibilities, $\tilde{\chi}_{\text{TM},\parallel} = (\partial m_{\text{TM}}/\partial H)_{H \rightarrow 0}$ and $\tilde{\chi}_{\text{RE},\parallel} = (\partial m_{\text{RE}}/\partial H)_{H \rightarrow 0}$ via the relations:

$$\begin{aligned}\Gamma_{\text{TM-TM}} &= \Lambda_{\text{TM-TM}}^{-1} = \frac{1}{\tilde{\chi}_{\text{TM},\parallel}} \left(1 + \frac{|J_{0,\text{TM-RE}}|}{\mu_{\text{TM}}} \tilde{\chi}_{\text{RE},\parallel} \right), \\ \Gamma_{\text{RE-RE}} &= \Lambda_{\text{RE-RE}}^{-1} = \frac{1}{\tilde{\chi}_{\text{RE},\parallel}} \left(1 + \frac{|J_{0,\text{RE-TM}}|}{\mu_{\text{RE}}} \tilde{\chi}_{\text{TM},\parallel} \right), \\ \Gamma_{\text{TM-RE}} &= \Lambda_{\text{TM-RE}}^{-1} = \frac{|J_{0,\text{TM-RE}}|}{\mu_{\text{TM}}} \frac{\tau_{e,\text{RE}}}{m_{e,\text{TM}}}, \\ \Gamma_{\text{RE-TM}} &= \Lambda_{\text{RE-TM}}^{-1} = \frac{|J_{0,\text{RE-TM}}|}{\mu_{\text{RE}}} \frac{\tau_{e,\text{TM}}}{m_{e,\text{RE}}}.\end{aligned}\tag{6.9.7}$$

Although the coupled equations for the two sublattices (equations 6.9.2 and 6.9.3) are similar to that of the ferromagnetic LLB, they differ, rather importantly, in the following ways; the field acting on one sublattice depends on the magnetisation from the other, the longitudinal relaxation depends on the projection of the opposing sublattice onto itself and the longitudinal term relies on the rates, Λ_{ij} , where i and j refer to sublattices. The projections of one sublattice onto another are shown schematically in figure 6.20 and, for example for the transition metal has the mathematical form $\tau_{\text{RE}} = \frac{|\mathbf{m}_{\text{TM}} \cdot \mathbf{m}_{\text{RE}}|}{m_{\text{TM}}}$.

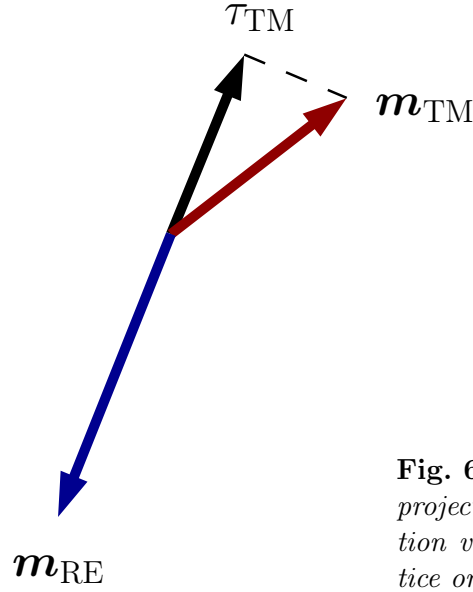


Fig. 6.20: Schematic of the projection of the magnetisation vector of the TM sublattice onto that of the RE.

6.9.2 The LLB Equation Close to the Curie Temperature

In the time resolved experiments and simulations presented in figures 6.3 and 6.6 we can see that at no point, before or after the end of the pulse, are both sublattices simultaneously completely demagnetised. For our analysis of switching using the FLLB, we assume a square pulse in temperature, going to zero after the pulse. We then consider the case just before and just after the pulse.

We begin by considering the temperature dependence of the relaxation rates, $\Gamma_{\text{TM-TM}}$ and $\Gamma_{\text{TM-RE}}$, as we focus on the dynamics of the TM species. Figure 6.21 shows the relaxation rates as given by equations 6.9.7 for GdFeCo. The susceptibilities and magnetisations for GdFeCo are calculated in the mean field using the model described in section 3.3. The calculations were performed by U. Atxitia and can be found in Ref. [134]. If we consider figure 6.21 in terms of our Ferrimagnetic LLB (FLLB) equation 6.9.2 for the transition metal, then, considering longitudinal relaxation (third and fourth terms) only, there is a sign change when $\Gamma_{\text{TM-TM}}$ becomes larger than $\Gamma_{\text{TM-RE}}$ as this leads to a change in sign of dm_{TM}^z/dt from negative to positive. However, unlike in Ref. [130], this change in sign of the relaxation rates cannot drive the reversal process. If one ignores the precessional term, in equilibrium dm_{TM}^z/dt goes to zero. The longitudinal relaxation process only contributes to the timescale of the switching process but does not drive the switching process. To understand the reversal mechanism we need to consider both transverse and longitudinal components of the process.

The next part of the analysis leads us to reduce the FLLB equation to a dynamical system, based on information from atomistic modelling. We know from numerical simulations that close to the reversal of the TM sublattice, the RE sublattice magnetisation is larger than that of the TM. We can assume then that $m_{\text{RE}}^x, m_{\text{RE}}^y, m_{\text{TM}}^x, m_{\text{TM}}^y, m_{\text{TM}}^z \ll m_{\text{RE}}^0$. In this limit, the longitudinal field, $h_{\text{TM}}^{\parallel}$ is positive and can be approximated by $h_{\text{TM}}^{\parallel} \simeq \alpha_{\text{TM}}^{\parallel} \frac{m_{\text{RE}}^0}{\Lambda_{\text{TM-RE}} m_{e,\text{RE}}}$ for the case before the heat pulse is removed ($m_{\text{TM}} < m_{e,\text{TM}=0}$), and $h_{\text{TM}}^{\parallel} \simeq (\alpha_{\text{TM}}^{\parallel}/2)[\Gamma_{\text{TM-TM}} -$

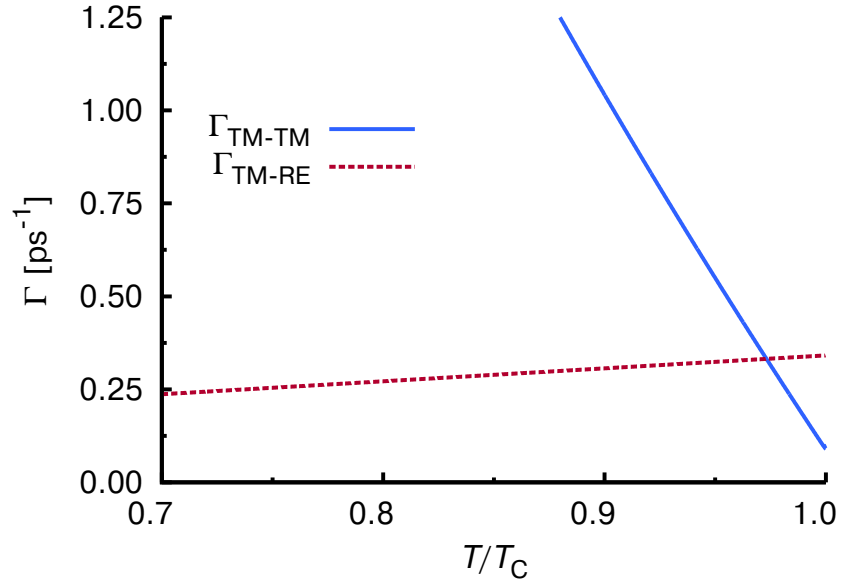


Fig. 6.21: Longitudinal relaxation rates as a function of temperature close to the Curie temperature in the LLB equation. The dashed line shows the TM-RE relaxation rate and the solid line shows the TM-TM rate. At low temperatures $\Gamma_{TM-TM} \gg \Gamma_{TM-RE}$, due to small susceptibility values (equation 6.9.7). Close to T_C there is a change in the trend where $\Gamma_{TM-TM} > \Gamma_{TM-RE}$. Calculations performed by U. Atritia and the figure taken from Ref. [134].

Γ_{TM-RE}] after the heat pulse ($m_{TM} < m_{e, TM}, T = 0K$). The LLB equation for the TM can then be reduced to the following dynamical system:

$$\begin{aligned} \frac{1}{|\Gamma_{TM}|} \frac{d\rho}{dt} &= 2\alpha_{TM}^{\perp} \Omega_{TM} \frac{\rho m_{TM}^z}{|m_{TM}|^2} + 2h_{TM}^{\parallel} m_{TM}^z \\ \frac{1}{|\Gamma_{TM}|} \frac{dm_{TM}^z}{dt} &= -\alpha_{TM}^{\perp} \Omega_{TM} \frac{\rho}{|m_{TM}|^2} + h_{TM}^{\parallel} m_{TM}^z, \end{aligned} \quad (6.9.8)$$

where $\rho = (m_{TM}^t)^2 = (m_{TM}^x)^2 + (m_{TM}^y)^2$ is the TM transverse magnetisation component and $\Omega_{TM}(T) = \alpha m_{RE}^0 |J_{TM-RE}| / \mu_{TM}$ is the precessional frequency of the anti-ferromagnetic exchange mode. Figure 6.22 shows the solutions of the dynamical equations 6.9.8 with a comparison from the atomistic model. Figure 6.22 shows how the perpendicular components of the magnetisation of the TM, m_{TM}^t , vary as a function of the z-component during heat induced switching. Panel a) shows the solutions to the dynamical equations 6.9.8 given a number of different starting values. These solutions show large precession induced as angular momentum is transferred from an unstable linear motion to the perpendicular component. Panel b) shows the phase portrait calculated using the atomistic model. A square pulse of temperature is applied to the system of width 500fs for a range over temperatures. Averages are taken over different instances of the random number generator in the atomistic model. Qualitatively the behaviour is similar with a lot of precession induced after the pulse is turned off, reducing the temperature to 0K. This kind of temperature profile makes the analysis with the LLB equation easier to apply the analysis of the two regions, before and

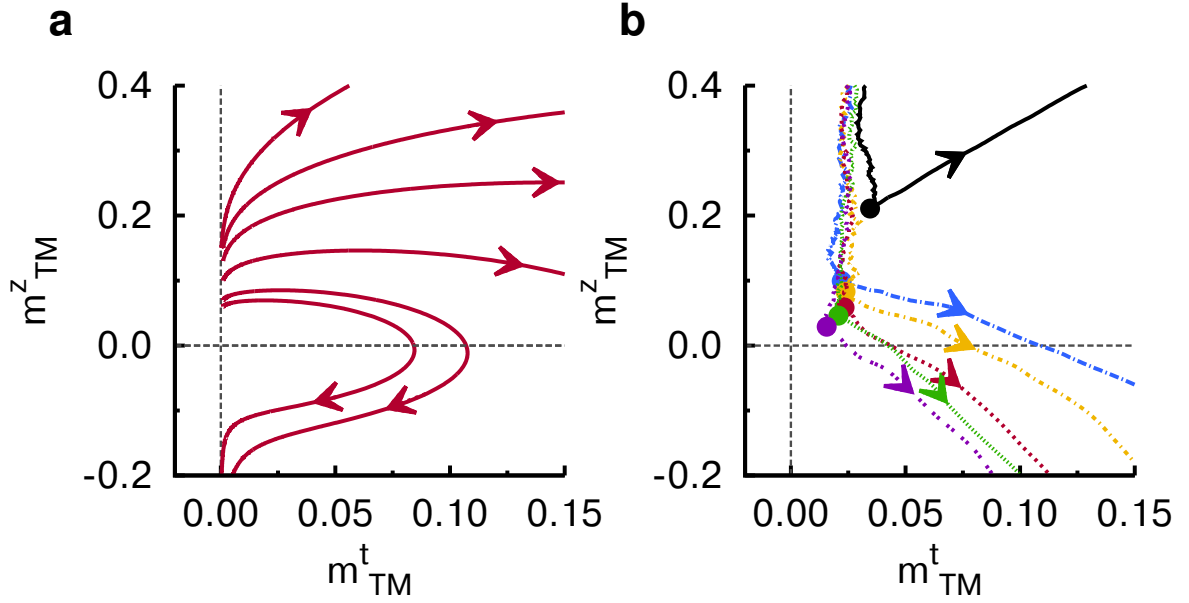


Fig. 6.22: Phase portrait showing the TM transverse components of magnetisation, m_{TM}^t , as a function of the z-component during heat induced switching. Panel a) shows the solution of the dynamical equations 6.9.8. Panel b) shows the same calculated in the atomistic model for a range of temperatures. The heat pulse applied is a square pulse of width 500fs.

after the heat pulse. As the temperature is increased, the smaller the transverse components of magnetisation induced.

The LLB analysis in figure 6.22 shows that the trajectory corresponding to $m_{TM}^t = 0$ is a linear mode that is trivially stable for $h_{TM}^{\parallel} < 0$, corresponding to the usual linear longitudinal relaxation we expect [8] and unstable for $h_{TM}^{\parallel} > 0$. As mentioned, the linear path does not lead to switching, however, if a small component of m_{TM}^t exists switching will then occur. The physical interpretation of this analysis is that perturbation from $m_{TM}^t = 0$ leads to the development of a perpendicular component of magnetisation, which is supported by the atomistic calculations.

In the same approximation as was applied to reach equations 6.9.8, the LLB dynamical equation for the RE reads:

$$\frac{1}{|\gamma_{RE}|} \frac{dm_{RE}^{x(y)}}{dt} = \mp \Gamma_{RE} m_{RE}^{x(y)} + \frac{\alpha_{RE}^{\perp}}{m_{RE}^0} \Omega_{RE} m_{TM}^{x(y)} - h_{RE}^{\parallel} m_{RE}^{x(y)}, \quad (6.9.9)$$

where the upper sign corresponds to the equation for m_{RE}^x and the lower sign for m_{RE}^y . The antiferromagnetic resonance frequency, $\Omega_{RE} = z(1-x)m_{RE}^0 |J_{TM-RE}| / \mu_{RE}$ and $h_{RE}^{\parallel} > 0$ is the RE longitudinal field. As equation 6.9.9 depends on the perpendicular components of the TM magnetisation, the induced perpendicular motion of the TM induces precessional motion of the RE via angular momentum transfer (the first two terms of equations 6.9.2 and 6.9.3 i.e. via perpendicular components) with the same frequency, Ω_{TM} but with different amplitude. This

kind of analysis does not necessarily require the formation of the transient state reported in section 6.2. The formation of the transient state arises because of the fact that the longitudinal change in the RE is slower than that of the TM. The motion of the TM around the RE and vice versa occurs during and after the ferromagnetic-like state until the system has relaxed to equilibrium.

One important consequence of the LLB analysis we have applied is that there must be some deviation from the unstable linear motion, producing an initial torque. Direct integration of the LLB without this initial deviation will not result in switching, but, a recovery of the magnetisation to its equilibrium. Figure 6.23 demonstrates the importance of this small deviation resulting in switching. In the atomistic model we see that reversal is deterministic and

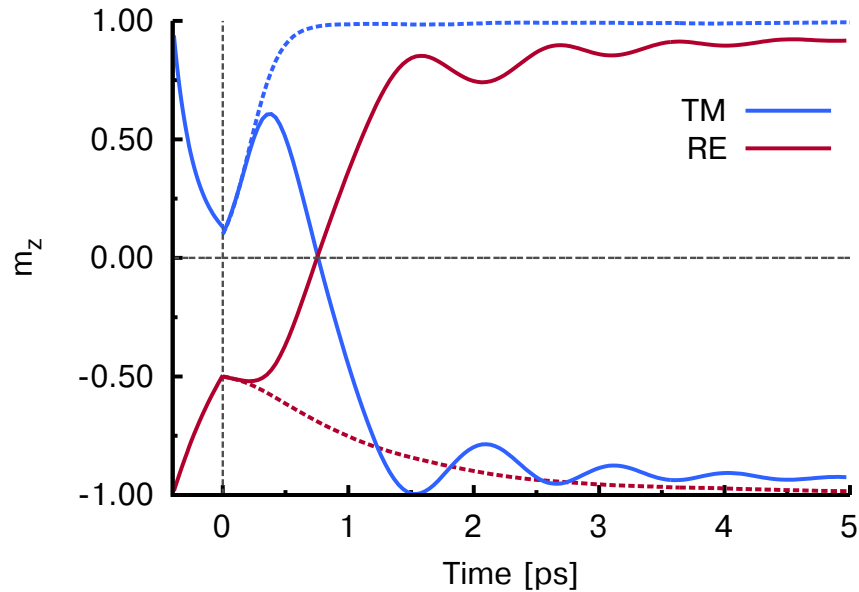


Fig. 6.23: *Z*-component of magnetisation as a function of time after excitation of a heat pulse. Dashed lines show the TM and RE sublattice magnetisations without an initial deviation between the ground state for the two sublattices, no reversal occurs. Solid lines shows the case where a 15 degree angle between the sublattices is applied, resulting in reversal.

always arises even though the transverse components of magnetisation are almost negligible for (as we will see) *large* systems. In the atomistic approach, however, the deviation from the ground state always occurs on some length scale due to the high temperatures involved in the femtosecond laser induced dynamics due to the high temperatures involved.

An outstanding question is whether this magnetisation precession, predicted to be central to the reversal mechanism, is observable experimentally on a large sample. If we consider the initial high temperatures involved in the laser heating, correlations will only exist over small length scales. This would mean that precession will be induced with different phases over the system. This would mean that its observation experimentally would not be possible without looking with very high spatial resolution at the spin-spin correlation function or structure factor. To demonstrate this effect, we present the results of numerical switching for a range

of different system sizes of GdFeCo. Figure 6.24 shows the x-component of magnetisation as a function of time for a range of system sizes. It is clearly observable in figure 6.24 that as

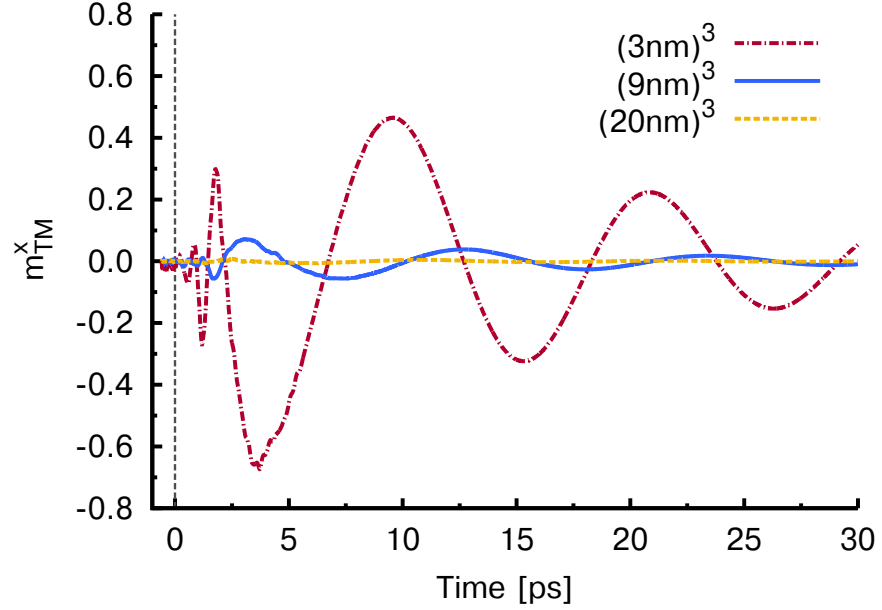


Fig. 6.24: System size dependence of the x-component of the magnetisation as a function of time during switching. A square pulse in temperature of 2000K and width 600fs. For large system sizes almost no precession is seen (dotted line). For the smallest system size, $(3\text{nm})^3$, large amplitude precession is induced at the frequency of the antiferromagnetic exchange mode.

the system size is decreased, with all other parameters the same, large amplitude precession is setup in the x-component of magnetisation. For large system sizes the effect disappears as the thermal noise brings about random phases in the amplitude and angle of precession. This observation is consistent with the predictions of the LLB model that there must be a deviation (a non-collinearity) of the two sublattices.

The above analysis using the LLB dynamical equations has also allowed us more insight into the transient ferromagnetic-like state presented in section 6.2. As the switching mechanism requires the oscillation of one sublattice around the other, using small inter-sublattice exchange would mean that a lower frequency would be achieved and more time would be required for the RE to precess back to align with the TM. Furthermore, the rate of longitudinal relaxation of the RE is a key parameter for the rate at which the RE sublattice reverses. Thus using small intrinsic coupling for the RE sites would mean that the transient state could be extended. Figure 6.25 shows atomistic model results of the effect of a 600fs square pulse of height 2000K, but with $\lambda_{\text{RE}} = 0.001$ and $J_{\text{TM-RE}} = -0.109 \times 10^{-21} \text{J}$. As figure 6.25 shows, by adjusting some of the physical parameters in the model we can engineer very a very long transient ferromagnetic-like state. Clearly this kind of manipulation of parameters is possible in a numerical simulations, however, experimentally it is not so trivial.

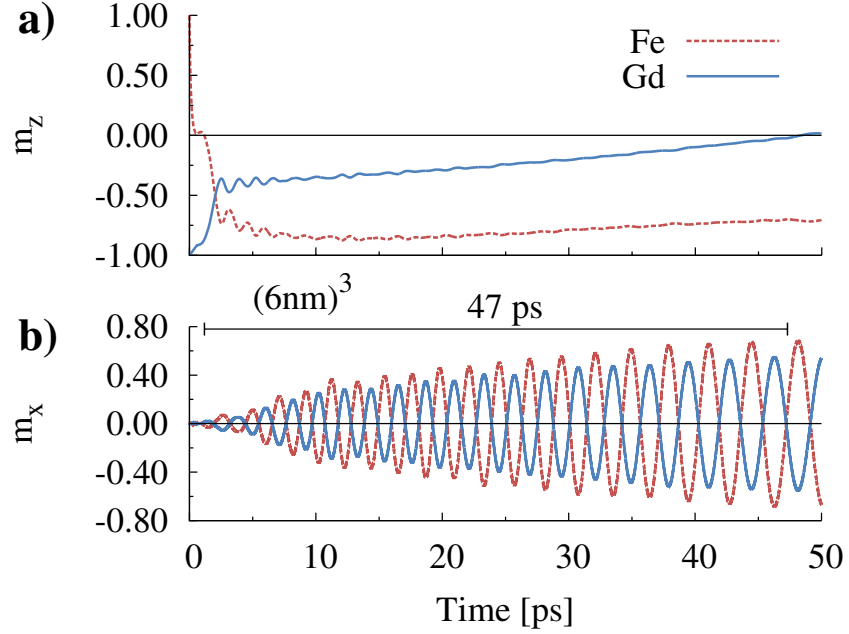


Fig. 6.25: Atomistic model calculations showing the z (panel a)) and x (panel b)) components of the magnetisation as a function of time. The intersublattice exchange constant and RE coupling to the thermal bath were 10% of their original value. Panel a) clearly shows a very long transient state of up to 50ps. Panel b) shows large amplitude precession of both sublattice at the exchange frequency.

6.10 Concluding Remarks

The atomistic model was used in this chapter to predict that very fast heat pulses alone can be used to reverse the magnetisation in a ferrimagnet. The uniform heating assumed means that we have induced reversal without providing a directional stimulus. This surprising result is confirmed experimentally by two sets of experiments, one on thin films and another on microstructures of GdFeCo. The measurements on thin films using polarised light lead us to discuss the role of the heat and the IFE, concluding that the heat is the most dominant effect here. This conclusion arises because the mechanism for reversal that we have presented occurs over a wider range of pump fluences. Furthermore, further work presented in Ref. [27] has shown that the control of magnetisation using circularly polarised light can be explained via a magnetic circular dichroism, where, more or less heat is absorbed depending on the combination of light polarisation and the initial orientation of the magnetisation of GdFeCo.

As well as showing both theoretically and experimentally that this type of heat driven deterministic reversal is possible, we have shown in this chapter that there is no role of the compensation point in the switching mechanism on this timescale. The demonstration of such a switching mechanism in the microstructures of GdFeCo, separated by a larger distance than their radius, precludes an explanation via stray field coupling between neighbouring domains. The reversal is shown to occur in microstructures with in and out-of-plane anisotropy. Calculations of the reversal probability as a function of the anisotropy constant in the atom-

istic model provided evidence that this heat driven reversal is of exchange origin.

Chapter 5 demonstrated that individual species in magnetic materials can demagnetise at different timescales in alloys when excited by femtosecond lasers. The atomistic model was successfully employed in demonstrating the importance of this differential demagnetisation by showing that no reversal occurred in systems with equal local atomic moments. The fact that the two sublattices of GdFeCo demagnetise at different rates means that the system can arrive in a non-equilibrium state.

The reversal was shown to be highly deterministic and not at all a fragile effect. By attempting to prevent the reversal of the TM sublattice, and therefore the formation of the transient ferromagnetic-like state, the atomistic model showed that (under a certain circumstances) fields of up to 40T are still not able to prevent the formation of the ferromagnetic-like state introduced in section 6.2. The magnitude of this field is further evidence of this heat driven reversal being of exchange origin.

Finally, we have have discussed a mechanism for reversal by excitation of a localised exchange mode. The analysis involved a new ferrimagnetic form of the Landau-Lifshitz-Bloch model. The analysis of the LLB model agreed well with the conclusions of the atomistic model, showing that the different longitudinal relaxation times of the sublattices is an important ingredient in the reversal process. The LLB analysis included only exchange terms in the fields, providing yet more evidence of this exchange driven effect. The mechanism for the heat driven reversal that we have proposed involves the excitation of a local exchange mode, where angular momentum is transferred from an unstable longitudinal mode to a transverse mode. We showed that within the FLLB formalism, without a small transfer of angular momentum to this transverse mode, no reversal occurs. Without this transfer the system relaxes back to its initial state along a longitudinal route. The switching is initiated by the TM which arrives at zero magnetisation before the RE, and responds dynamically to its exchange field. This allows us to conclude that the non-equivalence of the sublattices in terms of their longitudinal relaxation time is an essential part of the reversal process. We have made a prediction that this mechanism cannot be observed experimentally as its effect is averaged out over large samples due to the random phase of the deviations of the moments due to high thermal fluctuations.

The FLLB observations allowed us more insight into the key parameters controlling the transient ferromagnetic-like state. We have showed that this intriguing transient state can be made to last for up to 50ps by tuning the inter-sublattice exchange constant and the intrinsic coupling (damping) of the RE to the thermal bath.

Chapter 7

Conclusions

The main results of this thesis are the development and implementation of an atomistic model of disordered multi-element magnetic alloys. A model of GdFeCo was parameterised on experimental observations and successfully compared to a mean field model. A model of $\text{Ni}_x\text{Fe}_{1-x}$ was developed based on literature values of the physical constants and experimental observations. The two main focuses of the study were; to investigate the difference in the longitudinal relaxation time of the two sublattices and the generality across multi-component alloys, and the use of femtosecond laser pulses to reverse magnetisation. The work provides new insights into magnetisation processes on the femtosecond timescale, potentially important for engineering new devices. Furthermore, it has been made clear that any model of femtosecond laser induced dynamics must be able to account for the difference in the longitudinal relaxation of the different elemental species of an alloy. The observation, for the first time, that a non-directional stimulus (in the form of heat) is able to reverse magnetisation is scientifically intriguing and potentially technologically important.

Where possible, experimental observations have been compared with the results of the atomistic model, at least in a qualitative manner. In chapter 3 it was shown that, after parameterising the atomistic model from XMCD measurements of the Fe and Gd species in GdFeCo, calculations of the coercivity agreed qualitatively very well with experimental measurements. The compensation points as a function of composition also agreed well with the measurements. The model was also tested against an adapted mean field treatment and shown to compare very well as one would expect, validating the atomistic model.

Further validation of the atomistic model was also presented in chapter 4, where atomistic model calculations of the frequency and damping were presented and compared to derived analytic expressions. The power absorbed during FMR by ferrimagnetic materials, of different compositions, at zero K were shown to have interesting behaviour, the width of the spectrum diverging at magnetisation compensation. The effect of the angular momentum compensation point on the domain wall velocity showed that this kind of material could be important for technological applications, such as, race-track memory. It was in this chapter that we saw the initial calculations of the difference in relaxation time of the two sublattices of a ferrimagnetic material.

Chapter 4 predicted that a TM-RE alloy such as GdFeCo would have different demagnetisation rates for the different elements. In the following chapter this observation and its generality were further studied using the atomistic model and comparison with time-resolved XMCD measurements of $\text{Ni}_x\text{Fe}_{1-x}$ and GdFeCo. The result of this study was that the different demagnetisation rates were being driven, mainly, by the difference in the magnetic moments of the species and was not a unique feature of the antiferromagnetic inter-sublattice exchange in GdFeCo. The role of other physical parameters on the demagnetisation was also shown, namely, the coupling to the thermal bath and the exchange constants.

The final chapter of results focused on the switching behaviour of GdFeCo. The different demagnetisation dynamics of the Fe and Gd species after laser excitation was studied, showing that, rather unexpectedly, there was a reversal of the two species via a never before seen unstable alignment of the two sublattices. Importantly, these calculations confirmed the unexpected experimental observation of the transient ferromagnetic-like state by Dr. I. Radu (published in Ref. [24]). This alignment of the two sublattices was shown to last for around 1ps, and, occurred against the strong antiferromagnetic exchange interaction coupling them. This ferromagnetic-like state occurred around 300fs after excitation by the laser, giving the first indication that the (relatively weak) magnetic field was playing almost no role on this timescale. Atomistic model calculations confirmed, at least qualitatively, that this state was not simply a random artefact, but a reproducible feature during the heat induced switching in GdFeCo. Further investigations into the effect on the switching time of each of the sublattices, and of the physical properties of the model, provided evidence that this effect was an exchange driven phenomenon.

The previous experimental results of all-optical magnetisation control on thin films of GdFeCo (Ref. [17]) were considered in this thesis. In particular, the role of the field arising from the IFE was studied in the atomistic model. A systematic study showed that, in fact, no reversing field was required when using linearly polarised laser light. This suggested that the heat from the laser plays the main role in switching on this timescale. This conclusion has been further supported by recent experimental work, showing that the all-optical reversal using circularly polarised light, was in fact the heat induced mechanism presented here. The control of the magnetisation was explained via a magnetic circular dichroic effect [27]. The heat induced reversal process has also been confirmed experimentally by collaborating groups on thin films and microstructures of GdFeCo. Atomistic model and experimental results also confirm that, on this timescale, the compensation point plays no role in the reversal mechanism.

The atomistic model was also used to predict that no reversal occurs when the two sublattices of the TM-RE system demagnetise on the same timescale. Furthermore, it was used to predict the dependence of the reversal probability as a function of the strength of the anisotropy constant and applied field. The prediction that very high anisotropy values and opposing magnetic fields are required to prevent reversal, provides further evidence of the exchange origin of the reversal mechanism.

The prediction of the exchange origin of heat induced reversal has been supported by analysis

from a Landau-Lifshitz-Bloch equation for a ferrimagnet. The analysis shows that the reversal arises because of the excitation of a localised exchange mode, whereby angular momentum is transferred from an unstable longitudinal mode to the transverse mode. The transfer provides a *kick* to induce the precession associated with the antiferromagnetic exchange mode.

7.1 Further Work

The manipulation of TM-RE ferrimagnetic materials on the femtosecond timescale has shown that, because of the complex exchange interactions, unexpected dynamic behaviour can occur. The timescale of the reversal process could be a useful characteristic in terms of magnetic recording, though many scientific challenges remain. A number of goals that could improve upon the work presented here are listed below and expanded upon in detail in the subsequent text:

1. Parameterisation of the model based on an ab-initio approach.
2. Studies into the size dependence of switching.
3. A further study into the generality of the heat induced reversal shown in chapter 6.
4. Calculations of spinwave dispersion relations, spin-spin structure factors and dynamic structure factors.

Though the atomistic model of ferrimagnetic GdFeCo was successful in predicting the heat induced switching mechanism, it remains a simple nearest neighbour model that may lack some of the underlying physics of the material. Ab-initio exchange parameters of GdFeCo may show that the exchange interactions are more complex than was assumed in this thesis. Such different interactions could give more insight into further experimental observations. Any ab-initio model would have to determine which parts of the exchange matrix are important, for example, Dzyaloshinskii-Moriya interactions or anti-symmetric exchange contributions. Furthermore, if one were to consider creating nanometre sized arrays of TM-RE particles, the physical properties could also change, due to, for example, surface effects. The model developed here is parameterised on bulk observations, it would not be unreasonable to expect this parameterisation to be invalid for very small system sizes.

Although strong experimental and numerical evidence has been provided for the heat induced reversal mechanism in GdFeCo, the generality of this phenomena remains unclear. We believe that the switching mechanism presented here to be a general phenomena of TM-RE ferrimagnets. The mechanism presented in chapter 6 relied on differential demagnetisation of the two species and antiferromagnetic coupling. To this end, we believe that synthetic materials could be engineered to show the same mechanism of reversal. The timescale of demagnetisation could, in principle, be controlled by the thermal bath coupling constant or the magnetic moment. Spacer layers could be introduced at sample interfaces to modify the exchange interaction between materials, to give rise to AFM coupling.

The nature of the generation of spin waves after femtosecond heating was not addressed in this thesis. The presence of antiferromagnetically coupled sublattices means that there should be both optical and acoustic spinwave branches [135]. The role of the populations of high k -vector spinwaves, responsible for decreasing magnetic order is not clear and could provide further insights into the reversal process. Dispersion relations in the atomistic model can be calculated via dynamic structure factors (DSF) [125, 136], calculated by time and spatial Fourier transforms of the spin space. Along with structure factors, the spin-spin correlation function can be readily obtained via inverse Fourier transform and could provide insights into the localisation of the exchange mode.

Appendix A

Experimental Details of Measuring Time-Resolved Magnetisation Dynamics in NiFe

The measurements described in chapter 5, performed by I. Radu, were performed in a stroboscopic pump-and-probe mode, where the metallic magnets (the pure elements and alloys) were excited with 60fs laser pulses at a photon energy of 1.55eV. Subsequent magnetisation dynamics were probed by measuring the XMCD changes with circularly polarised 100fs X-ray pulses [114] at the Ni L₃ absorption edge (photon energy 853eV), the Fe L₃ edge (707eV) or at the Gd M₅ edge (1189eV). At these energies the dynamics of the 3d magnetic moment of Ni, Fe and the 4f moment of Gd, respectively, are probed. The laser-induced XMCD changes were measured in transmission for opposite orientations of the magnetic field (± 0.2 T for NiFe and ± 0.5 T for Gd(FeCo), oriented along the X-ray propagating direction) using an avalanche photodiode and a gated boxcar detection. The XMCD measurements were performed at a sample temperature of 300K. The typical incident laser fluence was $20\text{mJ}/\text{cm}^2$ for NiFe and $5.5\text{mJ}/\text{cm}^2$ for Gd(FeCo). The investigated Fe, Ni₅₀Fe₅₀, Ni₈₀Fe₂₀ (all 20 nm thick) and Gd₂₅Fe₆₆Co₉ (30 nm thick) samples were deposited by magnetron sputtering on Al foils and protected against oxidation using buffer and capping layers of Pt and Si₃N₄, respectively. The Fe and NiFe films are poly-crystalline with an in-plane magnetisation orientation while Gd(FeCo) is amorphous with an out-of-plane magnetic anisotropy.

The NiFe samples were characterized by static XAS/XMCD measurements at the Fe and Ni L_{3,2}-edges. Both NiFe alloys are samples are ferromagnetic and show in-plane anisotropy, as confirmed by element-specific hysteresis curves. The XAS/XMCD spectra of the NiFe alloys are shown in figure A.1.

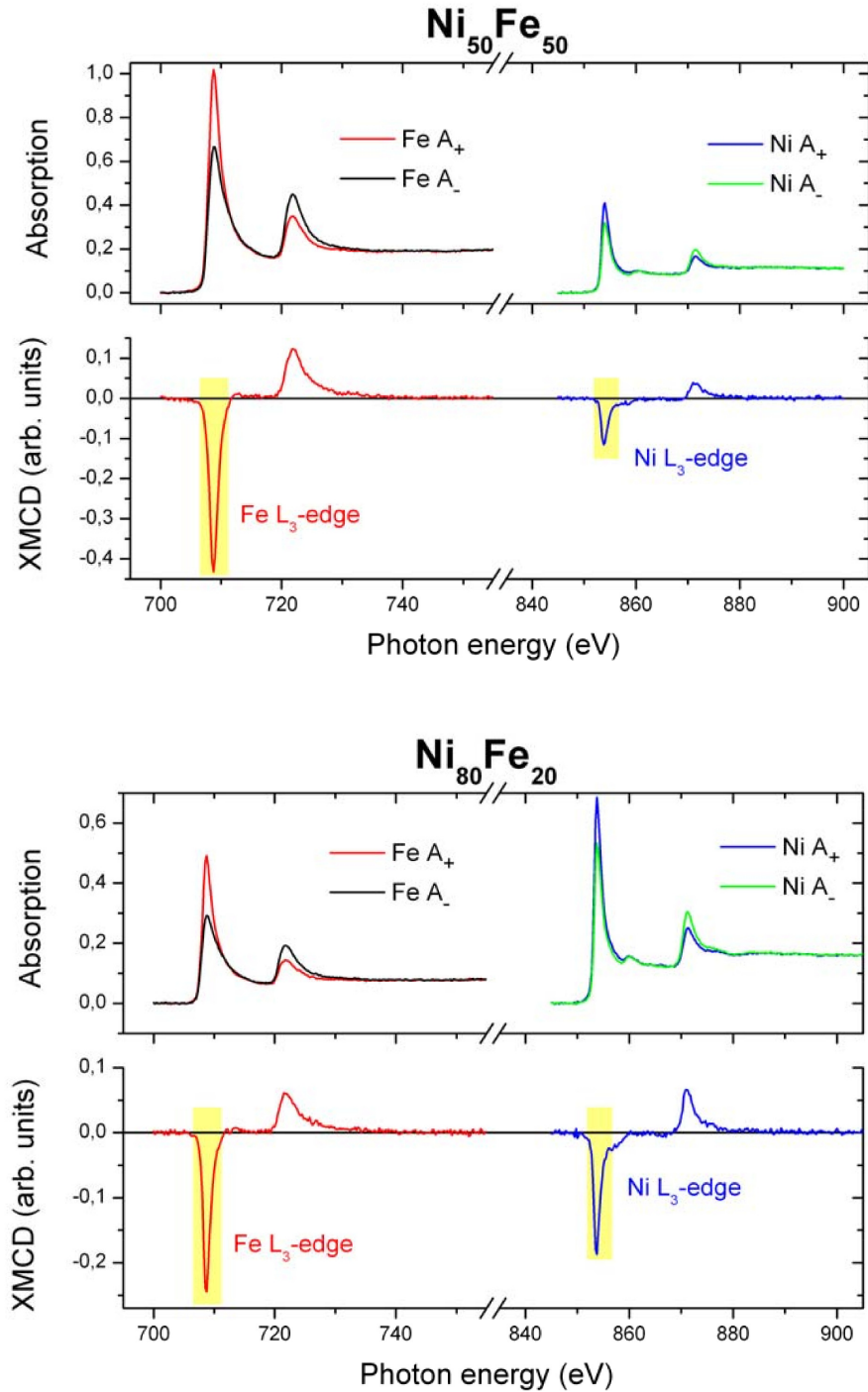


Fig. A.1: The absorption spectra of $Ni_{50}Fe_{50}$ (a) and $Ni_{80}Fe_{20}$ (b) were measured using circularly polarised X-rays at the Ni and Fe $L_{3,2}$ -edges, for opposite orientations of the applied external magnetic field of 0.2 T along the X-ray propagation direction (A_+ and A_-). The resulting XMCD spectra are plotted in the lower panels. The yellow regions indicate the absorption edges at which the time-resolved XMCD measurements were performed. Measurements were performed by I. Radu and are published in Ref. [116].

Appendix B

Experimental details of Time-Resolved XMCD Measurements on GdFeCo

The measurements described in section 6.2 of chapter 6 were performed by I. Radu. The investigated sample was a 30 nm $\text{Gd}_{25}\text{Fe}_{65.6}\text{Co}_{9.4}$ thin film deposited by magnetron sputtering on a free-standing Al foil of 500 nm thickness. To avoid oxidation of the GdFeCo layer, Si_3Ni_4 films of 100 nm and 60 nm thickness were used as buffer and capping layers, respectively. The out-of-plane magnetic anisotropy of GdFeCo samples has been deduced from the measured element-specific hysteresis curves. The measured hysteresis curves show a ferromagnetic alignment of Co and Fe and antiferromagnetic alignment of Fe and Gd magnetic moments as shown in figure B.1. Soft X-ray light covering the $L_{2,3}$ absorption edges of Fe and Co and the $M_{4,5}$ edges of Gd has been employed to measure the magnetic response of the elements in the composite alloy. The XMCD spectra of Fe and Gd are shown in figure 1.18. Figure B.1 shows results of static XMCD measurements as a function of magnetic field measured below and above T_M . The XMCD signals at the Fe and Gd edges reveal the respective sign change of the hysteresis loops on heating the alloy above T_M . Therefore, the data in figure B.1 confirm that XMCD serves as an element-specific probe of spins in this RE-TM alloy.

To observe the time-resolved sublattice magnetisations, the sample was excited with 60fs laser pulses at a photon energy of 1.55eV. The binding energy of the occupied spin-up 4f state is around 9eV. Subsequent laser-induced dynamics were probed by measuring the magnetisation-dependent absorption of circularly polarised 100 fs X-ray pulses at the Fe L_3 absorption edge (707 eV photon energy) and at the Gd M_5 edge (1189 eV photon energy). Figure B.2 shows a schematic of the pumping and probing mechanism in the electronic structure of the GdFeCo alloy. By varying the delay between the pump and probe pulses the time resolution was obtained for each element. The system was reset to the initial state after each measurement by the applied magnetic field. The laser induced changes of X-ray transmission were measured for opposite orientations of the magnetic field, thus giving the resulting XMCD signal. The typical size of the laser beam was $0.8 \times 0.4 \text{mm}^2$ giving an incident laser fluence of $4.4 \text{mJ}/\text{cm}^2$. The XMCD measurements were performed at a sample temperature of 83 K, below T_M of 250 K.

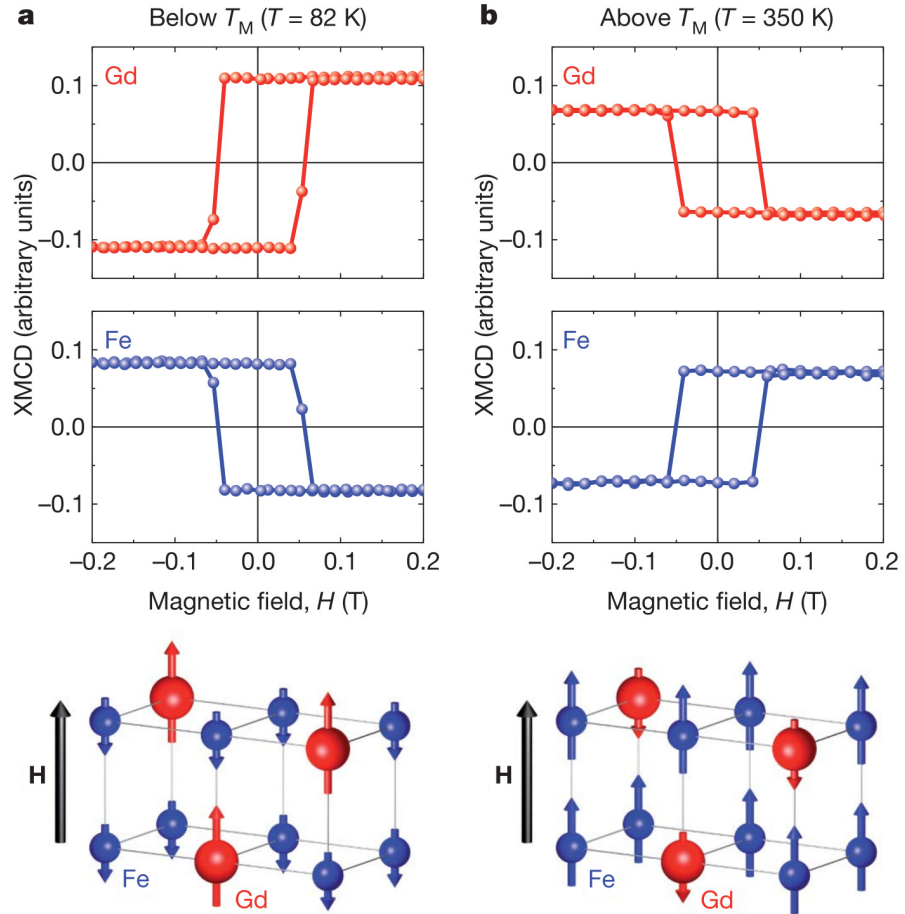


Fig. B.1: Ferrimagnetic alignment of the Fe and Gd magnetic moments as measured by element-specific XMCD hysteresis. The hysteresis curves (a and b) show XMCD signals measured at the Fe and Gd absorption edges as a function of applied magnetic field. Panel a) is measured below the magnetisation compensation temperature and b) is measured above. This demonstrates the ferrimagnetic alignment as the constituent magnetic elements align dominant sublattice to the applied field as shown schematically below. Measurements performed by I. Radu, figure published in Ref. [24].

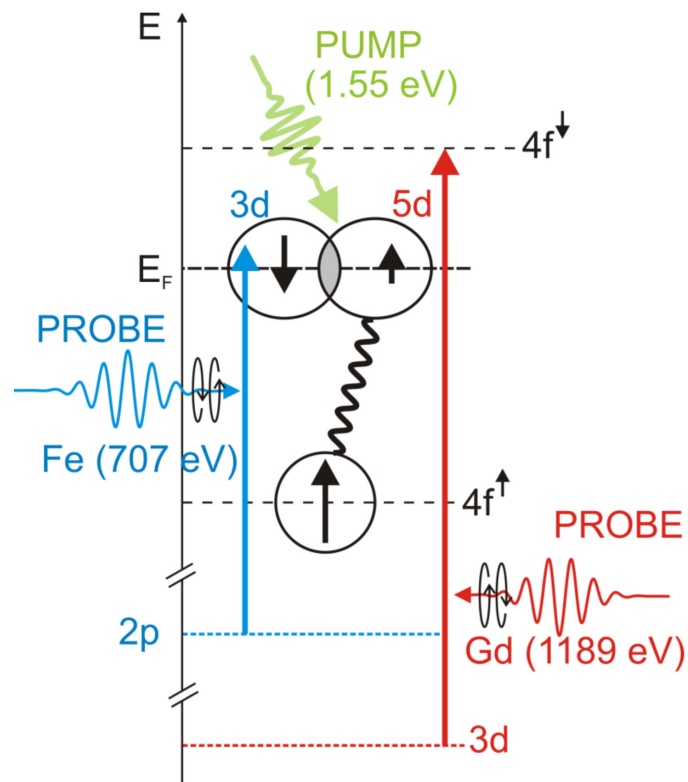


Fig. B.2: Schematic of the pumping and probing mechanism in schematic electronic structure of GdFeCo. The pump excites the Fe 3d and Gd 5d6s bands with 60fs laser pulses at a photon energy of 1.55eV. The probe then measures the L_3 and M_5 edges of Fe and Gd respectively. Figure from Ref. [24].

Appendix C

Details of Measurements on Microstructures of GdFeCo

The measurements of the microstructures of GdFeCo as discussed in chapter 6 were performed by the group of F. Nolting from the Paul Scherrer Institute, Switzerland. The structures shown in chapter 6 were produced via a *lift-off* technique [137]. A polymethylmethacrylate resist is first patterned with an electron beam writer on a glass/Ti(2 nm)/Pt(8 nm) substrate. This pattern was then transferred via lift-off after deposition by magnetron sputtering of the magnetic multilayer AlTi(10 nm)/Si₃N₄(5 nm)/Gd₂₄Fe_{66.6}Co_{9.4}(20 nm)/Si₃N₄(3 nm), resulting in isolated magnetic structures [138]. Unstructured areas of several 100 μm, quasi-continuous films, and arrays of squares and disks down to 1 μm were fabricated onto the same sample. In the work in chapter 6, 2 μm microstructures were focused on, however reversal was seen in the continuous part and in the structures down to 1 μm [126].

The magnetisation direction of the microstructures was measured with a Photo-emission Electron-Microscope (PEEM) at the SIM beamline [139] of the Swiss Light Source at the Paul Scherrer Institut (PSI) employing the XMCD effect. The 2 μm microstructures were then excited with linearly polarised laser light with a spot size of around 30 × 100 μm (full-width at half maximum), this was so that several structures could be excited simultaneously. The distance between the structures is as large as their diameter, thereby reducing dipolar interactions between the structures to a negligible degree. No correlations between the magnetisation directions of neighbouring structures were observed. The measurements on the microstructures were performed by the group of Frithjof Nolting from PSI.

Appendix D

Derivation of the Correlator

In section 2.2.1 we wrote the Landau-Lifshitz-Gilbert equation with an added noise term as a standard Langevin equation 2.2.11. The interpretation of the stochastic integrals is an important aspect of this type of differential equation, which historically has prompted a lot of debate [140]. The two interpretations of stochastic calculus discussed in Ref. [140] are referred to as Ito and Stratonovich. It is generally accepted that the Stratonovich solution gives physically more realistic results, however in Ref. [141], Berkov and Gorn showed that both interpretations lead to physically correct results. In this thesis we interpret the stochastic integrals in the Stratonovich form, the form widely used in the literature [91, 142]. The point at which one chooses the point to integrate the stochastic equations determines whether one is dealing with the Ito or Stratonovich calculus. In the Ito interpretation a drift term arises from the equations. The choice of how to define the integral determines the use of Ito or Stratonovich. A thorough review of the use of the stochastic form of the LLG equation can be found in the thesis of W. Scholz [143].

Let us consider the system of Langevin equations given by expression 2.2.11. In the Stratonovich interpretation the time evolution, $P(\mathbf{S}, t)$, of the non-equilibrium probability distribution of those Langevin equations is given by the Fokker-Planck [144] equation:

$$\begin{aligned} \frac{\partial P}{\partial t} = & - \frac{\partial}{\partial S_{i,\Gamma}} \left[\left(A_{i,\Gamma} + DB_{i,\Delta\Theta} \frac{\partial B_{i,\Gamma\Theta}}{\partial S_{i,\Delta}} \right) P \right] \\ & \frac{\partial^2}{\partial S_{i,\Gamma} \partial S_{i,\Theta}} [(DB_{i,\Gamma\Theta} B_{i,\Delta,\Theta}) P]. \end{aligned} \quad (\text{D.0.1})$$

Where D is the strength of the noise in the Langevin equation defined by:

$$\langle \zeta_{i,a}(t) \zeta_{j,b}(t') \rangle = 2D \delta_{ij} \delta_{ab} \delta(t - t') \quad (\text{D.0.2})$$

The following analysis can therefore be used to determine the constant D , based on the physical properties of the system. To do this the Fokker Planck equation D.0.1 must be transformed to a continuity equation for the probability by taking $S_{i,\Delta}$ derivatives of the

second term on the right hand side.

$$\frac{\partial P}{\partial t} = -\frac{\partial}{\partial S_{i,\Gamma}} \left[\left(A_{i,\Gamma} - DB_{i,\Gamma\Delta} \frac{\partial B_{i,\Gamma\Theta}}{\partial S_{i,\Delta}} - DB_{i,\Gamma\Theta} B_{i,\Delta\Theta} \frac{\partial}{\partial S_{i,\Delta}} \right) P \right]. \quad (\text{D.0.3})$$

Using the identity 2.2.10 rewritten in the form:

$$\begin{aligned} B_{i,\Gamma\Theta}(S_i, t) &= -\gamma'_i \epsilon_{\Gamma\Delta\Theta} S_{i,\Gamma} - \gamma'_i \lambda_i (S_{i,\Gamma} S_{i,\Theta} - \delta_{i,\Gamma\Theta} S_{i,\Gamma} S_{i,\Gamma}) \\ &\quad - \gamma'_i \epsilon_{\Gamma\Delta\Theta} S_{i,\Gamma} - \gamma'_i \lambda_i (\delta_{i,\Gamma\Xi} \delta_{i,\Delta\Theta} - \delta_{i,\Gamma\Theta} \delta_{i,\Delta\Xi}) S_{i,\Delta} S_{i,\Xi}, \end{aligned} \quad (\text{D.0.4})$$

the derivatives can be written:

$$\begin{aligned} \frac{\partial B_{i,\Gamma\Theta}}{\partial S_{i,\Delta}} &= -\gamma'_i \epsilon_{\Gamma\Delta\Theta} - \gamma'_i \lambda_i (\delta_{i,\Gamma\Delta} S_{i,\Theta} \delta_{i,\Delta\Theta} S_{i,\Gamma} - 2\delta_{i,\Gamma\Theta} S_{i,\Delta}) \\ \frac{\partial B_{i,\Delta\Theta}}{\partial S_{i,\Delta}} &= -\gamma'_i \epsilon_{\Delta\Delta\Theta} - \gamma'_i \lambda_i (\delta_{i,\Delta\Delta} S_{i,\Theta} \delta_{i,\Delta\Theta} S_{i,\Delta} - 2S_{i,\Theta}) (2\gamma'_i \lambda_i S_{i,\Gamma}) \\ &= -2\gamma'^2_i \lambda_i^2 (S_{i,\Delta} S_{i,\Theta} S_{i,\Theta} - \delta_{i,\Gamma\Theta} S_{i,\Delta}^2 S_{i,\Theta}) \\ &= 0. \end{aligned} \quad (\text{D.0.5})$$

We can make a similar expansion for the third term on the right hand side of equation D.0.3:

$$\begin{aligned} B_{i,\Gamma\Theta} B_{i,\Delta\Theta} \frac{\partial P}{\partial S_{i,\Delta}} &= \gamma'^2_i \left[-\epsilon_{\Gamma\Delta\Theta} S_{i,\Delta} - \lambda_i (S_{i,\Gamma} S_{i,\Theta} - \delta_{i,\Gamma\Theta} S_{i,\Delta} S_{i,\Delta}) \right] \\ &\quad \cdot \left[-\epsilon_{\Delta\Gamma\Theta} S_{i,\Gamma} - \lambda_i (S_{i,\Delta\Theta} - \delta_{i,\Delta\Theta} S_{i,\Delta} S_{i,\Delta}) \right] \frac{\partial P}{\partial S_{i,\Delta}} \\ &= \gamma'^2_i \left[(\delta_{i,\Gamma\Delta} \delta_{i,\Lambda\Gamma} - \delta_{i,\Gamma\Gamma} \delta_{i,\Delta\Lambda}) S_{i,\Lambda} S_{i,\Gamma} \right. \\ &\quad + \lambda_i (-S_{i,\Delta} S_{i,\Delta} \epsilon_{\Gamma\Gamma\Delta} S_{i,\Gamma} + \epsilon_{\Delta\Gamma\Theta} S_{i,\Gamma} S_{i,\Gamma} S_{i,\Theta} \\ &\quad - S_{i,\Delta} S_{i,\Delta} \epsilon_{\Gamma\Lambda\Delta} + \epsilon_{\Gamma\Lambda\Theta} S_{i,\Lambda} S_{i,\Delta} S_{i,\Theta}) \\ &\quad + \lambda_i^2 (S_{i,\Delta} S_{i,\Delta} S_{i,\Delta} S_{i,\Delta} \delta_{i,\Gamma\Theta} \delta_{i,\Delta\Theta} - S_{i,\Delta} S_{i,\Delta} (\delta_{i,\Delta\Theta} S_{i,\Gamma} S_{i,\Theta} \\ &\quad + \delta_{i,\Gamma\Theta} S_{i,\Delta} S_{i,\Theta}) + S_{i,\Delta} S_{i,\Delta} S_{i,\Gamma} S_{i,\Delta}) \left. \right] \frac{\partial P}{\partial S_{i,\Delta}} \\ &= \gamma'^2_i \left[\delta_{i,\Gamma\Delta} S_{i,\Delta} S_{i,\Delta} - S_{i,\Gamma} S_{i,\Delta} \right. \\ &\quad + \lambda_i (-S_{i,\Delta} S_{i,\Delta} \epsilon_{\Delta\Gamma\Gamma} S_{i,\Gamma} - S_{i,\Delta} S_{i,\Delta} \epsilon_{\Gamma\Lambda\Delta} S_{i,\Lambda}) \\ &\quad \left. + \lambda_i^2 (S_{i,\Delta} S_{i,\Delta} S_{i,\Delta} S_{i,\Delta} \delta_{i,\Delta\Gamma} - S_{i,\Delta} S_{i,\Delta} S_{i,\Gamma} S_{i,\Delta}) \right] \frac{\partial P}{\partial S_{i,\Delta}} \\ &= \gamma'^2_i \left[(S_{i,\Delta} S_{i,\Delta} - S_{i,\Gamma} S_{i,\Delta}) + \lambda_i^2 S_{i,\Delta} S_{i,\Delta} (S_{i,\Delta} S_{i,\Delta} \delta_{i,\Delta\Gamma} - S_{i,\Gamma} S_{i,\Delta}) \right] \frac{\partial P}{\partial S_{i,\Delta}} \\ &= \gamma'^2_i \left[(1 + \lambda_i^2) (S_{i,\Delta} S_{i,\Delta} \delta_{i,\Delta\Gamma} - S_{i,\Gamma} S_{i,\Delta}) \right] \frac{\partial P}{\partial S_{i,\Delta}}. \end{aligned} \quad (\text{D.0.6})$$

Notice that the right hand bracket of equation D.0.6 is in a similar form as equation 2.2.10,

representing a triple cross product, we can thus write equation D.0.6 as:

$$-\gamma'_i{}^2(1 + \lambda_i^2) \left[\mathbf{S}_i \times \mathbf{S}_i \times \frac{\partial P}{\partial \mathbf{S}_i} \right]. \quad (\text{D.0.7})$$

If we then collect the terms of our Fokker-Planck equation and include the expanded A and B terms from equations 2.2.8 and 2.2.10, our resulting equation is:

$$\begin{aligned} \frac{\partial P}{\partial t} = & - \frac{\partial}{\partial \mathbf{S}_i} \cdot \left(\left[-\gamma'_i \mathbf{S}_i \times \mathbf{H}_{\text{eff}} - \gamma' \lambda_i \mathbf{S}_i \times \mathbf{S}_i \times \mathbf{H}_{\text{eff}} - \right. \right. \\ & \left. \left. D\gamma'_i{}^2(1 + \lambda_i^2) \mathbf{S}_i \times \mathbf{S}_i \times \frac{\partial}{\partial \mathbf{S}_i} \right] P \right). \end{aligned} \quad (\text{D.0.8})$$

If we introduce the so-called Néel free diffusion time:

$$\frac{1}{\tau_N} = 2D\gamma'_i{}^2(1 + \lambda_i^2), \quad (\text{D.0.9})$$

and constrain the system to ensure that the stationary properties of our stochastic Landau-Lifshitz-Gilbert equation coincide with the appropriate thermal equilibrium properties, we can derive an expression for D . The stationary solution of the Fokker-Planck equation we write as P_0 whose time derivative is zero and we force to be a Boltzmann distribution:

$$P_0(\mathbf{S}) \propto \exp(-\beta\mathcal{H}(\mathbf{S})). \quad (\text{D.0.10})$$

Recalling the fact that $-\frac{\partial \mathcal{H}}{\partial \mathbf{S}} = \mathbf{H}_{\text{eff}}$:

$$\frac{\partial P_0}{\partial \mathbf{S}} \propto \beta \mathbf{H}_{\text{eff}} \exp(-\beta\mathcal{H}). \quad (\text{D.0.11})$$

Substituting P_0 and $\frac{\partial P_0}{\partial \mathbf{S}}$ throughout our Fokker-Planck equation D.0.8 and noting that $\frac{\partial}{\partial \mathbf{S}} \cdot \mathbf{S} \times \mathbf{H} = 0$ our stationary Fokker-Planck equation can be written:

$$-\frac{\partial}{\partial \mathbf{S}_i} \cdot \left(-\gamma'_i \lambda_i \mathbf{S}_i \times \mathbf{S}_i \times \mathbf{H}_{\text{eff}} \right) P_0 - \frac{\partial}{\partial \mathbf{S}_i} \left(\frac{1}{2\tau_N} \mathbf{S}_i \times \mathbf{S}_i \times \frac{\partial P_0}{\partial \mathbf{S}_i} \right) = 0. \quad (\text{D.0.12})$$

Thus one arrives at an expression for the Néel free diffusion time:

$$\begin{aligned} \gamma'_i \lambda_i \mathbf{S}_i \times \mathbf{S}_i \times \mathbf{H}_{\text{eff}} &= \frac{\beta}{2\tau_N} \mathbf{S}_i \times \mathbf{S}_i \times \mathbf{H}_{\text{eff}} \\ \gamma'_i \lambda_i &= \frac{\beta}{2\tau_N}. \end{aligned} \quad (\text{D.0.13})$$

Equating equations D.0.13 and D.0.9 and recalling that $\gamma'_i = \frac{\gamma_i}{(1+\lambda_i)\mu_i}$, one arrives at an expression for the strength of the noise, defined in equation D.0.2:

$$D = \frac{\lambda_i \mu_i k_B T}{\gamma_i}. \quad (\text{D.0.14})$$

The full definition of our correlator is then given by:

$$\langle \zeta_{i,a}(t) \zeta_{j,\beta}(t') \rangle = \frac{2\lambda_i k_B T \mu_i}{\gamma_i} \delta_{ij} \delta_{\alpha\beta} (t - t'). \quad (\text{D.0.15})$$

Appendix E

Table of Parameters Used for GdFeCo Simulations

The parameters used to calculate the initial magnetisation curves for comparison to XMCD experimental measurements for figures 3.8, 3.9 and 3.10 (unless otherwise stated) are shown in the table below.

Parameter	
$\mu_{\text{Gd}} [\mu_{\text{B}}]$	7.55
$\mu_{\text{Fe}} [\mu_{\text{B}}]$	2.217
$\gamma_{\text{Gd}} [\text{T}^{-1}\text{S}^{-1}]$	1.76×10^{11}
$\gamma_{\text{Fe}} [\text{T}^{-1}\text{S}^{-1}]$	1.76×10^{11}
$J_{\text{Fe-Fe}} [\text{J}]$	4.526×10^{-21}
$J_{\text{Fe-Gd}} [\text{J}]$	-1.09×10^{-21}
$J_{\text{Gd-Gd}} [\text{J}]$	1.26×10^{-21}
$K_{\text{Gd}} [\text{J}]$	0.807243×10^{-23}
$K_{\text{Fe}} [\text{J}]$	0.807243×10^{-23}
λ_{Gd}	1
λ_{Fe}	1
Crystal Structure	fcc
System Size	$30 \times 30 \times 30$ unit cells

Table E.1: *Physical parameters for GdFeCo in the atomistic model. The initial exchange parameters for the Fe-Fe interactions corresponds to the Curie temperature of bulk Fe. For the Gd-Gd interaction, the value used corresponds to the Curie temperature for bulk Gd. The magnetic moments were taken from the literature. The coupling constants (λ) were set to a high value as the parameters were used to calculate equilibrium properties. The gyromagnetic ratios were assumed to be independent of species in the first instance.*

For all other figures in chapter 3, the same parameters were the same as those shown in table E.1 except for the Fe-Fe exchange parameter used was now equal to 2.835×10^{-21} J and the damping constant was 0.1 except where explicitly stated.

For the calculations of GdFeCo in chapters 4 and 6, the parameters used differ slightly from those in table E.1 and are shown below in table E.2 except where explicitly stated in the text.

Parameter	
$\mu_{\text{Gd}} [\mu_{\text{B}}]$	7.63
$\mu_{\text{Fe}} [\mu_{\text{B}}]$	1.92
$\gamma_{\text{Gd}} [\text{T}^{-1}\text{S}^{-1}]$	1.76×10^{11}
$\gamma_{\text{Fe}} [\text{T}^{-1}\text{S}^{-1}]$	1.76×10^{11}
$J_{\text{Fe-Fe}} [\text{J}]$	2.835×10^{-21}
$J_{\text{Fe-Gd}} [\text{J}]$	-1.09×10^{-21}
$J_{\text{Gd-Gd}} [\text{J}]$	1.26×10^{-21}
$K_{\text{Gd}} [\text{J}]$	0.807243×10^{-23}
$K_{\text{Fe}} [\text{J}]$	0.807243×10^{-23}
λ_{Gd}	0.02
λ_{Fe}	0.02
Crystal Structure	fcc

Table E.2: *Physical parameters for GdFeCo in the atomistic model for dynamic calculations. The exchange parameters give the approximately correct temperature dependent behaviour, Curie temperature and compensation point as measured from XMCD and hysteresis. The lower value of the coupling constant (compared to table E.1 is within usual limits and gives qualitative agreement to experimental observations of the demagnetisation time.*

List of Symbols

A	Exchange stiffness
A	Affinity
\mathbf{B}	Applied field
C	Constant multiplying fitting function
C_e	Electron specific heat capacity
C_l	Phonon/lattice specific heat capacity
c_0	Material constant related to demagnetisation
D	Strength of correlator in noise process
e	Electron charge
\mathbf{e}_i	Vector component i of unit vector \mathbf{e}
E	Energy
\mathcal{F}	Free energy
g	g -factor
G	Gibb's free energy
\hbar	Plancks constant
h^{\parallel}	Longitudinal component of field in the ferrimagnetic LLB model
\mathcal{H}	Hamiltonian
$\mathcal{H}_{\text{Ising}}$	Ising Hamiltonian
\mathcal{H}^{MFA}	Hamiltonian in the mean field approximation
H_c	Coercive field
\bar{H}_c	Average coercive field
H_{det}	Deterministic part of effective field (no thermal term)
H_e	Mean field
H^{eff}	Effective field without thermal term
H^{th}	Thermal part of field
H'_i	Applied and anisotropy field acting on sub-lattice i
J_{ij}	Isotropic exchange integral between spins i and j
J	Total angular momentum
$J_{\text{TM-RE}}$	Transition metal-rare earth exchange
$J_{\text{TM-TM}}$	Transition metal-transition metal exchange
$J_{\text{RE-RE}}$	Rare earth-rare earth exchange
$J_{\text{TM-RE,max}}$	Maximum transition metal-rare earth exchange in the mean field
$J_{\text{TM-TM,max}}$	Maximum transition metal-transition metal exchange in the mean field

$J_{\text{RE-RE,max}}$	Maximum rare earth-rare earth exchange in the mean field
J_z	Z-component of total angular momentum
K_e	Electron thermal conductivity
K_l	Phonon/lattice thermal conductivity
K_i	Lowest order uniaxial anisotropy constant for spin i
K_1	Lowest order bulk anisotropy constant
K_2	Second order bulk anisotropy constant
K_1^c	Lowest order cubic anisotropy constant
K_2^c	Second order cubic anisotropy constant
\mathbf{L}	Mechanical angular momentum
L	Linear polarisation of light
m	Orbital angular momentum quantum number
m_e	Electron mass
m_e	Reduced equilibrium spin polarisation (reduced magnetisation)
\mathbf{m}	Reduced magnetisation vector
M	Scalar magnetisation
M^+	Magnetisation up
M^-	Magnetisation down
N	Number of spins
N_{TM}	Number of transitions metal spins
N_{RE}	Number of rare earth spins
\mathcal{N}	Number of spins
\mathbf{n}	Easy axis unit vector
P	Pressure
P_{FMR}	Power absorbed during ferromagnetic resonance experiment
q	Transition metal concentration
\mathbf{Q}_e	Electron heat flux vector
\mathbf{Q}_l	Phonon/lattice heat flux vector
\mathbf{r}	Spatial coordinate
S^\pm	Transverse spin components in rotating frame about z-axis
S_{hom}^\pm	Homogeneous part of S^\pm
S	Quantum spin number
\mathbf{S}	Classical spin vector
$S(\mathbf{r}, t)$	Volumetric laser heat source
t_c	Correlation time
t_{max}	Maximum number of timesteps
\mathbf{T}	Torque
T_C	Curie temperature
T_{eff}	Effective spin temperature
T_e	Electron temperature
T_e^{max}	Maximum electron temperature
T_l	Phonon/lattice temperature

T_M	Magnetisation compensation temperature
T_{start}	Starting temperature
\mathbf{u}	Unit vector in the direction of the total magnetisation
u^\pm	Transverse components of \mathbf{u} in rotating frame about z-axis
u_{hom}^\pm	Homogeneous part of u^+
V	Volume
x	Rare earth concentration
x_c	Critical concentration below which no compensation point exists
z	Number of nearest neighbours
\mathcal{Z}	Partition function
α_\perp	Transverse damping parameter
α_\parallel	Longitudinal damping parameter
γ	Gyromagnetic ratio for an isolated electron
γ_i	Relative (to γ) gyromagnetic ratio of species i
γ_{eff}	Effective gyromagnetic ratio
γ'	Gyroscopic factor for coupled ferrimagnet
Γ_{ij}	Relaxation rate parameters
Δ_c	Relative error in the coercivity measurement
ϵ	Levi-Civita symbol
ζ	Noise process
η	Coupling of bath variable to spin
θ	Angle from easy axis
ι	General parameters defining state of a system
κ	Mean field constant
λ	Thermal coupling/intrinsic damping parameter
λ_L	Effective damping parameter
Λ	The lattice
Λ_{ij}	Rate parameters of the LLB equation for a ferrimagnet
μ	Magnetic moment
ξ	$\mu H/k_B T$
Π	$\ln(\sinh(\xi)/\xi)$
ρ	Square of the magnitude of the transverse magnetisation components
σ	Spin polarisation
σ_c	Standard deviation in the coercivity measurement
σ^+	Right-handed Circularly Polarised Light
σ^-	Left-handed Circularly Polarised Light
$\underline{\sigma}$	Spin state
σ_e	Equilibrium spin polarisation
τ	Transverse relaxation time
τ_d	Characteristic demagnetisation time
τ_e	Electron energy relaxation time
τ_e	Equilibrium projection of one sublattice onto another

τ_R	Projection of rare earth sublattice onto transition metal
τ_T	Projection of transition metal sublattice onto rare earth
τ_{int}	Integral relaxation time
τ_l	Phonon energy relaxation time
φ	Single particle spatial wavefunction
Φ	Wavefunction
$\tilde{\chi}_{\parallel,\perp}$	Reduced parallel or perpendicular susceptibility
χ_i	Spin part of electron wavefunction
ψ_i	Spin dependent electron wavefunction
ω	Frequency
ω_0	Resonance frequency
Ω	Precession frequency of antiferromagnetic exchange mode

List of Abbreviations

AFM	Antiferromagnetic
ASD	Atomistic Spin Dynamics
bcc	Body-Centred Cubic
CCD	Charged Coupled Device
CPA	Coherent Potential Approximation
DFT	Density Functional Theory
DM	Dzyaloshinskii-Moriya
DSF	Dynamic Structure Factor
fcc	Face-Centred Cubic
FLLB	Ferrimagnetic Landau-Lifshitz-Bloch
FMR	Ferromagnetic Resonance
FWHM	Full Width Half Maximum
HAMR	Heat Assisted Magnetic Recording
IFE	Inverse Faraday Effect
IRT	Integral Relaxation Time
KKR	Korringa-Kohn-Rostoker Approximation
LLB	Landau-Lifshitz-Bloch
LLG	Landau-Lifshitz-Gilbert
MFA	Mean Field Approximation
PEEM	Photo-emission Electron Microscope
PSI	Paul Scherrer Institute
RKKY	Ruderman-Kittel-Kasuya-Yosida
TM-RE	Transition Metal-Rare Earth
TTM	Two Temperature Model
XAS	X-ray Absorption Spectroscopy
XMCD	X-ray Magnetic Circular Dichroism

References

- [1] M. Kryder, E. Gage, T. McDaniel, W. Challener, R. Rottmayer, and M. Erden, “Heat Assisted Magnetic Recording,” *Proceedings of the IEEE*, vol. 96, pp. 1810–1835, Nov. 2008.
- [2] M. El-Hilo, “Time-dependent coercivity in particulate recording media,” *Journal of Magnetism and Magnetic Materials*, vol. 272-276, pp. 1700–1702, May 2004.
- [3] M. El-Hilo, A. de Witte, K. O’Grady, and R. Chantrell, “The sweep rate dependence of coercivity in recording media,” *Journal of Magnetism and Magnetic Materials*, vol. 117, pp. L307–L310, Dec. 1992.
- [4] H. Callen and E. Callen, “The present status of the temperature dependence of magnetocrystalline anisotropy, and the power law,” *Journal of Physics and Chemistry of Solids*, vol. 27, pp. 1271–1285, Aug. 1966.
- [5] J. B. Staunton, L. Szunyogh, A. Buruzs, B. L. Gyorffy, S. Ostanin, and L. Udvardi, “Temperature dependence of magnetic anisotropy: An,” *Physical Review B*, pp. 1–13, 2006.
- [6] A. Buruzs, L. Szunyogh, L. Udvardi, P. Weinberger, and J. Staunton, “Temperature dependent magneto-crystalline anisotropy of thin films: A relativistic disordered local moment approach,” *Journal of Magnetism and Magnetic Materials*, vol. 316, pp. e371–e373, Sept. 2007.
- [7] U. Atxitia, O. Chubykalo-Fesenko, N. Kazantseva, D. Hinzke, U. Nowak, and R. W. Chantrell, “Micromagnetic modeling of laser-induced magnetization dynamics using the Landau-Lifshitz-Bloch equation,” *Applied Physics Letters*, vol. 91, no. 23, p. 232507, 2007.
- [8] J. Barker, R. F. L. Evans, R. W. Chantrell, D. Hinzke, and U. Nowak, “Atomistic spin model simulation of magnetic reversal modes near the Curie point,” *Applied Physics Letters*, vol. 97, no. 19, p. 192504, 2010.
- [9] M. Hall, “Paving the way for big hard drive capacity gains.” <http://storageeffect.media.seagate.com/2012/03/storage-effect/paving-the-way-for-big-hard-drive-capacity-gains/>. Accessed: 12/07/2012.

- [10] J. B. Staunton, S. Ostanin, S. S. A. Razee, B. L. Gyorffy, L. Szunyogh, B. Ginatempo, and E. Bruno, “Temperature Dependent Magnetic Anisotropy in Metallic Magnets from an Ab Initio Electronic Structure Theory : L1 0 -Ordered FePt,” *Physical Review Letters*, vol. 257204, no. December, pp. 1–4, 2004.
- [11] O. Mryasov, D. Hinzke, K. Guslienko, and R. Chantrell, “Temperature dependent magnetic properties of FePt: Effective spin Hamiltonian model,” *Europhysics Letters (EPL)*, vol. 69, pp. 805–811, 2005.
- [12] N. Kazantseva, D. Hinzke, U. Nowak, R. Chantrell, U. Atxitia, and O. Chubykalo-Fesenko, “Towards multiscale modeling of magnetic materials: Simulations of FePt,” *Physical Review B*, vol. 77, no. 18, p. 184428, 2008.
- [13] O. N. Mryasov, U. Nowak, K. Y. Guslienko, and R. W. Chantrell, “Temperature-dependent magnetic properties of FePt: Effective spin Hamiltonian model,” *Europhysics Letters (EPL)*, vol. 69, pp. 805–811, Mar. 2005.
- [14] D. Weller and A. Moser, “Thermal Effect Limits in Ultrahigh-Density Magnetic Recording,” *IEEE Transactions on Magnetics*, vol. 35, no. 6, pp. 4423–4439, 1999.
- [15] H. J. Richter, A. Lyberatos, U. Nowak, R. F. L. Evans, and R. W. Chantrell, “The thermodynamic limits of magnetic recording,” *Journal of Applied Physics*, vol. 111, no. 3, p. 033909, 2012.
- [16] T. Gerrits, H. A. M. Van Den Berg, J. Hohlfeld, L. Bär, and T. Rasing, “Ultrafast precessional magnetization reversal by picosecond magnetic field pulse shaping.,” *Nature*, vol. 418, pp. 509–12, Aug. 2002.
- [17] C. Stanciu, F. Hansteen, A. Kimel, A. Kirilyuk, A. Tsukamoto, A. Itoh, T. Rasing, P. Usachev, and R. Pisarev, “All-optical magnetic recording with circularly polarized light,” *Physical review letters*, vol. 99, p. 47601, July 2007.
- [18] A. Kimel, A. Kirilyuk, and T. Rasing, “Femtosecond opto-magnetism: ultrafast laser manipulation of magnetic materials,” *Laser & Photonics Review*, vol. 1, no. 3, pp. 275–287, 2007.
- [19] J. Hohlfeld, T. Gerrits, M. Bilderbeek, T. Rasing, H. Awano, and N. Ohta, “Fast magnetization reversal of GdFeCo induced by femtosecond laser pulses,” *Physical Review B*, vol. 65, p. 012413, Dec. 2001.
- [20] R. Gomez-Abal, O. Ney, and K. Satitkovitchai, “All-optical subpicosecond magnetic switching in NiO (001),” *Physical review letters*, vol. 92, p. 227402, June 2004.
- [21] C. Stanciu, F. Hansteen, A. Kimel, A. Kirilyuk, A. Tsukamoto, A. Itoh, and T. Rasing, “All-optical magnetic recording with circularly polarized light,” *Physical review letters*, vol. 99, p. 47601, July 2007.

- [22] R. Hertel, “Theory of the inverse Faraday effect in metals,” *Journal of Magnetism and Magnetic Materials*, vol. 303, pp. L1–L4, Aug. 2006.
- [23] P. Pershan, J. van der Ziel, and L. Malmstrom, “Theoretical Discussion of the Inverse Faraday Effect, Raman Scattering, and Related Phenomena,” *Physical Review*, vol. 143, pp. 574–583, Mar. 1966.
- [24] I. Radu, K. Vahaplar, C. Stamm, T. Kachel, N. Pontius, H. A. Dürr, T. A. Ostler, J. Barker, R. F. L. Evans, R. W. Chantrell, A. Tsukamoto, A. Itoh, A. Kirilyuk, T. Rasing, and A. V. Kimel, “Transient ferromagnetic-like state mediating ultrafast reversal of antiferromagnetically coupled spins,” *Nature*, vol. 472, pp. 205–8, Apr. 2011.
- [25] K. Vahaplar, A. Kalashnikova, A. Kimel, S. Gerlach, D. Hinzke, U. Nowak, R. Chantrell, A. Tsukamoto, A. Itoh, A. Kirilyuk, and T. Rasing, “All-optical magnetization reversal by circularly polarized laser pulses: Experiment and multiscale modeling,” *Physical Review B*, vol. 85, pp. 1–17, Mar. 2012.
- [26] K. Vahaplar, A. Kalashnikova, A. Kimel, D. Hinzke, U. Nowak, R. Chantrell, A. Tsukamoto, A. Itoh, A. Kirilyuk, and T. Rasing, “Ultrafast path for optical magnetization reversal via a strongly nonequilibrium state,” *Physical review letters*, vol. 103, no. 11, p. 117201, 2009.
- [27] A. Khorsand, M. Savoini, A. Kirilyuk, A. Kimel, A. Tsukamoto, A. Itoh, and T. Rasing, “Role of Magnetic Circular Dichroism in All-Optical Magnetic Recording,” *Physical Review Letters*, vol. 108, p. 127205, Mar. 2012.
- [28] S. Blundell, *Magnetism in Condensed Matter*. Oxford, England: Oxford University Press, 2009.
- [29] D. Jiles, *Introduction to Magnetism and Magnetic Materials*. London: Chapman and Hall, 1994.
- [30] K. H. J. Buschow, *Handbook of Magnetic Materials*. Amsterdam: North-Holland Pub. Co., 1991.
- [31] R. Skomski, *Simple Models of Magnetism*. Oxford, UK: Oxford University Press, 2008.
- [32] A. Sukhov, K. Usadel, and U. Nowak, “Ferromagnetic resonance in an ensemble of nanoparticles with randomly distributed anisotropy axes,” *Journal of Magnetism and Magnetic Materials*, vol. 320, pp. 31–35, Jan. 2008.
- [33] N. Kazantseva, D. Hinzke, R. W. Chantrell, and U. Nowak, “Linear and elliptical magnetization reversal close to the Curie temperature,” *EPL (Europhysics Letters)*, vol. 86, p. 27006, Apr. 2009.
- [34] U. Atxitia and O. Chubykalo-Fesenko, “Ultrafast magnetization dynamics rates within the Landau-Lifshitz-Bloch model,” *Physical Review B*, vol. 84, pp. 1–10, Oct. 2011.

- [35] R. Prange and V. Korenman, “Local-band theory of itinerant ferromagnetism. IV. Equivalent Heisenberg model,” *Physical Review B*, vol. 19, pp. 4691–4697, May 1979.
- [36] P.-W. Ma and S. L. Dudarev, “Longitudinal magnetic fluctuations in Langevin spin dynamics,” *Physical Review B*, vol. 86, p. 054416, Aug. 2012.
- [37] E. Beaurepaire, J.-C. Merle, A. Daunois, and J.-Y. Bigot, “Ultrafast Spin Dynamics in Ferromagnetic Nickel,” *Physical Review Letters*, vol. 76, pp. 4250–4253, May 1996.
- [38] B. Koopmans, G. Malinowski, F. Dalla Longa, D. Steiauf, M. Fähnle, T. Roth, M. Cinchetti, and M. Aeschlimann, “Explaining the paradoxical diversity of ultrafast laser-induced demagnetization..,” *Nature materials*, vol. 9, pp. 259–65, Mar. 2010.
- [39] D. Steiauf and M. Fähnle, “Elliott-Yafet mechanism and the discussion of femtosecond magnetization dynamics,” *Physical Review B*, vol. 79, pp. 1–3, Apr. 2009.
- [40] Y. Yafet, “g factors and spin-lattice relaxation of conduction electrons,” *Solid State Physics*, vol. 14, pp. 1–98, 1963.
- [41] M. Fähnle and C. Illg, “Electron theory of fast and ultrafast dissipative magnetization dynamics.,” *Journal of physics. Condensed matter : an Institute of Physics journal*, vol. 23, p. 493201, Dec. 2011.
- [42] J. Walowski, G. Müller, M. Djordjevic, M. Münzenberg, M. Kläui, C. Vaz, and J. Bland, “Energy Equilibration Processes of Electrons, Magnons, and Phonons at the Femtosecond Time Scale,” *Physical Review Letters*, vol. 101, pp. 1–4, Dec. 2008.
- [43] M. Fähnle, J. Seib, and C. Illg, “Relating Gilbert damping and ultrafast laser-induced demagnetization,” *Physical Review B*, vol. 82, pp. 1–4, Oct. 2010.
- [44] M. Krauß, T. Roth, S. Alebrand, D. Steil, M. Cinchetti, M. Aeschlimann, and H. Schneider, “Ultrafast demagnetization of ferromagnetic transition metals: The role of the Coulomb interaction,” *Physical Review B*, vol. 80, pp. 1–4, Nov. 2009.
- [45] M. Battiato and K. Carva, “Superdiffusive Spin Transport as a Mechanism of Ultrafast Demagnetization,” *Physical review letters*, vol. 105, p. 027203, July 2010.
- [46] J. Chen, D. Tzou, and J. Beraun, “A semiclassical two-temperature model for ultrafast laser heating,” *International journal of heat and mass transfer*, vol. 49, pp. 307–316, Jan. 2006.
- [47] M. Mansuripur, *The Physical Principles of Magneto-Optical Recording*. Cambridge, UK: Cambridge University Press, 1995.
- [48] M. Mansuripur and M. Ruane, “Mean-field analysis of amorphous rare earth-transition metal alloys for thermomagnetic recording,” *IEEE Transactions on Magnetics*, vol. 22, pp. 33–43, Jan. 1986.

- [49] L. Néel, “Proprietes magnetiques des ferrites - ferrimagnetisme et antiferromagnetisme,” *Compt. Rend.*, vol. 203, p. 304, 1936.
- [50] G. Buendía and R. Cardona, “Monte Carlo study of a mixed spin-3/2 and spin-1/2 Ising ferrimagnetic model,” *Physical Review B*, vol. 59, pp. 6784–6789, Mar. 1999.
- [51] R. C. Jones, “Impurity spin wave models in a simple cubic Heisenberg ferromagnet,” *Journal of Physics C: Solid State Physics*, vol. 4, pp. 2903–2918, Dec. 1971.
- [52] K. Binder, “Finite size scaling analysis of ising model block distribution functions,” *Zeitschrift für Physik B Condensed Matter*, vol. 43, pp. 119–140, June 1981.
- [53] T. Nakamura, “Nonequilibrium dynamic correlation-length scaling method,” *Physical Review B*, vol. 82, no. 1, p. 014427, 2010.
- [54] A. Biternas, R. Chantrell, and U. Nowak, “Behavior of the antiferromagnetic layer during training in exchange-biased bilayers within the domain state model,” *Physical Review B*, vol. 82, pp. 1–10, Oct. 2010.
- [55] M. Bartolozzi, T. Surungan, D. Leinweber, and A. Williams, “Spin-glass behavior of the antiferromagnetic Ising model on a scale-free network,” *Physical Review B*, vol. 73, pp. 1–8, June 2006.
- [56] W. P. Wolf, “The Ising model and real magnetic materials,” *Brazilian Journal of Physics*, vol. 30, pp. 794–810, Dec. 2000.
- [57] N. Metropolis, A. W. Rosenbluth, M. N. Rosenbluth, A. H. Teller, and E. Teller, “Equation of State Calculations by Fast Computing Machines,” *The Journal of Chemical Physics*, vol. 21, no. 6, p. 1087, 1953.
- [58] K. Binder, “Finite size scaling analysis of ising model block distribution functions,” *Zeitschrift für Physik B Condensed Matter*, vol. 43, pp. 119–140, June 1981.
- [59] T. Ostler, R. Evans, R. Chantrell, U. Atxitia, O. Chubykalo-Fesenko, I. Radu, R. Abrudan, F. Radu, A. Tsukamoto, A. Itoh, A. Kirilyuk, T. Rasing, and A. Kimel, “Crystallographically amorphous ferrimagnetic alloys: Comparing a localized atomistic spin model with experiments,” *Physical Review B*, vol. 84, pp. 1–9, July 2011.
- [60] N. Majlis, *The Quantum Theory of Magnetism*. Singapore: World Scientific, 2 ed., 2007.
- [61] F. Reif, *Fundamentals of Statistical and Thermal Physics*. New York: McGraw-Hill, 1 ed., 1965.
- [62] C. Kittel, *Introduction to Solid State Physics*. New York: John Wiley & Sons, 7 ed., 1996.
- [63] T. Gilbert, “Classics in Magnetism A Phenomenological Theory of Damping in Ferromagnetic Materials,” *IEEE Transactions on Magnetism*, vol. 40, pp. 3443–3449, Nov. 2004.

- [64] A. I. M. Rae, *Quantum Mechanics*. London, England: Institute of Physics, 3 ed., 1992.
- [65] L. D. Landau and E. M. Lifshitz, “Theory of the dispersion of magnetic permeability in ferromagnetic bodies,” *Journal of Physics Z Soviet Union*, vol. 8, pp. 153–169, 1935.
- [66] S. Iida, “The difference between gilbert’s and landau-lifshitz’s equations,” *Journal of Physics and Chemistry of Solids*, vol. 24, pp. 625–630, May 1963.
- [67] H. Suhl, *Relaxation Processes in Micromagnetics*. International Series of Monographs on Physics, Oxford: Oxford University Press, 2007.
- [68] D. A. Garanin, “Fokker-Planck and Landau-Lifshitz-Bloch equations for classical ferromagnets,” *Physical Review B*, vol. 55, p. 3050, Feb. 1997.
- [69] C. Schieback, D. Hinzke, M. Kläui, U. Nowak, and P. Nielaba, “Temperature dependence of the current-induced domain wall motion from a modified Landau-Lifshitz-Bloch equation,” *Physical Review B*, vol. 80, pp. 1–8, Dec. 2009.
- [70] O. Chubykalo-Fesenko, U. Nowak, R. Chantrell, and D. Garanin, “Dynamic approach for micromagnetics close to the Curie temperature,” *Physical Review B*, vol. 74, pp. 1–5, Sept. 2006.
- [71] P. Hansen, C. Clausen, G. Much, M. Rosenkranz, and K. Witter, “Magnetic and magneto-optical properties of rare-earth transition-metal alloys containing Gd, Tb, Fe, Co,” *Journal of applied physics*, vol. 66, no. 2, pp. 756–767, 1989.
- [72] Z. Chen, R. Gao, Z. Wang, C. Xu, D. Chen, and T. Lai, “Field-dependent ultrafast dynamics and mechanism of magnetization reversal across ferrimagnetic compensation points in GdFeCo amorphous alloy films,” *Journal of Applied Physics*, vol. 108, no. 2, p. 023902, 2010.
- [73] C. Stanciu, A. Tsukamoto, A. Kimel, F. Hansteen, A. Kirilyuk, A. Itoh, and T. Rasing, “Subpicosecond magnetization reversal across ferrimagnetic compensation points,” *Physical review letters*, vol. 99, p. 217204, Nov. 2007.
- [74] C. Stanciu, A. Kimel, F. Hansteen, A. Tsukamoto, A. Itoh, A. Kirilyuk, and T. Rasing, “Ultrafast spin dynamics across compensation points in ferrimagnetic GdFeCo: The role of angular momentum compensation,” *Physical Review B*, vol. 73, pp. 1–4, June 2006.
- [75] A. Tsukamoto, T. Sato, S. Toriumi, and A. Itoh, “Precessional switching by ultrashort pulse laser: Beyond room temperature ferromagnetic resonance limit,” *Journal of Applied Physics*, vol. 109, no. 7, p. 07D302, 2011.
- [76] T. Rasing, H. V. D. Berg, T. Gerrits, and J. Hohlfeld, “Ultrafast Magnetization and Switching Dynamics,” in *Spin Dynamics in Confined Magnetic Structures II* (K. Hillebrands, Burkard; Ounadjela, ed.), vol. 252, ch. 7, pp. 213–252, New York: Springer, 2003.

- [77] K. Helmut and P. Stuart, eds., *Novel Techniques for Characterizing and Preparing Samples*, vol. 3 of *Handbook of Magnetism and Advanced Magnetic Materials*. John Wiley and Sons, Ltd., 2007.
- [78] K. Vahaplar, *Ultrafast Path for Magnetization Reversal in Ferrimagnetic GdFeCo Films*. PhD thesis, Radboud University Nijmegen, 2011.
- [79] A. Delobbe, A.-M. Dias, M. Finazzi, L. Stichauer, J.-P. Kappler, and G. Krill, “X-ray magnetic circular dichroism study on CeFe₂,” *Europhysics Letters (EPL)*, vol. 43, pp. 320–325, Aug. 1998.
- [80] W. Heisenberg, “Zur Theorie des Ferromagnetismus,” *Zeitschrift für Physik*, vol. 49, pp. 619–636, Sept. 1928.
- [81] H. Brown, “Heisenberg Ferromagnet with Biquadratic Exchange,” *Physical Review B*, vol. 4, pp. 115–121, July 1971.
- [82] O. N. Mryasov, A. J. Freeman, and A. I. Liechtenstein, “Theory of non-Heisenberg exchange: Results for localized and itinerant magnets,” *Journal of Applied Physics*, vol. 79, no. 8, p. 4805, 1996.
- [83] J. de Jong, I. Razdolski, A. Kalashnikova, R. Pisarev, A. Balbashov, A. Kirilyuk, T. Rasing, and A. Kimel, “Coherent Control of the Route of an Ultrafast Magnetic Phase Transition via Low-Amplitude Spin Precession,” *Physical Review Letters*, vol. 108, pp. 1–5, Apr. 2012.
- [84] P. Kloeden and E. Platen, *Numerical Solution of Stochastic Differential Equations*. Berlin Heidelberg: Springer, 1999.
- [85] U. Atxitia, O. Chubykalo-Fesenko, R. Chantrell, U. Nowak, and A. Rebei, “Ultrafast Spin Dynamics: The Effect of Colored Noise,” *Physical Review Letters*, vol. 102, pp. 1–4, Feb. 2009.
- [86] K. Miyazaki and K. Seki, “Brownian motion of spins revisited,” *The Journal of Chemical Physics*, vol. 108, no. 17, p. 7052, 1998.
- [87] W. Coffey, Y. Kalmykov, and J. T. Waldron, *The Langevin Equation: With Applications to Stochastic Problems in Physics, Chemistry, and Electrical Engineering*, vol. 14 of *World Scientific Series in Contemporary Chemical Physics*. Singapore: World Scientific, 2 ed., 2004.
- [88] J. Barker, B. Craig, R. Lamberton, a. Johnston, R. W. Chantrell, and O. Heinonen, “A model of the exchange bias setting process in magnetic read sensors,” *Applied Physics Letters*, vol. 95, no. 2, p. 022504, 2009.
- [89] A. Greiner, W. Strittmatter, and J. Honerkamp, “Numerical integration of stochastic differential equations,” *Journal of Statistical Physics*, vol. 51, pp. 95–108, Apr. 1988.

- [90] J. H. Mentink, M. V. Tretyakov, A. Fasolino, M. I. Katsnelson, and T. Rasing, “Stable and fast semi-implicit integration of the stochastic Landau-Lifshitz equation.,” *Journal of physics. Condensed matter : an Institute of Physics journal*, vol. 22, p. 176001, May 2010.
- [91] M. D’Aquino, C. Serpico, G. Coppola, I. D. Mayergoyz, and G. Bertotti, “Midpoint numerical technique for stochastic Landau-Lifshitz-Gilbert dynamics,” *Journal of Applied Physics*, vol. 99, no. 8, p. 08B905, 2006.
- [92] M. A. Ruderman and C. Kittel, “Indirect Exchange Coupling of Nuclear Magnetic Moments by Conduction Electrons,” *Physical Review*, vol. 96, pp. 99–102, Oct. 1954.
- [93] P. Yu, X. Jin, J. Kudrnovský, D. Wang, and P. Bruno, “Curie temperatures of fcc and bcc nickel and permalloy: Supercell and Green’s function methods,” *Physical Review B*, vol. 77, pp. 1–8, Feb. 2008.
- [94] C. Kittel, “On the gyromagnetic ratio and spectroscopic splitting factor of ferromagnetic substances,” *Physical Review*, vol. 76, no. 6, p. 743, 1949.
- [95] G. Connell, “Magneto-optics and amorphous metals: an optical storage revolution,” *Journal of Magnetism and Magnetic Materials*, vol. 54-57, pp. 1561–1566, Feb. 1986.
- [96] A. H. Morrish, *The Physical Principles of Magnetism*. New York: IEEE Press, 2001.
- [97] H. Kachkachi and D. Garanin, “Magnetic free energy at elevated temperatures and hysteresis of magnetic particles,” *Physica A*, vol. 291, p. 485, 2001.
- [98] G. S. Rushbrooke, J. Baker, and P. J. Wood, *Phase Transitions and Critical Phenomena*. New York: Academic Press, 1974.
- [99] N. Kazantseva, U. Nowak, R. W. Chantrell, J. Hohlfeld, A. Rebei, H. Search, C. Journals, A. Contact, M. Iopscience, and I. P. Address, “Slow recovery of the magnetisation after a sub-picosecond heat pulse,” *EPL (Europhysics Letters)*, vol. 81, p. 27004, Jan. 2008.
- [100] M. Binder, A. Weber, O. Mosendz, G. Woltersdorf, M. Izquierdo, I. Neudecker, J. Dahn, T. Hatchard, J.-U. Thiele, C. Back, and M. Scheinfein, “Magnetization dynamics of the ferrimagnet CoGd near the compensation of magnetization and angular momentum,” *Physical Review B*, vol. 74, pp. 1–5, Oct. 2006.
- [101] N. Smith, M. Carey, and J. Childress, “Measurement of Gilbert damping parameters in nanoscale CPP-GMR spin valves,” *Physical Review B*, vol. 81, no. 18, p. 184431, 2010.
- [102] M. Farle, “Ferromagnetic resonance of ultrathin metallic layers,” *Reports on Progress in Physics*, vol. 61, p. 755, 1998.
- [103] B. Schulz and K. Baberschke, “Crossover from in-plane to perpendicular magnetization in ultrathin Ni/Cu(001) films,” *Physical Review B*, vol. 50, pp. 13467–13471, Nov. 1994.

- [104] M. Corte-Real, Jun Du, K. Unruh, and J. Xiao, “Ferromagnetic resonance in granular soft magnetic films,” *Magnetics, IEEE Transactions on*, vol. 39, no. 5, pp. 3091–3093, 2003.
- [105] R. Wangsness, “Effective Ferrimagnetic Resonance Parameters with Gilbert-Type Relaxation Terms,” *Physical Review*, vol. 113, no. 3, p. 771, 1959.
- [106] R. Wangsness, “Magnetic Resonance in Ferrimagnetics,” *Physical Review*, vol. 93, no. 1, p. 68, 1954.
- [107] R. Weng and M. Kryder, “A new model of the erase process in single layer direct overwrite magneto-optical recording media,” *IEEE Transactions on Magnetics*, vol. 29, pp. 2177–2182, July 1993.
- [108] B. Koopmans, J. Ruigrok, F. Longa, and W. de Jonge, “Unifying Ultrafast Magnetization Dynamics,” *Physical Review Letters*, vol. 95, pp. 1–4, Dec. 2005.
- [109] I. Radu, G. Woltersdorf, M. Kiessling, A. Melnikov, U. Bovensiepen, J.-U. Thiele, and C. H. Back, “Laser-induced magnetization dynamics of lanthanide-doped permalloy thin films,” *Physical review letters*, vol. 102, p. 117201, Mar. 2009.
- [110] D. A. Garanin, “New integral relaxation time for thermal activation of magnetic particles,” *Europhysics Letters (EPL)*, vol. 48, pp. 486–490, Dec. 1999.
- [111] D. Hinzke and U. Nowak, “Domain Wall Motion by the Magnonic Spin Seebeck Effect,” *Physical Review Letters*, vol. 107, pp. 1–4, July 2011.
- [112] S. S. P. Parkin, M. Hayashi, and L. Thomas, “Magnetic domain-wall racetrack memory,” *Science (New York, N. Y.)*, vol. 320, pp. 190–4, Apr. 2008.
- [113] E. H. Wasserman, *Ferromagnetic Materials*, vol. 5. Holland: Elsevier, 1990.
- [114] C. Stamm, T. Kachel, N. Pontius, R. Mitzner, T. Quast, K. Holldack, S. Khan, C. Lupulescu, E. F. Aziz, M. Wietstruk, H. A. Dürr, and W. Eberhardt, “Femtosecond modification of electron localization and transfer of angular momentum in nickel,” *Nature materials*, vol. 6, pp. 740–3, Oct. 2007.
- [115] S. Khan, K. Holldack, T. Kachel, R. Mitzner, and T. Quast, “Femtosecond undulator radiation from sliced electron bunches,” *Physical Review Letters*, vol. 97, p. 074801, 2006.
- [116] I. Radu, C. Stamm, A. Eschenlohr, K. Vahaplar, T. Kachel, N. Pontius, R. Mitzner, K. Holldack, A. Föhlisch, F. Radu, R. F. L. Evans, T. A. Ostler, J. Mentink, R. W. Chantrell, A. Tsukamoto, A. Itoh, A. Kirilyuk, A. V. Kimel, and T. Rasing, “Ultrafast and distinct spin dynamics in magnetic alloys and heterostructures,” *Submitted*, 2012.
- [117] B. Glaubitz, S. Buschhorn, F. Brüßing, R. Abrudan, and H. Zabel, “Development of magnetic moments in $\text{Fe}_{1-x}\text{Ni}_x$ alloys,” *Journal of Physics: Condensed Matter*, vol. 23, p. 254210, June 2011.

- [118] Y. Kakehashi, "Theory of the invar effect in nife alloys," *Journal of the Physical Society of Japan*, vol. 51, pp. 3183–3191, 1982.
- [119] R. J. Wakelin and E. L. Yates, "A study of the order-disorder transformation in iron-nickel alloys in the region $FeNi_3$," *Proceedings of the Physical Society B.*, vol. 66, p. 221, 1952.
- [120] G. G. Scott and H. W. Sturmer, "Magnetomechanical ratios for fe-co alloys," *Physical Review*, vol. 184, p. 490, 1969.
- [121] J. Heron, M. Trassin, K. Ashraf, M. Gajek, Q. He, S. Yang, D. Nikonov, Y.-H. Chu, S. Salahuddin, and R. Ramesh, "Electric-Field-Induced Magnetization Reversal in a Ferromagnet-Multiferroic Heterostructure," *Physical Review Letters*, vol. 107, pp. 1–5, Nov. 2011.
- [122] J.-E. Wegrowe, S. Santos, M.-C. Ciornei, H.-J. Drouhin, and J. Rubí, "Magnetization reversal driven by spin injection: A diffusive spin-transfer effect," *Physical Review B*, vol. 77, pp. 1–9, May 2008.
- [123] A. G. Gurevich, *Magnetization Oscillations and Waves*. USA: CRC Press, 1976.
- [124] R. Radwański, "Anisotropic ferrimagnets in high magnetic fields," *Physica B+C*, vol. 142, pp. 57–64, Sept. 1986.
- [125] B. Skubic, J. Hellsvik, L. Nordström, and O. Eriksson, "A method for atomistic spin dynamics simulations: implementation and examples," *Journal of Physics: Condensed Matter*, vol. 20, p. 315203, Aug. 2008.
- [126] T. A. Ostler, J. Barker, R. F. L. Evans, R. W. Chantrell, U. Atxitia, O. Chubykalo-Fesenko, S. El Moussaoui, L. Le Guyader, E. Mengotti, L. J. Heyderman, F. Nolting, A. Tsukamoto, A. Itoh, D. Afanasiev, B. A. Ivanov, A. M. Kalashnikova, K. Vahaplar, J. Mentink, A. Kirilyuk, T. Rasing, and A. V. Kimel, "Ultrafast heating as a sufficient stimulus for magnetization reversal in a ferrimagnet.," *Nature communications*, vol. 3, p. 666, Jan. 2012.
- [127] N. A. Spaldin and M. Fiebig, "Materials science. The renaissance of magnetoelectric multiferroics.," *Science (New York, N.Y.)*, vol. 309, pp. 391–2, July 2005.
- [128] S. Gamble, M. Burkhardt, A. Kashuba, R. Allenspach, S. Parkin, H. Siegmann, and J. Stöhr, "Electric Field Induced Magnetic Anisotropy in a Ferromagnet," *Physical Review Letters*, vol. 102, pp. 1–4, May 2009.
- [129] U. A. Macizo, *Modeling of ultrafast laser-induced magnetization dynamics within the Landau-Lifshitz-Bloch approach*. PhD thesis, Instituto de Ciencia de Materiales de Madrid, 2012.
- [130] J. Mentink, J. Hellsvik, D. Afanasiev, B. Ivanov, A. Kirilyuk, A. Kimel, O. Eriksson, M. Katsnelson, and T. Rasing, "Ultrafast Spin Dynamics in Multisublattice Magnets," *Physical Review Letters*, vol. 108, pp. 1–5, Jan. 2012.

- [131] H. B. Callen, *Thermodynamics and an Introduction to Thermostatistics*. New York: John Wiley and Sons, 2 ed., 1985.
- [132] V. G. Bar'yakhtar, "Phenomenological description of relaxation processes in magnetic materials," *Zh. Eksp. Teor. Fiz*, vol. 87, pp. 1501–1508, 1984.
- [133] M. D'aquino, C. Serpico, and G. Miano, "Geometrical integration of Landau-Lifshitz-Gilbert equation based on the mid-point rule," *Journal of Computational Physics*, vol. 209, pp. 730–753, Nov. 2005.
- [134] U. Atxitia, T. A. Ostler, J. B. and R. F. L. Evans, R. W. Chantrell, and O. Chubykalo-Fesenko, "Ultrafast dynamical path for the switching of a ferrimagnet after femtosecond heating," *in preparation*, 2012.
- [135] A. Haug, *Theoretical Solid State Physics*, vol. 1. Oxford, UK: Pergamon Press, 1 ed., 1972.
- [136] A. Bergman, A. Taroni, L. Bergqvist, J. Hellsvik, B. Hjörvarsson, and O. Eriksson, "Magnon softening in a ferromagnetic monolayer: A first-principles spin dynamics study," *Physical Review B*, vol. 81, pp. 1–5, Apr. 2010.
- [137] A. Tseng, C. Chen, and K. Ma, "Electron beam lithography in nanoscale fabrication: recent development," *IEEE Transactions on Electronics Packaging Manufacturing*, vol. 26, pp. 141–149, Apr. 2003.
- [138] L. L. Guyader, S. E. Moussaoui, E. Mengotti, L. J. Heyderman, F. Nolting, A. Tsukamoto, A. Itoh, A. Kirilyuk, T. Rasing, and A. V. Kimel, "Nanostructuring of gdfeco thin films for laser induced magnetization switching," *Journal of the Magnetism Society of Japan*, vol. 36, no. 1-2, pp. 21–23, 2012.
- [139] A. Scholl, H. Ohldag, F. Nolting, J. Stöhr, and H. A. Padmore, "X-ray photoemission electron microscopy, a tool for the investigation of complex magnetic structures (invited)," *Review of Scientific Instruments*, vol. 73, no. 3, p. 1362, 2002.
- [140] J. Smythe, F. Moss, and P. McClintock, "Ito versus Stratonovich revisited," *Physics Letters A*, vol. 24, no. 1, pp. 175–187, 1983.
- [141] D. V. Berkov and N. L. Gorn, "Thermally activated processes in magnetic systems consisting of rigid dipoles: equivalence of the Ito and Stratonovich stochastic calculus," *Journal of Physics: Condensed Matter*, vol. 14, pp. L281–L287, Apr. 2002.
- [142] L. Szunyogh, B. Lazarovits, L. Udvardi, J. Jackson, and U. Nowak, "Giant magnetic anisotropy of the bulk antiferromagnets IrMn and IrMn₃ from first principles," *Physical Review B*, vol. 79, pp. 1–4, Jan. 2009.
- [143] W. Scholz, *Micromagnetic Simulation of Thermally Activated Switching in Fine Particles*. PhD thesis, Vienna University of Technology, 1999.

- [144] H. Risken, *The Fokker-Planck Equation: Methods of Solution and Applications*. Springer Series in Synergetics, Berlin: Springer, 2 ed., 1989.

List of Publications by T. A. Ostler

- [1] *T. A. Ostler, R. F. L. Evans, R. W. Chantrell, U. Atxitia, O. Chubykalo-Fesenko, I. Radu, R. Abrudan, F. Radu, A. Tsukamoto, A. Itoh, A. Kirilyuk, Th. Rasing and A. Kimel*
“*Crystallographically Amorphous Ferrimagnetic Alloys: Comparing a Localized Atomistic Spin Model with Experiments*”
Physical Review B, **84**, 024407 (2011)
- [2] *I. Radu, K. Vahaplar, C. Stamm, T. Kachel, N. Pontius, H. A. Dürr, T. A. Ostler, J. Barker, R. F. L. Evans, R. W. Chantrell, A. Tsukamoto, A. Itoh, A. Kirilyuk, Th. Rasing and A. V. Kimel*
“*Transient Ferromagnetic-Like State Mediating Ultrafast Reversal of Antiferromagnetically Coupled Spins*”
Nature, **472**, 205-208 (2011)
- [3] *T. A. Ostler, J. Barker, R. F. L. Evans, R. W. Chantrell, U. Atxitia, O. Chubykalo-Fesenko, S. El Moussaoui, L. Le Guyader, E. Mengotti, L. J. Heyderman, F. Nolting, A. Tsukamoto, A. Itoh, D. Afanasiev, B. A. Ivanov, A. M. Kalashnikova, K. Vahaplar, J. Mentink, A. Kirilyuk, T. Rasing, and A. V. Kimel*
“*Ultrafast heating as a sufficient stimulus for magnetization reversal in a ferrimagnet.*”
Nature communications, **3**, 666 (2012)
- [4] *I. Radu, C. Stamm, A. Eschenlohr, K. Vahaplar, T. Kachel, N. Pontius, R. Mitzner, K. Holldack, A. Föhlisch, F. Radu, R. F. L. Evans, T. A. Ostler, J. Mentink, R. W. Chantrell, A. Tsukamoto, A. Itoh, A. Kirilyuk, A. V. Kimel, and T. Rasing*
“*Ultrafast and Distinct Spin Dynamics in Magnetic Alloys and Heterostructures*”
Submitted, 2012
- [5] *U. Atxitia, T. A. Ostler, J. Barker, R. F. L. Evans, R. W. Chantrell, and O. Chubykalo-Fesenko*
“*Ultrafast Dynamical Path for the Switching of a Ferrimagnet After Femtosecond Heating*”
Submitted, 2012

- [6] M. Ellis, *T. A. Ostler* and R. W. Chantrell
“*Classical Spin Model of the Relaxation Dynamics of Rare Earth Doped Permalloy*”
Submitted, 2012